Preparation and Application of Two-dimensional and Three-dimensional Reticular Materials: Metal Organic Frameworks and Covalent Organic Frameworks

DISSERTATION

zur Erlangung des akademischen Grades eines Doktors

der Naturwissenschaften (Dr. rer. nat.)

in der Bayreuther Graduiertenschule für Mathematik und

Naturwissenschaften (BayNAT)

der Universität Bayreuth

vorgelegt von

Chenhui Ding

Fuzhou City, Jiangxi Province, China

Bayreuth, April 2024

This doctoral thesis was prepared at the department of Macromolecular Chemistry II at the University of Bayreuth from 12/2019 until 12/2023 and was supervised by Prof. Dr. Seema Agarwal.

This is a full reprint of the thesis submitted to obtain the academic degree of Doctor of Natural Sciences (Dr. ret. nat.) and approved by the Bayreuth Graduate School of Mathematical and Natural Sciences (BayNAT) of the University of Bayreuth.

From of the dissertation: cumulative dissertation

Date of submission: 15.04.2024

Admission by the executive board: 15.05.2024

Date of defense: 27.11.2024

Acting director: Prof. Dr. Jürgen Köhler

Doctoral committee:

Prof. Dr. Seema Agarwal (reviewer)

Prof. Dr. Jürgen Senker (reviewer)

Prof. Dr. André Gröschel (chairman)

Prof. Dr. Nella Vargas Barbosa

Prof. Dr. Arne Thomas (external reviewer)

The presented dissertation is written as cumulative dissertation.

The following papers originated from this dissertation:

(1) Chenhui Ding, Marion Breunig, Jana Timm, Roland Marschall, Jürgen Senker, Seema Agarwal. Flexible, Mechanically Stable, Porous Self-Standing Microfiber Network Membranes of Covalent Organic Frameworks: Preparation Method and Characterization. Advanced Functional Materials, **2021**, 31(49), 2106507.
DOI: 10.1002/adfm.202106507

Discussion in **section 2.1**, reprinted in **section 4.1**.

(2) Yingying Du, **Chenhui Ding**, Jana Timm, Roland Marschall, Seema Agarwal. Template - assisted Preparation of Self-standing 2D-MOF Membranes for Application in Cascade Reactions. ChemCatChem, **2022**, 14(22), e202201040.
DOI: 10.1002/cctc.202201040

Discussion in **section 2.2**, reprinted in **section 4.2**.

(3) Marion Breunig, Jian Zhu, **Chenhui Ding**, Renée Siegel, Seema Agarwal, Jürgen Senker. Electrospun, non-woven fiber membranes of porous polyimides with high carbon dioxide uptakes and selectivities. Microporous and Mesoporous Materials, **2022**, 329, 111519.
DOI: 10.1016/j.micromeso.2021.111519

Discussion in **section 2.3**, reprinted in **section 4.3**.

(4) Chenhui Ding, Yingying Du, Seema Agarwal. Open-Cell Robust COF-Nanowire Network Sponges as Sustainable Adsorbent and Filter. Advanced Functional Materials, **2023**, 2309938.
DOI: 10.1002/adfm.202309938

Discussion in **section 2.4**, reprinted in **section 4.4**.

(5) Yingying Du, **Chenhui Ding**, Seema Agarwal. Sustainable Hierarchically Porous Reusable Metal-Organic Framework Sponge as a Heterogeneous Catalyst and Catalytic Filter for Degradation of Organic Dyes. Advanced Energy and Sustainability Research, **2023**, 2300218.
DOI: 10.1002/aesr.202300218

Discussion in **section 2.5**, reprinted in **section 4.5**.

Table of Contents

List of Symbols and Abbreviations

MOFs	Metal Organic Frameworks
COFs	Covalent Organic Frameworks
1D	One-dimensional
2D	Two-dimensional
3D	Three-dimensional
MOPI	Microporous organic polyimides
H	Hydrogen
B	Boron
C	Carbon
N	Nitrogen
O	Oxygen
S	Sulfur
ChCl	Choline chloride
HEIP	Hexafluorisopropanol
DESs	Deep eutectic solvents
BET	Brunauer Emmet and Teller
INA	Isonicotinic acid
CTAB	Cetyltrimethylammonium bromide
SEM	Scanning Electron Microscope
TEM	Transmission Electron Microscope
DLS	Dynamic Light Scattering
SLS	Scheduler Load Simulator
FCS	Fluorescence Correlation Spectroscopy
XRD	X-ray Diffraction
SAXS	Small Angle X-ray Scattering
NTA	Nanoparticle Tracking Analysis
TRPS	Tunable Resistive Pulse Sensing

List of Symbols and Abbreviations

AFM	Atomic Force Microscope
SEC	Size-Exclusion Chromatography
DSC	Differential scanning calorimetry
DTAB	Dodecyltrimethylammonium bromide
PAN	Polyacrylonitrile
PES	Polyethersulfone
PSF	Polysulfone
PS	Polystyrene
PVDF	Poly(vinylidene fluoride)
$\alpha\text{-}Al_2O_3$	α-alumina porous substrate
APTES	3-aminopropyltriethoxysilane
HBT	2-(2-Hydroxyphenyl)-benzothiazole
PMMA	Poly(methyl methacrylate)
MMMs	Mixed matrix membranes
$Co(AC)_2$	Cobalt(II) acetate tetrahydrate
2-MeIm	2-methylimmidazole
CO_2	Carbon dioxide
CH_4	Methane
N_2	Nitrogen
AG	Agarose
CB	Chlorobenzene
GO	Graphene oxide
rGO	Reduced graphene oxide
PTSA	p-Toluenesulfonic acid
Dq	Diaminoanthraquinone
$ZnCl_2$	Zinc chloride
PM	Particulate matter
PVP	Poly(vinyl pyrrolidone)
NaCl	Sodium Chloride

List of Symbols and Abbreviations

$MgCl_2$	Magnesium chloride
$AlCl_3$	Aluminum chloride
$CuCl_2$	Copper(II) chloride
$CaCl_2$	Calcium chloride
KH_2PO_4	Monopotassium phosphate
NaH_2PO_4	Natriumdihydrogenphosphate
PEO	Poly(ethylene oxide)
PLLA	Poly(l-lactide)
CH_2Cl_2	Dichloromethane
DMF	Dimethylformamide
CA	Cellulose acetate
PVA	Poly(vinyl alcohol)
HA	Hyaluronic acid
CS	Chitosan
SF	Silk fibroin
SA	Sodium alginate
PMA	Polyacrylamide
PC	Polycarbonate
PA	Polyamide
PI	Polyimide
LiCl	Lithium chloride
H_2O	Water
DMAc	Dimethylacetamide
$CHCl_3$	Chloroform
TiO_2	Titanium dioxide
SiO_2	Silicon dioxide
BN	Boron nitride
ZnO	Zinc oxide
Al_2O_3	Aluminium oxide

List of Symbols and Abbreviations

CuO	Copper(II) oxide
CdS	Cadmium sulfide
ZnS	Zinc sulfide
Ag	Silver
Au	Gold
Cu	Copper
Ni	Nickel
CNT	Carbon nanotube
PVAc	Poly(vinyl acetate)
PU	Polyurethane
$ZrOCl_2$	Zirconyl chloride
ZrO_2	Zirconium dioxide
Fe_3O_4	Iron oxide
Tp	1,3,5-triformylphloroglucinol
Pa	p-Phenylenediamine
FT-IR	Fourier-transform infrared spectroscopy
DMSO	Dimethyl sulfoxide
r.t	Room temperature
°C	Degree Celsius
cm	Centimeter
μm	Micrometer
nm	Nanometer
kPa	Kilopascal
h	Hour
min	Minute
$m^2\ g^{-1}$	Square meter per gram
K	Kelvin
%	Percent
TAPM	Tetrakis (4-aminophenyl) methane

NTCA   Naphthalene-1,4,5,8-tetracarboxylic acid

Pa-SO$_3$H   2,5-diaminobenzenesulfonic acid

QSDFT   Quenched solid density functional theory

NLDFT   Non-local density functional theory

MB   Methylene blue

Rh B   Rhodamine B

8

Summary/Zusammenfassung

Summary

Over the past decade, metal-organic frameworks (MOFs) and covalent organic frameworks (COFs) have undeniably emerged as a leading class of advanced reticular materials, demonstrating considerable potential in environmental science, energy, chemical engineering, biomedical engineering, and other areas. However, the insoluble nature and processing challenges associated with COF and MOF powders significantly impede their practical applications. My work aims to develop methods for processing reticular MOFs and COFs into self-standing, two-dimensional (2D) and three-dimensional (3D) membranes and open-cell sponges. These self-standing materials with hierarchical porous structures, mechanical stability, and functional properties, thereby expected to unlock new possibilities for their applications. Moreover, recovering frameworks after use as self-standing membranes and sponges, rather than as powder, should be more efficient enhancing the recycling efficiency and cost-effectiveness, making it a more sustainable option for use. Therefore, the use of the self-standing MOF and COF objects in water purification and catalysis is also shown with recyclability possibility in a collaborative work.

Initially, my efforts were focused on devising a template-assisted process for creating porous, self-standing COF membranes. The method utilizes an electrospun polymer membrane as a sacrificial template skeleton on which in the first step COFs are grown. In the second step the template electrospun polymer is removed by solvent extraction to leave large dimension porous self-standing membranes entirely made-up of only COF. These COF membranes have high crystallinity, large surface area (1153 m² g^{-1}), and notable mechanical stability and flexibility, demonstrated by their ability to withstand bending over 10,000 times. Building on this groundwork, the method was adapted to fabricate functional (acidic and basic) self-standing MOF membranes. The effectiveness of functional MOF membranes as catalysts for one-pot cascade reactions

over multiple cycles has been demonstrated in collaboration with my laboratory colleague, Ms. Yingying Du.

The innovative aspect of this template-assisted framework synthesis involves immobilizing one of the MOF/COF components on the template electrospun polymer membranes by mixing it into the electrospinning solution. Upon exposure of the electrospun membrane to the second MOF/COF component under appropriate conditions, the in-situ framework growth on the template commences. Combining both framework components from the start with the template electrospinning polymer solution, followed by electrospinning and subsequent solid-state polymerization on the electrospun template, resulted in a non-crystalline porous organic polymer framework. This framework was utilized by Prof. Senker's group for CO_2 uptake and gas separation analysis (CO_2/N_2 and CO_2/CH_4). The CO_2 uptake was recorded at 3.0 mmol g^{-1} (0 °C, 1 bar), with CO_2/CH_4 selectivity approximately 20 (0 °C, 1 bar).

3D open-cell sponges, with their hierarchical porous structure, offer higher porosity and pore volume compared to 2D membranes, enhancing mass transfer. Despite challenges in achieving a mechanically stable pure framework (MOF/COF) sponge, this work successfully developed a composite sponge. This was accomplished by the in-situ growth of frameworks (MOF/COF) on a lightweight, open-cell skeleton sponge made from polyimide (PI) electrospun short fibers using poly acrylonitrile as binder. This work also demonstrates the utility and recyclability of these sponges as adsorbents and filters, exemplified by the removal of organic dyes from water.

The results are published in five peer-reviewed journals as follows: Advanced Functional Materials, 2021, 31(49), 2106507; ChemCatChem, 2022, 14(22), e202201040; Microporous and Mesoporous Materials, 2022, 329, 111519; Advanced Functional Materials, 2023, 2309938; Advanced Energy and Sustainability Research, 2023, 2300218.

Zusammenfassung

Über das letzte Jahrzehnt hinweg haben sich metallorganische Gerüstverbindungen (MOFs) und kovalente organische Gerüstverbindungen (COFs) zweifellos als führende Klasse fortschrittlicher netzartiger Materialien etabliert und dabei beträchtliches Potenzial in Umweltwissenschaften, Energie, chemischer Verfahrenstechnik, Biomedizintechnik und anderen Bereichen gezeigt. Allerdings behindern die unlösliche Natur und die Verarbeitungsherausforderungen von COF- und MOF-Pulvern erheblich ihre praktische Anwendung. Meine Arbeit zielt darauf ab, Methoden zur Verarbeitung von netzartigen MOFs und COFs zu selbsttragenden zweidimensionalen (2D) und dreidimensionalen (3D) Membranen und offenzelligen Schwämmen zu entwickeln. Diese selbsttragenden Materialien mit hierarchisch porösen Strukturen, mechanischer Stabilität und funktionalen Eigenschaften sollen somit neue Möglichkeiten für ihre Anwendungen erschließen. Darüber hinaus sollte die Rückgewinnung der Gerüstverbindungen nach ihrer Verwendung als selbsttragende Membranen und Schwämme, anstatt als Pulver, effizienter sein und die Recyclingeffizienz und Kosteneffektivität verbessern, was sie zu einer nachhaltigeren Option für den Einsatz macht. Daher wird in einer kooperativen Arbeit auch die Verwendung der selbsttragenden MOF- und COF-Objekte in der Wasseraufbereitung und Katalyse mit der Möglichkeit der Wiederverwertbarkeit gezeigt.

Zunächst lag der Fokus meiner Bemühungen auf der Entwicklung eines templateunterstützten Prozesses zur Herstellung poröser, selbsttragender COF-Membranen. Die Methode nutzt eine elektrogesponnene Polymermembran als opferhaften Vorlagengerüstrahmen, auf dem in einem ersten Schritt COFs wachsen. In einem zweiten Schritt wird das Vorlagen elektrogesponnene Polymer durch Lösungsmittelextraktion entfernt, um große dimensionale poröse selbsttragende Membranen vollständig aus COF zu hinterlassen. Diese COF-Membranen weisen eine hohe Kristallinität, eine große Oberfläche (1153 m² g^{-1}) und eine bemerkenswerte mechanische Stabilität und Flexibilität auf, die sich in ihrer Fähigkeit zeigen, über 10.000-mal gebogen zu werden. Aufbauend auf dieser Grundlage wurde die Methode

angepasst, um funktionale (saure und basische) selbsttragende MOF-Membranen herzustellen. Die Wirksamkeit von funktionalen MOF-Membranen als Katalysatoren für Ein-Topf-Kaskadenreaktionen über mehrere Zyklen hinweg wurde in Zusammenarbeit mit meiner Laborkollegin Frau Yingying Du demonstriert.

Das innovative Merkmal dieser templateunterstützten Rahmen-Synthese besteht darin, eines der MOF/COF-Komponenten auf den elektrogesponnenen Polymermembranen zu immobilisieren, indem es in die Elektrospinnlösung gemischt wird. Bei Einwirkung der elektrogesponnenen Membran auf die zweite MOF/COF-Komponente unter geeigneten Bedingungen beginnt das in-situ Rahmenwachstum auf der Vorlage. Durch die Kombination beider Rahmenkomponenten von Anfang an mit der Elektrospinn-Polymerlösung, gefolgt von der Elektrospinnung und anschließender Feststoffpolymerisation auf der elektrogesponnenen Vorlage, entstand ein nicht-kristallines poröses organisches Polymergerüst. Dieses Gerüst wurde von der Gruppe von Prof. Senker für CO_2-Aufnahme und Gasabscheidungsanalyse (CO_2/N_2 und CO_2/CH_4) genutzt. Die CO_2-Aufnahme wurde mit 3,0 mmol g^{-1} (0 °C, 1 bar) gemessen, mit einer CO_2/CH_4-Selektivität von etwa 20 (0 °C, 1 bar).

3D offenzellige Schwämme bieten aufgrund ihrer hierarchisch porösen Struktur eine höhere Porosität und Porenvolumen im Vergleich zu 2D-Membranen und verbessern so den Stofftransport. Trotz der Herausforderungen, einen mechanisch stabilen reinen Rahmen (MOF/COF)-Schwamm zu erreichen, wurde in dieser Arbeit erfolgreich ein Verbundschwamm entwickelt. Dies wurde durch das in-situ-Wachstum von Gerüsten (MOF/COF) auf einem leichten, offenzelligen Gerüstschwamm aus elektrogesponnenen kurzen Polyimidfasern unter Verwendung von Polyacrylnitril als Bindemittel erreicht. Diese Arbeit zeigt auch die Nützlichkeit und Recyclingfähigkeit dieser Schwämme als Adsorbentien und Filter, wie am Beispiel der Entfernung organischer Farbstoffe aus Wasser.

Die Ergebnisse sind in fünf peer-reviewed Zeitschriften wie folgt veröffentlicht: Advanced Functional Materials, 2021, 31(49), 2106507; ChemCatChem, 2022, 14(22), e202201040; Microporous and Mesoporous Materials, 2022, 329, 111519; Advanced Functional Materials, 2023, 2309938; Advanced Energy and Sustainability Research,

2023, 2300218.

1. Introduction

1.1 Motivation

In recent decades, the rapid and sustained development of the world economy has intensified social concerns about energy shortages and global environmental issues, causing many scientists in academia and industry to turn their attention to the materials world, especially porous materials [1-5]. Among these, crystalline porous reticular framework materials constructed through reticular chemistry, metal-organic frameworks (MOFs) and covalent organic frameworks (COFs) have gained prominence. Their swift advancement has broadened the scope of porous materials in numerous applications, such as gas separation and storage [6-8], sensors [9-10], optoelectronics [11-12], catalysis [13], environmental remediation [14-15], biomedical engineering [16-17] and energy [18-19].

MOFs are composed of organic linkers and metal ions/clusters through strong coordination bonds, while COF are formed by organic linkers through strong covalent bonds. Compared with traditional porous materials, MOFs and COFs exhibit large surface areas, high porosity, designable and modifiable framework structures. Despite several favourable properties, MOFs and COFs are usually one-dimensional (1D) micro/nano powders synthesized through solvothermal synthesis, which are insoluble in the common organic solvents and difficult-to-process, and greatly limits their practical applications. Therefore, in order to promote the application of porous materials in real life, it is necessary to develop new methods of constructing mechanically stable, self-standing monolithic MOF and COF architectures (two-dimensional (2D) films/membranes and three-dimensional (3D) aerogels/sponges/foams). [20-24] This is the aim of my research also. The various dimensionality COFs and MOFs would be highly promising for various applications (**Figure 1-1**).
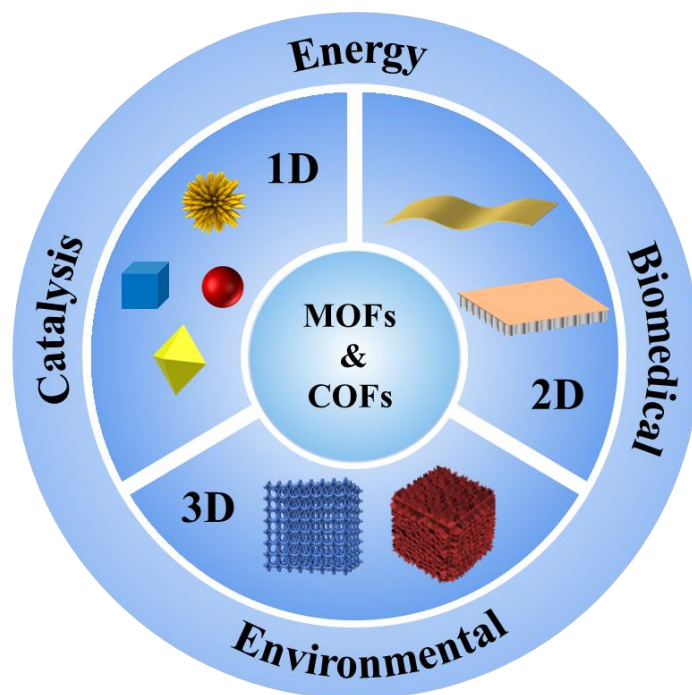
Figure. 1-1. 1D, 2D and 3D MOF and COF materials and their applications are demonstrated.

The versatile method of electrospinning is used in my research work to construct 2D MOF and COF porous membranes and 3D MOF and COF sponges.

In the following section, I review the available knowledge regarding the synthesis and applications of MOFs, COFs and other organic porous polymers, as well as the challenges faced in practical applications. At the same time, the electrospinning process and its characteristics and advantages in preparing 2D nanofiber membranes and 3D nanofiber monolithic materials are also introduced.

1.2 Reticular chemistry: MOFs and COFs

Reticular chemistry, derived from the Latin term "reticulum", meaning "small net" or "net-like", and involves using strong bonds to join individual building blocks (such as molecules and clusters) in a designed way to form broad and coherent structures with highly ordered arrangements. [25-26] Taking MOFs and COFs as examples, through the design of reticular chemistry and using different individual building blocks, the crystal framework structure and chemical composition can be accurately predicted, and give

them properties such as high surface area and porosity, well-defined pore size and good stability. [27-29] These unique properties make MOFs and COFs widely used in fields such as catalysis, environmental remediation, sensors, gas adsorption and separation, energy and biomedicine engineering.

MOFs are the first type of porous crystalline materials synthesized through reticular chemistry, composed of organic linkers and metal ions/clusters through strong coordination bonds, **Figure 1-2**. Yaghi and Li et al. [30] synthesized rectangular crystal MOFs in 1995 through solvothermal process using aromatic ligands and copper ions as raw materials, as show in **Figure 1-3**. The way in which the organic and inorganic units are connected through strong directional bonds allows the surface area of MOFs to far exceed that of all porous materials known so far. And the infinite combination of organic and inorganic chemistry has resulted in MOFs becoming the most diverse class of crystals (more than 20,000). [31]
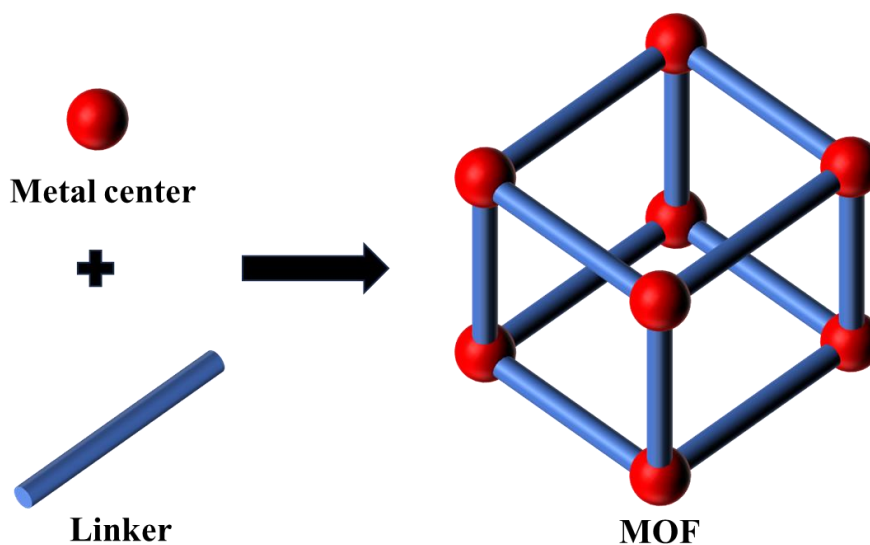

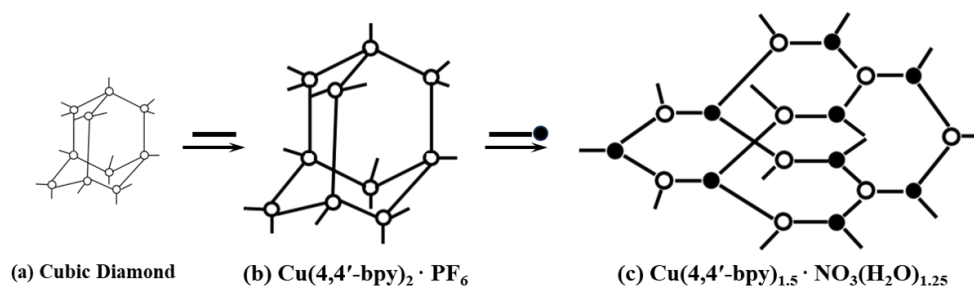**Figure 1-2.** Schematic structure of the MOF.

(a) Cubic Diamond   (b) $Cu(4,4'\text{-bpy})_2 \cdot PF_6$ (c) $Cu(4,4'\text{-bpy})_{1.5} \cdot NO_3(H_2O)_{1.25}$

Figure 1-3. Schematic illustration presenting the structural analogy recognized

between diamond and two new Cu(4,4'-bipyridine) solids. The length of the rod-like 4,4'-bipyridine ligand (shown as dark lines) allows the formation of open frameworks b and c that are based on tetrahedral coordination of Cu(I). The Cu(I) centers in parts b and c are distinguished as open and dark spheres for clarity.

COFs are the second type of reticular framework materials, which are composed entirely of molecular organic structural units connected by covalent bonds, **Figure 1-4**. Synthesis conditions need to be carefully designed to make the formation of covalent bonds microscopically reversible, thereby achieving crystallization. Moreover, COFs are porous crystals composed entirely of light elements (H, B, C, N, O, and S), showing low density and good chemical stability. Since Yaghi and colleagues first synthesized COFs (**Figure 1-5**) in 2005,[32] a variety of connections have been found for the synthesis of COFs, including boroxine-linked [33-34], imine-linked [35-36], azine-linked [37-38], hydrazone-linked [39-40], β-ketoenamine-linked [41-42], phenazine-linked [43-44], triazine-linked [45-46], and SP^2-carbon-linked [47-48]. However, compared to MOFs, the number of known COFs is relatively small (greater than 570).[49]
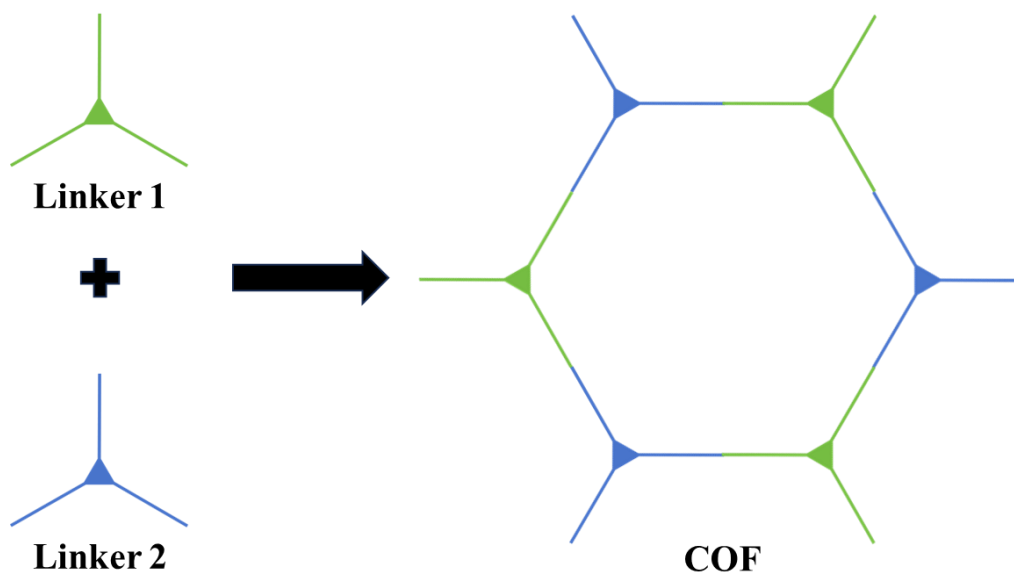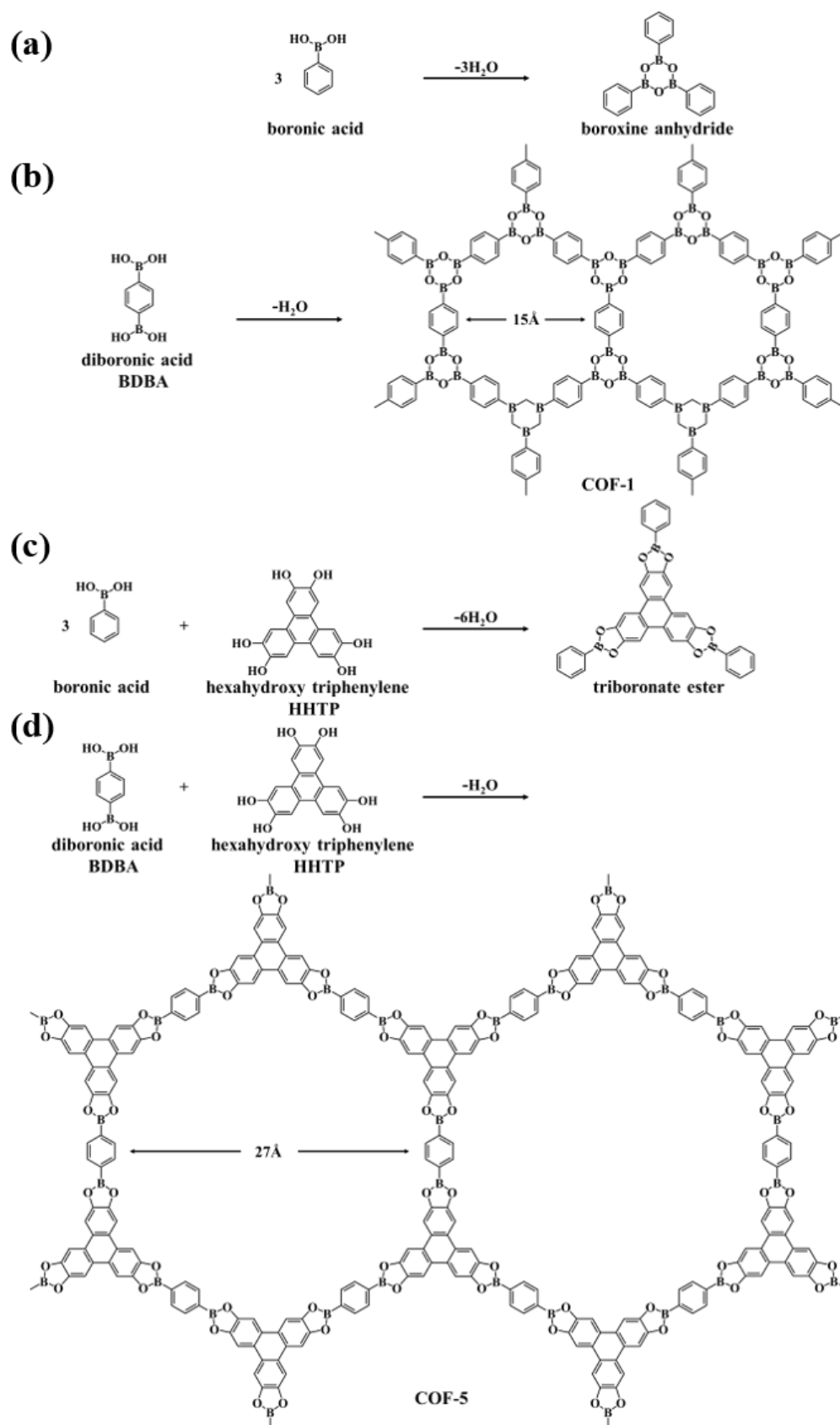

Figure 1-4. Schematic structure of the COF.

Figure 1-5. (a to d) Condensation reactions of boronic acids used to produce discrete molecules and extended COFs.

The solvothermal method is one of the common methods of preparing frameworks. It refers to a synthesis method in which the reaction is carried out in an autoclave in an organic solvent and the reactants are reacted at a certain temperature and the autogenous pressure of the solution. [50-51] It is the earliest method used to synthesize MOFs and COFs. However, in order to comply with the principles of safety and green chemistry in daily production, scientists have developed a variety of green solvents for the synthesis of MOFs and COFs. UiO-66 is one of the most common MOFs, and DMF is usually used as the reaction solvent, as show in **Figure 1-6**. Vaccaro et al. [52] chose 40 green solvents with low cost, low toxicity and complete biodegradability to synthesize UiO-66. Gao's research group [53] used choline chloride (ChCl)-hexafluoroisopropanol (HFIP) linked deep eutectic solvents (DESs) as the reaction solvent to synthesize highly crystalline COF particles without the need for additional catalysts. And by simply changing the molar ratio of ChCl and HFIP in DES, various imine-linked COFs with high crystallinity can be synthesized. Therefore, environmentally friendly solvothermal synthesis of MOFs and COFs is an important direction for future development. Although solvothermal method is the most commonly used method, the maintenance of high temperature, high pressure and long reaction time make it unsuitable for the large-scale production of MOFs and COFs.
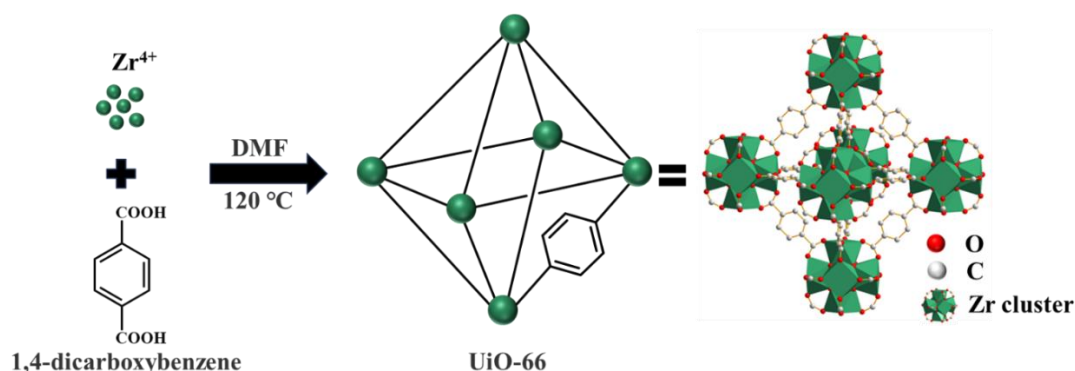

Figure 1-6. Schematic structure of UiO-66.

Microwave-assisted synthesis has been widely used in the preparation of nanoporous materials. [54-55] Based on the ability of the material to absorb microwave and convert it into heat, the material is heated rapidly by two mechanisms: ion conduction (for ions)

and dipole polarization (for dipoles), which shows the characteristics of fast heating speed, high thermal energy utilization rate, sensitive response and high product quality. As a result, the resulting particles exhibit uniform morphology and narrow particle size distribution. As many theories and experiments have shown, the nucleation and growth of MOFs and COFs crystals are thermodynamically controlled. Microwave-assisted synthesis can accelerate the nucleation and growth of crystals and shorten the entire synthesis time. Back in 2005, Chang et al. [56] synthesized chromium trimesate (designated as MIL-100) with microwave assistance for the first time. In addition, the yield of the product synthesized by this method in 4 hours is equivalent to that of the traditional electric heating in 4 days, and the synthesis speed is 20 times faster. Subsequently, Cooper and co-workers [57] obtained COF-5 by microwave heating in 20 minutes with a good yield (68-95%) and a high surface area ($S_{BET} = 2099$ m^2 g^{-1}), which is 200 times faster than conventional solvothermal synthesis. In conclusion, microwave-assisted synthesis could be a simple option for enhancing the production efficiency of MOFs and COFs.

Another step in the direction of green synthesis of frameworks is by using mechanochemistry, which is the generation of sufficient energy through mechanical action (grinding, extrusion, shearing) to induce changes in the structure and physical and chemical properties of substances, and induce chemical reactions. [58-59] Different from ordinary thermochemical reactions, mechanochemistry can quickly synthesize products without solvent or with a small amount of solvent, which is in line with the concept of low energy consumption and solvent-free green chemistry. In recent years, it has been widely used to synthesize porous organic polymers such as MOFs and COFs. In 2006, James and colleagues [60] were the first to produce MOF (Cu(INA)$_2$) in 10 min by mechanochemistry using a dry grinding reaction between copper (II) acetate monohydrate and isonicotinic acid (INA). The formed byproducts (water and acetic acid) can be captured by the micropores and can be expelled by heating. Another study showed that a rapid (90 mins) synthesis of Zr-based MOFs (UiO-66 and UiO-66-NH$_2$) grams was possible at room temperature using liquid-assisted grinding. [61] Banerjee's group [62] first synthesized three β-ketoenamine-linked COFs by room temperature

solvent-free mechanochemical grinding in 2013. The color change of the product can be clearly detected during the grinding process. In the mechanochemical synthesis process, the graphene-like layer of COF can be obtained, which is different from the solvothermal synthesis of COF. Therefore, compared with traditional solvothermal synthesis, mechanochemical synthesis is an environmentally friendly, fast and convenient method for large-scale synthesis of MOFs and COFs, which has great potential in industrial scale production.

The shape and size of MOF and COF particles can be effectively controlled by adding the modulating agents. In the process of solvothermal synthesis of MOFs, the addition of modulating agent can lead to the deprotonation of organic ligands and thus accelerate the nucleation rate of crystals. Secondly, the modulating agent can also compete with the organic ligand for the coordination sites of the metal clusters, resulting in a slowing down of the reaction kinetics, resulting in the formation of nanoparticles of different shapes and sizes. [63-64] Lu et al. [65] reported an acid/base (acetic acid/triethylamine) co-modulation method for the synthesis of monodisperse Zr-based MOF (UiO-66). Acetic acid is used to regulate the shape of the crystal, and triethylamine is used as a coregulator to control the nucleation of the crystal, so as to accurately control the shape, size and defects of UiO-66. Yaghi's research group [66] used aniline as a nucleation inhibitor and a competitive regulator of amino organic linking units to slow down the nucleation and growth of crystals. At the same time, the reversibility of imide bond formation and error correction process was enhanced, and several imide 3D COFs (COF-300, COF-303, LZU-79, and LZU-111) single crystals with particle sizes of tens of microns were obtained.

Surfactants are another class of modulators added during the synthesis of MOFs and COFs. In solution, a certain concentration of surfactant forms micelles and a stable layer of nano-sized droplets is formed at the interface of two immiscible phases. [67-68] Zhu and co-workers [69] synthesized the hierarchical mesoscopic structure Cr-based MOF (MIL-101) with various morphisms (microcrystals, nanospheres, and nanoflowers) using cationic surfactant cetyltrimethylammonium bromide (CTAB) as a structure-directing agent. Compared with bulk MIL-101, hierarchical mesoscopic MIL-

101 showed a faster adsorption rate for dyes. Zhao et al. [70] used dodecyltrimethylammonium bromide (DTAB) as a modulating agent to prepare hollow COFs microspheres through emulsion interfacial polymerization. The COF microsphere serves as an effective host for laccase immobilization and exhibits excellent adsorption performance and rapid degradation rate for tetracycline.

In addition to the above modulating agents, inorganic salts and ionic liquids can also be used as modulators for the synthesis of MOFs and COFs, and the size of the crystals can be changed by controlling the growth rate of the crystals. [71-72]

The highlighted extensive work shows that researchers have developed many methods for synthesizing MOF and COF particles. Their composition and functionalization are diverse, with different physical and chemical properties. To deepen the understanding of their properties, characterization of morphology, shape, size, porosity, and surface charge is required. Several methods are reported in the literature which are used in combination for a precise characterization of MOFs and COFs (**Figure 1-7**).[73]
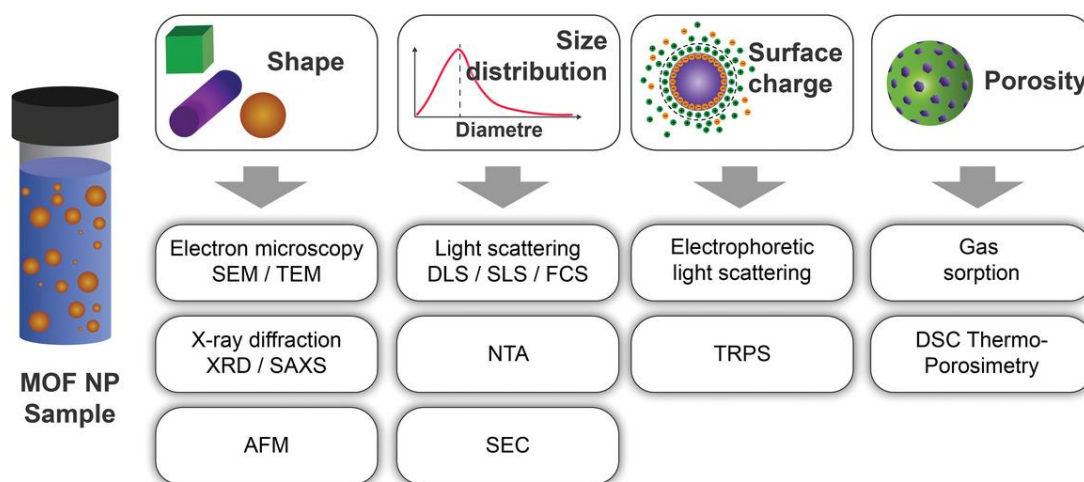

Figure 1-7. Characterization methods of reticular nanoparticles. The full names of NTA, TRPS, DSC, AFM and SEC are nanoparticle tracking analysis, tunable resistive pulse sensing, differential scanning calorimetry, atomic force microscopy and size exclusion chromatography respectively. Reprinted with permission from ref. [73]. Copyright (2020) Wiley-VCH.

1.2.1 2D MOF and COF films/membranes

In recent years, the size and shape of MOF and COF particles have been controlled through different methods, but powdered MOF and COF materials cannot meet the requirements of many practical applications. [13,74] The physical properties of micro/nanoparticles make it easy for MOFs and COFs to block reactors and pipelines during separation, catalysis and other industrial applications. At the same time, its poor processing performance leads to the problem of difficulty in recycling, and serious material loss inevitably occurs when flushed with fluid (gas or liquid). This has greatly hindered the development and application in the industrial field. Moreover, with the rapid development of economy and society, more and more membrane materials are developed, both in industrial development and in daily life. [75-76] Especially with the rapid development of low energy consumption, scalable and easy-to-operate membrane separation processes, various polymer membranes emerge like polyacrylonitrile (PAN) [77], polyethersulfone (PES) [78], polysulfone (PSF) [79], and poly(vinylidene fluoride) (PVDF) [80]. However, compared with MOFs and COFs, these polymers lack ordered nanopores and high porosity, which is not conducive to material transport. Therefore, processing MOFs and COFs into membranes can not only improve their processability, but also have help stimulate more research interest and applications in MOF and COF materials. Described below are some literature examples for the preparation of MOF/COF membranes.

a). *In-situ* solvothermal method

In situ solvothermal method of making framework membranes is also called direct growth method. In this process COF/MOF is grown as a thin film on a substrate. The substrate is put in the reaction solution (vertically or horizontally) during the solvothermal synthesis of frameworks. [81-82] Lai et al. [83] successfully synthesized the first continuous and well-intergrown $Zn_4O(BDC)_3$ (MOF-5) membranes on a porous substrate (α-Al_2O_3) through a solvothermal method. And the thickness of the membrane can be adjusted by controlling the reaction time. In 2011, Dichtel and co-workers [84] reported the growth of oriented 2D COF (COF-5) films on single-layer graphene via

in-situ solvothermal method. Moreover, compared with traditional solvothermal synthesized COF powders, COF films exhibit higher crystallinity.

In-situ solvothermal method is the most direct and convenient method for MOF and COF membranes preparation. However, it is usually difficult for organic linkers to form bonds with the surface of the substrate, resulting in poor heterogeneous nucleation of MOFs and COFs, and not easy to nucleate and grow directly on the surface of the substrate. Many studies have shown that functional modification of the substrate surface is an effective way to prepare dense MOF and COF membranes. [7,85] Huang and colleagues [86-87] successfully modified porous alumina substrates using 3-aminopropyltriethoxysilane (APTES), and subsequently prepared ZIF-22 and ZIF-90 membranes with high separation performance. In this study, the ethoxy group in APTES interacts with the -OH on the surface of alumina, while the $-NH_2$ at the other end reacts with the aldehyde group in the organic ligand and acts as a bridge between porous alumina and MOFs, allowing the MOFs to nucleate and grow at a fixed site and form a complete membrane.

In another study, [88] APTES was also used to modify an alumina substrate with amino functional groups, and imine-linked COF-LZU1 layer and azine-linked ACOF-1 layer were sequentially grown on the substrate through an in-situ solvothermal method. The formed COF-COF double-layer composite membrane has a staggered pore network and has excellent gas separation performance.

In addition, COF-MOF composite membranes can be obtained through similar methods. Qiu et al. [89] sequentially grew COF (COF-300) membrane and MOF (ZIF-8) membrane on the surface of polyaniline-modified SiO_2 discs to form COF-MOF composite membranes. The COF-MOF composite membranes have higher H_2/CO_2 gas mixture separation selectivity than individual single phase (COF or MOF) membranes. Therefore, the in-situ solvothermal method is one of the most effective methods for preparing MOF membranes, COF membranes, and their composite membranes.

b). Interface synthesis

Interfacial synthesis means that two highly reactive monomers are dissolved in two mutually incompatible solvents, polymerization occurs at the interface of the two liquid

phases, and a film is formed. [90-91] It is characterized by low reaction temperature and relatively simple process equipment, and is often used in the preparation of polymer films. In recent years, it has also been used in the preparation of MOF and COF films. Zhu's research group [92] used benzenehexathiol (HBT) as an organic ligand and prepared 2D π-d conjugated MOF (Cu-HBT) film through liquid/liquid (dichloromethane/water) interface reaction. The Cu-HBT film is composed of highly oriented nanosheets and has a room temperature conductivity of up to 1.580 S cm^{-1}, which was the highest value reported for coordination polymers at the time. Banerjee and colleagues [93] synthesized four different free-standing Schiff base COF films at room temperature via liquid/liquid interfacial polymerization.

And they can be easily transferred to various substrates and exhibit high solvent permeability for selective molecular separation in a variety of solvents.

MOF and COF films can also form at the gas/liquid interface. Hu et al. [94] developed a polymer-assisted space-confined strategy and successfully formed large-area free-standing MOF (Cu-CAT) based film at the air-liquid interface. Lai et al. [95] used the gas/liquid interface to synthesize large-area COF membranes for high-throughput organic solvent nanofiltration.

In summary, interfacial synthesis can synthesize large-area MOF and COF films at room temperature, but the lower reaction temperature also makes the time taken for the preparation of the films too long.

c). Layer-by-layer stacking

Layer-by-layer stacking was first used to prepare large-area graphene or graphene oxide films. In short, bulk materials are first transformed into nanosheets through methods such as ultrasound, mechanical grinding, and liquid intercalation. The nanosheets are then stacked layer by layer on the porous substrate via vacuum-assisted filtration or high-temperature evaporation to form a continuous large-area film. [96-97] This method is also suitable for preparing continuous MOF and COF films. Yang's research team [98] used methanol to destroy the interlayer interaction of the block to obtain MOF nanosheets, and adsorbed n-propanol on the surface of the resulting nanosheets to prevent their aggregation. The nanosheet dispersion did not precipitate for at least two

weeks. Finally, the nanosheet dispersion is coated on the porous alumina surface to form a sub-10 nm thick MOF film in a high temperature environment. And the MOF film exhibits excellent H_2/CO_2 separation performance. Jiang and colleagues [99] deposited 2D COF nanosheets and 1D cellulose nanofibers on the surface of a polyacrylonitrile membrane through vacuum-assisted filtration to form mixed-dimensional assembled COF composite membranes. The multiple interactions between COF nanosheets and cellulose nanofibers improve the stability of the COF membranes. Moreover, the COF membranes exhibit excellent performance in molecular separation.

d). Mixed Matrix Membranes

Mixed matrix membranes (MMMs) are made of mixture of fillers and matrix materials, consisting of the interaction of dispersed particulate phase (filler) and continuous polymer phase (matrix material). The filler and matrix are usually inorganic and polymer respectively, which makes MMMs have the advantages of organic and inorganic membrane materials at the same time, and the comprehensive performance is better. It is usually used to prepare reverse osmosis, forward osmosis and nanofiltration membranes. [100-101] Using powder MOF and COF materials as fillers not only improves their processability, but also integrates their own characteristics into the MMMs, improving the performance of the MMMs. [102-103] The dispersion of fillers in the matrix is one of the main challenges in preparing high-performance MMMs. Based on the theory of similar miscibility, Li et al. [104] selected appropriate polymers to form a 5-10 nm thick polymer layer on the surface of MOF particles, thereby achieving statistically random dispersion of MOF particles in the MMMs. Most COFs are purely organic structures and are easily prepared as 2D nanosheets with good compatibility in MMMs. Since the first report of COFs-based MMMs for efficient CO_2 separation in 2016, [105] COFs with various structures and functions have been used as fillers for MMMs and have achieved surprising results in separation. [106-107]

e). Electrospinning process

Electrospinning is a top-down, simple and effective method for preparing various nanofiber architectures. It has been also widely used to prepare composite fiber (organic, inorganic, and organic/inorganic materials) membranes. [108-109] Generally speaking, the

preparation of MOF composite fiber membranes through electrospinning is mainly divided into two methods: 1) direct electrospinning of MOF particles and polymer mixed solutions; 2) in-situ growth of MOF particles on electrospun fibers. [110-111] Wang et al. [112] dispersed four kinds of MOF (ZIF-8, Mg-MOF-74, MOF-199, and UiO-66-NH$_2$) particles in PAN solution or PS solution respectively, and directly prepared a series of high-loading MOF composite fiber membranes through electrospinning, which showed excellent performance in air filtration as filter membranes. Zhang et al. [113] first dissolved Cobalt (II) acetate tetrahydrate (Co(AC)$_2$) in PAN solution, obtained Co(AC)$_2$/PAN fibers through electrospinning, and then immersed them in an ethanol solution containing 2-methylimidazole (2-MeIm) ligand to prepare ZIF-67/PAN fiber membranes. Compared with embedding MOF particles in polymer fibers, MOF particles grow in situ on the surface of polymer fibers, which can expose more active sites and exhibit better mechanical properties.

Yan et al. [114] dispersed COF-SCU1 particles in PAN solution and obtained PAN@COF-SCU1 nanofibers through electrospinning. Thomas and colleagues [115] prepared a series of PAN@COF nanofiber membranes by in situ growing vertically aligned COF nanoplates on amino-functionalized electrospun PAN fiber substrate. I show in the present research methods of making self-standing pure COF membranes as described in the later section. The method is extended to the preparation of MOF membranes in collaboration with my Laboratory colleague Yingying Du.

1.2.2 3D MOF and COF monolithic materials

In today's society, with the rapid development of industrialization, the damage of heavy metals and organic pollutants to aquatic ecosystems has become an environmental issue of increasing concern. Among many water environment remediation methods, adsorption method is one of the most important and effective methods to remove pollutants from wastewater. [116-117] Many porous materials have been used as efficient adsorbents for pollutants, such as porous carbon materials, [118] porous organic polymers, [119] and zeolite [120]. Compared with other traditional porous materials, MOFs and COFs

have the characteristics of large surface area, high porosity and customizable framework structure. They are perfect materials as adsorbents, and substantial progress has been made. [14,121-122] However, MOFs and COFs are usually difficult-to-process powders that are difficult to separate and easy to lose during the water environment remediation process. Processing them into 3D monolithic materials (aerogel, sponge, and foam) is an effective way to solve this problem. Among them, 3D monolithic materials have the characteristics of well-defined hierarchical structure, high porosity and good mechanical stability, which are conducive to mass transfer, and the recovery and reuse of adsorbents. Therefore, processing MOFs and COFs into 3D monolithic materials can not only improve their processability, but also combine their advantages with the characteristics of the monolithic materials to develop adsorbents with better performance.

a). Pure MOF and COF monolithic materials

MOFs and COFs crystals nucleate and symbiosis occur in the solution, then excess solvent is removed through supercritical drying or freeze-drying to form pure MOF and COF monolithic materials. Kaskel et al. [123] dissolved trimesic acid and iron nitrate in ethanol, obtained iron-based MOF (MIL-100-Fe) gel through vigorous stirring, and obtained MOF aerogel through supercritical CO_2 drying. The combination of micropores and macropores in the MOF aerogel is beneficial to mass transfer, providing a possibility for designing new MOFs-based catalysts or catalytic carriers. Zamora and colleagues [124] synthesized three 2D imine-based COF aerogels with hierarchical porous structures, low density, and high porosity through three steps of sol-gel transition, solvent exchange, and supercritical CO_2 drying. Further, they compressed the COF aerogels into centimeter-scale COF-membranes, and showed excellent separation performance for CO_2/CH_4 or CO_2/N_2 mixed gases. [125] This also provides a new path for preparing self-standing COF membranes.

b). MOF-based and COF-based composite monolithic materials

Pure MOF and COF monolithic materials inherit the brittleness of crystals, resulting in poor mechanical stability. By combining MOFs and COFs with other carriers (wood, graphene, and commercial sponge), mechanically stable MOF-based and COF-based

composite monolithic materials can be obtained. [126-131] And there are usually two methods to achieve this: 1) MOF and COF powders are encapsulated inside the carrier; 2) MOF and COF powders are grown in-situ on the surface of the carrier.

Yamauchi and colleagues [132] dispersed MOF powders in aqueous solution of agarose (AG) and obtained MOF/AG aerogels by freeze-drying. MOF/AG aerogels exhibit excellent mechanical stability and flexibility, and can remove dyes from wastewater multiple times. Dong et al. [133] used a similar method to prepare COF@chitosan aerogels. At the same time, Pd was loaded into COF powders to form Pd@COF@chitosan composite aerogel, which can be used to construct high-efficiency continuous flow microreactor for chlorobenzene (CB) dechlorination in water at room temperature.

Encapsulating MOF and COF powders in carriers makes it easy to prepare MOF-based and COF-based composite monolithic materials, but it may cause some of the pores of MOFs and COFs to be blocked. This problem can be avoided by growing MOF and COF powders in-situ on the surface of the carrier.

Wang's research group [134] used strong wood aerogel as a carrier and loaded a large amount of Zr-MOF (UiO-66-NH$_2$) on its surface through two in-situ growths, thus achieve MOF-based aerogels with high MOF loading. And because the wood aerogel itself has directional and penetrating tubular microchannels, which is conducive to the rapid transmission of UO_2^{2+}, the MOF-based composite aerogels can efficiently extract uranium from natural seawater. The surface of layered graphene oxide (GO) is rich in oxygen-containing functional groups, which is conducive to the growth of COFs on its surface. Thomas et al. [23] dispersed graphene oxide (GO) nanosheets in the precursor solution of COFs. During the hydrothermal synthesis process, GO was reduced to reduced graphene oxide (rGO), and a large number of COFs grew on the surface. COF/rGO aerogels were further obtained by freeze-drying.

Electrospinning is employed as the primary tool in my research; therefore, the fundamentals of electrospinning are elucidated in the following section.

1.3 Electrospinning

Fiber has always been present in nature. Spiders rely on webs constructed of spider silk to capture food. Silkworms use cocoons of silk to protect them from harm. Humans make natural fibers into fabrics, clothes and paper, driving the development of society. [135-136] With the advent of the industrialization era, humans have developed many kinds of polymers and processed them into chemical fibers (polymer fibers). Chemical fibers have wide sources of raw materials, high yields and simple preparation methods. They have gradually replaced natural fibers and expanded the application of fibers in human life and production. [137]

With the rapid development of nanotechnology, nanofibers have received widespread attention due to their small diameter, high surface area, low density and excellent mechanical properties, and have been applied in many fields, including energy, environment, biomedicine, sensor and catalysis. [138-139] However, the diameter of fibers prepared by traditional methods (wet, dry, melt and gel spinning) is usually in the range of 10~100 μm and cannot form nanofibers. Therefore, scientists have developed many nanofiber fabrication techniques, including bicomponent fiber splitting, physical stretching, template synthesis, thermally induced phase separation, self-assembly, and electrospinning. [140-141] Taking into account the controllability of the preparation process, the complexity of the equipment, and the cost, electrospinning is currently the simplest, most effective, and the only method that can prepare continuous nanofibers on a large scale. Moreover, electrospinning can be used to obtain fabrics of different shapes (curled fibers, beaded fibers, aligned fibers, patterned fibers, and aerogels/sponges) and materials (metals, ceramics, organic, organic/inorganic hybrid), which have huge application potential in various fields. [142]

1.3.1 History of electrospinning

Electrospinning can be traced back to 1887, when Charles V. Boys [143] first reported the application of an external electric field to a viscous fluid to draw out fibers. This is

the prototype of the electrospinning process. In 1902, John Francis Cooley and William Morton [144-145] applied for two electrospinning patents respectively and introduced the electrospinning device. Subsequently, Zeleny [146] further supplemented electrospinning. It was not until 1934 that Antonin Formhals [147] published a patent for electrospinning equipment for producing cellulose acetate using acetone as a solvent. In the following years, he applied for a series of patents and disclosed electrospinning equipment, which promoted the development of electrospinning. [148] In 1936, Norton [149] applied for a patent for current- and air-flow-assisted melt electrospinning. In 1938 and 1939, Rozenblum and Sokolov used electrospinning to prepare cellulose acetate nanofibers for use as air filters and mass-produced them. [150] Since then, as scientists have gradually deepened their understanding of the principles of electrospinning. Between 1964 and 1969, Geoffrey Taylor proposed the "Taylor cone" mathematical model through systematic research on the shape change of fluid from spherical to conical during the electrospinning process. [151-153] In the following 20 years, scientists published many articles on the application of electrospinning, but they did not receive much attention. [154-155] With the development of science and technology, scientists can intuitively observe nanoscale materials through scientific instruments, and electrospinning has been further developed. In 1996, Darrell Reneker et al. [156] obtained more than 20 types of polymer nanofibers through electrospinning and studied the changes in fiber diameter. Since then, electrospinning has entered a stage of rapid development. Scientists have conducted extensive research on the process parameters and equipment types during the electrospinning process, as well as the synthesis and characterization of nanofibers. [157-159] Nowadays, electrospinning has become one of the most commonly used methods for preparing nanofibers, and has achieved surprising results in many fields. [160-162] And the number of publications on electrospinning is also increasing year by year, as shown in **Figure 1-8**. **Table 1-1** lists the development history of electrospinning.
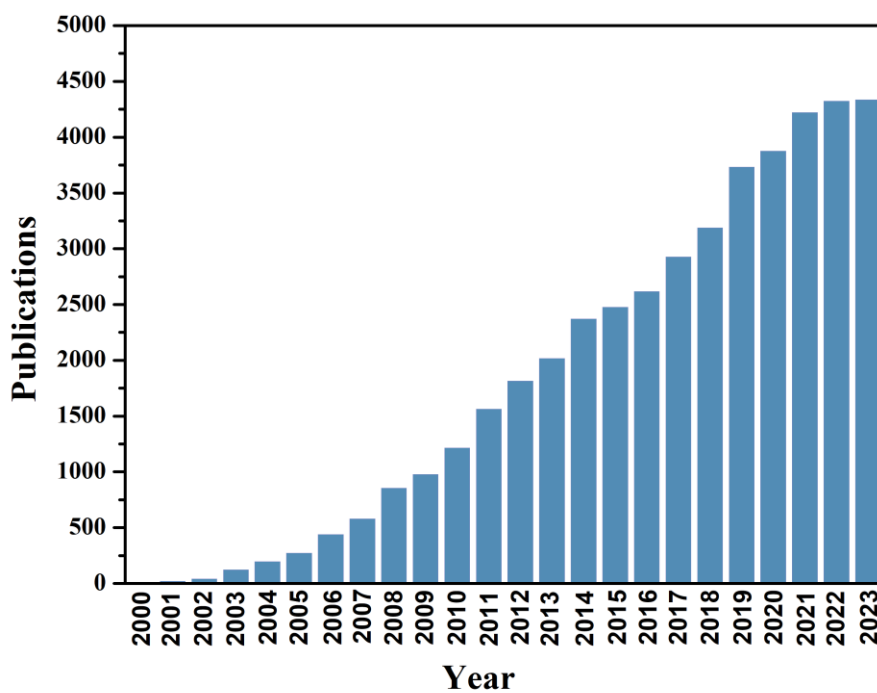
Figure 1-8. Number of publications on electrospinning. All data used are from Web of Science. The function we use is to analyze the results and create a citation report.

Table 1-1. A comprehensive account on the advancements in electrospinning process

Year	Nature of Advancements	Ref.
1887	Under an external electric field, Charles V. Boys pulled fibers out of the viscous fluid for the first time	[143]
1902	Cooley and Morton published patent on the electrospinning process	[144-145]
1914	John Zeleny discovers jets at the tip of metal capillaries	[146]
1934	Formhals publishes patent on electrospinning equipment for manufacturing cellulose acetate using acetone as solvent	[147]
1936	Norton Company publishes patent for melt-formed air fibers	[148]
1938-1940	Rozenblum and Sokolov use electrospinning to mass-produce air filters	[149]
1964-1969	Geoffrey Taylor established a mathematical model of the "Taylor cone"	[150]
1971	Baumgarten invents device to electrospinning acrylic microfibers	[151-153]
1978	Annis prepared polyurethane pads for use as vascular prostheses by electrospinning	[154-155]
1996	Darrell Reneker et al. obtained more than 20 polymer nanofibers through electrospinning	[156]
1997-2005	Research on process parameters and equipment types during electrospinning, synthesis and characterization of nanofibers	[157-159]
2006-Now	Electrospinning is used in many fields	[160-162]

1.3.2 Principle of electrospinning

The basic principle of electrospinning is that polymer liquid is ejected under the action of high-voltage electric field and forms continuous polymer nanofibers. An electrospinning device usually consists of three main parts: a sampling device

(including a syringe pump, a syringe and a spinneret), a high-voltage power supply and a collector, as shown in **Figure 1-9a**. In the process of electrospinning, the polymer liquid is extruded from the spinneret by the injection pump, and spherical droplets are formed under the action of surface tension. When a high voltage electric field is applied, a large amount of electric charge will accumulate on the surface of the droplet. When the charge repulsion on the droplet surface is greater than its surface tension, the spherical droplet changes shape, transforms into a "Taylor cone", and then ejected a polymer jet. The polymer jet experienced short distance steady stretching and whipping instability. In this process, the diameter of polymer jet decreases sharply, the solvent evaporates rapidly, forms solid fibers and accumulates on the collector, as shown in **Figure 1-9b**. [109]
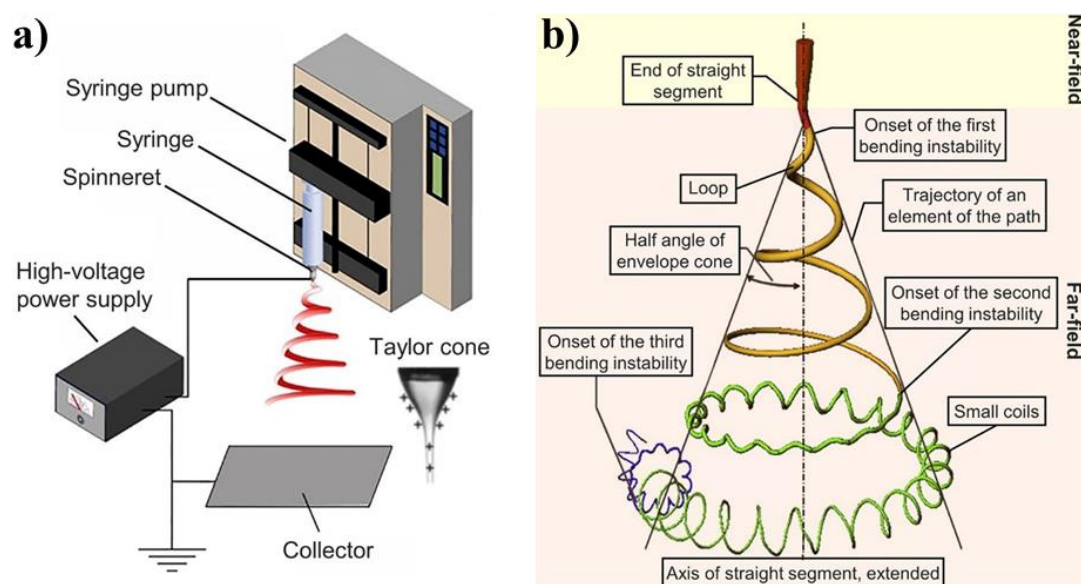
Figure 1-9. (a) The basic device for electrospinning. (b) Diagram showing the path of an electrospinning jet. Reprinted with permission from ref. [109]. Copyright (2019) American Chemical Society.

1.3.3 Parameters affecting electrospinning

One of the major advantages of preparing nanofibers by electrospinning is that the morphology of the fibers can be precisely controlled by adjusting various parameters

during the electrospinning process to meet different needs. It can be mainly divided into three influencing parameters, namely solution parameters, environmental parameters and process parameters. [163-164]

a). Solution parameters

Solution parameters include concentration/viscosity, molecular weight, conductivity, surface tension, and solvent type. [165-166] The molecular weight of the polymer directly affects the viscosity, surface tension and conductivity of the solution, and is an important parameter in the electrospinning process. During the electrospinning process, the molecular chains in the solution become entangled, increasing the viscosity of the solution and solidifying into continuous nanofibers, which requires the polymer to have sufficient molecular weight. When the molecular weight of the polymer is fixed, the concentration and viscosity of the polymer solution are increased, and the entanglement concentration of the molecular chains is also increased and the surface tension is reduced, which is conducive to the formation of larger diameter and smooth continuous nanofibers, as shown in **Figure 1-10**. Greiner et al. [167] found that continuous and smooth nanofibers could be obtained when the concentration of Poly-L-lactide (PLA) electrospinning solution was 5%. As the concentration of the solution decreases, the diameter of the nanofibers also decreases. Moreover, when the solution concentration is less than 3%, the fiber diameter further decreases, and there are a large number of spherical beads or spindle-shaped beads on the nanofibers.

During the electrospinning process, the polymer jet is stretched under the action of a high-voltage electric field to form nanofibers. Increasing the conductivity of the polymer solution allows the jet to be more fully stretched and form nanofibers with smaller diameters. Some inorganic salts are usually added to improve the conductivity of the polymer solution, such as $NaCl$ [168], $MgCl_2$ [169], $AlCl_3$ [170], $CuCl_2$ [171], $CaCl_2$ [172], KH_2PO_4 and NaH_2PO_4 [173]. Reneker's research group [174] added NaCl to increase the conductivity of the polyethylene oxide (PEO) aqueous solution. The diameter of the prepared nanofibers was reduced, and the bead-like structure was also greatly reduced. The properties of the solvent, such as surface tension, conductivity, volatility, and interaction with the polymer, will affect electrospinning, resulting in nanofibers of

different shapes. Generally speaking, the main function of the solvent is to dissolve the polymer into a polymer solution, and the selected solvent must meet the dissolution needs of the polymer. Secondly, the conductivity of the solvent itself will also affect the conductivity of the electrospinning solution. The better the conductivity, the more fully it can stretch the jet and form nanofibers with smaller diameters. Finally, the volatility of the solvent should be moderate. During the electrospinning process, excessive volatility will cause the solution to solidify rapidly at the outlet of the spinneret, blocking the outlet, making continuous spinning impossible. Too low volatility will cause the jet to be incompletely solidified when it reaches the receiver, causing adhesion between fibers. [175-176] In addition, when the polymer is dissolved in a multi-component solvent, the volatilization rates of different solvents are different, which will cause phase separation of the polymer jet during the curing process, forming a porous structure on the fiber surface, and obtaining porous fibers. Wang et al. [177] dissolved poly(l-lactide) (PLLA) in a mixed solvent of CH_2Cl_2/DMF to form an electrospinning solution. When the nanofibers are solidified, CH_2Cl_2 is easy to volatilize, forming a porous PLLA fiber membrane. And the porous PLLA fiber membrane has high adsorption capacity for dyes and excellent oil/water separation capabilities.
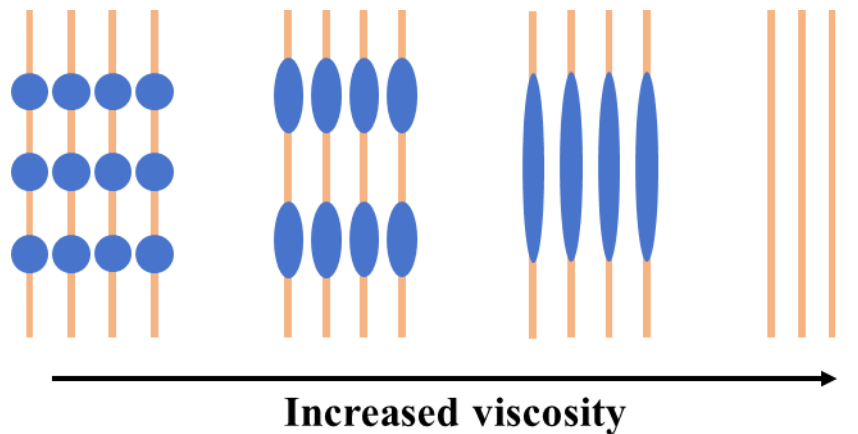

Increased viscosity

Figure 1-10. Effect of increasing polymer solution viscosity on electrospun fibers morphology.

b). Processing parameters

The process parameters that affect electrospinning mainly include the working voltage,

the flow rate of the solution, the distance from the spinneret to the collector, and the type of spinneret (needle). The polymer solution forms droplets at the spinneret, and is affected by the high-voltage electric field to accumulate charges on the surface and form electrostatic repulsion. At the same time, it overcomes its own surface tension and transforms into "Taylor cone", which further forms tiny jets and solidifies into nanofibers on the collector. Therefore, the operating voltage that just makes the droplet transform into a "Taylor cone" is called the critical voltage.

When the working voltage is lower than the critical voltage, the electrostatic repulsive force cannot overcome the surface tension of the droplets, the jet cannot be ejected, and nanofibers cannot be formed. When the working voltage is greater than the critical voltage and is within a reasonable range, a jet is ejected on the surface of the droplet to form nanofibers. Moreover, the diameter of nanofibers decreases with the increase of operating voltage. When the working voltage is too large, a large amount of charge accumulates on the surface of the droplet, and the electrostatic repulsion is too large, which leads to the instability of the jet, and has a certain influence on the forming of nanofibers. [178]

The flow rate of electrospinning solution is usually affected by the working voltage. When the working voltage is fixed and the flow rate of the solution is too low, the outflowing polymer droplets will not be enough to form a continuous jet, resulting in interruptions in the electrospinning. When the flow rate of the solution is too high, the operating voltage is insufficient to completely convert the large number of droplets flowing out simultaneously into "Taylor cone" and jets, resulting in the formation of beaded fibers and even dripping. When the solution flow rate is appropriate, the diameter of the nanofibers increases with the increase of the flow rate. [179-180]

The distance between the spinneret and the collector is usually called the electrospinning distance. When other parameters are appropriate, if the electrospinning distance is too short, the solvent will not be fully volatilized, forming beaded fibers, and adhesion will occur between nanofibers. When the electrospinning distance is too long, the whipping instability of the jet will be aggravated, causing the collector to be unable to collect enough nanofibers. Therefore, a reasonable electrospinning distance

is an important parameter in the electrospinning process, which is beneficial to fiber collection. [181]

A single needle is generally used for electrospinning, and the diameter of the needle directly affects the diameter of the nanofiber. The smaller the diameter of the needle, the less polymer is delivered per unit time, forming a finer jet under the same working voltage, and thus the smaller the diameter of the nanofibers formed. In order to form multi-component or different morphology nanofibers, scientists have also developed coaxial needles to prepare nanofibers with core-shell structure and side-by-side structure. Moreover, hollow fibers are formed by selectively removing the core part of the core-shell structure fiber. Jiang's research group [182] added PVP and titanium isopropoxide ethanol solution and paraffin oil into the outer and inner needles respectively to form core-shell nanofibers in independent compartmented chambers, and removed the paraffin oil by calcination to form multichannel microtubes. Moreover, through the design of the coaxial needle, multichannel microtubes with channel numbers of 2 to 5 can be obtained. In order to increase the yield of electrospinning, multi-needle electrospinning devices have been developed. In one study, researchers designed a 64 (8×8 array) needles simultaneous melt electrospinning device with a production rate of 18 $m^2 h^{-1}$, which greatly improved production efficiency.[183]

In addition, by changing the type of collector, different products can be obtained, such as non-woven fabrics, aligned fibers, honeycomb structured fibers, and yarns.

c). Ambient parameters

Ambient parameters are mainly temperature and humidity. The increase in temperature will reduce the viscosity and surface tension of the polymer solution, accelerate the movement of molecules, and make the jet easier to stretch, resulting in a smaller fiber diameter. In addition, the increase in temperature is conducive to the volatilization of the solvent and further reduces the diameter of the fiber. Clerck et al. [184] found that an increase in temperature would lead to a decrease in the average diameter of the nanofibers during the electrospinning process of cellulose acetate (CA) and polyvinyl pyrrolidone (PVP) nanofibers.

Humidity, as another ambient parameter, has an equally complex impact on

electrospinning. Simply put, an increase in humidity will slow down the solidification speed of the jet, causing the fiber diameter to decrease. However, when the humidity is too high, the diameter of the formed nanofibers is unevenly distributed and the surface is rougher, and even beaded fibers may be produced.

Kocbek and colleagues[185] studied the effect of humidity on the diameter of electrospun polyvinyl alcohol (PVA), polyethylene oxide (PEO), polyvinyl alcohol/hyaluronic acid (PVA/HA), and polyethylene oxide/chitosan (PEO/CS) nanofibers. When the ambient humidity increased from 4% to 60%, the diameter of PVA nanofibers decreased from 667 nm to 161 nm, and the diameter of PEO nanofibers decreased from 252 nm to 75 nm. When the ambient humidity increased from 4% to 50%, the diameter of the PVA/HA composite nanofibers decreased from 231 nm to 46 nm, while the diameter of the PEO/CS composite nanofibers also decreased from 179 nm to 41 nm.

1.3.4 Materials of electrospinning

In early research, people basically mastered the principles of electrospinning and its influencing parameters by studying the electrospinning process of polymers. And further developed melt electrospinning and sol-gel electrospinning. As people gradually realize the importance of composite materials, electrospinning has become one of the simplest and most effective methods to prepare organic/inorganic composite nanofibers and is widely used in various fields. [186]

a). Organic nanofibers

In the early stages of the development of electrospinning, polymer nanofibers were mainly prepared by dissolving polymers in solvents through solution electrospinning. To date, more than 100 polymers have been prepared into nanofibers through electrospinning, including some natural polymers (gelatin, cellulose, chitin, chitosan) and synthetic polymers (polystyrene, polyacrylonitrile, polyimide and polyvinyl alcohol), as show in **Table 1-2**. Some small organic molecules can also be used for electrospinning. The key is that there needs to be sufficient interaction between the small molecules. Long et al. [187] obtained phospholipid nonwoven electrospun

membranes through electrospinning for the first time. When the concentration of phospholipids is large enough, their micellar morphology evolves from spherical to cylindrical, and stacks and winds in a polymer-like manner, so that electrospun fibers with a diameter of 1 to 5 μm can be obtained.

In addition, multi-component polymer composite nanofibers can be prepared by electrospinning, and the properties of different polymers can be combined with each other. The preparation methods mainly include the following four methods: 1) blended electrospinning, in which a variety of polymers are dissolved in the same solvent in a certain proportion to obtain composite nanofibers; 2) multi-layer electrospinning, different polymers are deposited on the collector successively through electrospinning to form multi-layer composite nanofibers; 3) electrospinning with multiple spinnerets, different polymers are placed in different syringes, and different fibers are stacked together through electrospinning to form polymer composite nanofibers; 4) coaxial electrostatic spinning, the use of coaxial needles for electrostatic spinning, so as to obtain core-shell structure of polymer composite nanofibers.

Table 1-2. Common polymer nanofibers.

Polymer	Solvent	Ref.
Cellulose	LiCl/DMAc	[188]
Chitin	Ionic liquid	[189]
CS	CH_2Cl_2	[190]
Gelatin	Acetic acid	[191]
SF	H_2O	[192]
SA	H_2O	[193]
CA	Acetone and DMAc	[194]
PVA	H_2O	[195]
PAM	H_2O and DMF	[196]
PVP	Ethanol	[197]
PLLA	$CHCl_3$ and DMF	[198]
PS	DMF	[199]
PAN	DMF	[200]
PC	$CHCl_3$	[201]
PI	DMAc	[202]
PU	DMF	[203]
PVDF	DMAc	[204]
PA	Formic acid and Acetic acid	[205]

b). Organic/inorganic composite nanofibers

Inorganic nanomaterials are dispersed in polymer nanofibers to form organic/material composite nanofibers. The main methods are divided into hybrid electrospinning and sol-gel electrospinning.

Hybrid electrospinning refers to directly electrospinning inorganic nanomaterials (including ceramics, metals, metal oxides, metal sulfides and carbon materials) dispersed in a polymer solution to prepare composite nanofibers. Hou et al. [206] dispersed rGO in polyimide nanofibers, and the PI/rGO nanofibers prepared showed excellent mechanical properties, with the tensile strength and Young's modulus of a single composite nanofiber up to 4.2GPa and 121GPa, respectively.

Sol-gel electrospinning is to disperse the precursor (sol-gel) in a polymer solution and prepare organic/inorganic composite nanofibers through electrospinning. Among them, during the electrospinning process, the precursor is rapidly hydrolyzed in the air and converted into inorganic nanomaterials. Xia and Li [207] dissolved titanium tetraisopropoxide and PVP in ethanol to obtain as-spun composite nanofibers by electrospinning. The as-spun composite nanofibers were then exposed to air for 5 h to ensure that titanium tetraisopropoxide was completely hydrolyzed to TiO_2, resulting in the formation of TiO_2/PVP composite nanofibers. **Table 1-3** lists common organic/inorganic composite nanofibers.

Table 1-3. Common organic/inorganic composite nanofibers.

Inorganic	Polymer	Ref.
SiO_2	Cellulose Acetate	[208]
BN	PVP	[209]
TiO_2	PVAc	[210]
ZnO	PVA	[211]
Al_2O_3	PVDF	[212]
CuO	PVDF	[213]
CdS	PVP	[214]
ZnS	PVA	[215]
Ag	PAN	[216]
Au	PVP	[217]
Cu	PAN	[218]
Ni	PU	[219]
CNT	PAN	[220]
rGO	PI	[206]

c). Inorganic nanofibers

In recent decades, inorganic nanomaterials have been widely used in many fields due to their excellent physical and chemical properties such as mechanical, catalytic, optical, thermal, electrical and magnetic properties. Among the many current methods, electrospinning is one of the important methods for preparing 1D inorganic nanofibers. And inorganic nanofibers can be divided into four categories: oxide nanofibers, metal

nanofibers, carbon nanofibers and inorganic hybrid nanofibers.

Lukas et al. [221] obtained $ZrOCl_2$/PVP nanofibers by electrospinning, and then calcined them in air or argon at a temperature of 600 °C to 1000 °C for 2 h to form ZrO_2 nanofibers. Further, the metal oxide nanofibers can be reduced to metal nanofibers. Bognitzki et al. [222] obtained Cu-based composite nanofibers through electrospinning and converted them into CuO nanofibers under high-temperature combustion. Finally, the CuO nanofibers are treated in a hydrogen atmosphere at 300 °C to form Cu nanofibers.

Carbon nanofibers are usually formed from polyacrylonitrile nanofibers through carbonization. To avoid the shrinkage of carbon nanofibers during heat treatment, the entire process is usually divided into a stabilization step and a carbonization step. [223] In addition, inorganic nanofibers can also be composed of multiple components, such as SiO_2/TiO_2 [224], ZnO/Cu/C [225], and C/Fe_3O_4 [226] composite nanofibers.

1.3.5 3D electrospun fiber sponges

3D porous materials find extensive applications in various fields, including catalysis, energy, environmental remediation, thermal insulation, biomedicine, and sensors, owing to their attributes such as low density, high porosity, large surface area, and robust mechanical stability. [227-228] Typically, traditional electrospun fibers are assembled into 2D fiber membranes, and their restricted porosity poses a limitation in certain fields, such as tissue engineering. Hence, the conversion of 2D fiber membranes into 3D fiber materials proves to be an effective strategy for expanding the application fields of electrospinning.

Currently, the preparation of 3D fiber materials through electrospinning is primarily categorized into two methods: direct electrospinning and the 2D fiber membrane reconstruction method. [229-230] The direct electrospinning method involves depositing fibers on a collector and directly forming 3D fiber materials by adjusting electrospinning parameters. The 2D fiber membrane reconstruction method encompasses embedding in hydrogels, 3D printing, gas-foaming, and freeze-drying.

Notably, the freeze-drying method has gained significant attention due to its simplicity, controllable shape, and microstructure. In the freeze-drying method, a 2D fiber membrane is cut in a solvent to create a fiber slurry, and subsequently, a 3D electrospun fiber sponge is formed through freeze-drying. Throughout the freeze-drying process, the solvent transitions from the liquid phase to the solid phase at low temperatures. Subsequently, it directly sublimates to the gas phase under low ambient pressure, resulting in the formation of a porous structure. The fibers are stacked to create a porous structural framework, ensuring the mechanical stability of the 3D electrospun fiber sponge. Furthermore, the manipulation of the internal structure and external shape of the 3D electrospun fiber sponge is easily achievable by adjusting freeze-drying procedures and modifying molds. [231] This approach demonstrates remarkable performance in diverse fields, including environmental applications (e.g., water purification and desalination), energy applications (e.g., supercapacitors), biomedical engineering (e.g., drug delivery), electronics (e.g., pressure sensors), and chemical engineering (e.g., catalyst supports, thermal insulation), yielding promising results.[232] The unique characteristics of 3D electrospun fiber sponges provide a solution to the challenges of processing difficulty, recycling issues, and agglomeration tendency encountered with MOFs and COFs. Consequently, in the present research, I illustrate the fabrication of hierarchically porous COF sponges utilizing 3D electrospun fiber sponges as carriers. Collaborating with my laboratory colleague, Yingying Du, we successfully extended this approach to the preparation of MOF sponges.

1.4 References

[1] Wu L, Li Y, Fu Z, et al. Hierarchically structured porous materials: synthesis strategies and applications in energy storage[J]. National Science Review, 2020, 7(11): 1667-1701.

[2] Kong L, Zhong M, Shuang W, et al. Electrochemically active sites inside crystalline porous materials for energy storage and conversion[J]. Chemical Society Reviews, 2020, 49(8): 2378-2407.

[3] Zheng B, Lin X, Zhang X, et al. Emerging functional porous polymeric and carbonaceous materials for environmental treatment and energy storage[J]. Advanced Functional Materials, 2020, 30(41): 1907006.

[4] Zhu L, Shen D, Luo K H. A critical review on VOCs adsorption by different porous materials: Species, mechanisms and modification methods[J]. Journal of Hazardous Materials, 2020, 389: 122102.

[5] Tian W, Zhang H, Duan X, et al. Porous carbons: structure-oriented design and versatile applications[J]. Advanced Functional Materials, 2020, 30(17): 1909265.

[6] Yuan F, Yang Z, Zhang X, et al. Judicious design functionalized 3D-COF to enhance CO_2 adsorption and separation[J]. Journal of Computational Chemistry, 2021, 42(13): 888-896.

[7] Knebel A A, Caro J. Metal-organic frameworks and covalent organic frameworks as disruptive membrane materials for energy-efficient gas separation[J]. Nature Nanotechnology, 2022, 17(9): 911-923.

[8] Cui B, Fu G. Process of metal-organic framework (MOF)/covalent-organic framework (COF) hybrids-based derivatives and their applications on energy transfer and storage[J]. Nanoscale, 2022, 14(5): 1679-1699.

[9] Yuan H, Li N, Fan W, et al. Metal-organic framework based gas sensors[J]. Advanced Science, 2022, 9(6): 2104374.

[10] Liu X, Huang D, Lai C, et al. Recent advances in covalent organic frameworks (COFs) as a smart sensing material[J]. Chemical Society Reviews, 2019, 48(20): 5266-5302.

[11] Zhi Y, Wang Z, Zhang H L, et al. Recent progress in metal-free covalent organic frameworks as heterogeneous catalysts[J]. Small, 2020, 16(24): 2001070.

[12] Goetjen T A, Liu J, Wu Y, et al. Metal-organic framework (MOF) materials as polymerization catalysts: a review and recent advances[J]. Chemical Communications, 2020, 56(72): 10409-10418.

[13] Ren X, Liao G, Li Z, et al. Two-dimensional MOF and COF nanosheets for next-generation optoelectronic applications[J]. Coordination Chemistry Reviews, 2021, 435: 213781.

[14] Rego R M, Kuriya G, Kurkuri M D, et al. MOF based engineered materials in water remediation: Recent trends[J]. Journal of Hazardous Materials, 2021, 403: 123605.

[15] Ahmed I, Jhung S H. Covalent organic framework-based materials: Synthesis, modification, and application in environmental remediation[J]. Coordination Chemistry Reviews, 2021, 441: 213989.

[16] Bhunia S, Deo K A, Gaharwar A K. 2D covalent organic frameworks for biomedical applications[J]. Advanced Functional Materials, 2020, 30(27): 2002046.

[17] Shyngys M, Ren J, Liang X, et al. Metal-organic framework (MOF)-based biomaterials for tissue engineering and regenerative medicine[J]. Frontiers in Bioengineering and Biotechnology, 2021, 9: 603608.

[18] Ren J, Huang Y, Zhu H, et al. Recent progress on MOF-derived carbon materials for energy storage[J]. Carbon Energy, 2020, 2(2): 176-202.

[19] Li J, Jing X, Li Q, et al. Bulk COFs and COF nanosheets for electrochemical energy storage and conversion[J]. Chemical Society Reviews, 2020, 49(11): 3565-3604.

[20] Dey K, Kunjattu H S, Chahande A M, et al. Nanoparticle size-fractionation through self-standing porous covalent organic framework films[J]. Angewandte Chemie International Edition, 2020, 132(3): 1177-1181.

[21] Zhou Z, Mukherjee S, Hou S, et al. Porphyrinic MOF film for multifaceted electrochemical sensing[J]. Angewandte Chemie International Edition, 2021, 60(37): 20551-20557.

[22] Xu Y, Zhai X, Wang X H, et al. Fabrication of a robust MOF/aerogel composite

via a covalent post-assembly method[J]. Chemical Communications, 2021, 57(48): 5961-5964.

[23] Li C, Yang J, Pachfule P, et al. Ultralight covalent organic framework/graphene aerogels with hierarchical porosity[J]. Nature Communications, 2020, 11(1): 4712.

[24] Huang L, Yang J, Zhao Y, et al. Monolithic covalent organic frameworks with hierarchical architecture: attractive platform for contaminant remediation[J]. Chemistry of Materials, 2023, 35(7): 2661-2682.

[25] Freund R, Canossa S, Cohen S M, et al. 25 years of reticular chemistry[J]. Angewandte Chemie International Edition, 2021, 60(45): 23946-23974.

[26] Chafiq M, Chaouiki A, Ko Y G. Recent Advances in Multifunctional Reticular Framework Nanoparticles: A Paradigm Shift in Materials Science Road to a Structured Future[J]. Nano-Micro Letters, 2023, 15(1): 213.

[27] Chen Z, Kirlikovali K O, Li P, et al. Reticular chemistry for highly porous metal-organic frameworks: The chemistry and applications[J]. Accounts of Chemical Research, 2022, 55(4): 579-591.

[28] Jiang H, Alezi D, Eddaoudi M. A reticular chemistry guide for the design of periodic solids[J]. Nature Reviews Materials, 2021, 6(6): 466-487.

[29] Li Y, Karimi M, Gong Y N, et al. Integration of metal-organic frameworks and covalent organic frameworks: Design, synthesis, and applications[J]. Matter, 2021, 4(7): 2230-2265.

[30] Yaghi O M, Li H. Hydrothermal synthesis of a metal-organic framework containing large rectangular channels[J]. Journal of the American Chemical Society, 1995, 117(41): 10401-10402.

[31] González C M O, Kharisov B I, Kharissova O V, et al. Synthesis and applications of MOF-derived nanohybrids: A review[J]. Materials Today: Proceedings, 2021, 46: 3018-3029.

[32] Cote A P, Benin A I, Ockwig N W, et al. Porous, crystalline, covalent organic frameworks[J]. Science, 2005, 310(5751): 1166-1170.

[33] Evans A M, Castano I, Brumberg A, et al. Emissive single-crystalline boroxine-linked colloidal covalent organic frameworks[J]. Journal of the American Chemical

Society, 2019, 141(50): 19728-19735.

[34] Wang R N, Zhang X R, Wang S F, et al. Flatbands in 2D boroxine-linked covalent organic frameworks[J]. Physical Chemistry Chemical Physics, 2016, 18(2): 1258-1264.

[35] Matsumoto M, Dasari R R, Ji W, et al. Rapid, low temperature formation of imine-linked covalent organic frameworks catalyzed by metal triflates[J]. Journal of the American Chemical Society, 2017, 139(14): 4999-5002.

[36] Uribe-Romo F J, Hunt J R, Furukawa H, et al. A crystalline imine-linked 3-D porous covalent organic framework[J]. Journal of the American Chemical Society, 2009, 131(13): 4570-4571.

[37] Dalapati S, Jin S, Gao J, et al. An azine-linked covalent organic framework[J]. Journal of the American Chemical Society, 2013, 135(46): 17310-17313.

[38] Li Z, Feng X, Zou Y, et al. A 2D azine-linked covalent organic framework for gas storage applications[J]. Chemical Communications, 2014, 50(89): 13825-13828.

[39] Bunck D N, Dichtel W R. Bulk synthesis of exfoliated two-dimensional polymers using hydrazone-linked covalent organic frameworks[J]. Journal of the American Chemical Society, 2013, 135(40): 14952-14955.

[40] Qian C, Zhou W, Qiao J, et al. Linkage engineering by harnessing supramolecular interactions to fabricate 2D hydrazone-linked covalent organic framework platforms toward advanced catalysis[J]. Journal of the American Chemical Society, 2020, 142(42): 18138-18149.

[41] DeBlase C R, Silberstein K E, Truong T T, et al. β-Ketoenamine-linked covalent organic frameworks capable of pseudocapacitive energy storage[J]. Journal of the American Chemical Society, 2013, 135(45): 16821-16824.

[42] Liu L, Meng W K, Zhou Y S, et al. β-Ketoenamine-linked covalent organic framework coating for ultra-high-performance solid-phase microextraction of polybrominated diphenyl ethers from environmental samples[J]. Chemical Engineering Journal, 2019, 356: 926-933.

[43] Önfelt B, Lincoln P, Nordén B. Enantioselective DNA threading dynamics by phenazine-linked [Ru(phen)$_2$dppz]$^{2+}$ dimers[J]. Journal of the American Chemical Society, 2001, 123(16): 3630-3637.

[44] Yang C, Yang Z D, Dong H, et al. Theory-driven design and targeting synthesis of a highly-conjugated basal-plane 2D covalent organic framework for metal-free electrocatalytic OER[J]. ACS Energy Letters, 2019, 4(9): 2251-2258.

[45] Yue C, Wang W, Li F. Building N-Heterocyclic Carbene into Triazine-Linked Polymer for Multiple CO_2 Utilization[J]. ChemSusChem, 2020, 13(22): 5996-6004.

[46] Phan H, Herng T S, Wang D, et al. Room-temperature magnets based on 1, 3, 5-triazine-linked porous organic radical frameworks[J]. Chem, 2019, 5(5): 1223-1234.

[47] Ma S, Deng T, Li Z, et al. Photocatalytic Hydrogen Production on a sp^2-Carbon-Linked Covalent Organic Framework[J]. Angewandte Chemie International Edition, 2022, 134(42): e202208919.

[48] Xu Y, Wu C, Chu N, et al. Design and synthesis of stable sp^2-carbon-linked two-dimensional conjugated covalent organic framework for efficient capture of iodine[J]. Separation and Purification Technology, 2023, 307: 122776.

[49] Freund R, Zaremba O, Arnauts G, et al. The current status of MOF and COF applications[J]. Angewandte Chemie International Edition, 2021, 60(45): 23975-24001.

[50] Lai J, Niu W, Luque R, et al. Solvothermal synthesis of metal nanocrystals and their applications[J]. Nano Today, 2015, 10(2): 240-267.

[51] Inoue M. Solvothermal synthesis[J]. MATERIALS ENGINEERING-NEW YORK-, 2005, 28: 21.

[52] Venturi D M, Campana F, Marmottini F, et al. Extensive screening of green solvents for safe and sustainable UiO-66 synthesis[J]. ACS Sustainable Chemistry & Engineering, 2020, 8(46): 17154-17164.

[53] Deng L, Wang L, Liu S, et al. A general synthetic strategy for the synthesis of imine-linked covalent organic frameworks in choline chloride-hexafluoroisopropanol-based deep eutectic solvents[J]. Macromolecules, 2023, 56(19): 7707-7720.

[54] Głowniak S, Szczęśniak B, Choma J, et al. Advances in microwave synthesis of nanoporous materials[J]. Advanced Materials, 2021, 33(48): 2103477.

[55] Głowniak, S.; Szczęśniak, B.; Choma, J.; Jaroniec, M. J. M., Recent Developments in Sonochemical Synthesis of Nanoporous Materials. 2023, 28, 2639.

[56] Jhung S H, Lee J H, Chang J S. Microwave synthesis of a nanoporous hybrid

material, chromium trimesate[J]. Bulletin of the Korean Chemical Society, 2005, 26(6): 880-881.

[57] Campbell N L, Clowes R, Ritchie L K, et al. Rapid microwave synthesis and purification of porous covalent organic frameworks[J]. Chemistry of Materials, 2009, 21(2): 204-206.

[58] Tsuzuki T, McCormick P G. Mechanochemical synthesis of nanoparticles[J]. Journal of Materials Science, 2004, 39: 5143-5146.

[59] Leonardi M, Villacampa M, Menéndez J C. Multicomponent mechanochemical synthesis[J]. Chemical Science, 2018, 9(8): 2042-2064.

[60] Pichon A, Lazuen-Garay A, James S L. Solvent-free synthesis of a microporous metal-organic framework[J]. CrystEngComm, 2006, 8(3): 211-214.

[61] Užarević K, Wang T C, Moon S Y, et al. Mechanochemical and solvent-free assembly of zirconium-based metal-organic frameworks[J]. Chemical Communications, 2016, 52(10): 2133-2136.

[62] Biswal B P, Chandra S, Kandambeth S, et al. Mechanochemical synthesis of chemically stable isoreticular covalent organic frameworks[J]. Journal of the American Chemical Society, 2013, 135(14): 5328-5331.

[63] Tsuruoka T, Furukawa S, Takashima Y, et al. Nanoporous nanorods fabricated by coordination modulation and oriented attachment growth[J]. Angewandte Chemie International Edition, 2009, 121(26): 4833-4837.

[64] Schaate A, Roy P, Godt A, et al. Modulated synthesis of Zr-based metal-organic frameworks: from nano to single crystals[J]. Chemistry-A European Journal, 2011, 17(24): 6643-6651.

[65] Zhao Y, Zhang Q, Li Y, et al. Large-scale synthesis of monodisperse UiO-66 crystals with tunable sizes and missing linker defects via acid/base co-modulation[J]. ACS Applied Materials & Interfaces, 2017, 9(17): 15079-15085.

[66] Ma T, Kapustin E A, Yin S X, et al. Single-crystal x-ray diffraction structures of covalent organic frameworks[J]. Science, 2018, 361(6397): 48-52.

[67] Cui X, Mao S, Liu M, et al. Mechanism of surfactant micelle formation[J]. Langmuir, 2008, 24(19): 10771-10775.

[68] Dwars T, Paetzold E, Oehme G. Reactions in micellar systems[J]. Angewandte Chemie International Edition, 2005, 44(44): 7174-7199.

[69] Huang X X, Qiu L G, Zhang W, et al. Hierarchically mesostructured MIL-101 metal-organic frameworks: supramolecular template-directed synthesis and accelerated adsorption kinetics for dye removal[J]. CrystEngComm, 2012, 14(5): 1613-1617.

[70] Tang Y, Li W, Muhammad Y, et al. Fabrication of hollow covalent-organic framework microspheres via emulsion-interfacial strategy to enhance laccase immobilization for tetracycline degradation[J]. Chemical Engineering Journal, 2021, 421: 129743.

[71] Zhao L, Liu H, Du Y, et al. An ionic liquid as a green solvent for high potency synthesis of 2D covalent organic frameworks[J]. New Journal of Chemistry, 2020, 44(36): 15410-15414.

[72] Li P, Cheng F F, Xiong W W, et al. New synthetic strategies to prepare metal-organic frameworks[J]. Inorganic Chemistry Frontiers, 2018, 5(11): 2693-2708.

[73] Ploetz E, Engelke H, Lächelt U, et al. The chemistry of reticular framework nanoparticles: MOF, ZIF, and COF materials[J]. Advanced Functional Materials, 2020, 30(41): 1909062.

[74] Wang J, Li N, Xu Y, et al. Two-dimensional MOF and COF nanosheets: synthesis and applications in electrochemistry[J]. Chemistry-A European Journal, 2020, 26(29): 6402-6422.

[75] Matsuura T. Synthetic membranes and membrane separation processes[M]. CRC press, 2020.

[76] Baker R W. Membrane technology and applications[M]. John Wiley & Sons, 2023.

[77] Vatanpour V, Pasaoglu M E, Kose-Mutlu B, et al. Polyacrylonitrile in the Preparation of Separation Membranes: A Review[J]. Industrial & Engineering Chemistry Research, 2023, 62(17): 6537-6558.

[78] Zhao C, Xue J, Ran F, et al. Modification of polyethersulfone membranes–A review of methods[J]. Progress in Materials Science, 2013, 58(1): 76-150.

[79] Kheirieh S, Asghari M, Afsari M. Application and modification of polysulfone membranes[J]. Reviews in Chemical Engineering, 2018, 34(5): 657-693.

[80] Kang G, Cao Y. Application and modification of poly (vinylidene fluoride) (PVDF) membranes-a review[J]. Journal of Membrane Science, 2014, 463: 145-165.

[81] Lin Y S. Metal organic framework membranes for separation applications[J]. Current Opinion in Chemical Engineering, 2015, 8: 21-28.

[82] Zhang C, Wu B H, Ma M Q, et al. Ultrathin metal/covalent-organic framework membranes towards ultimate separation[J]. Chemical Society Reviews, 2019, 48(14): 3811-3841.

[83] Liu Y, Ng Z, Khan E A, et al. Synthesis of continuous MOF-5 membranes on porous α-alumina substrates[J]. Microporous and Mesoporous Materials, 2009, 118(1-3): 296-301.

[84] Colson J W, Woll A R, Mukherjee A, et al. Oriented 2D covalent organic framework thin films on single-layer graphene[J]. Science, 2011, 332(6026): 228-231.

[85] Fan H, Peng M, Strauss I, et al. MOF-in-COF molecular sieving membrane for selective hydrogen separation[J]. Nature Communications, 2021, 12(1): 38.

[86] Huang A, Bux H, Steinbach F, et al. Molecular-sieve membrane with hydrogen permselectivity: ZIF-22 in LTA topology prepared with 3-aminopropyltriethoxysilane as covalent linker[J]. Angewandte Chemie International Edition, 2010, 29(49): 4958-4961.

[87] Huang A, Dou W, Caro J. Steam-stable zeolitic imidazolate framework ZIF-90 membrane with hydrogen selectivity through covalent functionalization[J]. Journal of the American Chemical Society, 2010, 132(44): 15562-15564.

[88] Fan H, Mundstock A, Feldhoff A, et al. Covalent organic framework-covalent organic framework bilayer membranes for highly selective gas separation[J]. Journal of the American Chemical Society, 2018, 140(32): 10094-10098.

[89] Fu J, Das S, Xing G, et al. Fabrication of COF-MOF composite membranes and their highly selective separation of H_2/CO_2[J]. Journal of the American Chemical Society, 2016, 138(24): 7673-7680.

[90] Dong R, Zhang T, Feng X. Interface-assisted synthesis of 2D materials: trend and challenges[J]. Chemical reviews, 2018, 118(13): 6189-6235.

[91] Raaijmakers M J T, Benes N E. Current trends in interfacial polymerization

chemistry[J]. Progress in Polymer Science, 2016, 63: 86-142.

[92] Huang X, Sheng P, Tu Z, et al. A two-dimensional π-d conjugated coordination polymer with extremely high electrical conductivity and ambipolar transport behaviour[J]. Nature Communications, 2015, 6(1): 7408.

[93] Dey K, Pal M, Rout K C, et al. Selective molecular separation by interfacially crystallized covalent organic framework thin films[J]. Journal of the American Chemical Society, 2017, 139(37): 13083-13091.

[94] Yuan K, Song T, Yang C, et al. Polymer-Assisted Space-Confined Strategy for the Foot-Scale Synthesis of Flexible Metal-Organic Framework-Based Composite Films[J]. Journal of the American Chemical Society, 2021, 143(42): 17526-17534.

[95] Shinde D B, Sheng G, Li X, et al. Crystalline 2D covalent organic framework membranes for high-flux organic solvent nanofiltration[J]. Journal of the American Chemical Society, 2018, 140(43): 14342-14349.

[96] Assunção I C C, Sério S, Ferreira Q, et al. Graphene oxide layer-by-layer films for sensors and devices[J]. Nanomaterials, 2021, 11(6): 1556.

[97] Lee T, Min S H, Gu M, et al. Layer-by-layer assembly for graphene-based multilayer nanocomposites: synthesis and applications[J]. Chemistry of Materials, 2015, 27(11): 3785-3796.

[98] Peng Y, Li Y, Ban Y, et al. Two-dimensional metal-organic framework nanosheets for membrane-based gas separation[J]. Angewandte Chemie International Edition, 2017, 129(33): 9889-9893.

[99] Yang H, Yang L, Wang H, et al. Covalent organic framework membranes through a mixed-dimensional assembly for molecular separations[J]. Nature Communications, 2019, 10(1): 2101.

[100] Dechnik J, Gascon J, Doonan C J, et al. Mixed-matrix membranes[J]. Angewandte Chemie International Edition, 2017, 56(32): 9292-9310.

[101] Vinh-Thang H, Kaliaguine S. Predictive models for mixed-matrix membrane performance: a review[J]. Chemical Reviews, 2013, 113(7): 4980-5028.

[102] Cheng Y, Ying Y, Zhai L, et al. Mixed matrix membranes containing MOF@ COF hybrid fillers for efficient CO_2/CH_4 separation[J]. Journal of membrane science, 2019,

573: 97-106.

[103] Aydin S, Altintas C, Erucar I, et al. Computational investigation of dual filler-incorporated polymer membranes for efficient CO_2 and H_2 separation: MOF/COF/Polymer mixed matrix membranes[J]. Industrial & Engineering Chemistry Research, 2023, 62(6): 2924-2936.

[104] Li C, Liu J, Zhang K, et al. Coating the right polymer: achieving ideal metal–organic framework particle dispersibility in polymer matrixes using a coordinative crosslinking surface modification method[J]. Angewandte Chemie International Edition, 2021, 133(25): 14257-14264.

[105] Kang Z, Peng Y, Qian Y, et al. Mixed matrix membranes (MMMs) comprising exfoliated 2D covalent organic frameworks (COFs) for efficient CO_2 separation[J]. Chemistry of Materials, 2016, 28(5): 1277-1285.

[106] Wang S, Wei X, Li Z, et al. Recent advances in developing mixed matrix membranes based on covalent organic frameworks[J]. Separation and Purification Technology, 2022, 301: 122004.

[107] Buddin M M H S, Ahmad A L. A review on metal-organic frameworks as filler in mixed matrix membrane: Recent strategies to surpass upper bound for CO_2 separation[J]. Journal of CO_2 Utilization, 2021, 51: 101616.

[108] Sawicka K M, Gouma P. Electrospun composite nanofibers for functional applications[J]. Journal of Nanoparticle Research, 2006, 8: 769-781.

[109] Xue J, Wu T, Dai Y, et al. Electrospinning and electrospun nanofibers: Methods, materials, and applications[J]. Chemical Reviews, 2019, 119(8): 5298-5415.

[110] Dou Y, Zhang W, Kaiser A. Electrospinning of metal–organic frameworks for energy and environmental applications[J]. Advanced Science, 2020, 7(3): 1902590.

[111] Liu X, Zhang Y, Guo X, et al. Electrospun metal-organic framework nanofiber membranes for energy storage and environmental protection[J]. Advanced Fiber Materials, 2022, 4(6): 1463-1485.

[112] Zhang Y, Yuan S, Feng X, et al. Preparation of nanofibrous metal-organic framework filters for efficient air pollution control[J]. Journal of the American Chemical Society, 2016, 138(18): 5785-5788.

[113] Bian Y, Wang R, Wang S, et al. Metal-organic framework-based nanofiber filters for effective indoor air quality control[J]. Journal of Materials Chemistry A, 2018, 6(32): 15807-15814.

[114] Wang R, Li C, Li Q, et al. Electrospinning fabrication of covalent organic framework composite nanofibers for pipette tip solid phase extraction of tetracycline antibiotics in grass carp and duck[J]. Journal of Chromatography A, 2020, 1622: 461098.

[115] Zhao X, Li Q, Pachfule P, et al. Construction of covalent organic framework nanofiber membranes for efficient adsorption of antibiotics[J]. Small, 2023, 19(26): 2301200.

[116] Ullah I, Ali S, Hanif M A, et al. Nanoscience for environmental remediation: A Review[J]. International Journal of Chemical and Biochemical Sciences, 2012, 2(1): 60-77.

[117] Wu Y, Pang H, Liu Y, et al. Environmental remediation of heavy metal ions by novel-nanomaterials: A review[J]. Environmental Pollution, 2019, 246: 608-620.

[118] Beniwal K, Kaur H, Saini A K, et al. Synthesis and applications of carbon porous nano-materials for environmental remediation[J]. Nanofabrication, 2022, 7: 174-194.

[119] Fajal S, Dutta S, Ghosh S K. Porous organic polymers (POPs) for environmental remediation[J]. Materials Horizons, 2023.

[120] Rad L R, Anbia M. Zeolite-based composites for the adsorption of toxic matters from water: A review[J]. Journal of Environmental Chemical Engineering, 2021, 9(5): 106088.

[121] Ahmadijokani F, Ghaffarkhah A, Molavi H, et al. COF and MOF hybrids: advanced materials for wastewater treatment[J]. Advanced Functional Materials, 2023: 2305527.

[122] Cai Y, Ling Q, Yi Y, et al. Application of covalent organic frameworks in environmental pollution management[J]. Applied Catalysis A: General, 2022, 643: 118733.

[123] Lohe M R, Rose M, Kaskel S. Metal-organic framework (MOF) aerogels with high micro-and macroporosity[J]. Chemical Communications, 2009 (40): 6056-6058.

[124] Martín-Illán J Á, Rodríguez-San-Miguel D, Castillo O, et al. Macroscopic Ultralight Aerogel Monoliths of Imine-based Covalent Organic Frameworks[J]. Angewandte Chemie International Edition, 2021, 133(25): 14088-14096.

[125] Martín-Illán J Á, Suárez J A, Gómez-Herrero J, et al. Ultralarge free-standing imine-based covalent organic framework membranes fabricated via compression[J]. Advanced Science, 2022, 9(7): 2104643.

[126] Lu Y, Fan D, Shen Z, et al. Design and performance boost of a MOF-functionalized-wood solar evaporator through tuning the hydrogen-bonding interactions[J]. Nano Energy, 2022, 95: 107016.

[127] Wan Y, Wang J, Huang F, et al. Synergistic effect of adsorption coupled with catalysis based on graphene-supported MOF hybrid aerogel for promoted removal of dyes[J]. RSC advances, 2018, 8(60): 34552-34559.

[128] Fang Z, Lin Y, Dong Z, et al. Interfacial synthesis of covalent organic framework composited woods for ultrafast ion conduction[J]. Cell Reports Physical Science, 2023, 4(7).

[129] An N, Guo Z, Xin J, et al. Hierarchical porous covalent organic framework/graphene aerogel electrode for high-performance supercapacitors[J]. Journal of Materials Chemistry A, 2021, 9(31): 16824-16833.

[130] He Z, Wu H, Shi Z, et al. Mussel-inspired durable superhydrophobic/superoleophilic MOF-PU sponge with high chemical stability, efficient oil/water separation and excellent anti-icing properties[J]. Colloids and Surfaces A: Physicochemical and Engineering Aspects, 2022, 648: 129142.

[131] Li J, Yang Y, Ma W, et al. One-pot room-temperature synthesis of covalent organic framework-coated superhydrophobic sponges for highly efficient oil-water separation[J]. Journal of Hazardous Materials, 2021, 411: 125190.

[132] Cheng P, Kim M, Lim H, et al. A General Approach to Shaped MOF-Containing Aerogels toward Practical Water Treatment Application[J]. Advanced Sustainable Systems, 2020, 4(8): 2000060.

[133] Li F, Ding L G, Yao B J, et al. Pd loaded and covalent-organic framework involved chitosan aerogels and their application for continuous flow-through aqueous

CB decontamination[J]. Journal of Materials Chemistry A, 2018, 6(24): 11140-11146.

[134] Liu T, Zhang X, Gu A, et al. In-situ grown bilayer MOF from robust wood aerogel with aligned microchannel arrays toward selective extraction of uranium from seawater[J]. Chemical Engineering Journal, 2022, 433: 134346.

[135] Jagadeesh P, Puttegowda M, Mavinkere Rangappa S, et al. A review on extraction, chemical treatment, characterization of natural fibers and its composites for potential applications[J]. Polymer Composites, 2021, 42(12): 6239-6264.

[136] Thapliyal D, Verma S, Sen P, et al. Natural fibers composites: Origin, importance, consumption pattern, and challenges[J]. Journal of Composites Science, 2023, 7(12): 506.

[137] Quye A. Factors influencing the stability of man-made fibers: A retrospective view for historical textiles[J]. Polymer Degradation and Stability, 2014, 107: 210-218.

[138] Kim B S, Kim I S. Recent nanofiber technologies[J]. Polymer Reviews, 2011, 51(3): 235-238.

[139] Lim C T. Nanofiber technology: current status and emerging developments[J]. Progress in Polymer Science, 2017, 70: 1-17.

[140] Jayaraman K, Kotaki M, Zhang Y, et al. Recent advances in polymer nanofibers[J]. Journal of Nanoscience and Nanotechnology, 2004, 4(1-2): 52-65.

[141] Pelipenko J, Kocbek P, Kristl J. Critical attributes of nanofibers: Preparation, drug loading, and tissue regeneration[J]. International Journal of Pharmaceutics, 2015, 484(1-2): 57-74.

[142] Zhang X, Xie L, Wang X, et al. Electrospinning super-assembly of ultrathin fibers from single-to multi-Taylor cone sites[J]. Applied Materials Today, 2022, 26: 101272.

[143] Boys C V. On the production, properties, and some suggested uses of the finest threads[J]. Proceedings of the Physical Society of London, 1887, 9(1): 8.

[144] Cooley J F. Apparatus for electrically dispersing fluids: U.S. Patent 692,631[P]. 1902-2-4.

[145] Cooley J F. Electrical method of dispersing fluids: U.S. Patent 745,276[P]. 1903-11-24.

[146] Zeleny J. The electrical discharge from liquid points, and a hydrostatic method of

measuring the electric intensity at their surfaces[J]. Physical Review, 1914, 3(2): 69.

[147] Anton F. Process and apparatus for preparing artificial threads: U.S. Patent 1,975,504[P]. 1934-10-2.

[148] Anton F. Method and apparatus for spinning, 1939[J]. Google Patents.

[149] Norton C L. Method of and apparatus for producing fibrous or filamentary material: U.S. Patent 2,048,651[P]. 1936-7-21.

[150] Filatov Y, Budyka A, Kirichenko V. Electrospinning of micro-and nanofibers[J]. Fundamentals in Separation and filtration process, Minneapolis: Donaldson Co, 2007.

[151] Taylor G I. Disintegration of water drops in an electric field[J]. Proceedings of the Royal Society of London. Series A. Mathematical and Physical Sciences, 1964, 280(1382): 383-397.

[152] Taylor G I. The force exerted by an electric field on a long cylindrical conductor[J]. Proceedings of the Royal Society of London. Series A. Mathematical and Physical Sciences, 1966, 291(1425): 145-158.

[153] Taylor G I. Electrically driven jets[J]. Proceedings of the Royal Society of London. A. Mathematical and Physical Sciences, 1969, 313(1515): 453-475.

[154] Baumgarten P K. Electrostatic spinning of acrylic microfibers[J]. Journal of Colloid and Interface Science, 1971, 36(1): 71-79.

[155] Annis D, Bornat A, Edwards R O, et al. An elastomeric vascular prosthesis[J]. ASAIO Journal, 1978, 24(1): 209-214.

[156] Reneker D H, Chun I. Nanometre diameter fibres of polymer, produced by electrospinning[J]. Nanotechnology, 1996, 7(3): 216.

[157] Huang Z M, Zhang Y Z, Kotaki M, et al. A review on polymer nanofibers by electrospinning and their applications in nanocomposites[J]. Composites science and technology, 2003, 63(15): 2223-2253.

[158] Frenot A, Chronakis I S. Polymer nanofibers assembled by electrospinning[J]. Current Opinion in Colloid & Interface Science, 2003, 8(1): 64-75.

[159] Subbiah T H, Bhat G S, Tock R W, et al. Self-assembled honeycomb polyurethane nanofibers[J]. Applied Polymer Science, 2005, 96: 557-559.

[160] Li Y, Zhu J, Cheng H, et al. Developments of advanced electrospinning

techniques: A critical review[J]. Advanced Materials Technologies, 2021, 6(11): 2100410.

[161] Teo W E, Ramakrishna S. A review on electrospinning design and nanofibre assemblies[J]. Nanotechnology, 2006, 17(14): R89.

[162] Rutledge G C, Fridrikh S V. Formation of fibers by electrospinning[J]. Advanced Drug Delivery Reviews, 2007, 59(14): 1384-1391.

[163] Thompson C J, Chase G G, Yarin A L, et al. Effects of parameters on nanofiber diameter determined from electrospinning model[J]. Polymer, 2007, 48(23): 6913-6922.

[164] Li D, Xia Y. Electrospinning of nanofibers: reinventing the wheel?[J]. Advanced Materials, 2004, 16(14): 1151-1170.

[165] Pillay V, Dott C, Choonara Y E, et al. A review of the effect of processing variables on the fabrication of electrospun nanofibers for drug delivery applications[J]. Journal of Nanomaterials, 2013, 2013.

[166] Haider S, Al-Zeghayer Y, Ahmed Ali F A, et al. Highly aligned narrow diameter chitosan electrospun nanofibers[J]. Journal of Polymer Research, 2013, 20: 1-11.

[167] Zeng J, Haoqing H, Schaper A, et al. Poly-L-lactide nanofibers by electrospinning–Influence of solution viscosity and electrical conductivity on fiber diameter and fiber morphology[J]. e-Polymers, 2003, 3(1): 009.

[168] Kim B, Park H, Lee S H, et al. Poly (acrylic acid) nanofibers by electrospinning[J]. Materials letters, 2005, 59(7): 829-832.

[169] Alipour J, Shoushtari A M, Kaflou A. Enhancement in glass transition and tensile properties of PMMA nanofibres by incorporation of $MgCl_2$ in the electrospun polymer solution[J]. Fibers and Polymers, 2015, 16: 819-825.

[170] Sukwisute P, Yuennan J, Muensit N. Effects of the electric field and $AlCl_3 \cdot 6H_2O$ salt on the crystal, morphology and dielectric properties of P (VDF-HFP) fibres[C]//Journal of Physics: Conference Series. IOP Publishing, 2018, 1144(1): 012179.

[171] Jabur A R, Abdulmajeed M H, Abd S Y. Effect of copper chloride salt ($CuCl_2$) addition on DC, AC conductivity and tensile strength of PVA electrospun polymeric film[C]//AIP Conference Proceedings. AIP Publishing, 2019, 2190(1).

[172] Sasithorn N, Martinová L. Effect of calcium chloride on electrospinning of silk fibroin nanofibres[C]//Proceedings of the 4th RMUTP International Conference: Textiles & Fashion. 2012: 51-58.

[173] Zong X, Kim K, Fang D, et al. Structure and process relationship of electrospun bioabsorbable nanofiber membranes[J]. Polymer, 2002, 43(16): 4403-4412.

[174] Fong H, Chun I, Reneker D H. Beaded nanofibers formed during electrospinning[J]. Polymer, 1999, 40(16): 4585-4592.

[175] Bhardwaj N, Kundu S C. Electrospinning: A fascinating fiber fabrication technique[J]. Biotechnology Advances, 2010, 28(3): 325-347.

[176] Son W K, Youk J H, Lee T S, et al. The effects of solution properties and polyelectrolyte on electrospinning of ultrafine poly (ethylene oxide) fibers[J]. Polymer, 2004, 45(9): 2959-2966.

[177] Zhang D, Zhang N, Ma F, et al. One-step fabrication of functionalized poly (l-lactide) porous fibers by electrospinning and the adsorption/separation abilities[J]. Journal of Hazardous Materials, 2018, 360: 150-162.

[178] Sencadas V, Correia D M, Areias A, et al. Determination of the parameters affecting electrospun chitosan fiber size distribution and morphology[J]. Carbohydrate Polymers, 2012, 87(2): 1295-1301.

[179] He J H, Wan Y Q, Yu J Y. Scaling law in electrospinning: relationship between electric current and solution flow rate[J]. Polymer, 2005, 46(8): 2799-2801.

[180] Zargham S, Bazgir S, Tavakoli A, et al. The effect of flow rate on morphology and deposition area of electrospun nylon 6 nanofiber[J]. Journal of Engineered Fibers and Fabrics, 2012, 7(4): 155892501200700414.

[181] Matabola K P, Moutloali R M. The influence of electrospinning parameters on the morphology and diameter of poly (vinyledene fluoride) nanofibers-effect of sodium chloride[J]. Journal of Materials Science, 2013, 48: 5475-5482.

[182] Zhao Y, Cao X, Jiang L. Bio-mimic multichannel microtubes by a facile method[J]. Journal of the American Chemical Society, 2007, 129(4): 764-765.

[183] Hutmacher D W, Dalton P D. Melt electrospinning[J]. Chemistry-An Asian Journal, 2011, 6(1): 44-56.

[184] De Vrieze S, Van Camp T, Nelvig A, et al. The effect of temperature and humidity on electrospinning[J]. Journal of materials science, 2009, 44: 1357-1362.

[185] Pelipenko J, Kristl J, Janković B, et al. The impact of relative humidity during electrospinning on the morphology and mechanical properties of nanofibers[J]. International Journal of Pharmaceutics, 2013, 456(1): 125-134.

[186] Zhao R, Lu X, Wang C. Electrospinning based all-nano composite materials: recent achievements and perspectives[J]. Composites Communications, 2018, 10: 140-150.

[187] McKee M G, Layman J M, Cashion M P, et al. Phospholipid nonwoven electrospun membranes[J]. Science, 2006, 311(5759): 353-355.

[188] Kim C W, Kim D S, Kang S Y, et al. Structural studies of electrospun cellulose nanofibers[J]. Polymer, 2006, 47(14): 5097-5107.

[189] Barber P S, Griggs C S, Bonner J R, et al. Electrospinning of chitin nanofibers directly from an ionic liquid extract of shrimp shells[J]. Green Chemistry, 2013, 15(3): 601-607.

[190] Ohkawa K, Cha D, Kim H, et al. Electrospinning of chitosan[J]. Macromolecular Rapid Communications, 2004, 25(18): 1600-1605.

[191] Okutan N, Terzi P, Altay F. Affecting parameters on electrospinning process and characterization of electrospun gelatin nanofibers[J]. Food Hydrocolloids, 2014, 39: 19-26.

[192] Ju H W, Lee O J, Lee J M, et al. Wound healing effect of electrospun silk fibroin nanomatrix in burn-model[J]. International Journal of Biological Macromolecules, 2016, 85: 29-39.

[193] Dodero A, Donati I, Scarfi S, et al. Effect of sodium alginate molecular structure on electrospun membrane cell adhesion[J]. Materials Science and Engineering: C, 2021, 124: 112067.

[194] Chattopadhyay S, Hatton T A, Rutledge G C. Aerosol filtration using electrospun cellulose acetate fibers[J]. Journal of Materials Science, 2016, 51: 204-217.

[195] Li X, Kanjwal M A, Lin L, et al. Electrospun polyvinyl-alcohol nanofibers as oral fast-dissolving delivery system of caffeine and riboflavin[J]. Colloids and Surfaces B:

Biointerfaces, 2013, 103: 182-188.

[196] Smirnov M A, Tarasova E V, Vorobiov V K, et al. Electroconductive fibrous mat prepared by electrospinning of polyacrylamide-g-polyaniline copolymers as electrode material for supercapacitors[J]. Journal of Materials Science, 2019, 54: 4859-4873.

[197] Contardi M, Kossyvaki D, Picone P, et al. Electrospun polyvinylpyrrolidone (PVP) hydrogels containing hydroxycinnamic acid derivatives as potential wound dressings[J]. Chemical Engineering Journal, 2021, 409: 128144.

[198] Smyth M, Poursorkhabi V, Mohanty A K, et al. Electrospinning highly oriented and crystalline poly (lactic acid) fiber mats[J]. Journal of Materials Science, 2014, 49: 2430-2441.

[199] Lee M W, An S, Latthe S S, et al. Electrospun polystyrene nanofiber membrane with superhydrophobicity and superoleophilicity for selective separation of water and low viscous oil[J]. ACS Applied Materials & Interfaces, 2013, 5(21): 10597-10604.

[200] Wu M, Wang Q, Li K, et al. Optimization of stabilization conditions for electrospun polyacrylonitrile nanofibers[J]. Polymer Degradation and Stability, 2012, 97(8): 1511-1519.

[201] Li Q, Xu Y, Wei H, et al. An electrospun polycarbonate nanofibrous membrane for high efficiency particulate matter filtration[J]. RSC Advances, 2016, 6(69): 65275-65281.

[202] Chen Y, Han D, Ouyang W, et al. Fabrication and evaluation of polyamide 6 composites with electrospun polyimide nanofibers as skeletal framework[J]. Composites Part B: Engineering, 2012, 43(5): 2382-2388.

[203] Yanilmaz M, Kalaoglu F, Karakas H, et al. Preparation and characterization of electrospun polyurethane-polypyrrole nanofibers and films[J]. Journal of Applied Polymer Science, 2012, 125(5): 4100-4108.

[204] Szewczyk P K, Gradys A, Kim S K, et al. Enhanced piezoelectricity of electrospun polyvinylidene fluoride fibers for energy harvesting[J]. ACS Applied Materials & Interfaces, 2020, 12(11): 13575-13583.

[205] De Schoenmaker B, Van der Heijden S, De Baere I, et al. Effect of electrospun polyamide 6 nanofibres on the mechanical properties of a glass fibre/epoxy

composite[J]. Polymer Testing, 2013, 32(8): 1495-1501.

[206] Zhou X, Ding C, Cheng C, et al. Mechanical and thermal properties of electrospun polyimide/rGO composite nanofibers via in-situ polymerization and in-situ thermal conversion[J]. European Polymer Journal, 2020, 141: 110083.

[207] Li D, Xia Y. Fabrication of titania nanofibers by electrospinning[J]. Nano Letters, 2003, 3(4): 555-560.

[208] Nasir M, Subhan A, Prihandoko B, et al. Nanostructure and property of electrospun SiO_2-cellulose acetate nanofiber composite by electrospinning[J]. Energy Procedia, 2017, 107: 227-231.

[209] Nasr M, Viter R, Eid C, et al. Enhanced photocatalytic performance of novel electrospun BN/TiO_2 composite nanofibers[J]. New Journal of Chemistry, 2017, 41(1): 81-89.

[210] Song M Y, Ihn K J, Jo S M, et al. Electrospun TiO_2 electrodes for dye-sensitized solar cells[J]. Nanotechnology, 2004, 15(12): 1861.

[211] Wu H, Pan W. Preparation of zinc oxide nanofibers by electrospinning[J]. Journal of the American Ceramic Society, 2006, 89(2): 699-701.

[212] Zhang R, Zhang T, Cai Y, et al. Synthesis and characterization of a spun membrane with modified Al_2O_3[J]. Journal of Plastic Film & Sheeting, 2019, 35(4): 380-400.

[213] Lyu J Y, Chen S, He W, et al. Fabrication of high-performance graphene oxide doped PVDF/CuO/Al nanocomposites via electrospinning[J]. Chemical Engineering Journal, 2019, 368: 129-137.

[214] Lu X, Zhao Y, Wang C, et al. Fabrication of CdS nanorods in PVP fiber matrices by electrospinning[J]. Macromolecular Rapid Communications, 2005, 26(16): 1325-1329.

[215] Wang H, Lu X, Zhao Y, et al. Preparation and characterization of ZnS: Cu/PVA composite nanofibers via electrospinning[J]. Materials Letters, 2006, 60(20): 2480-2484.

[216] Shi Q, Vitchuli N, Nowak J, et al. Durable antibacterial Ag/polyacrylonitrile (Ag/PAN) hybrid nanofibers prepared by atmospheric plasma treatment and

electrospinning[J]. European polymer journal, 2011, 47(7): 1402-1409.

[217] Wang Y, Li Y, Sun G, et al. Fabrication of Au/PVP nanofiber composites by electrospinning[J]. Journal of Applied Polymer Science, 2007, 105(6): 3618-3622.

[218] Xu T, Li C, Li H, et al. Synthesis of well-dispersed copper nanoparticles in electrospun polyacrylonitrile nanofibres[J]. Micro & Nano Letters, 2013, 8(12): 849-852.

[219] Khandaker M, Nikfarjam S, Raj H A, et al. Assessment of Polyurethane Nanofiber with Nikel as Terahertz Metamaterial and Strain Sensor[C]//2022 12th International Conference on Electrical and Computer Engineering (ICECE). IEEE, 2022: 116-119.

[220] Eskizeybek V, Yar A, Avcı A. CNT-PAN hybrid nanofibrous mat interleaved carbon/epoxy laminates with improved Mode I interlaminar fracture toughness[J]. Composites Science and Technology, 2018, 157: 30-39.

[221] Stanishevsky A, Yager R, Tomaszewska J, et al. Structure and mechanical properties of nanofibrous ZrO_2 derived from alternating field electrospun precursors[J]. Ceramics International, 2019, 45(15): 18672-18682.

[222] Bognitzki M, Becker M, Graeser M, et al. Preparation of sub-micrometer copper fibers via electrospinning[J]. Advanced Materials, 2006, 18(18): 2384-2386.

[223] Yang X, Chen Y, Zhang C, et al. Electrospun carbon nanofibers and their reinforced composites: Preparation, modification, applications, and perspectives[J]. Composites Part B: Engineering, 2023, 249: 110386.

[224] Lee S W, Kim Y U, Choi S S, et al. Preparation of SiO_2/TiO_2 composite fibers by sol-gel reaction and electrospinning[J]. Materials Letters, 2007, 61(3): 889-893.

[225] Shen X, Mu D, Chen S, et al. Electrospun composite of ZnO/Cu nanocrystals-implanted carbon fibers as an anode material with high rate capability for lithium ion batteries[J]. Journal of Materials Chemistry A, 2014, 2(12): 4309-4315.

[226] Wang L, Yu Y, Chen P C, et al. Electrospinning synthesis of C/Fe_3O_4 composite nanofibers and their application for high performance lithium-ion batteries[J]. Journal of Power Sources, 2008, 183(2): 717-723.

[227] Yan Z, Yao W, Hu L, et al. Progress in the preparation and application of three-

dimensional graphene-based porous nanocomposites[J]. Nanoscale, 2015, 7(13): 5563-5577.

[228] Yang X Y, Chen L H, Li Y, et al. Hierarchically porous materials: synthesis strategies and structure design[J]. Chemical Society Reviews, 2017, 46(2): 481-558.

[229] Blakeney B A, Tambralli A, Anderson J M, et al. Cell infiltration and growth in a low density, uncompressed three-dimensional electrospun nanofibrous scaffold[J]. Biomaterials, 2011, 32(6): 1583-1590.

[230] Dilamian M, Joghataei M, Ashrafi Z, et al. From 1D electrospun nanofibers to advanced multifunctional fibrous 3D aerogels[J]. Applied Materials Today, 2021, 22: 100964.

[231] Zong D, Zhang X, Yin X, et al. Electrospun fibrous sponges: principle, fabrication, and applications[J]. Advanced Fiber Materials, 2022, 4(6): 1434-1462.

[232] Xu T, Ding Y, Liang Z, et al. Three-dimensional monolithic porous structures assembled from fragmented electrospun nanofiber mats/membranes: Methods, properties, and applications[J]. Progress in Materials Science, 2020, 112: 100656.

68

2. Aim and Overview of the Thesis

Aim

MOFs and COFs have the characteristics of high porosity, large surface area, designable framework structure and easy functionalization, and have been widely used in fields such as energy, environmental remediation, sensors, biomedical engineering and catalysis. However, their insolubility in solvents and non-melting character due to the network structure makes their processing to the desired object difficult. This has hindered the sustainable application of frameworks in several fields. Generally, they are used in the form of powder. The recovery of framework powders after use for recycling is inefficient and cost intensive process. If available in the form of self-standing architectures like membranes and sponges, the sustainable use of frameworks in catalysis, water purification and energy sector would be possible highlighting the possibility of their use for several cycles. Therefore, the purpose of this research is to provide versatile preparation methods to process polymer frameworks, such as MOFs and COFs into monolithic materials, including 2D membranes, and 3D sponges. The main processing tool used in this work is electrospinning. The utility of the successfully prepared self-standing framework architectures is then shown in catalysis for cascade reactions in one pot, water purification and gas separation in collaboration with Ms. Yingying Du (Agarwal group) and Ms. Marion Breunig (Senker group). The results are presented in the form of cumulative thesis with five published articles in peer-reviewed journals (Advanced Functional Materials, ChemCatChem, Microporous and Mesoporous Materials, Advanced Functional Materials and Advanced Energy and Sustainability Research) (**section 2.1** to **section2.5**). The work is summarized graphically in **Figure 2-1**.
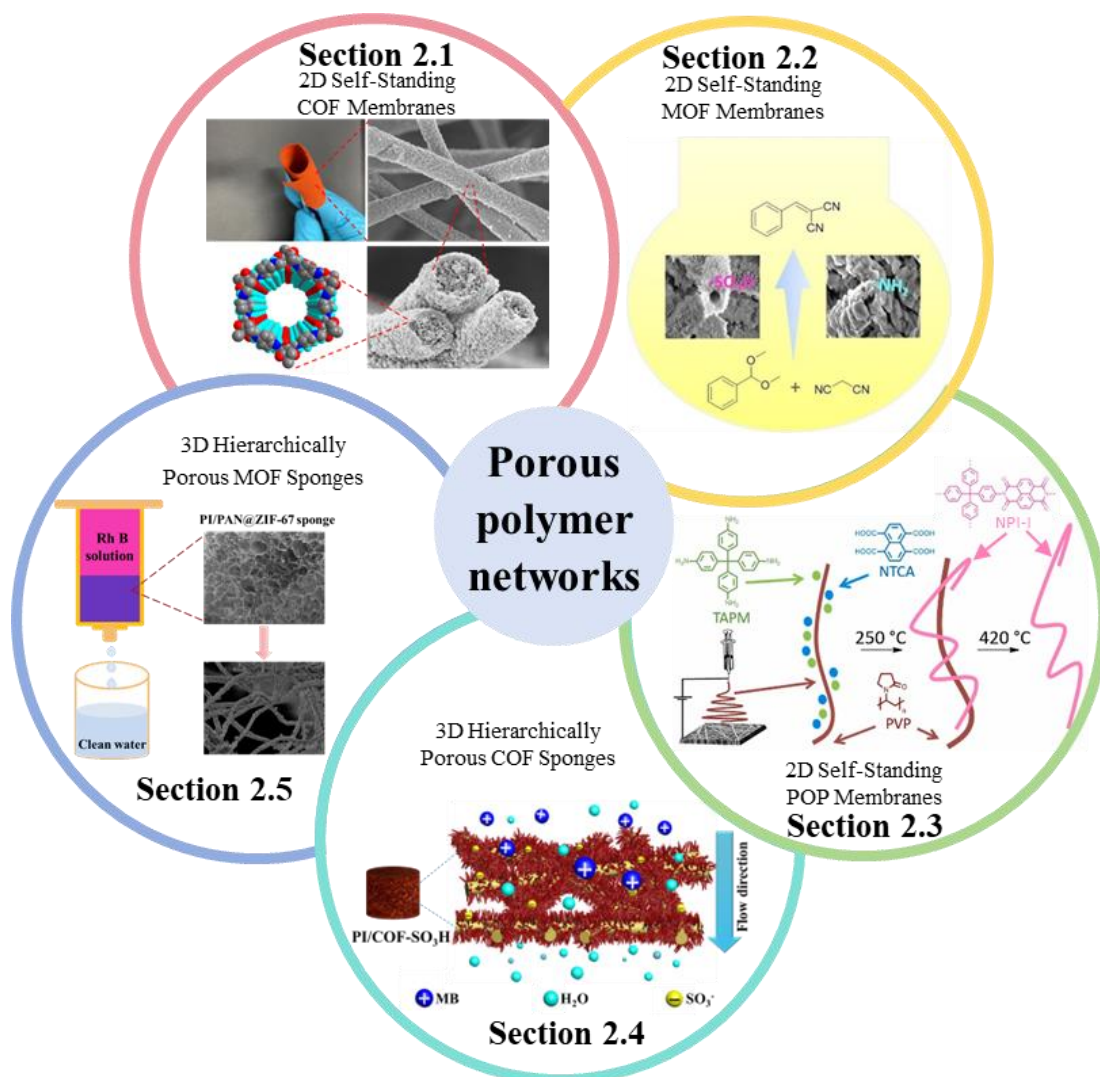
Figure 2-1. Context of this thesis showing preparation methods and applications of (i) 2D covalent organic framework (COF) membranes, (ii) 2D metal-organic framework (MOF) membranes, (iii) 2D porous organic polymer (POP) membranes, (iv) 3D COF sponges, (v) 3D MOF sponges.

Overview

In the first section (**section 2.1**), I proposed a template-assisted process to prepare porous self-standing COF membranes. The method uses an electrospun polymer membrane as a sacrificial large dimension template skeleton on which in the first step COFs were grown. In the second step the template electrospun polymer was removed by solvent extraction to obtain large dimension porous self-standing COF membranes

with high crystallinity, large surface area, mechanical stability and flexibility. The applicability of the established template-assisted framework preparation method was studied for the preparation of acid and base functional MOF membranes (**section 2.2**). This work was carried out in collaboration with my laboratory colleague Ms. Yingying Du. The functional MOF membranes were highly effective in acid and based catalyzed cascade reactions in one-pot and reusable for several cycles. In the template assisted framework preparation method one of the components of COF/MOF was immobilized on the template electrospun polymer membranes by mixing them in the electrospinning solution. When such polymer membrane with one of the framework components comes in contact with the second component of COF/MOF and suitable reaction conditions, the in-situ growth on the template started.

Mixing both the components of a framework with the template electrospinning polymer solution and exposing such membrane to suitable framework formation reaction conditions led to non-crystalline porous organic polymer framework which was used by Prof. Senker's group for CO_2 uptake and for gas (CO_2/N_2 and CO_2/CH_4) separation (**section 2.3**).

Compared to 2D fiber membranes, 3D fiber sponges have hierarchical porous structure and exhibit higher porosity, which is beneficial to mass transfer. **Sections 2.4** and **2.5** describe preparation procedures for making 3D COF and MOF sponges and their applications in waste water purification. Polyimide (PI) electrospun short fibers with high thermal/chemical stability are used as the network skeleton of the 3D fiber sponge, on which COFs and MOFs are grown in situ, to construct COF and MOF 3D sponges, and use them for wastewater treatment. Based on the hierarchical structure and excellent mechanical stability of 3D COF fiber sponges and 3D MOF fiber sponges, they can be repeatedly used to remove organic dyes from water quickly and efficiently. In the following section, the aforementioned work is elaborated in detail.

2.1 Flexible, Mechanically Stable, Porous Self-Standing Microfiber Network Membranes of Covalent Organic Frameworks: Preparation Method and Characterization
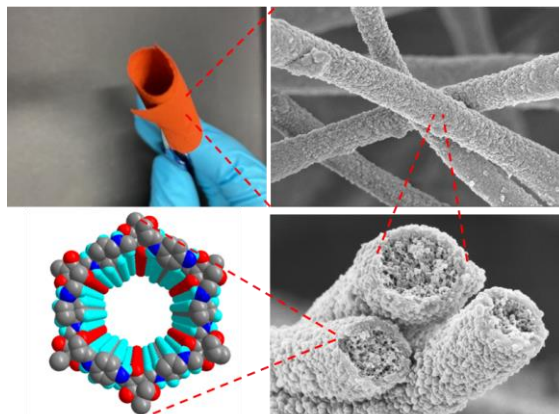
Chenhui Ding, Marion Breunig, Jana Timm, Roland Marschall, Jürgen Senker, Seema Agarwal. Flexible, Mechanically Stable, Porous Self-Standing Microfiber Network Membranes of Covalent Organic Frameworks: Preparation Method and Characterization. Advanced Functional Materials, **2021**, 31(49), 2106507.

Specific contributions by authors:

In this publication, I was the lead author. I carried out all experiments for membrane preparation and, most of the characterization, and writing of the manuscript. Dr. Marion Breunig performed and analyzed the XRD and solid-state NMR measurements in guidance of Prof. Jürgen Senker. Dr. Jana Timm and Professor Roland Marschall were responsible for BET measurements and analysis. Professor Seema Agarwal designed, guided and supervised the project. All authors contributed to discussions and finalizing the manuscript.

In this work a highly versatile preparation procedure for making a self-standing, flexible and crystalline COF membrane is established. As an example, the COF membrane based on p-phenylenediamine (Pa) and 1,3,5-triformylphloroglucino (Tp) was prepared, as shown in **Figure 2-2a**. The method is named as template-assisted framework (TAF) preparation process as the framework is grown on a polymer electrospun template

membrane made of randomly laid polymer fibers. The TAF preparation procedure is divided into three steps. The first step is the immobilization of one of the reactants of the framework, i.e. diamine (Pa) on the template polymer (polyacrylonitrile (PAN)) electrospun membrane. This is done by electrospinning PAN solution mixed with the diamine. In the second step, the electrospun PAN/Pa fiber membrane is dipped into dichloromethane (CH_2Cl_2) solution of the second reactant of the COF, a trialdehyde (Tp) containing acetic acid as catalyst. In this step the growth of COF on the template PAN fiber is started at 120 °C. In the last step, the template polymer (PAN) was removed by solvent extraction giving porous self-standing COF membrane (~ 100 micron thick). The complete TAF process is shown in **Figure 2-2b**. Several experiments were carried out by changing temperature, reactant amounts, electrospinning conditions, template removal method to establish the optimum parameters for obtaining mechanically stable, self-standing flexible and crystalline COF membranes.
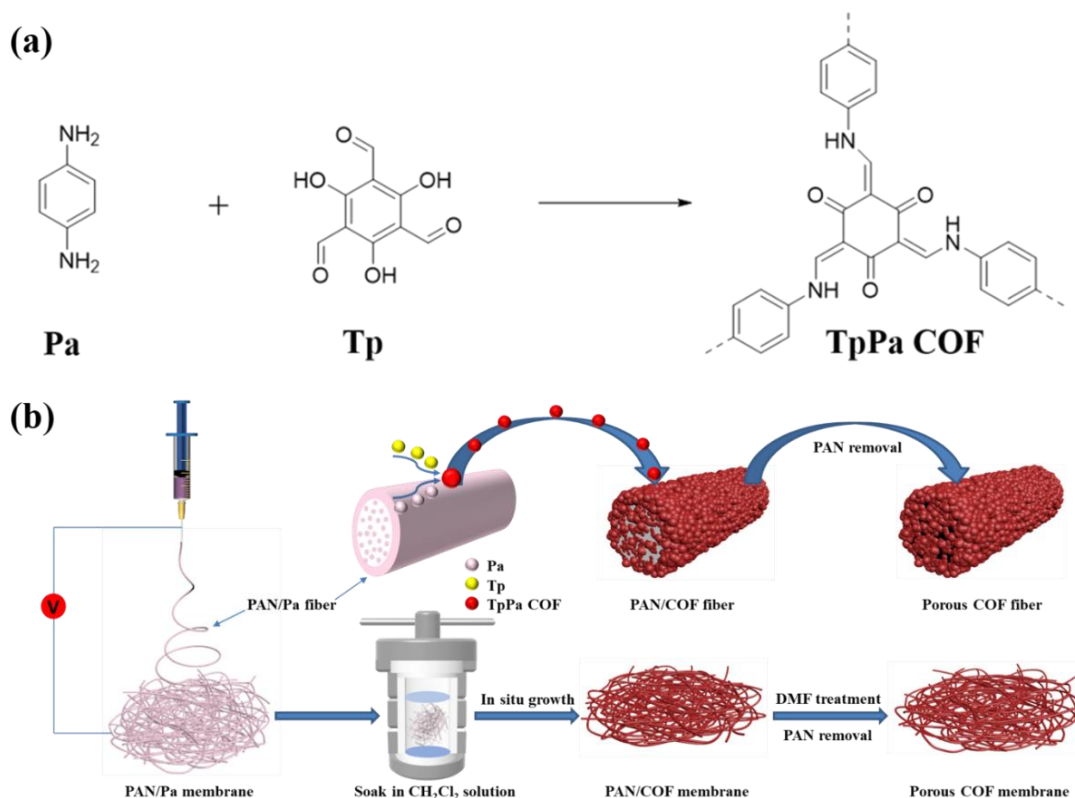
Figure 2-2. General schematic of TpPa COF (a). Preparation of porous self-standing COF fiber membranes by template-assisted framework (TAF) process (b). PAN = polyacrylonitrile, Pa = p-phenylenediamine, Tp = 1,3,5-triformylphloroglucinol.

Scanning electron microscope (SEM) was used to study the morphology of COF and the fiber membranes (**Figure 2-3**). It is obvious from the SEM pictures that COF nanoparticles grow both on the surface and in the bulk of the template PAN fibers. After removing PAN, the porous COF fiber formed has a core-shell structure. The inner core exhibits a hierarchical porous structure and is composed of loosely packed COF nanoparticles; the outer shell is composed of COF nanoparticles closely packed to form a dense wall. The structural characterization of the COF membranes was carried out using a combination of different analytical methods including ^{13}C and ^{15}N NMR techniques (collaboration with Prof. Senker group). The analysis by NMR, FT-IR spectra and XRD patterns showed complete removal of the template polymer (PAN) and formation of highly crystalline COF membranes (**Figure 2-4a-d**). N_2 physisorption isotherms were conducted to examine the surface areas, the pore size distributions, and the cumulative pore volumes of TpPa COF powders and material from different steps of the TAF process (**Figure 2-4e-f**). The pore size distribution of the COF fiber membranes exhibits maxima between 1.7-1.8 nm, matching the pore sizes of the TpTa COF powder and the ones determined from the XRD data. The surface area of COF membrane is as high as 1153 m^2 g^{-1}, exceeding even that obtained for the TpPa COF powder. The removal of the template polymer by solvent extraction creates a hierarchically porous material with a microporosity, that renders all COF nanoparticles accessible (including in the bulk).
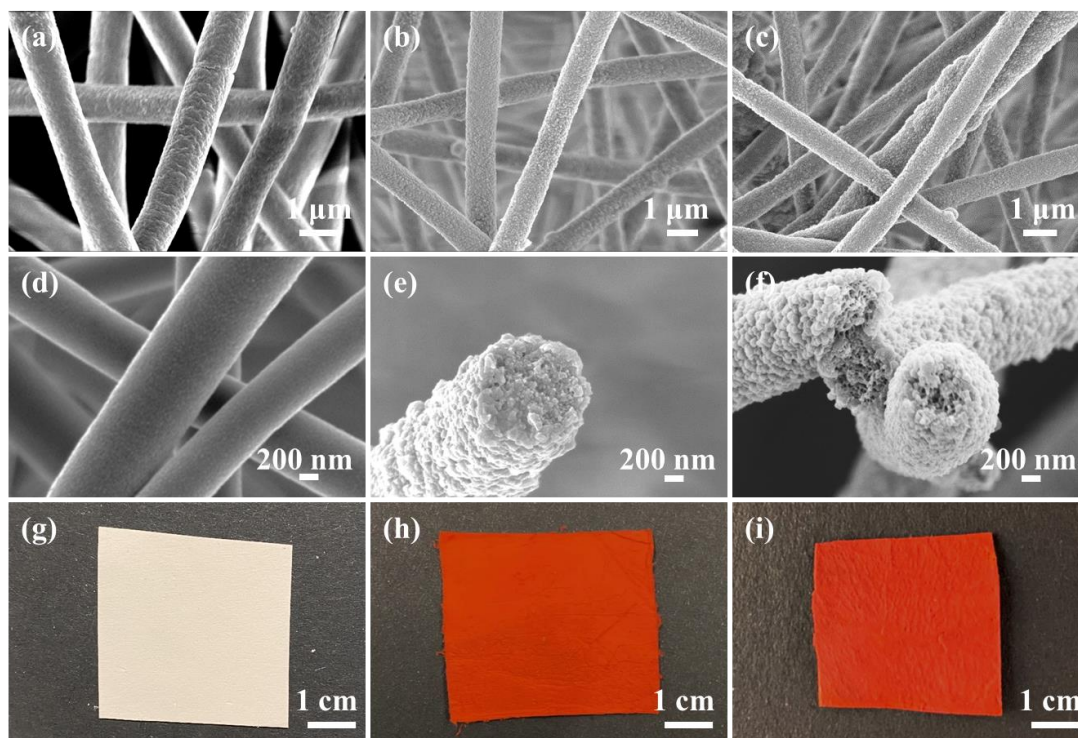
Figure 2-3. SEM images of PAN/Pa fiber (a) and (b), PAN/COF fiber (b) and (e), and COF fiber (c) and (f). Photographs of PAN/Pa fiber membrane (g), PAN/COF fiber membrane (h), and c) porous self-standing COF fiber membrane (i).
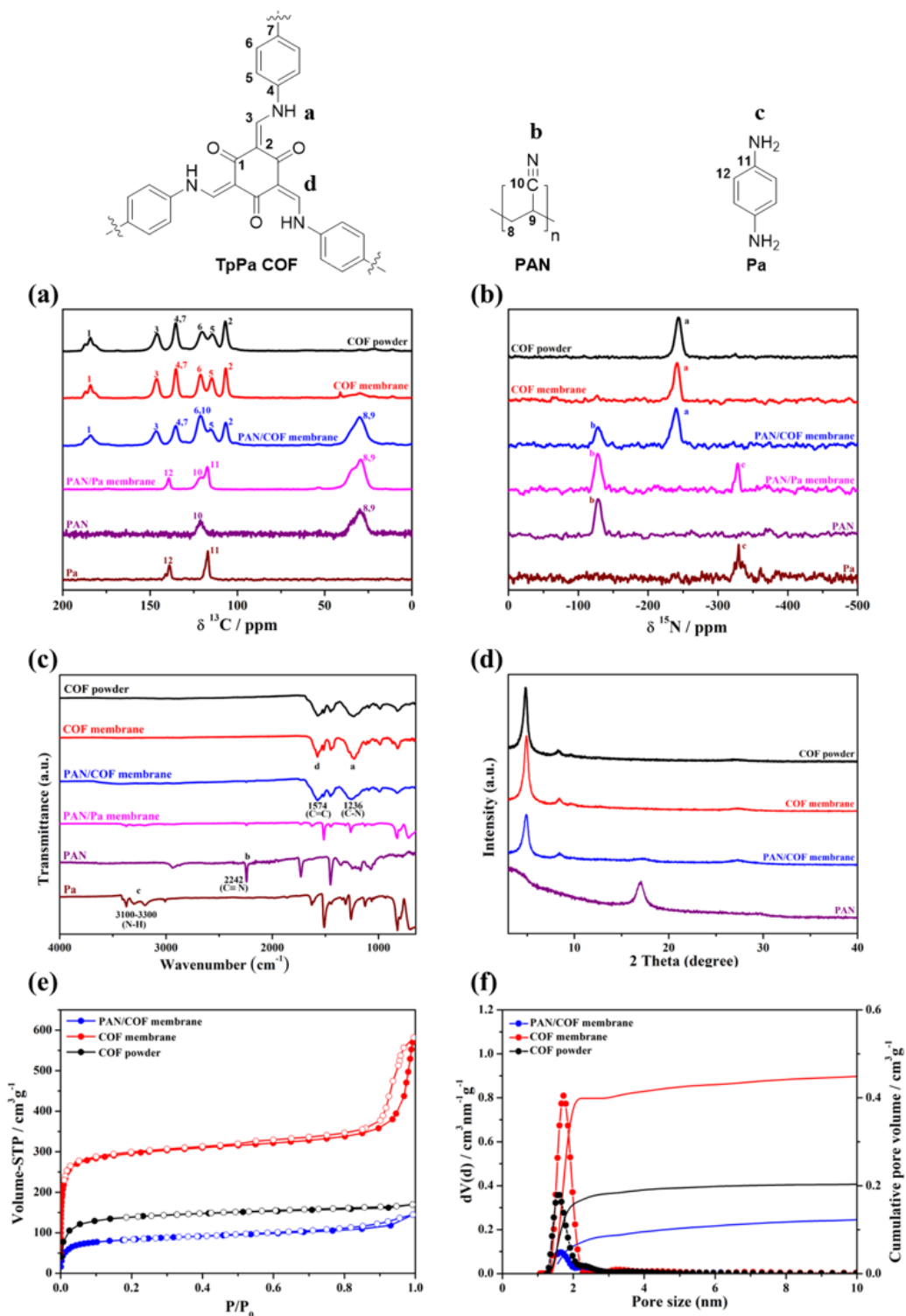
Figure 2-4. ^{13}C (a), ^{15}N (b) CP MAS NMR, FT-IR (c) spectrum and XRD (d) patterns of Pa, PAN, PAN/Pa fiber membranes, COF membrane and COF powder. N_2 adsorption–desorption isotherms of PAN/COF membrane, COF membrane, and COF powder (a), their pore size distribution, and cumulative pore volume obtained using the quenched solid density functional theory method (b).

The highest tensile strength of COF membrane in this work is 0.64 MPa (**Figure 2-5a**). Although the value seems low but sufficient to handle membranes for different applications as shown in the later part of the work. A 10 000-cycle bending test with a compression of 50% was carried out to study the flexibility of the COF membranes. Excellent bending stability, and flexibility was proved as the mechanical properties remain unchanged after 10 000 bending tests (**Figure 2-5a, d**). The sample that underwent a bending cycle did not show any cracks as seen by SEM images (**Figure 2-5b-c**).
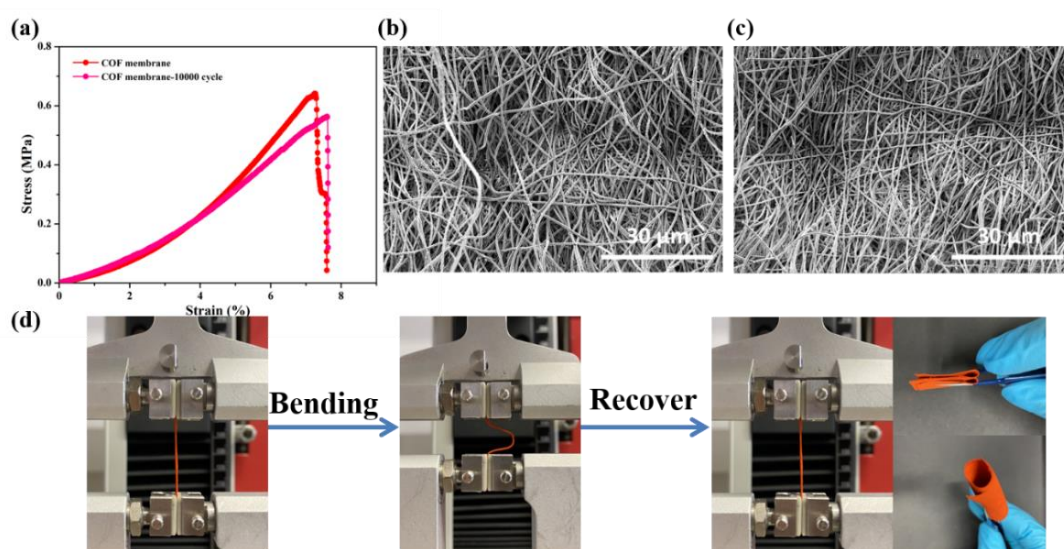
Figure 2-5. Typical stress–strain curves of COF membrane, and COF membrane after 10 000 cycles of bending (a). SEM images of COF membrane (b), and COF membrane-10000 cycle (c). Bending and recovery processes for the COF, and the test at different bending states (d).

In summary, I could successfully establish a method (template-assisted framework process) for preparing a large-sized porous self-standing crystalline COF membranes with high surface area, good mechanical stability and flexibility. This was a big challenge in the field of COFs. The field of preparation and characterization of COFs is developing very fast and the existence of COFs in the form of 2D membranes is expected to open several new application areas, such as catalysis, water purification and energy storage.

The next question is if same method can also be extended to the preparation of other types of frameworks like MOFs. Consequently, efforts were dedicated to studying the preparation and properties of self-standing MOF membranes using the TAF process, as described in the following section.

2.2 Template-assisted Preparation of Self-standing 2D-MOF Membranes for Application in Cascade Reactions
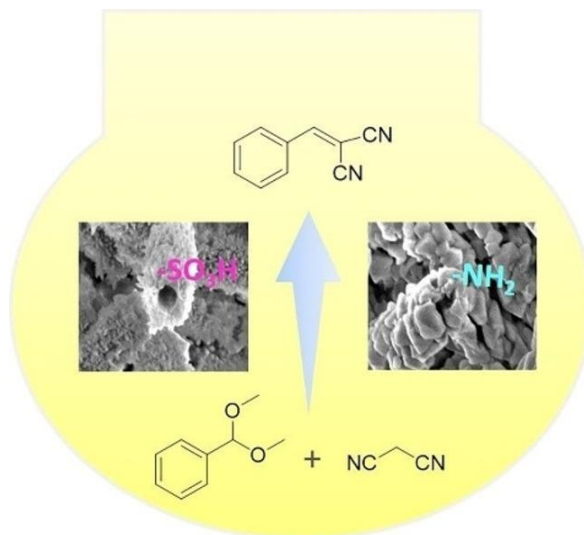
Yingying Du, **Chenhui Ding**, Jana Timm, Roland Marschall, Seema Agarwal. Template‑assisted Preparation of Self‑standing 2D‑MOF Membranes for Application in Cascade Reactions. ChemCatChem, **2022**, 14(22), e202201040.

Specific contributions by authors:

In this work the experiments for making MOF powder and membranes were carried out by me and Yingying Du. In addition, characterization of samples by SEM and X-ray was done by me. Yingying Du is the lead author and carried out FTIR and experiments for use of MOF membranes as catalysts in cascade reactions. Dr. Jana Timm and Professor Roland Marschall were responsible for BET measurements and analysis. Prof. Seema Agarwal designed, guided and supervised the project. The manuscript was written by Yingying Du and all authors contributed to discussions and finalizing the manuscript.

In this work, two different functional self-standing MOF (UiO-66-SO$_3$H and UiO-66-NH$_2$) membranes with acid and base functional groups were prepared using TAF process. The UiO-66-SO$_3$H and UiO-66-NH$_2$ MOF powders are in general prepared by reaction of ZrCl$_4$ with 2-aminobenzenedicarboxylic acid (BDC-NH$_2$) and 2-

sulfobenzenedicarboxylic acid monosodium salt (BDC-SO$_3$Na), respectively (**Figure 2-6a)**. For the preparation of the self-standing membranes, the template polymer (PAN) is electrospun with ZrCl$_4$. The resulting electrospun membrane is then dipped in aqueous solutions of BDC-NH$_2$ or BDC-SO$_3$Na containing acetic acid as catalyst, and reacted at 120 °C to obtain the PAN/MOF membranes. Finally, through solvent extraction, PAN is removed to obtain the self-standing MOF UiO-66-SO$_3$H and UiO-66-NH$_2$ membranes (thickness 240 ± 12 μm and 265 ± 10 μm, respectively) (**Figure 2-6b)**.
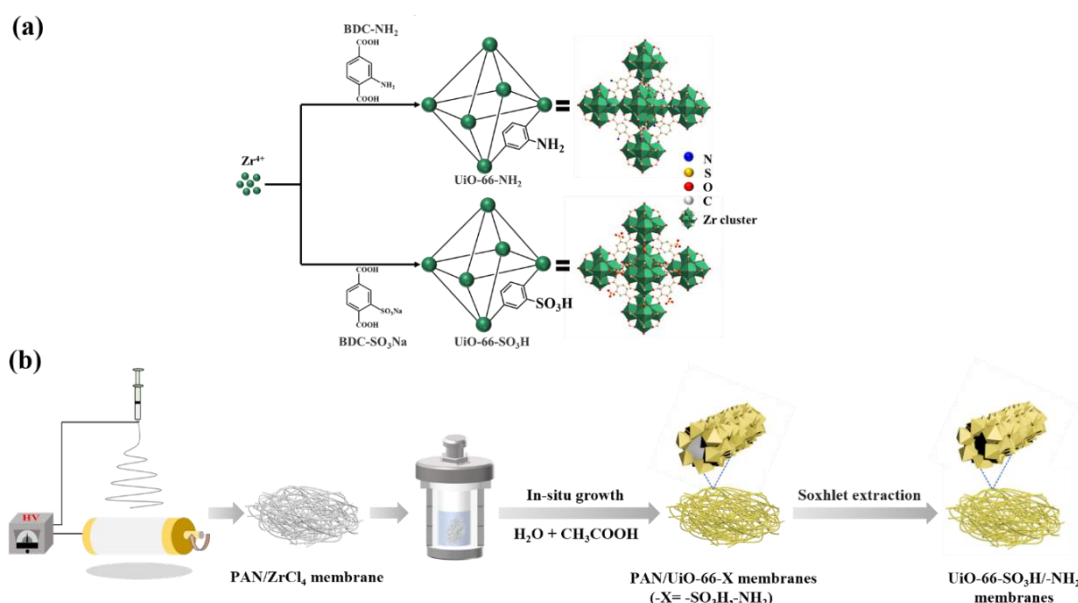
Figure 2-6. General schematic of UiO-66-SO$_3$H and UiO-66-NH$_2$ (a). Strategy to fabricate the self-standing UiO-66-SO$_3$H and UiO-66-NH$_2$ membranes (b).

SEM was used to characterize the morphology of the self-standing MOF membranes before and after removal of PAN. A large amount of MOF can be found growing on the surface of the PAN fiber and completely wrapping it. After removing the PAN, the MOF membranes with randomly laid hollow MOF fibers were formed (**Figure 2-7**). The COF fibers as described in the previous section showed slightly different morphology with COF growing in the bulk of the template PAN fibers also. Whereas, MOF grew only on the surface of the template fibers leading to hollow MOF fibers after removal of the template. The difference is ascribed to the size of the framework particles.
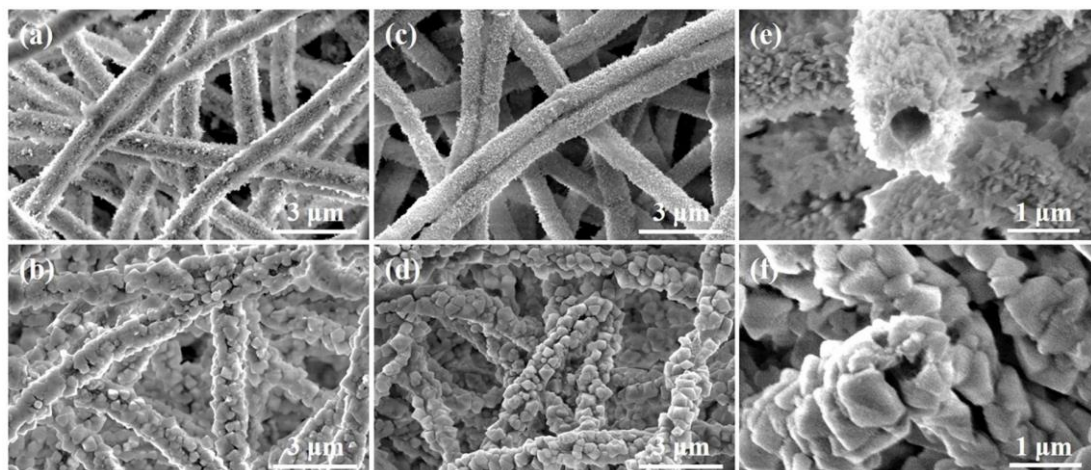
Figure 2-7. SEM images of PAN/UiO-66-SO$_3$H (a), PAN/UiO-66-NH$_2$ (b), UiO-66-SO$_3$H (c), UiO-66-NH$_2$ (d). Cross-sectional SEM images of UiO-66-SO$_3$H (e), UiO-66-NH$_2$ (f).

The combination of analytical methods like XRD and FTIR confirmed the successful preparation of crystalline UiO-66-SO$_3$H/-NH$_2$ membranes (**Figure 2-8a-b**).

The N$_2$ physisorption isotherms indicated the presence of micropores and mesopores (**Figure 2-8c-d**). The specific surface areas of the membranes, as calculated using the BET (Brunauer Emmet Teller) model with the Roquerol correction for microporous materials are 330 and 84 m^2 g^{-1} for UiO-66-NH$_2$ and UiO-66-SO$_3$H respectively. The values are lower than the specific surface areas of powder samples (UiO-66-NH$_2$: 1051 m^2 g^{-1}, UiO-66-SO$_3$H: 539 m^2 g^{-1}). This decrease in the surface area could be explained by the partial change in the crystal structure of the crystals of the UiO-66 materials, which was already observed due to the broadening of the reflections in the XRD pattern.
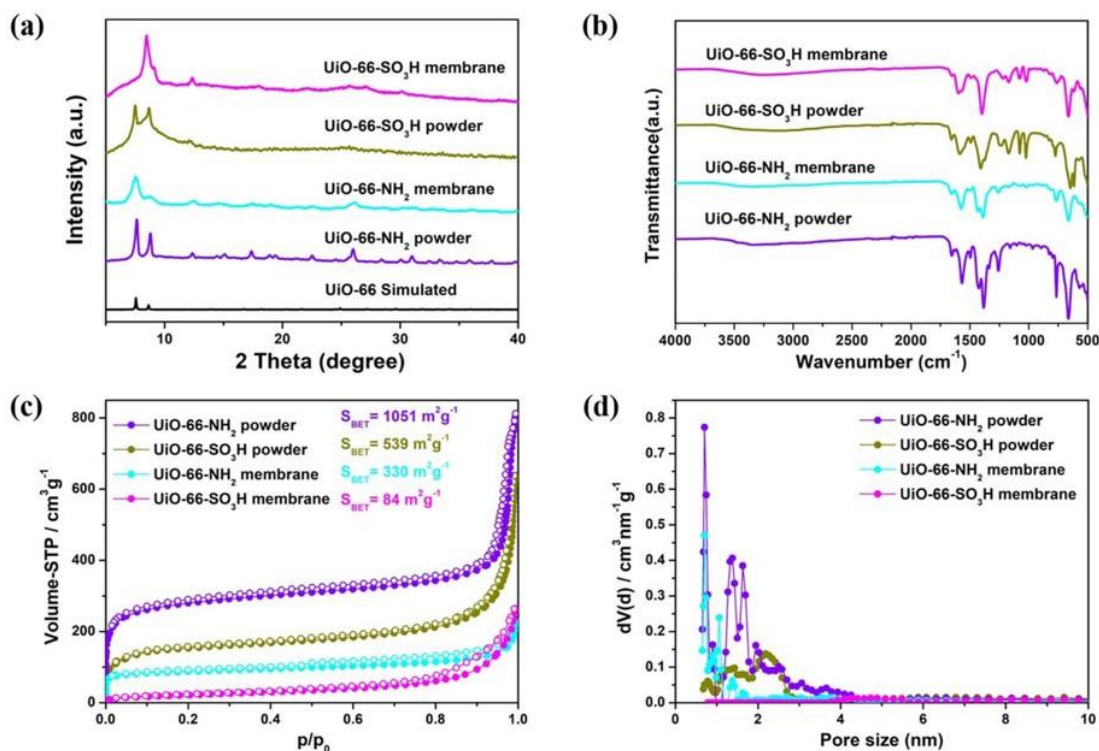
Figure 2-8. XRD patterns of UiO-66 simulated, UiO-66-SO$_3$H powder, UiO-66-SO$_3$H membrane, UiO-66-NH$_2$ powder and UiO-66-NH$_2$ membrane (a). FT-IR spectra of UiO-66-SO$_3$H powder, UiO-66-SO$_3$H membrane, UiO-66-NH$_2$ powder and UiO-66-NH$_2$ membrane (b). N$_2$ physisorption isotherms of UiO-66-SO$_3$H powder, UiO-66-SO$_3$H membrane, UiO-66-NH$_2$ powder and UiO-66-NH$_2$ membrane (c). Pore size distribution and cumulative pore volume of UiO-66-SO$_3$H powder, UiO-66-SO$_3$H membrane, UiO-66-NH$_2$ powder and UiO-66-NH$_2$ membrane (d).

Still, the fiber morphology in membranes, acid-base functionalities and capability of using the individual membranes in a modular way led to their use in two-step cascade reactions within a one-pot. The use of acid-base catalysts in one pot is not trivial due to the Wolf-Lamb-type character deactivating each other. Also, the membrane nature of the catalysts is expected to provide easy recovery and reuse. The membranes prepared by me were given to Ms. Yingying Du for studying their utility in a one-pot cascade reaction as a part of her Ph.D. work. The two step cascade reactions were: the acid catalyzed conversion of benzaldehyde dimethyl acetal to benzaldehyde and base catalyzed subsequent reaction of benzaldehyde with different active methylene

compounds, such as malononitrile, ethyl cyanoacetate, and diethyl malonate. The system worked very well for cascade reactions involving malononitrile, ethyl cyanoacetate in the second step with the yield of the product was as high as 99.9%. The catalytic membranes were reusable without any significant loss in activity (**Figure 2-9**).
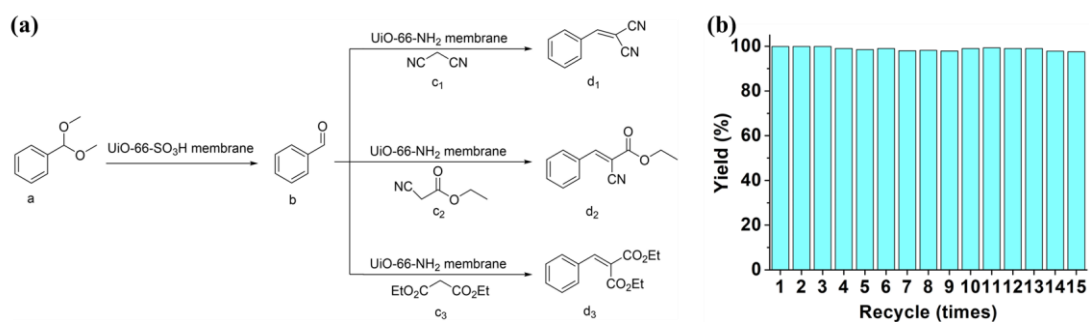
Figure 2-9. One-pot acid-base cascade reactions were studied in the present work (a). Research on catalyst recycling of self-supporting MOF membranes (b).

In conclusion, the TAF procedure has demonstrated versatility by its extension to the preparation of self-standing, functional MOF membranes. The utility of these membranes as sustainable catalysts for cascade reactions in a one-pot setup has been effectively shown. This work signifies an important advancement towards the preparation and utilization of macroscopically sized MOF membranes as sustainable catalysts.

My subsequent research question explored the possibility of immobilizing both framework-forming components on a template electrospun fiber and then initiating framework formation simply by establishing the appropriate reaction conditions.

2.3 Electrospun, non-woven fiber membranes of porous polyimides with high carbon dioxide uptakes and selectivities
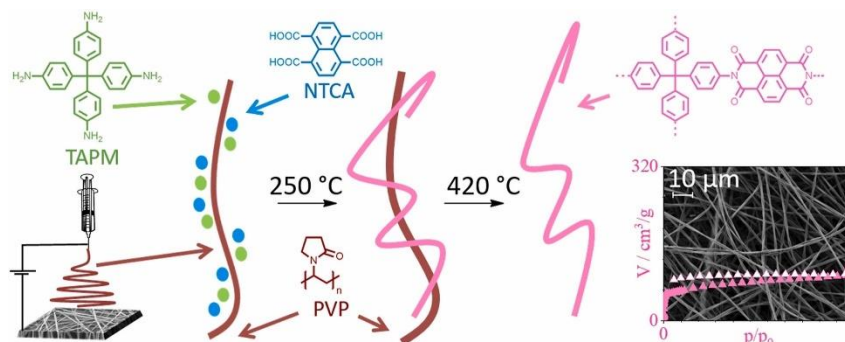
Marion Breunig, Jian Zhu, **Chenhui Ding**, Renée Siegel, Seema Agarwal, Jürgen Senker. Electrospun, non-woven fiber membranes of porous polyimides with high carbon dioxide uptakes and selectivities. Microporous and Mesoporous Materials, **2022**, 329, 111519.

Specific contributions by authors:

In this work, Marion Breunig was the lead author responsible for the, data processing, making experiments regarding bulk films and gas uptake studies. She was also responsible for writing, reviewing, and editing the manuscript. Jian Zhu and I were responsible for the experiments establishing electrospinning of the framework components with template polymers, their solid-state polymerizations and mechanical stability tests. SEM characterization of samples was done by me. I also contributed to writing the manuscript. Renée Siegel completed writing the first draft. Professors Seema Agarwal and Jürgen Senker directed and supervised the project.

The concept of the work is to prepare the self-standing framework membranes by immobilizing the starting components on the electrospun polymer template membrane followed by the solid-state polymerization with the simultaneous removal of the template polymer by thermal degradation. For this, polyimide (PI) framework formation by reaction between tetrakis (4-aminophenyl) methane (TAPM) and naphthalene-1,4,5,8-tetracarboxylic acid (NTCA) was considered. Poly(vinyl

pyrrolidone) (PVP) was used as the template polymer.

The entire preparation process can be divided into three steps, as shown in **Figure 2-10**. First, a DMF solution of linkers (TAPM and NTCA in 1:2 molar ratio) and template polymer (PVP) was electrospun into precursor fiber membranes (PIM_pre). In the second and third step, the precursor fiber membranes are heated with a stepwise heating profile to first start polymerization of TAPM and NTCA to initiate polyimide framework formation and later on to complete imidization and hence the framework formation with the simultaneous removal of the template polymer by thermal degradation to obtain the porous polyimide fiber membranes (PIM_420).
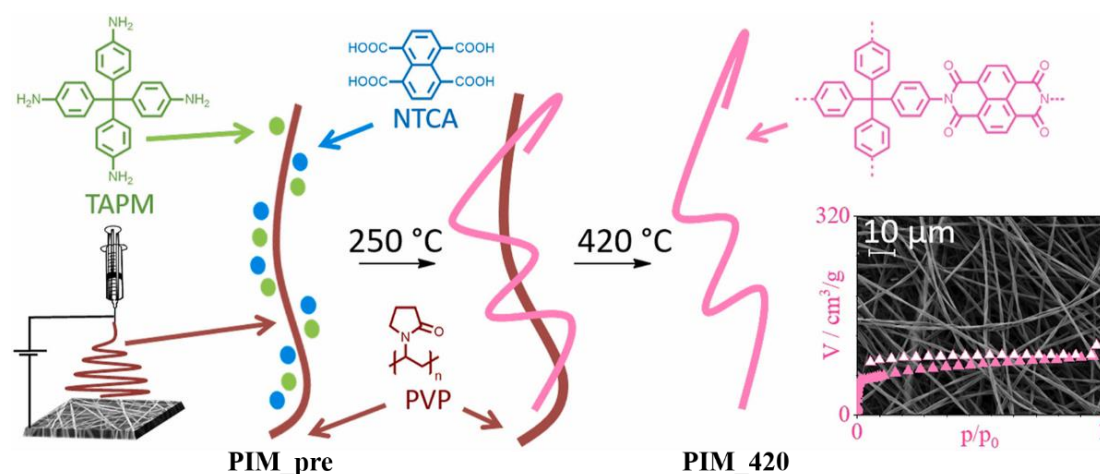
Figure 2-10. Preparation of framework membranes by template-assisted process. TAPM = tetrakis (4-aminophenyl) methane, NTCA = naphthalene-1,4,5,8-tetracarboxylic acid, PVP = polymer polyvinylpyrrolidone.

The process was optimized by varying the amount of PVP, and heating temperatures (350 °C and 420 °C). The ^{13}C and ^{15}N CP MAS as well as FTIR were used to prove the incorporation of the two educts (TAPM and NTCA) in the electrospun PVP fibers and the formation of PI framework and the removal of the template polymer after programmed heating (**Figure 2-11a-c**). Unlike COF and MOF in the previous sections, the PI framework is amorphous based on XRD measurements. An apparent BET surface area of 222 m^2 g^{-1} was measured and membrane exhibits a remarkable microporosity with a high amount of ultramicropores (**Figure 2-11d-f**). The framework membranes are flexible and showed a carbon dioxide uptake of 13.1 wt% (0 °C, 1 bar) and very

low affinity for nitrogen and methane, thereby promising high CO_2/N_2 selectivities for separation applications (**Table 2-1**). The gas permeation experiments were carried out by Ms. Marion Breunig (Senker group).
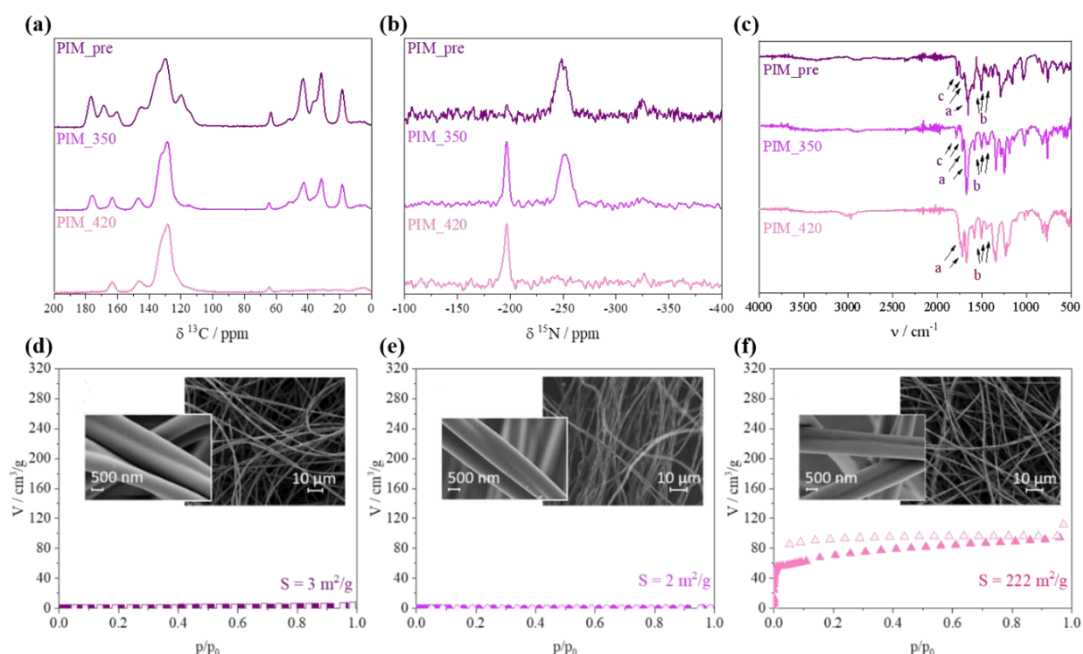
Figure 2-11. ^{13}C (a) and ^{15}N (b) CP MAS NMR, FT-IR (c) spectra of PIM_pre, PIM_350 and PIM_420. Argon isotherms measured at 87 K with the surface area calculated based on the BET equation, and SEM images of PIM_pre (d), PIM_350 (e), and PIM_420 (f).

Table 2-1. Uptakes taken from individual Isotherms. The values were determined at p = 1 bar.

Polymer	CO_2 / mmol g^{-1}			N_2 / mmol g^{-1}			CH_4 / mmol g^{-1}		
	0 °C	25 °C	40 °C	0 °C	25 °C	40 °C	0 °C	25 °C	40 °C
PIM_420	3.0	2.4	1.9	0.1	-	-	0.6	0.3	0.3

Figure 2-12. The PIM_420 fiber membranes exposed to different bending states. They include folding, twisting and curling and indicate good flexibility and mechanical stability of the membranes.

In summary, the feasibility of transforming microporous organic polyimide frameworks into self-standing, flexible membranes via a template-assisted process has been established. These porous polyimide fiber membranes exhibit notable flexibility and mechanical stability, allowing for bending, curling, and twisting actions as demonstrated in Figure 2-12. The membranes are thermally stable and promising for use in gas separation. The membrane fabrication method introduced in this study holds potential for broader application across various porous polymer framework systems, offering a novel approach to the processing and shaping of challenging porous polymers. After establishing preparation procedures for 2D framework membranes and showing applications in catalysis and gas separation, the next question is if the TAF process can also be extended to the preparation of 3D sponges. The following section will elaborate on research related to 3D framework sponges.

2.4 Open-Cell Robust COF-Nanowire Network Sponges as Sustainable Adsorbent and Filter
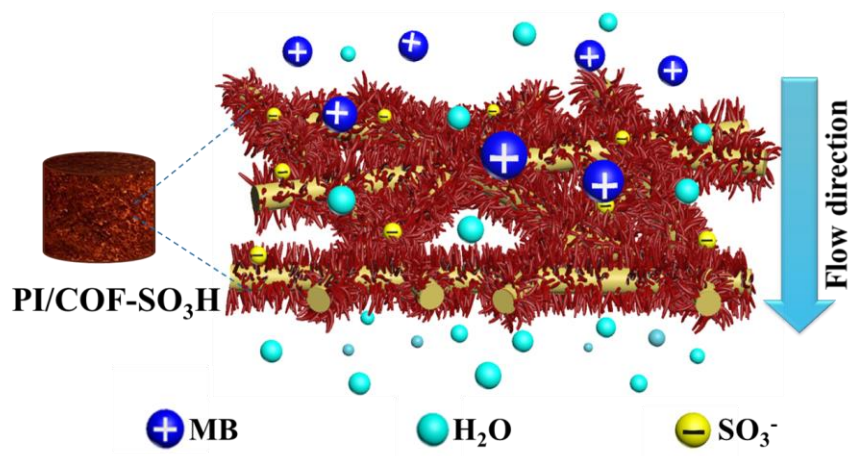
Chenhui Ding, Yingying Du, Seema Agarwal. Open-Cell Robust COF-Nanowire Network Sponges as Sustainable Adsorbent and Filter. Advanced Functional Materials, **2023**, 2309938.

Specific contributions by authors:

Concepts and resources were generated by Professor Seema Agarwal. I designed experiments in consultation with Professor Seema Agarwal. I performed all experiments, and analyzed data. Yingying Du performed filtration experiments with me. The manuscript was written with the help of all coauthors.

In this work, a simple scalable procedure is shown for making a robust, highly compressible 3D crystalline COF nanowire interconnected porous open-cell sponge. Utilizing the TAF process requires a template in the form of a sponge. Extensive research by the research groups of Greiner and Agarwal has focused on the preparation and properties of polymer sponges made from electrospun short fibers. Typically, electrospun fibers are continuously long, but mechanical cutting can produce short fibers ranging from 20-100 microns in length. These short fibers can be dispersed in a water/organic solvent mixture and freeze-dried to form an open-cell porous structure (sponge). The sponge's density is determined by the concentration of short fibers in the dispersion and the cooling step during the freeze-drying process. Such sponges are

promising candidates for use as templates in the TAF process. Given that PAN was utilized as the template polymer in previous sections, I opted to use an electrospun PAN sponge prepared by the aforementioned method as the template sponge. However, growing a COF framework on the PAN sponge and then removing the PAN resulted in the collapse of the structure, failing to yield a mechanically stable pure COF sponge. Consequently, a composite sponge was prepared, in which COF frameworks grow on a high-temperature stable and mechanically strong template sponge without removing the template. The preparation process comprises two steps. First, polyimide (PI) short fibers and 2,5-diaminobenzenesulfonic acid (Pa-SO_3H) are dispersed in a dimethyl sulfoxide (DMSO) solution containing polyacrylonitrile (PAN), and a PI/Pa-SO_3H composite sponge is obtained through freeze-drying. Here, PI short fibers form the network skeleton of the composite sponge, ensuring mechanical stability; PAN acts as a binder to enhance the sponge's strength; Pa-SO_3H serves as one of the organic connectors in the sulfonic acid-functionalized COF (COF-SO_3H), as shown in **Figure 2-13a**. In the second step, the PI/Pa-SO_3H composite sponge is soaked in a solution of 1,3,5-triformylphloroglucinol (Tp, another organic linker for COF-SO_3H) in 1,4-dioxane and acetic acid. COF-SO_3H nanowires grow on the PI short fibers at 120 °C, resulting in a PI/COF-SO_3H composite sponge, as shown in **Figure 2-13b**.

89
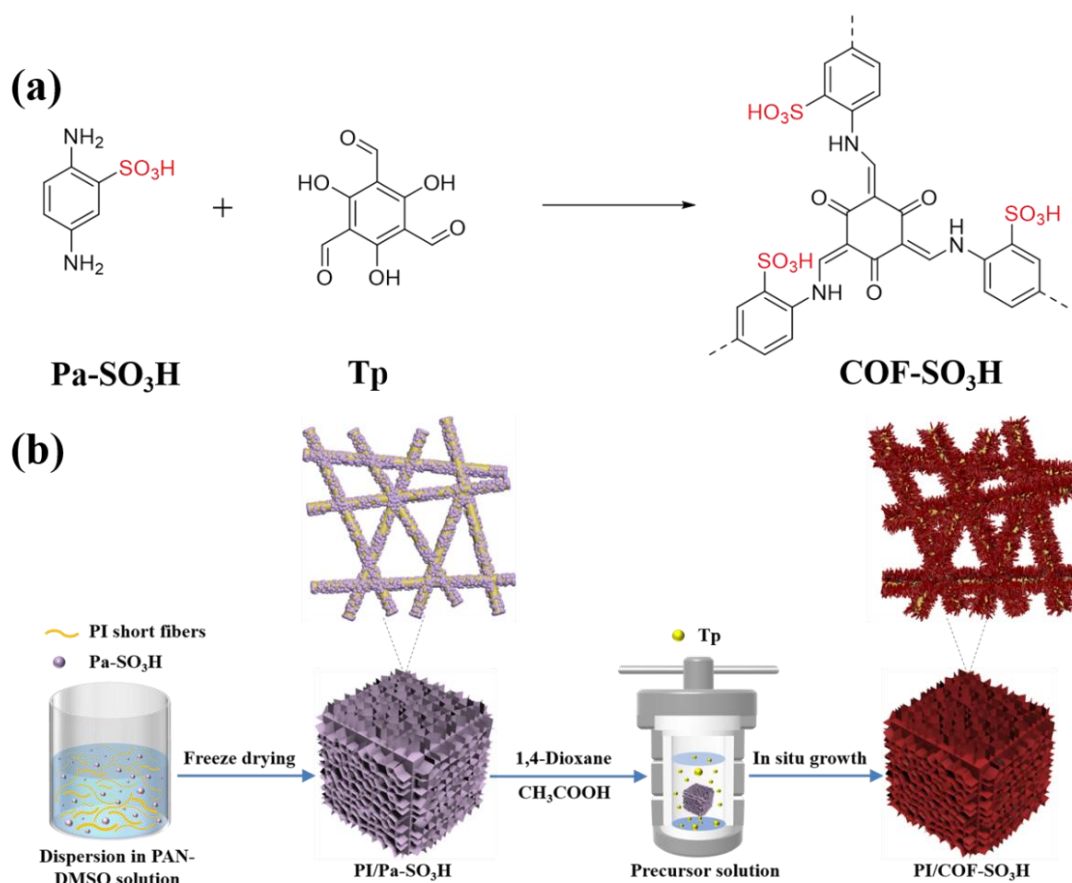
Figure 2-13. General schematic of COF-SO3H (a). Schematic illustration of the preparation of PI/COF-SO$_3$H composite sponges (b). PI = polyimide, PAN = polyacrylonitrile, Pa-SO$_3$H = 2,5-diaminobenzenesulfonic acid, Tp = 1,3,5-triformylphloroglucinol, DMSO = dimethylsulfoxide, CH$_3$COOH = acetic acid.

Through SEM, it can be found that PI short fibers build highly interconnected open-cell structures, which is conducive to mass transfer. And a large number of COF nanowires are densely grown on its surface (**Figure 2-14**). Compared with COF-SO$_3$H powder, PI/COF-SO$_3$H composite sponge exposes more active sites, which is conducive to dye adsorption.
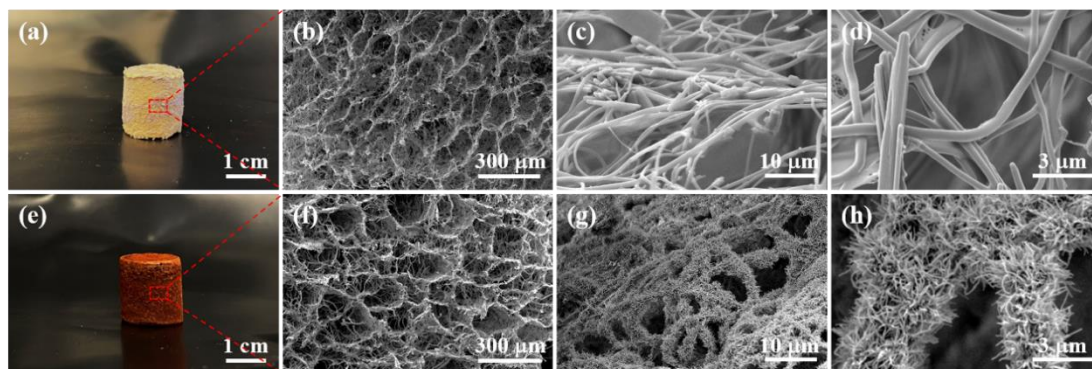
Figure 2-14. Photographs and SEM images of PI/Pa-SO$_3$H (a-d), and PI/COF-SO$_3$H (e-h).

Next, we explored the mechanical stability of the PI/COF-SO$_3$H composite sponges and its dye removal performance in wastewater. Before the PI/Pa-SO$_3$H composite sponges is freeze-dried, different contents of Pa-SO$_3$H are added to finally obtain a series of PI/COF-SO$_3$H composite sponges with different COF-SO$_3$H loading contents. The PI/COF-SO$_3$H composites sponge have good mechanical stability, and their height does not change significantly after 50 compression-release cycles (50% strain). Secondly, as the COF-SO$_3$H loading increases, the compressive strength and deformation recovery performance of the PI/COF-SO$_3$H composite sponges also increase (**Figure 2-15**). This is because COF-SO$_3$H nanowires serve as a protective layer to enhance the mechanical stability of the composite sponges.
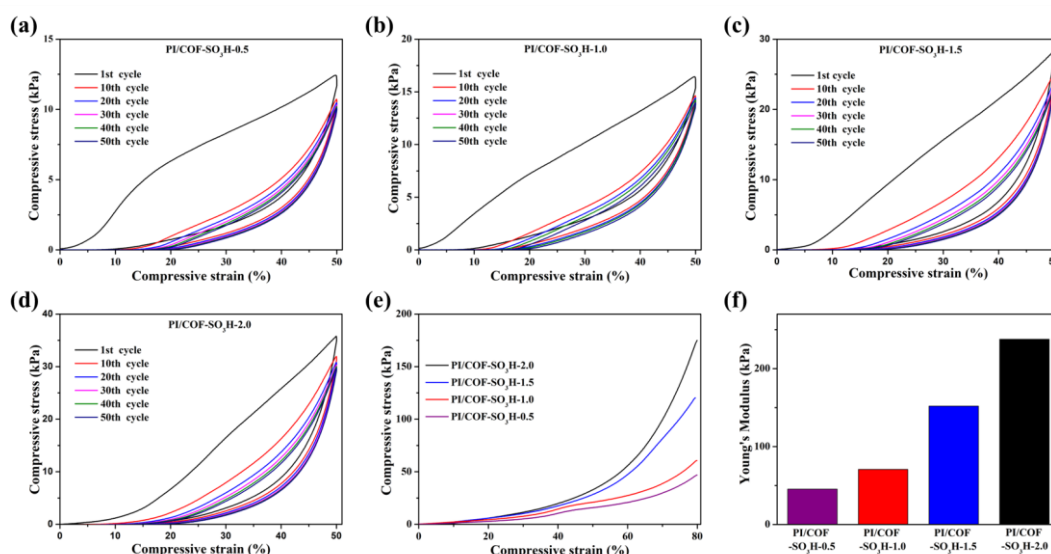
Figure 2-15. Compression-release stress-strain (a-d), compressive stress-strain curves

(e), and the corresponding compressive Young's modulus (f) of PI/COF-SO$_3$H composite sponges.

Since COF-SO$_3$H contains sulfonic acid functional groups, it can be used to adsorb the cationic dye methylene blue (MB). It can be found that the adsorption capacity and removal efficiency of PI/COF-SO$_3$H composite sponges for MB increases with the increase of COF-SO$_3$H content in the sponges (**Figure 2-16**).
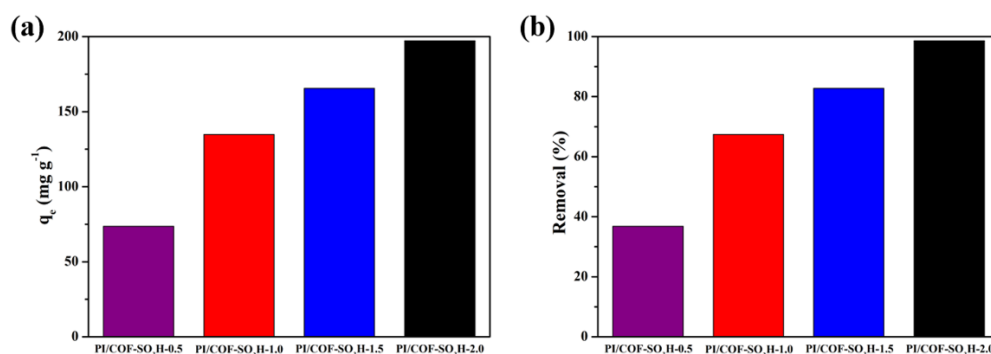
Figure 2-16. Adsorption capacity (a), and removal efficiency (b) of MB by PI/COF-SO$_3$H composite sponges.

Because PI/COF-SO$_3$H composite sponges have a highly porous structure, good mechanical stability, and excellent dye adsorption capacity, they can also be used as wastewater filters. Take the PI/COF-SO$_3$H-2.0 composite sponge as an example, put it into a syringe and build a simple filtration device (**Figure 2-17a**). At the same time, four simple filtration units are combined into one system for the continuous filtration of wastewater for a long time (**Figure 2-17b**). The system can work continuously for 24 h and exhibits excellent filtration performance for MB solutions (basically complete removal of MB within 12 h) (**Figure 2-17c**). Additionally, it exhibits a high water flux (2355 L h^{-1} m^{-2}).
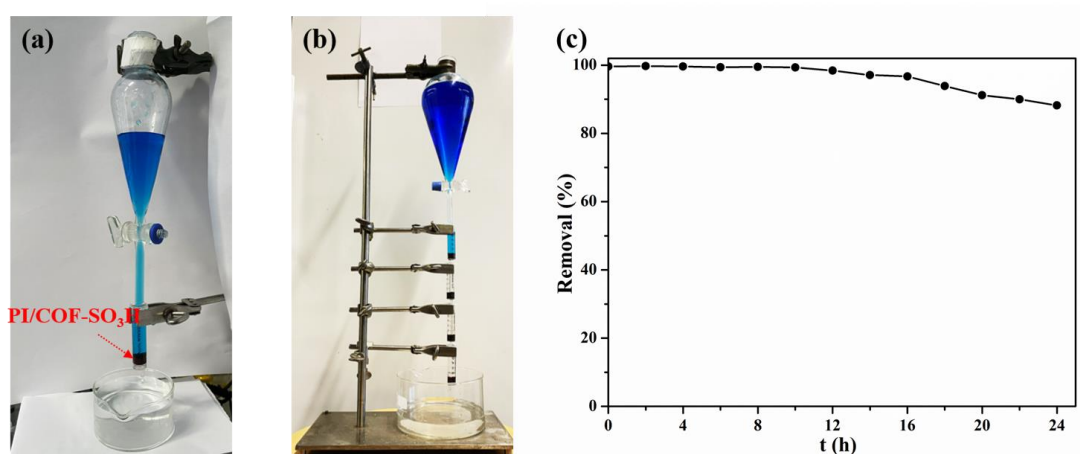
Figure 2-17. Photograph of PI/COF-SO$_3$H sponges and syringe assembled facile filter for removal of MB, one syringe (a), and four syringes (b). Filtration removal efficiency of MB by PI/COF-SO$_3$H-2.0 within 24 h.

In summary, this work establishes a simple method to construct strong, compressible 3D COF sponges with highly interconnected open-cell structures. The COF sponges can be used as an adsorbent and filter respectively, showing high removal efficiency and long service life for dye wastewater. Combining the functional diversity of COFs with the network framework structure of sponges not only improves the processability of COFs, but also expands the application fields of COFs. Moreover, COF sponges are prepared based on electrospinning and freeze-drying, and are expected to be prepared on a large scale.

My subsequent research question explores the possibility of applying a similar methodology to develop 3D MOF sponges. Detailed operational procedures and methodologies will be elaborated in the following section.

2.5 Sustainable Hierarchically Porous Reusable Metal-Organic Framework Sponge as a Heterogeneous Catalyst and Catalytic Filter for Degradation of Organic Dyes
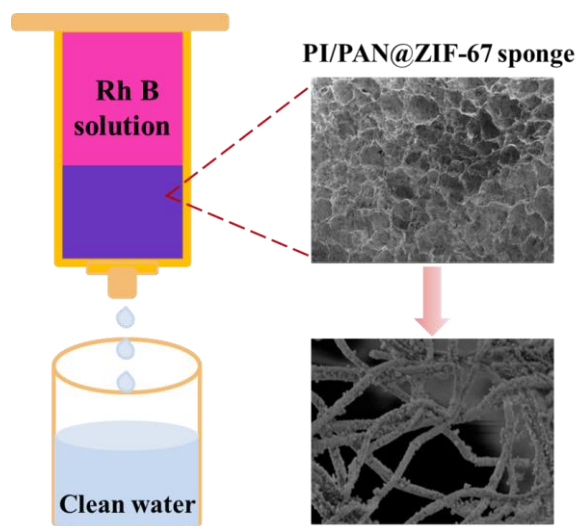
Yingying Du, **Chenhui Ding**, Seema Agarwal. Sustainable Hierarchically Porous Reusable Metal–Organic Framework Sponge as a Heterogeneous Catalyst and Catalytic Filter for Degradation of Organic Dyes. Advanced Energy and Sustainability Research, **2023**, 2300218.

Specific contributions by authors:

Concepts and resources presented by Prof. Seema Agarwal. Yingying Du and I designed the experiments in consultation with prof. Agarwal. The sponges were prepared by both. I completed the measurement and analysis of SEM and XRD. Yingying Du performed all other experiments and analyzed data. The manuscript was written with the help of all co-authors.

In this work, we successfully prepared 3D MOF sponges using a similar method to the previous work. Using ZIF-67 (**Figure 2-18a**) as a functional MOF. Specifically, PI (polyimide) short fibers (length $L = 77 \pm 33 \, \mu m$), PAN (polyacrylonitrile) and $Co(NO_3)_2 \cdot 6H_2O$ are dispersed in dimethyl sulfoxide (DMSO), and freeze-dried to form PI/PAN/Co^{2+} sponge with honeycomb structure. Then PI/PAN/Co^{2+} sponge is put into

the precursor solution of ZIF-67 (an aqueous solution of $Co(NO_3)_2\cdot 6H_2O$ and 2-methylimidazole (2-MeIm)), and ZIF-67 grows in situ on the surface of the PI short fiber to obtain the PI/PAN@ZIF-67 sponge. As shown in **Figure 2-18b**.
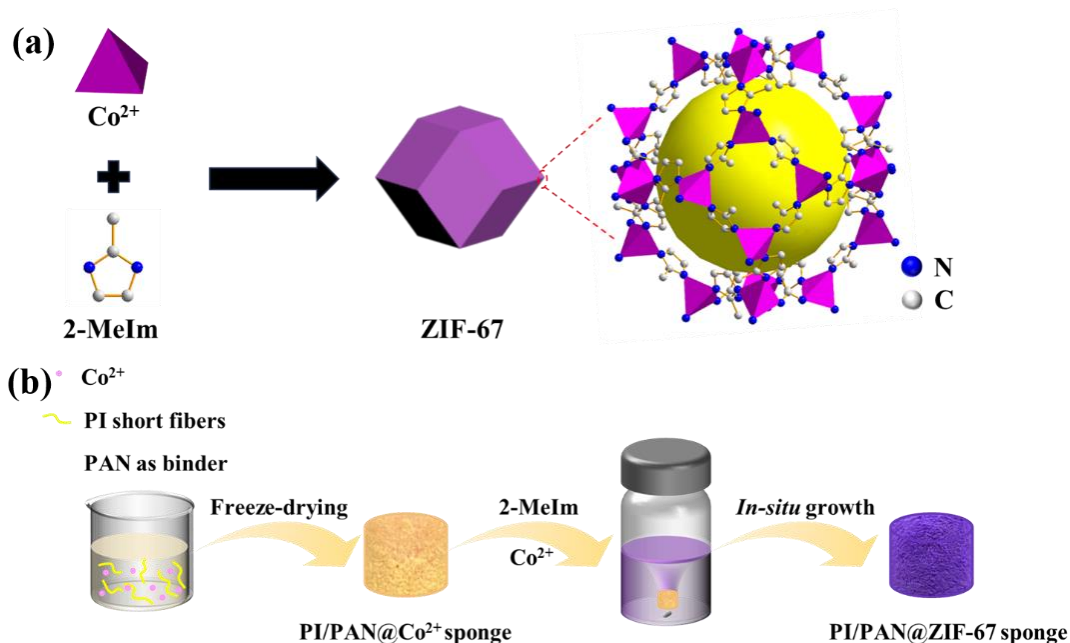
Figure 2-18. General schematic of ZIF-67 (a). Preparation of the PI/PAN@ZIF-67 sponge (b). Co^{2+} comes from $Co(NO_3)_2\cdot 6H_2O$; 2-MeIm is 2-methylimidazole.

Through SEM analysis of the internal morphology of the PI/PAN@ZIF-67 sponge, it can be found that it has hierarchical porous structure, and a large number of ZIF-67 particles grow on the surface of PI short fibers (**Figure 2-19a-c**). The hierarchical porous structure is conducive to the absorption and release of stress. The compressive strength of the PI/PAN@ZIF-67 sponge is 23.5 kPa (50% strain), and after 300 compression cycles, the height only dropped by 9.9% (**Figure 2-19d**). It shows that the PI/PAN@ZIF-67 sponge has good compressive resistance and mechanical stability.
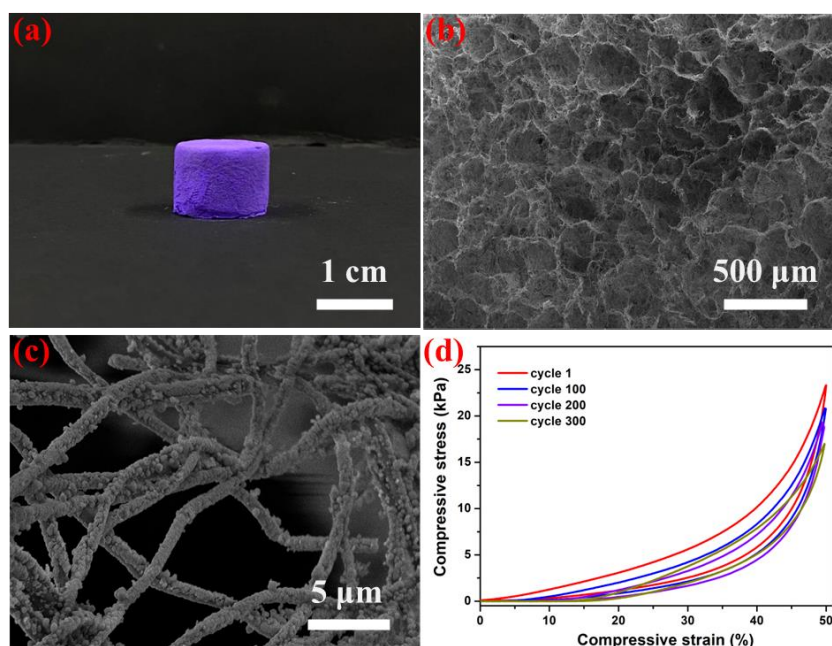
Figure 2-19. The photo of PI/PAN@ZIF-67 sponge (a). SEM image of PI/PAN@ZIF-67 sponge (b and c). Cyclic compressive stress-strain curves at 50% strain for PI/PAN@ZIF-67 sponge (d).

Taking Rh B as a typical example, we explored the potential of PI/PAN@ZIF-67 sponge as a catalyst to activate peroxomonosulfate (PMS) to degrade organic dyes. **Figure 2-20a** shows the degradation of Rh B under different catalytic systems. The PI/PAN@ZIF-67 sponge can quickly degrade Rh B, with a degradation rate of up to 97.4% within 5 minutes and almost complete degradation within 30 minutes. Furthermore, the PI/PAN@ZIF-67 sponge can be easily separated and washed, and reused to degrade dyes. After 5 cycles of use, the degradation efficiency of Rh B by the sponge remained basically unchanged (**Figure 2-20b**). In addition, we constructed PI/PAN@ZIF-67 sponge as a simple filtration device to evaluate its performance in the continuous treatment of dye wastewater (**Figure 2-20c**). Based on the hierarchical porous structure of PI/PAN@ZIF-67 sponge, Rh B solution can quickly pass through PI/PAN@ZIF-67 sponge under the action of self-gravity, and after catalytic degradation, the clarified solution is obtained. After continuous treatment of Rh B solution for 6 h, the removal rate of Rh B is still as high as 95% (**Figure 2-20d**).
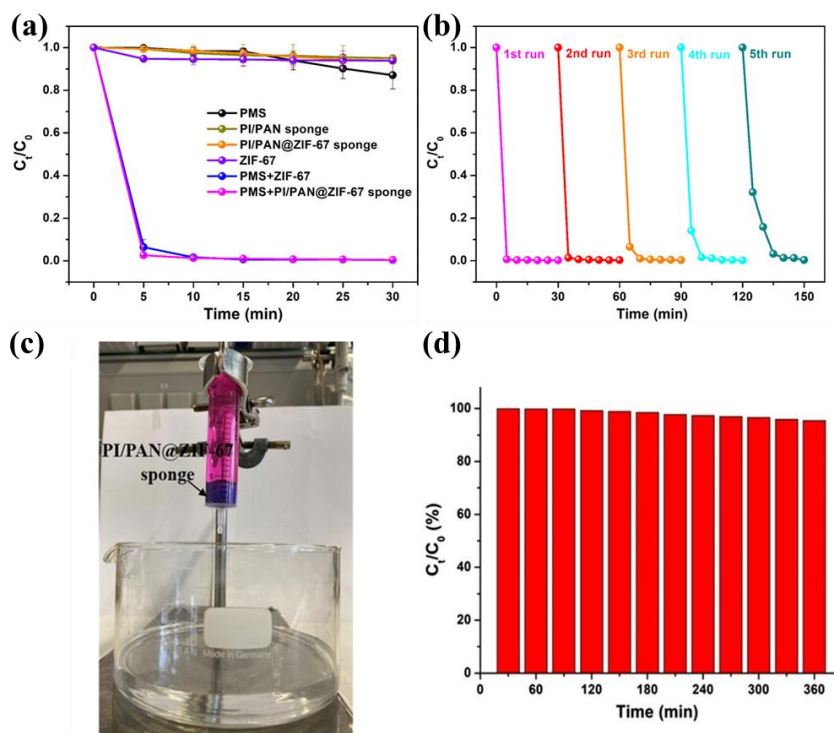
Figure 2-20. Plots of C_t/C_0 versus time for studying the degradation of Rh B under different conditions (a). Reusability test of PI/PAN@ZIF-67 sponge (b). Photograph of the assembly showing the degradation of Rh B through the filtration process. The PI/PAN@ZIF-67 sponge was installed in the syringe as a catalytic filter to degrade Rh B (c). Continuous degradation experiment of Rh B using PI/PAN@ZIF-67 sponge as filter (d).

In summary, we successfully prepared a 3D MOF sponge (PI/PAN@ZIF-67) through in-situ solvothermal growth of ZIF-67. The PI/PAN@ZIF-67 sponge has good compression resistance and mechanical stability. And as a catalyst for PMS activated degradation of dyes, it shows excellent degradation performance and can be reused many times. Secondly, the PI/PAN@ZIF-67sponge is used as a catalytic filter for flowing degraded dyes, showing excellent degradation performance and long service life. This research provides a new method for 3D MOF monolithic materials and expands the application fields of MOFs.

3. Outlook

In the past two decades, metal-organic frameworks (MOFs) and covalent organic frameworks (COFs) have become an emerging and booming class of crystalline porous materials. They have large surface area, high porosity, tailor-made structures, adjustable pore size and good thermal/chemical stability, and have been used in many fields, including energy, environment, biomedical engineering, chemical engineering, and optoelectronics. Despite unprecedented progress, MOFs and COFs are typically processed into powders that are difficult to dissolve, melt, and process. This leads to unavoidable losses during use and difficulty in reuse, which greatly hinders their further development.   Therefore, in this work, based on the electrospinning process, combined with the template-assisted process and freeze-drying method, we obtained mechanically stable 2D MOF and COF fiber membranes, and 3D MOF and COF sponges, respectively, and their practical applications are studied. Further, we expanded to other porous materials and prepared 2D Microporous organic polyimide (MOPI) fiber membranes. In order to further deepen the combination of electrospinning technology with MOFs and COFs, and prepare macro-objects (MOFs-based and COFs-based) with diverse structures and functionalities, research needs to be conducted from multiple aspects. How does microstructure influence the properties of macroscopic objects is an important question? By manipulating specific structural units or applying post-synthesis modifications, it is possible to precisely control the microstructural characteristics of MOFs and COFs-such as chemical composition, pore size, and porosity-to investigate their effects on the macroscopic properties of these materials. The targeted use of MOF/COF macro-objects for specific applications, like energy storage devices and fuel cells would also be interesting.

4. Publications

4.1 Flexible, Mechanically Stable, Porous Self-Standing Microfiber Network Membranes of Covalent Organic Frameworks: Preparation Method and Characterization

RESEARCH ARTICLE

Flexible, Mechanically Stable, Porous Self-Standing Microfiber Network Membranes of Covalent Organic Frameworks: Preparation Method and Characterization

Chenhui Ding, Marion Breunig, Jana Timm, Roland Marschall, Jürgen Senker, and Seema Agarwal**

Covalent organic frameworks (COFs) show advantageous characteristics, such as an ordered pore structure and a large surface area for gas storage and separation, energy storage, catalysis, and molecular separation. However, COFs usually exist as difficult-to-process powders, and preparing continuous, robust, flexible, foldable, and rollable COF membranes is still a challenge. Herein, such COF membranes with fiber morphology for the first time prepared via a newly introduced template-assisted framework process are reported. This method uses electrospun porous polymer membranes as a sacrificial large dimension template for making self-standing COF membranes. The porous COF fiber membranes, besides having high crystallinity, also show a large surface area (1153 m^2 g^{-1}), good mechanical stability, excellent thermal stability, and flexibility. This study opens up the possibility of preparation of large dimension COF membranes and their derivatives in a simple way and hence shows promise in technical applications in separation, catalysis, and energy in the future.

1. Introduction

Covalent organic frameworks (COFs) are crystalline porous macromolecular networks linked through strong covalent

C. Ding, S. Agarwal
Macromolecular Chemistry and Bavarian Polymer Institute
University of Bayreuth
Universitätsstrasse 30, 95440 Bayreuth, Germany
E-mail: agarwal@uni-bayreuth.de
M. Breunig, J. Senker
Department of Chemistry
Inorgnaic Chemistry III and Northern Bavarian NMR Centre (NBNC)
University of Bayreuth
Universitätsstrasse 30, 95440 Bayreuth, Germany
E-mail: juergen.senker@uni-bayreuth.de
J. Timm, R. Marschall
Department of Chemistry
Physical Chemistry III
University of Bayreuth
Universitätsstrasse 30, 95440 Bayreuth, Germany

bonds in the form of a 2D or 3D structure.[1] Their controllable crystalline structure, high chemical and thermal stability, and permanent porosity with high specific surface areas have made them promising for a wide range of applications in fields, including gas storage,[2] separation,[3] catalysis,[4] water purification,[5] molecular separations,[6] energy storage,[7] and light-emitting diodes.[8] Despite several advantages and suitability for various application areas, the actual use is limited due to their nonprocessability originating from the cross-linked insoluble and infusible structure.[9] To solve this problem, researchers have adopted various methods to obtain COFs with different morphologies, including hollow tubes,[10] core–shell structures,[11] membranes,[12] and foams.[13]

Recently, some research efforts were invested in preparing COF membranes which can be categorized into four types. The first is to grow the COF composite membranes directly on the supporting carrier in situ, but this requires a supporting carrier, and there is a problem of adhesion.[14] The second method is to obtain COF nanosheets by mechanical grinding or chemical treatment, but the weak interaction force between COF nanosheets usually leads to poor mechanical properties of the assembled COF films.[15] The third method is to prepare COF membranes through liquid–liquid interface polymerization, but the COF membranes have poor mechanical properties and low crystallinity.[16] The fourth method is to obtain the COF membranes by baking the organic linking agent with the corresponding aldehydes, but the thickness of the COF membranes is several hundred microns.[9] Therefore, there is an urgent need for new preparation methods for self-standing COF membranes with large dimensions, excellent crystallinity, and mechanical properties. Without large dimension processable self-standing flexible COF membranes, their applications are limited.

We set this as our goal and report the preparation of porous, crystalline COF membranes of large dimensions and mechanical stability in a new three-step easy to perform synthesis, which we refer to in the following as template-assisted framework (TAF) process. The method utilizes electrospun porous polymer membranes as a sacrificial large dimension template. Electrospinning is the simplest and most effective method to prepare continuous polymer nanofibers and the corresponding porous membranes of large dimensions, large specific

surface areas, large porosity, and high flexibility.[17] The polymer membranes, electrospun with the help of a template polymer, support the in situ growth of the COF. The subsequent removal of the template polymer leaves behind self-standing crystalline COF membranes with high surface area (1153 m^2 g^{-1}), good mechanical stability (tensile strength of 0.64 MPa and excellent bending stability), and flexibility (the mechanical properties remain unchanged after 10 000 bending tests).

2. Results and Discussions

The TAF process used for the preparation of self-standing porous COF membranes is shown in **Figure 1**.

In the first step of the TAF process, one of the COF reactants, the diamine (p-phenylenediamine (Pa)), was immobilized on an electrospun polyacrylonitrile (PAN) fibrous membrane in different amounts by electrospinning of a solution of PAN and Pa. The resulting PAN/Pa fiber membranes with different loadings of Pa (100% and 200% to the amount of PAN) are called PAN/Pa-100 and PAN/Pa-200, respectively. To explore the in situ growth of the COF within the fibers and the resulting morphology, we performed scanning electron microscope (SEM) characterization (**Figure 2**). Figure 2a–c shows the SEM images of PAN, PAN/Pa-100, and PAN/Pa-200 fibrous membranes. The pure PAN fibers have a smooth surface, while the PAN/Pa-100 and PAN/Pa-200 show a rough surface and are covered with a layer of Pa. Pa is expected to mix with PAN in the bulk of the fibers and to deposit on the surface.

Moreover, as the content of Pa in PAN/Pa fibers increases, the fiber diameter increases significantly. The average diameter of the PAN fibers, PAN/Pa-100 fibers, and PAN/Pa-200 fibers are 348 ± 84, 1312 ± 103, and 1699 ± 147 nm, respectively. This shows that Pa was successfully doped into PAN fibers. In the second step, the COF was grown in situ on PAN fiber membranes by reaction of immobilized Pa with the 1,3,5-triformylphloroglucinol (Tp) (catalyst: acetic acid, temperature: 120 °C, time: 1 day). The corresponding COFs generated on PAN/Pa-100 and PAN/Pa-200 are called PAN/COF-100 and PAN/COF-200, respectively. For comparison, the conventional synthesis of COF by mixing Tp and Pa led to spherical particles (Figure 2d). Figure 2e,e',f,f' shows the surface and cross-section morphologies of PAN/COF-100 and PAN/COF-200 fibers. It can be found that with the reaction of Pa and Tp, TpPa COF nanoparticles grow uniformly on the surface of the PAN fibers. Moreover, the cross-section morphology of PAN/COF fibers shows that TpPa COF nanoparticles also grow in the bulk of the fibers. This shows that during the reaction process, Tp not only reacts with Pa on the fiber surface but also penetrates into the bulk of the fiber and reacts with Pa to generate TpPa COF nanoparticles.

In the third step, the removal of the template polymer PAN from the membranes by solvent extraction provided the self-standing porous TpPa COF membranes, COF-100 and COF-200, respectively. Figure 2g,g',h,h' shows the surface and cross-section morphology of COF-100 and COF-200 fibers. Compared with PAN/COF fibers, the surface of the porous COF fibers is basically unchanged, and the fiber morphology remains intact. By observing the cross-sectional morphology, it can be found that the porous COF fibers possess porous core–shell-type structures with varied densities of COF particles in the shell and core. This is because, during the in situ growth of TpPa COFs, the surface of the PAN fiber provides enough Pa and enough growth space to form a dense shell composed of TpPa COF nanoparticles. In the bulk of PAN fiber, TpPa COF nanoparticles are wrapped by PAN during the growth process, which leads to a lack of sufficient growth space. Therefore, after the PAN is removed, leaving a porous core is formed by the accumulation of TpPa COF nanoparticles. In addition, the core–shell structure of porous COF fibers ensures that it has good mechanical stability and high specific surface area, as described in the later section. The optical photographs of membranes are shown in Figure 2 (bottom).

The Fourier-transform infrared (FT-IR) spectra of the samples are shown in Figures S1 and S2 in the Supporting Information. The characteristic stretching bands at 3100–3300, 2242, 1574, and 1236 cm^{-1} are attributed to the N−H group of Pa, the C≡N group of the PAN, C=C, and C−N of the TpPa
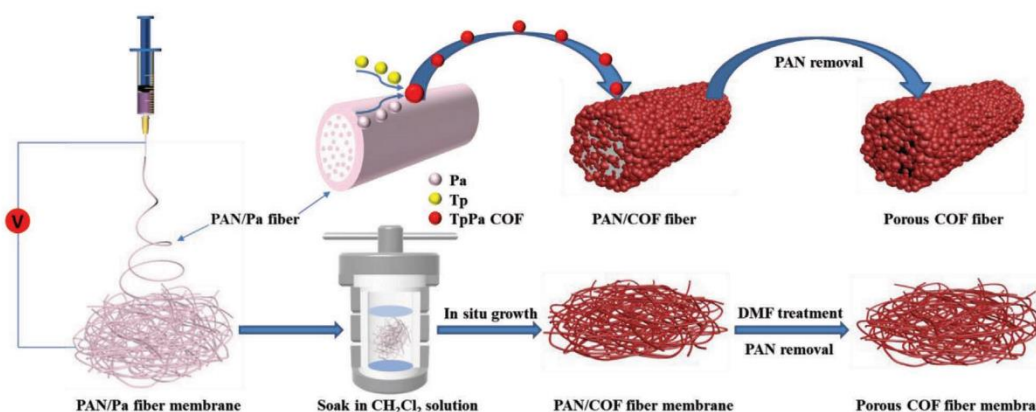

Figure 1. The three-step preparation process of porous COF membranes. PAN = polyacrylonitrile, Pa = p-phenylenediamine, Tp = 1,3,5-triformylphloroglucinol.
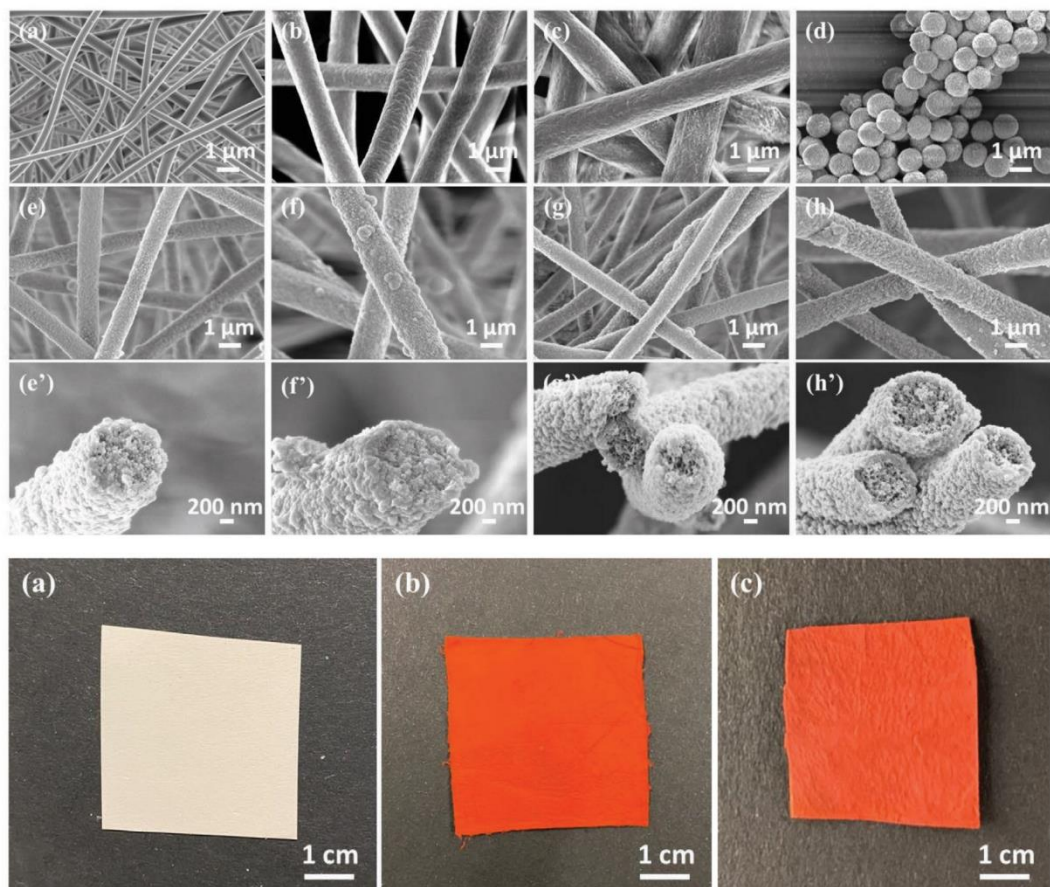
Figure 2. Top: SEM images of a) PAN, b) PAN/Pa-100, c) PAN/Pa-200, d) TpPa COF powder, e) PAN/COF-100, f) PAN/COF-200, g) COF-100, and h) COF-200 with e',f',g',h') their cross-section, respectively. Bottom: Photographs of a) PAN/Pa-100, b) PAN/COF-100, and c) COF-100.

COF, respectively.[18] In fact, after 1 day of synthesis at 120 °C, the color of PAN/Pa fiber membranes changed from lavender to red. This means that TpPa COF has grown on PAN fibers. It can be found from Figure S1 in the Supporting Information that the characteristic stretching band at 3100–3300 cm^{-1} (N−H) has disappeared, and the characteristic stretching band at 1574 cm^{-1} (C=C) and 1236 cm^{-1} (C−N) is displayed on COF formation. In addition, through the *N,N*-dimethylformamide (DMF) post-treatment for the removal of PAN, the FT-IR spectra of the porous COF fiber membranes and the TpPa COF powders are basically the same. This shows that PAN was effectively removed without changing the chemical structure of TpPa COF, and the porous COF fiber membranes were successfully obtained. The FT-IR spectrum of COF-200 series and Tp are shown in Figure S2 in the Supporting Information.

The ^{13}C (**Figure 3**a and Figure S3, Supporting Information), as well as ^{15}N (Figure 3b) cross polarized magic angle spinning (CP MAS) NMR spectra, demonstrate for the PAN/Pa-100

fiber mat to be composed of a mixture of PAN and Pa. This is particularly obvious by the characteristic ^{15}N NMR peaks at −127 ppm for the nitrile unit of PAN and at −328 ppm for the amino groups of Pa, as well as by the ^{13}C NMR shifts at around 30 ppm for the aliphatic PAN backbone and at 139 ppm for the aromatic CH groups of Pa. After the reaction of PAN/Pa-100 with Tp, the characteristic peaks for Pa disappear, and resonances typical for COF-100 were observed. Pronounced are shifts at −241 ppm (^{15}N) and 106, 146, and 184 ppm (^{13}C) for the keto-enamine groups arise. The absence of peaks characteristic for amino functions confirms very high cross-linking degrees (>95 %) and thus the success of the polycondensation of the two monomers to COF-100. The remaining PAN peaks demonstrate that PAN/COF-100 represents a composite membrane of PAN and COF-100. PAN could subsequently be removed by Soxhlet extraction, as evident by the disappearance of PAN peaks at −126 ppm (^{15}N) and at 30 and 121 ppm (^{13}C). For the second synthesis series (higher Pa content) similar behavior
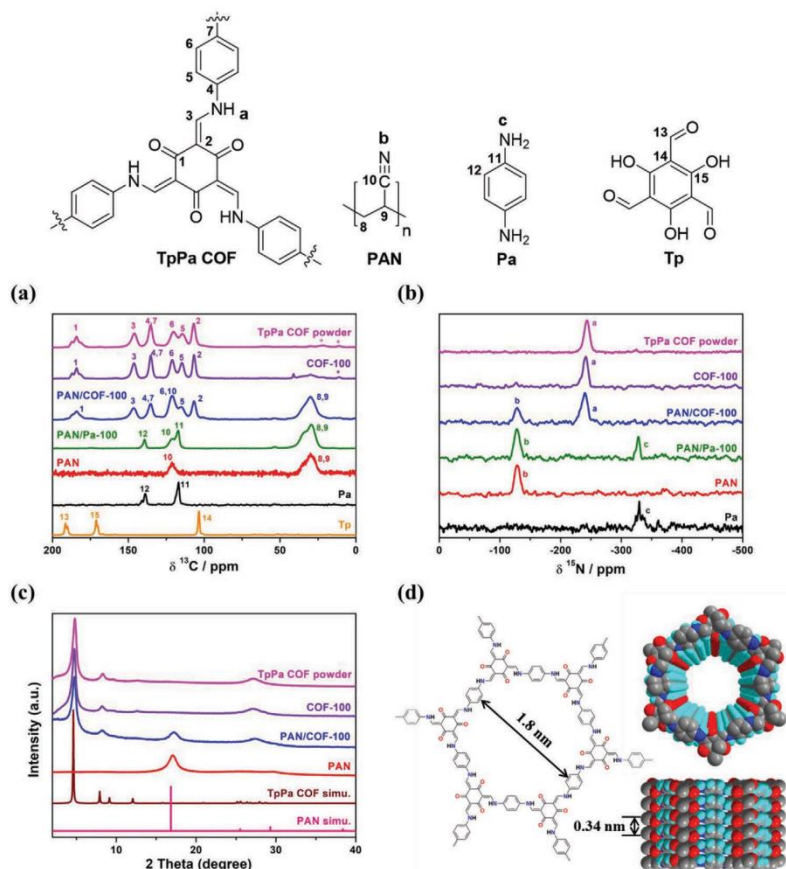
2106507 (3 of 7)

Figure 3. a) ^{13}C and b) ^{15}N CP MAS NMR spectra of the COF-100 series. The asterisks mark spinning sidebands. PXRD patterns of TpPa COF powder (magenta), COF-100 (violet), PAN/COF-100 (blue), and PAN (red). c) The simulated PXRD patterns of TpPa COF (wine) and PAN (pink) are also shown. d) The structure and space-filled model of TpPa COF.

was observed. The data of the COF-200 series are shown in Figure S3 in the Supporting Information.

The X-ray diffraction (XRD) patterns of TpPa COF powder, PAN, PAN/COF, and porous COF fiber membranes are shown in Figure 3c and Figure S4 in the Supporting Information. They show the typical reflexes for the hexagonal metric of TpTa COF[19] at $2\theta = 4.8°$ (100), 8.5° (210), and 26.9° (001), while the reflex at $2\theta = 17.2°$ is attributed to PAN. According to Bragg's Law, the d spacings of the (100) and (001) reflexes are 1.8 and 0.33 nm, respectively. This is basically consistent with the pore size and eclipse stacking between the layers of TpPa COF reported in the literature.[19] The XRD data also confirmed that the PAN/COF and porous COF fiber membranes were successfully obtained in this work with a crystallinity comparable to the one of the TpTa COF bulk material.

N_2 and Ar physisorption isotherms were conducted to examine the surface areas, the pore size distributions, and the cumulative pore volumes of TpPa COF powders and material from different steps of the TAF process (PAN/COF and porous COF fiber membranes). As 2D COFs are sensitive to swelling when exposed in particular to N_2,[20] the pore size distribution and specific surface area of TpPa COF powder were determined using an Ar physisorption isotherm at 87 K (Figure S5, Supporting Information). The isotherm is typical for a microporous material.[21] The surface area amounts to 463 m^2 g^{-1}, the pore size distribution exhibits a maximum at 1.6 nm, and the maximum cumulative pore volume results in 0.2 cm^3 g^{-1}, which is in good agreement with the observation from the PXRD patterns and values reported for the traditional solvent synthesis method.[20] Further gas physisorption measurements of the series PAN/COF and COF fiber membranes were conducted with N_2 at 77 K. Interestingly, only the PAN/COF samples show a slight swelling behavior (adsorption branch and desorption branch not closing at low p/p_0), which derives from the high amount of nonrigid, polymeric material. The absence of swelling for COF-100 and COF-200 indicates that the COF

2106507 (4 of 7)

fiber membranes production creates improved stability against swelling and an additional stiffness compared to the TpPa COF powders. The nitrogen physisorption isotherm of COF-100 is again typical for a microporous material, while the isotherm of COF-200 shows an additional increase at high relative pressures (p/p_0), resulting from voids between the single fibers of COF-200, which might be explained with the larger fiber diameter of COF-200 compared to COF-100.[21] The pore size distribution of the PAN/COF and COF fiber membranes exhibit maxima between 1.7 and 1.8 nm (**Figure 4**b), matching the pore sizes of the TpTa COF and the ones determined from the XRD data. An additional micropore diameter of 1.4 nm could be observed for the COF-200 sample. The cumulative pore volumes of COF-100 and COF-200 are more than doubled compared to TpPa COF powder and almost quadrupled compared to PAN/COF. This is because PAN wraps the TpPa COF nanoparticles in the bulk of the PAN fiber, and only the nanoparticles on the fiber's surface are exposed. After PAN removal, the pores are accessible, resulting in a strongly increased pore volume and surface area. The specific surface areas of PAN/COF-100 and PAN/COF-200 are comparable to each other with 229 and 224 m^2 g^{-1}, respectively, and are much lower than TpPa COF powders. However,

the surface areas of porous COF-100 and porous COF-200 fiber self-standing membranes are much higher and exceed 1120 and 1153 m^2 g^{-1}, respectively, even the one obtained for the TpPa COF powders. The removal of PAN by solvent extraction creates a hierarchically porous material with a macroporosity (Figure 2) that renders all COF nanoparticles accessible (including in the bulk). Additionally, the TpPa COF particles from the bulk syntheses are larger by one to two orders of magnitude (Figure 2), which makes the latter particles prone to pore blocking. This, in turn, reduces the accessible pore space leading to smaller surface areas for TpPa COF powder compared to COF-100 and COF-200. In particular, the hierarchical build-up of the COF fibers obtained by the TAF process is advantageous for potential applications.

Excellent thermal stability is conducive to expanding the application of TpPa COF. Figure S6 in the Supporting Information shows the thermogravimetric analysis curves of TpPa COF powders, PAN, PAN/COF, and porous COF fiber membranes in a nitrogen atmosphere. $T_{5\%}$ (the temperature at which 5% mass loss takes place) and a residual mass at 800 °C were used to evaluate the thermal stability of the samples, as shown in Table S3 in the Supporting Information. It can be observed that all the samples have good thermal stability, and there is basically no loss before 300 °C. This indicates that PAN/COF and porous COF fiber membranes have potential applications in the high-temperature field. In addition, the residual masses of PAN/COF and porous COF fiber membranes at 800 °C are both greater than 45%, making their carbon derivatives broad application prospects.

Tensile test and cycle test analyze the mechanical properties and flexibility of materials. By changing the content of Pa in the PAN fiber, the mechanical properties of PAN/COF and porous COF fiber membranes were studied, as shown in **Figure 5**, and the corresponding results are shown in Table S4 in the Supporting Information. The PAN/COF fiber membranes show good mechanical properties, but as the content of Pa increases, the mechanical properties of PAN/COF fiber membranes decrease. This may be due to the fact that more TpPa COF nanoparticles have grown inside the fiber, resulting in more structural defects. In addition, after DMF post-treatment, the PAN is completely removed, and the fibers in COF membranes (COF-100 and COF-200 had thickness around 53 and 59 μm, respectively (Table S4, Supporting Information)) are only composed of TpPa COF nanoparticles. The porous COF-200 fibers may contain more nanoparticles, which results in dense porous COF-200 fiber membranes having better mechanical properties than porous COF-100 fiber membranes. At the same time, the dense TpPa COF nanoparticles shell on the surface of the porous COF fibers ensures its mechanical stability. Few other literature references show the mechanical characteristics of different COF membranes. The membrane prepared in this work shows better mechanical stability than the COF membrane prepared by interfacial polymerization using 1,3,5-triformylbenzene and 2,5-diethoxyterephthalohydrazide as the starting materials (tensile stress 0.26 MPa).[22] Although mechanical stability of COF membrane in the present work is sufficient for use in several applications, like separation and catalysis, it can be tuned to different values by use of fillers, modified multifunctional polymers as building blocks, etc. The highest tensile strength of
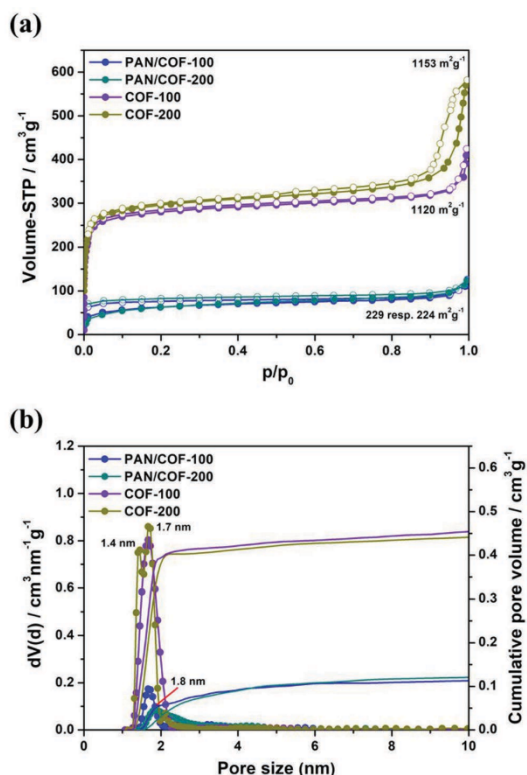

Figure 4. a) N$_2$ adsorption–desorption isotherms of PAN/COF-100, PAN/COF-200, COF-100, and COF-200, b) their pore size distribution, and cumulative pore volume obtained using the quenched solid density functional theory method.
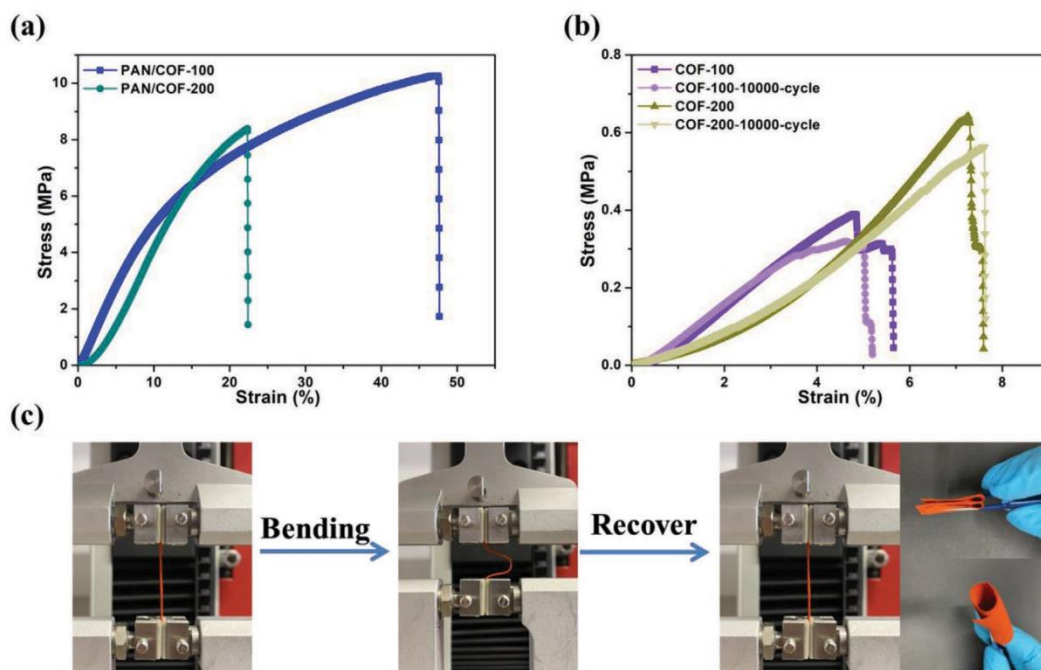
Figure 5. a) Typical stress–strain curves of PAN/COF-100, PAN/COF-200 and b) COF-100, COF-200, and porous COF fiber membranes after 10 000 cycles of bending. c) Bending and recovery processes for the COF, and the test at different bending states.

91.2 ± 6 MPa is reported for sulfonic acid-functionalized COF membranes prepared by self-assembling COF nanosheets.[23]

To characterize the flexibility of the porous COF fiber membranes, we performed a 10 000 cycle bending test with a compression of 50% and showed the flexibility of the porous COF fiber membranes under different bending states (folding and curling), as shown in Figure 5c. Also, the tensile test showed that the mechanical properties of the porous COF fiber membranes remained basically unchanged, as shown in Figure 5b. Additionally, the sample that underwent a bending cycle did not show any cracks as seen by SEM images, confirming the excellent flexibility and bending stability of porous COF fiber membranes (Figure S7, Supporting Information).

3. Conclusions

The TAF preparation method is successfully established, exemplary for the synthesis of a flexible porous COF membranes with a high specific surface area. The resulting COF membranes were produced in large dimensions, good crystallinity, and excellent hierarchical porosity. In addition, porous COF fiber membranes also show good mechanical stability and outstanding flexibility. After 10 000 cycle bending tests, its mechanical properties are unchanged. The present procedure could be used in the future for making COFs with other organic linkages. The only condition for transferring the current approach

to other COFs is that one of the monomers (starting component) needs to be preloaded on the template polymer fiber. The versatility of the electrospinning procedure allows for preloading during fiber formation by mixing different components either in the form of molecular solution or dispersions in a simple way, making the present procedure very promising.

At the same time, the porous COF fiber membranes also has excellent thermal stability. Therefore, the porous COF fiber membranes and their derivatives have great application prospects in the fields of separation, catalysis, and energy. It is worth mentioning that here prepared membranes are different from the conventional barrier membranes. Our membranes show a hierarchical porosity providing very little resistance for gas mixtures to pass through. Their use within pressure swing or temperature swing adsorption will be beneficial. The macropores allow for an easy gas flow and small pressure drops, at the same time, the ultramicroporosity ensures a good gas uptake and separation. Compared to the often used particle fillings with their problems of compacting, the here prepared membranes can be rolled and thus easily packed into the columns.

4. Experimental Section

Materials: PAN (Mw = 80 000, Carl Roth), Pa, and Tp were purchased from Sigma-Aldrich. DMF (99.9%), dichloromethane (CH_2Cl_2, 99.9%),

and acetic acid (AcOH, 99.7%) were purchased from Fisher Chemical. All chemicals can be used directly without further purification.

Preparation of the Porous COF Fiber Membranes: The porous COF fiber membranes were prepared in three steps. The preparation process is shown in Figure 1. In the first step, PAN/Pa fiber membranes were prepared by electrospinning. 1.5 g of PAN and a certain amount of Pa (1.5 and 3.0 g, respectively) were dissolved in 8.5 of DMF and stirred for 3 h to form a uniformly dispersed PAN/Pa electrospinning solution. The working voltage, the tip-to-collector distance, and the flow rate were set at 15 kV, 25 cm, and 0.8 mL h^{-1}, respectively. The PAN/Pa fiber membranes with different loading ratios of Pa (100% and 200%) were prepared, which were called PAN/Pa-100 and PAN/Pa-200, respectively. All the prepared PAN/Pa fiber membranes were vacuum dried at room temperature for 12 h. In the second step, PAN/COF fiber membranes were prepared by in situ growth. Take PAN/Pa-200 as an example. The PAN/Pa-200 fiber membrane (100 mg) was added to a dichloromethane (43.2 g) solution containing Tp (86.4 mg) and acetic acid (0.86 g) and reacted at 120 °C for 1 day to obtain red PAN/COF fiber membranes. Then it was washed three times with dichloromethane and acetone, and dried under vacuum at 60 °C for 12 h. The prepared membranes were named PAN/COF-100 and PAN/COF-200, respectively. In the third step, the PAN/COF fiber membranes were washed at 160 °C for 1 day using a Soxhlet extractor and DMF to completely remove PAN and obtain porous COF fiber membranes and dried under vacuum at 60 °C for 12 h. The prepared membranes were named COF-100 and COF-200, respectively. And, the thickness of the porous COF fiber membranes can be easily changed by using electrospun template polymer membranes of different thicknesses, which in turn is controlled by the time of electrospinning keeping all other spinning parameters the same. In addition, PAN fiber membranes and TpPa COF powders were prepared through similar steps for other characterization and testing.

Supporting Information

Supporting Information is available from the Wiley Online Library or from the author.

Conflict of Interest

The authors declare no conflict of interest.

Data Availability Statement

Research data are not shared.

Keywords

covalent organic frameworks, electrospinning, porosity

[1] a) A. P. Cote, A. I. Benin, N. W. Ockwig, M. O'Keeffe, A. J. Matzger, O. M. Yaghi, *Science* **2005**, *310*, 1166; b) N. Huang, P. Wang, D. Jiang, *Nat. Rev. Mater.* **2016**, *1*, 16068; c) C. S. Diercks, O. M. Yaghi, *Science* **2017**, *355*, eaal1585; d) M. S. Lohse, T. Bein, *Adv. Funct. Mater.* **2018**, *28*, 1705553.

[2] Y. Zeng, R. Zou, Y. Zhao, *Adv. Mater.* **2016**, *28*, 2855.

[3] a) H. Fan, A. Mundstock, A. Feldhoff, A. Knebel, J. Gu, H. Meng, J. R. Caro, *J. Am. Chem. Soc.* **2018**, *140*, 10094; b) S. Yuan, X. Li, J. Zhu, G. Zhang, P. Van Puyvelde, B. Van der Bruggen, *Chem. Soc. Rev.* **2019**, *48*, 2665.

[4] a) S. He, B. Yin, H. Niu, Y. Cai, *Appl. Catal. B* **2018**, *239*, 147; b) H. Xu, J. Gao, D. Jiang, *Nat. Chem.* **2015**, *7*, 905.

[5] a) H. Yang, L. Yang, H. Wang, Z. Xu, Y. Zhao, Y. Luo, N. Nasir, Y. Song, H. Wu, F. Pan, *Nat. Commun.* **2019**, *10*, 2101; b) K. Dey, S. Kunjattu H, A. M. Chahande, R. Banerjee, *Angew. Chem., Int. Ed.* **2020**, *132*, 1177.

[6] K. Dey, M. Pal, K. C. Rout, S. Kunjattu H, A. Das, R. Mukherjee, U. K. Kharul, R. Banerjee, *J. Am. Chem. Soc.* **2017**, *139*, 13083.

[7] a) Y. Yusran, H. Li, X. Guan, D. Li, L. Tang, M. Xue, Z. Zhuang, Y. Yan, V. Valtchev, S. Qiu, *Adv. Mater.* **2020**, *32*, 1907289; b) J. Li, X. Jing, Q. Li, S. Li, X. Gao, X. Feng, B. Wang, *Chem. Soc. Rev.* **2020**, *49*, 3565.

[8] X. Li, Q. Gao, J. Wang, Y. Chen, Z.-H. Chen, H.-S. Xu, W. Tang, K. Leng, G.-H. Ning, J. Wu, *Nat. Commun.* **2018**, *9*, 2335.

[9] S. Kandambeth, B. P. Biswal, H. D. Chaudhari, K. C. Rout, S. Kunjattu H, S. Mitra, S. Karak, A. Das, R. Mukherjee, U. K. Kharul, *Adv. Mater.* **2017**, *29*, 1603945.

[10] P. Pachfule, S. Kandmabeth, A. Mallick, R. Banerjee, *Chem. Commun.* **2015**, *51*, 11717.

[11] Y. Peng, M. Zhao, B. Chen, Z. Zhang, Y. Huang, F. Dai, Z. Lai, X. Cui, C. Tan, H. Zhang, *Adv. Mater.* **2018**, *30*, 1705454.

[12] a) H. S. Sasmal, H. B. Aiyappa, S. N. Bhange, S. Karak, A. Halder, S. Kurungot, R. Banerjee, *Angew. Chem., Int. Ed.* **2018**, *130*, 11060; b) M. Matsumoto, L. Valentino, G. M. Stiehl, H. B. Balch, A. R. Corcos, F. Wang, D. C. Ralph, B. J. Mariñas, W. R. Dichtel, *Chem* **2018**, *4*, 308.

[13] a) A. K. Mohammed, S. Usgaonkar, F. Kanheerampockil, S. Karak, A. Halder, M. Tharkar, M. Addicoat, T. G. Ajithkumar, R. Banerjee, *J. Am. Chem. Soc.* **2020**, *142*, 8252; b) C. Li, J. Yang, P. Pachfule, S. Li, M.-Y. Ye, J. Schmidt, A. Thomas, *Nat. Commun.* **2020**, *11*, 4712.

[14] H. Fan, J. Gu, H. Meng, A. Knebel, J. Caro, *Angew. Chem., Int. Ed.* **2018**, *57*, 4083.

[15] a) S. Chandra, S. Kandambeth, B. P. Biswal, B. Lukose, S. M. Kunjir, M. Chaudhary, R. Babarao, T. Heine, R. Banerjee, *J. Am. Chem. Soc.* **2013**, *135*, 17853; b) D. W. Burke, C. Sun, I. Castano, N. C. Flanders, A. M. Evans, E. Vitaku, D. C. McLeod, R. H. Lambeth, L. X. Chen, N. C. Gianneschi, *Angew. Chem., Int. Ed.* **2020**, *59*, 5165.

[16] W. Zhang, L. Zhang, H. Zhao, B. Li, H. Ma, *J. Mater. Chem. A* **2018**, *6*, 13331.

[17] a) S. Agarwal, A. Greiner, J. H. Wendorff, *Adv. Funct. Mater.* **2009**, *19*, 2863; b) S. Jiang, Y. Chen, G. Duan, C. Mei, A. Greiner, S. Agarwal, *Polym. Chem.* **2018**, *9*, 2685; c) X. Yang, J. Wang, H. Guo, L. Liu, W. Xu, G. Duan, *e-Polymers* **2020**, *20*, 682.

[18] a) Y. Han, Q. Zhang, N. Hu, X. Zhang, Y. Mai, J. Liu, X. Hua, H. Wei, *Chin. Chem. Lett.* **2017**, *28*, 2269; b) H. Hou, J. J. Ge, J. Zeng, Q. Li, D. H. Reneker, A. Greiner, S. Z. Cheng, *Chem. Mater.* **2005**, *17*, 967.

[19] S. Kandambeth, A. Mallick, B. Lukose, M. V. Mane, T. Heine, R. Banerjee, *J. Am. Chem. Soc.* **2012**, *134*, 19524.

[20] a) K. E. Hart, J. M. Springmeier, N. B. McKeown, C. M. Colina, *Phys. Chem. Chem. Phys.* **2013**, *15*, 20161; b) J. Weber, N. Du, M. D. Guiver, *Macromolecules* **2011**, *44*, 1763.

[21] M. Thommes, K. Kaneko, A. V. Neimark, J. P. Olivier, F. Rodriguez-Reinoso, J. Rouquerol, K. S. Sing, *Pure Appl. Chem.* **2015**, *87*, 1051.

[22] Z. Wang, Q. Yu, Y. Huang, H. An, Y. Zhao, Y. Feng, X. Li, X. Shi, J. Liang, F. Pan, *ACS Cent. Sci.* **2019**, *5*, 1352.

[23] L. Cao, H. Wu, Y. Cao, C. Fan, R. Zhao, X. He, P. Yang, B. Shi, X. You, Z. Jiang, *Adv. Mater.* **2020**, *32*, 2005565.

ADVANCED FUNCTIONAL MATERIALS

Supporting Information

Flexible, Mechanically Stable, Porous Self-Standing Microfiber Network Membranes of Covalent Organic Frameworks: Preparation Method and Characterization

Chenhui Ding, Marion Breunig, Jana Timm, Roland Marschall, Jürgen Senker,* and Seema Agarwal*

Supporting Information

Flexible, mechanically stable, porous self-standing microfiber network membranes of covalent organic frameworks: Preparation method and characterization

Chenhui Ding,[1] Marion Breunig[2], Jana Timm[3], Roland Marschall[3], Jürgen Senker [2*], Seema Agarwal,[1]*

[1] C. Ding, Prof. S. Agarwal

Macromolecular Chemistry and Bavarian Polymer Institute

University of Bayreuth

Universitätsstrasse 30, 95440 Bayreuth, Germany

E-mail: agarwal@uni-bayreuth.de

[2] M. Breunig, Prof. J. Senker

Department of Chemistry, Inorganic Chemistry IIII, and and Northern Bavarian NMR Centre (NBNC)

University of Bayreuth

Universitätsstrasse 30, 95440 Bayreuth, Germany

E-mail: juergen.senker@uni-bayreuth.de

[2] J. Timm, Prof. R. Marschall

Department of Chemistry, Physical Chemistry IIII

University of Bayreuth

Universitätsstrasse 30, 95440 Bayreuth, Germany

Characterization

The Fourier transform infrared spectra (FTIR, 650–4000 cm^{-1}) were obtained using a spectrometer (Digilab Excalibur FTS-3000). ^{13}C solid-state NMR spectra were acquired on a Bruker Avance III or Bruker Avance III HD spectrometer operating at a B_0 field of 9.4 T ($v_0(^{13}C)$ = 100.6 MHz and 100.7 MHz). The samples were spun at 12.5 kHz in a 4.0 mm MAS double resonance or 3.2 mm MAS triple resonance probe, respectively. MAS spectra were obtained with ramped cross-polarization (CP) experiments where the ^{13}C nutation was set to 70 kHz (4.0 mm) or 50 kHz (3.2 mm), and the ^{1}H nutation frequency v_{nut} was varied linearly from 50-100% on average matching the Hartmann-Hahn conditions. The contact time was set between 1 to 3 ms. Proton broadband decoupling with spinal-64 and v_{nut} = 70 kHz was applied during acquisition. The spectra were referenced with respect to TMS (tetramethylsilane) using the secondary standard adamantine. ^{15}N solid-state NMR spectra were acquired on a Bruker Avance III spectrometer operating at a B_0 field of 9.4 T ($v_0(^{15}N)$ = 40.6 MHz). A ramp (70-100 %) CP with a contact time of 5 ms where the ^{15}N nutation was set to 21 kHz was employed. The samples were spun at 10.0 kHz in a 4 mm MAS double-resonance probe. Proton broadband decoupling with spinal-64 and v_{nut} = 70 kHz was applied during acquisition. The spectra are referenced with respect to CH_3NO_2 using the secondary standard glycine. The X-ray diffraction (XRD, Cu Kα, λ = 1.540598 Å) patterns were recorded on a Bragg-Brentanotype diffractometer (XPERT-PRO, PANalytical B.V.), and each XRD pattern was scanned over a range of 2θ = 2° to 40° at a rate of 0.5° min^{-1}. The morphologies of the fiber membranes were performed on scanning electron microscopy (SEM, Zeiss Leo 1530). N_2 adsorption/desorption isotherms were measured on Quantachrome iQ, and kept at 77 K by a liquid nitrogen bath. Argon sorption measurements were carried out on a Micro 100 Surface Area and Pore Size Analyzer at 87 K. The data were analyzed using the ASIQ v 3.0 software package. For the argon-based isotherms, the specific surface area was calculated with Brunauer-Emmet-Teller (BET) as well as with quasistationary density functional theory (QSDFT) kernels. The valid points for determining the BET surface area were calculated for microporous materials according to the method by Rouquerol et al.[1]. The choice of the QSDFT adsorption branch kernel for cylindrical pores in carbon-based materials depended on the calculated fitting error. The samples were degassed under vacuum (10^{-2} kPa) at 120 °C for 24 h before starting the adsorption experiments. Tensile testing machine (ZwickiLine Z0.5; BT1-FR0.5TN.D14; Zwick

/ Roell, Germany) was used for the measurement of the tensile strength (sample length 30 mm, width 30 mm, and initial effective tensile length 10 mm), and under the same measurement conditions, a 10 000-cycle bending test with a compression of 50% was measured. The thermal stability analysis of the PAN, TpPa COF powders, PAN/COF, and porous COF fiber membranes was carried out using a thermogravimetric analyzer (TGA, TG 209 F1 Libra).
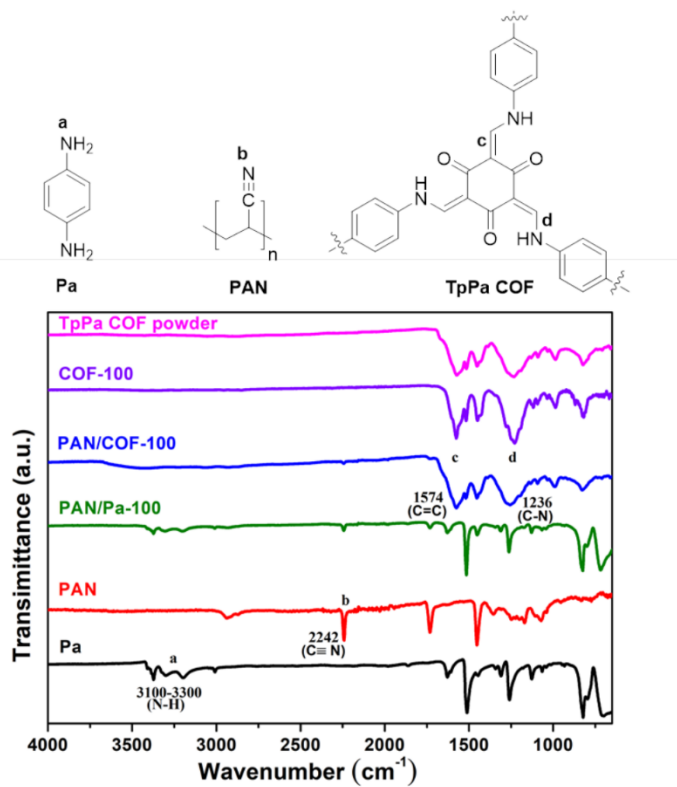

Figure S1. FT-IR spectrum of Pa, PAN, PAN/Pa-100, PAN/COF-100, COF-100, and TpPa COF powder.
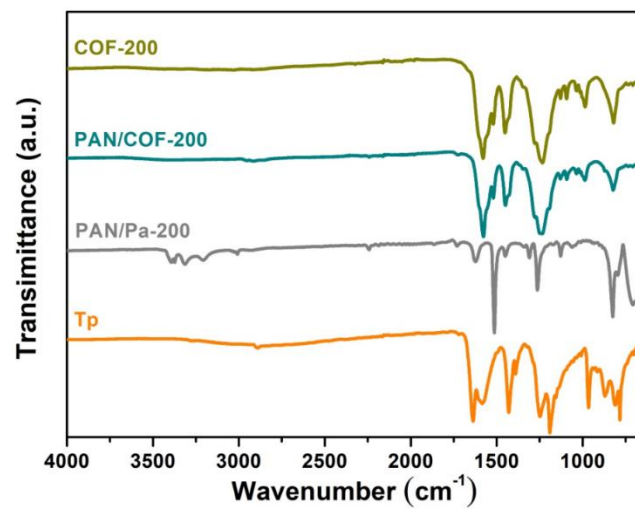
Figure S2. FT-IR spectrum of Tp, PAN/Pa-200, PAN/COF-200 and COF-200.
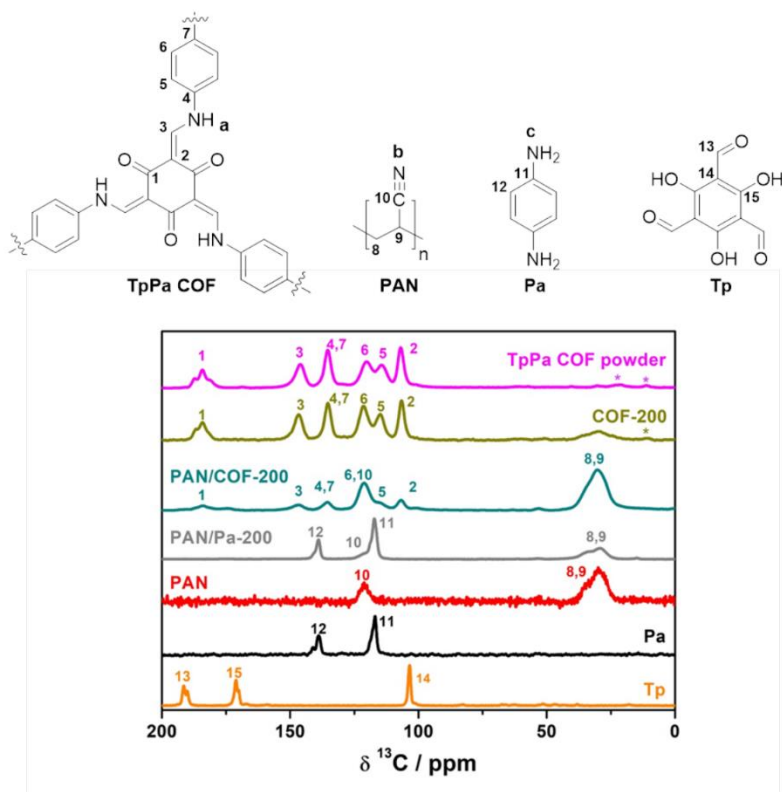
Figure S3: ^{13}C CP MAS NMR spectra of the COF-200 series. The asterisks mark spinning side bands.

Table S1: Assignment of ^{13}C NMR shifts (All values are given in ppm).

Sample	1	2	3	4	5	6	7	8	9	10	11	12	13	14	15
COF powder	184	107	146	136	114	120	136	-	-	-	-	-	-	-	-
COF-100	184	106	146	135	115	121	135	-	-	-	-	-	-	-	-
PAN/COF-100	184	107	146	136	115	121	136	30	30	121	-	-	-	-	-
PAN/Pa-100	-	-	-	-	-	-	-	30	30	121	117	139	-	-	-
PAN	-	-	-	-	-	-	-	30	30	121	-	-	-	-	-
Pa	-	-	-	-	-	-	-	-	-	-	117	139	-	-	-
Tp	-	-	-	-	-	-	-	-	-	-	-	-	192	104	171
COF-200	184	106	147	135	115	121	135				-	-	-	-	-
PAN/COF-200	184	107	147	136	116	121	136	31	31	121	-	-	-	-	-
PAN/Pa-200	-	-	-	-	-	-	-	29	29	122	117	139	-	-	-

Table S2: Assignment of ^{15}N NMR shifts (All values are given in ppm).

Sample	*a*	*b*	*c*
COF powder	-244	-	-
COF-100	-241	-	-
PAN/COF-100	-239	-126	-
PAN/Pa-100	-	-127	-328
PAN	-	-128	-
Pa	-	-	-329
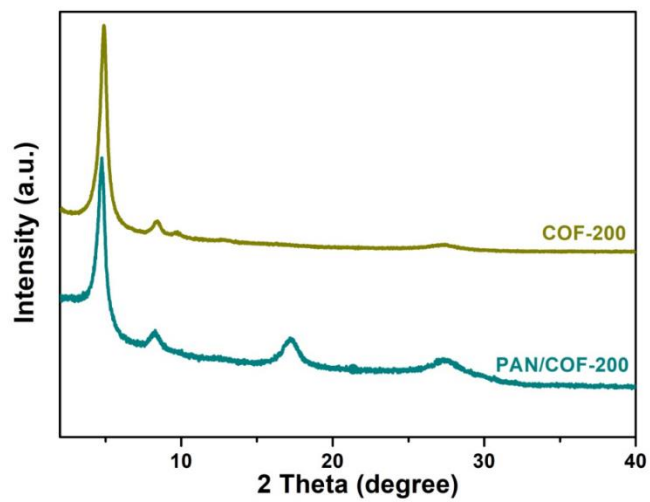
Figure S4. PXRD patterns of PAN/COF-200 and COF-200.
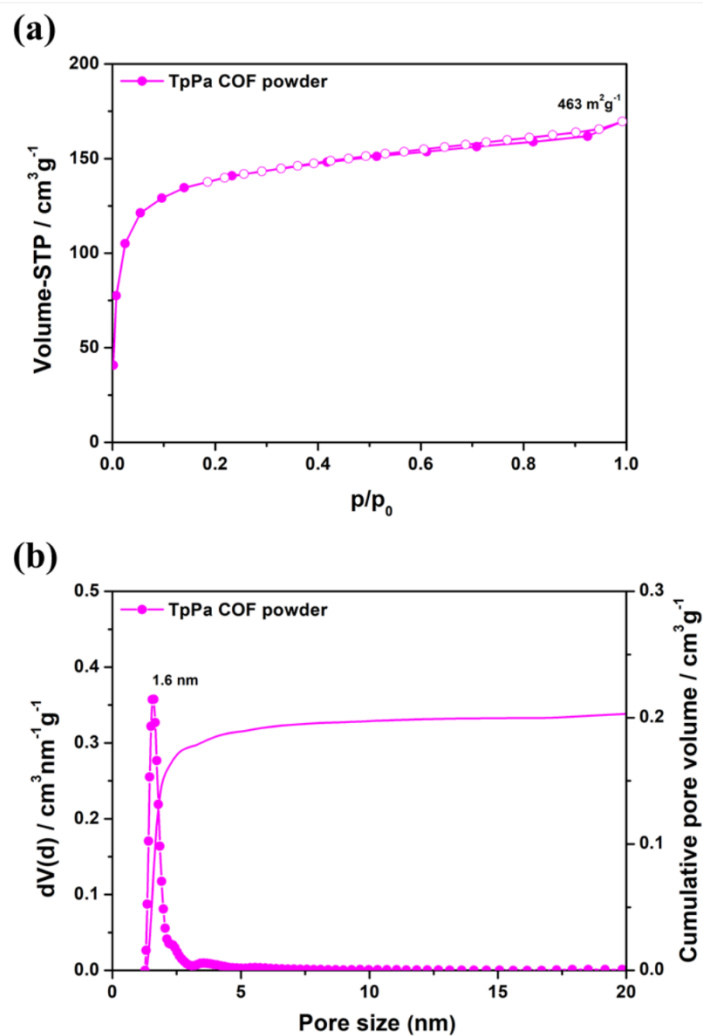
Figure S5. Argon physisorption isotherm of TpPa COF powder at 87 K (specific surface area of 463 m^2/g indicated) a), corresponding pore size distribution and cumulative pore volume b).
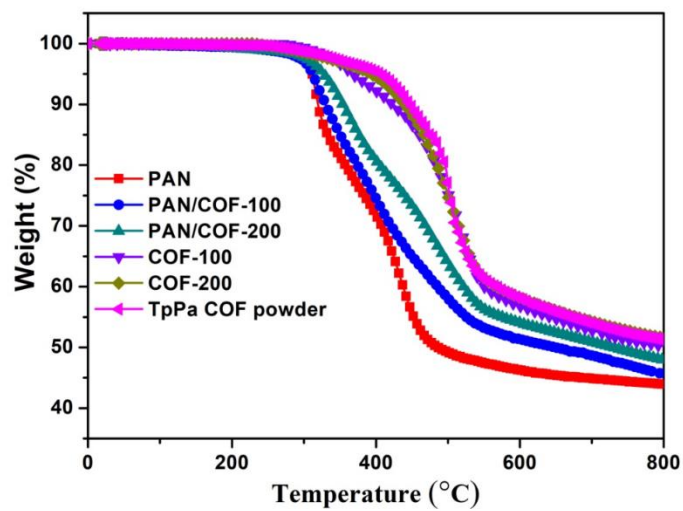
Figure S6. TGA curves of PAN, PAN/COF-100, PAN/COF-200, COF-100, COF-200 and TpPa COF powder.

Table S3. Summary of thermal properties of PAN, PAN/COF-100, PAN/COF-200, COF-100, COF-200 and TpPa COF powder.

Samples	$T_{5\%}$	Residue at 800 °C
	[°C]	[%]
PAN	310	44
PAN/COF-100	308	46
PAN/COF-200	312	47
COF-100	368	50
COF-200	393	52
TpPa COF powder	407	52

Table S4. Summary of mechanical properties of PAN/COF-100, PAN/COF-200, COF-100, COF-200 and porous COF fiber membranes after 10 000-cycles of bending.

Samples	thickness [μm]	strength [MPa]	modulus [MPa]	strain start break [%]
PAN/COF-100	53	10.2±0.5	61.5±3.8	47.9±1.2
PAN/COF-200	59	7.9±0.4	53.5±5.2	23.1±0.7
COF-100	54	0.33±0.07	8.1±1.9	4.5±0.3
COF-200	57	0.64±0.11	4.3±0.3	7.5±0.2
COF-100-10000-cycle	53	0.29±0.05	7.8±2.1	4.4±0.3
COF-200-10000-cycle	56	0.50±0.10	3.8±0.2	7.3±0.2
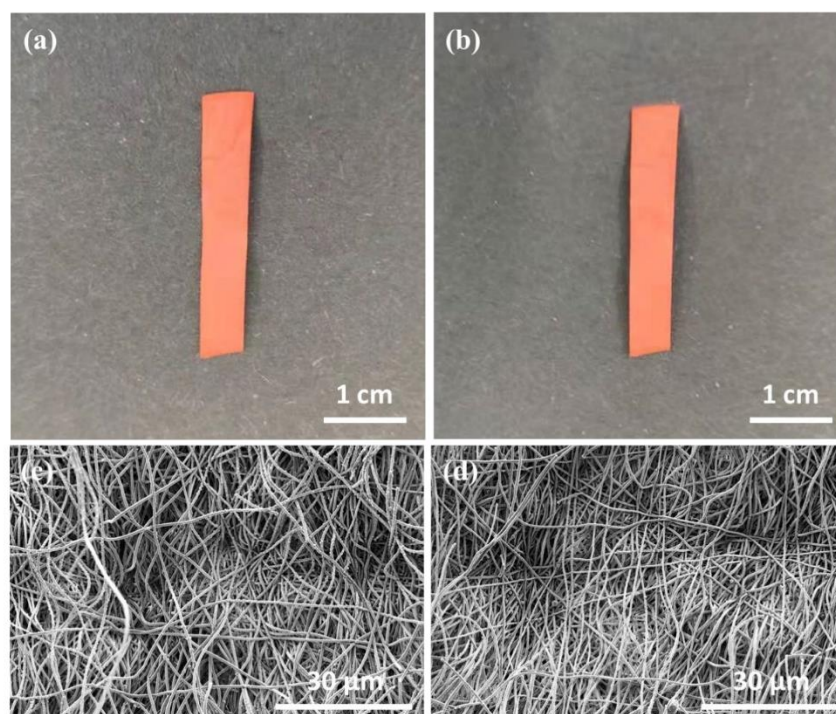
Figure S7. Photographs of COF-100 a), COF-100-10000-cycle b). And SEM images of COF-100 c), COF-100-10000-cycle d).

Reference

[1] J. Rouquerol, F. Rouquerol, P. Llewellyn, G. Maurin, K. S. Sing, *Adsorption by powders and porous solids: principles, methodology and applications,* Academic press, **2013**.

4.2 Template-assisted Preparation of Self-standing 2D-MOF Membranes for Application in Cascade Reactions

Template-assisted Preparation of Self-standing 2D-MOF Membranes for Application in Cascade Reactions

Yingying Du,[a] Chenhui Ding,[a] Jana Timm,[b] Roland Marschall,[b] and Seema Agarwal*[a]

Self-standing metal-organic framework (MOF) membranes open up several application areas where their use in the powder form is either not possible or non-sustainable. Most MOF membranes are prepared as a thin layer either on a supporting substrate or used as a composite membrane with additional supporting material. In this work, we present the preparation procedure for making highly stable, easy-to-handle, reusable, efficient pure MOF membranes (UiO-66-SO$_3$H and UiO-66-NH$_2$ membranes; thickness 240 ± 12 μm and 265 ± 10 μm, respectively) with hollow fiber morphology and their use in cascade reactions in one-pot catalyzed by incompatible acid-base in tea-bag-type concept. The catalytic performance of the catalyst membranes was tested by reacting benzaldehyde dimethyl acetal with three active methylene compounds. The membranes exhibited excellent catalytic activity in cascade reactions in one pot (the yield of the product was as high as 99.9%) and can be reutilized up to 15 times without any significant loss in activity. Stable pure MOF membranes, as shown in this work, would be of interest for several other applications beyond catalysis.

Introduction

Metal-organic frameworks (MOFs) with large surface area, tunable pore size, porosities, and high thermal and chemical stability emerged as important porous materials for several applications, such as gas separation, oil-water separation, etc.[1] MOFs are framework structures formed by the self-assembly of metal clusters and organic ligands through coordination bonds as an insoluble and post-synthesis non-processable powder.[2] MOF was grown on a substrate using an in-situ growth method to enable their use in several application areas where a film is required. One of the methods utilizes immersion of an inorganic substrate in a MOF reaction solution.[3] Further improvement is made by modifying the inorganic surface that provides nucleation sites for MOF's growth and improves the substrate-MOF adhesion.[4] Other methods using already prepared MOF nanoparticles (e.g., ZIF-8) as seeds for the growth of thin MOF film on an inorganic or polymer substrate are also studied.[5]

The use of MOF in heterogenous catalysis in one-pot cascade reactions is recently getting more and more attention as a sustainable alternative to multi-step reactions.[6] The intermediate processing steps, such as the removal and purification of products at each stage, are eliminated in one-pot cascade reactions, simplifying the synthetic procedure, reducing the solvents' use, and minimizing waste generation.[7] Besides MOF, several examples of cascade reactions using different catalysts (homogeneous, enzymes, and heterogenous) for an individual sequence of reactions in a cascade are also known.[8]

One-pot cascade reactions with catalysts that deactivate each other are more challenging as they require carefully designed catalyst support architectures that keep the individual catalysts isolated from each other in an active state.[9] The incompatible catalysts which deactivate each other on coming into contact are called Wolf-Lamb-type catalysts. Moreover, easy and complete recovery after the reaction is of utmost importance for the sustainable use of catalysts. The recovered catalysts can be reused in several other catalytic reactions without losing activity. This makes the design of catalyst support architecture furthermore challenging.

Several efforts are invested in providing solutions to this challenge, and different catalytic supports keeping the two or more incompatible active catalysts isolated from each other in one part are reported in the literature. For this, polymer resins and magnetic nanoparticles,[10] acidic- and basic-layered silicates,[11] zeolites,[12] and metal-organic frameworks (MOFs)[13] are highlighted.

MOFs as catalyst support has increased in the last years due to high porosity, specific surface area, and possibilities of tuning their structure.[14] In particular, acid-base bifunctional MOF powder is an effective catalyst for cascade reactions in one pot.[15] Complex catalyst supports, such as egg yolk-shell structured covalent organic framework (COF)@ MOF (YS-COF@MOF), were also used for the site-separation of acidic and basic groups.[16] MOF is prepared and subsequently used mostly in the form of nanoparticles, which can agglomerate during reactions. Also, retrieving MOF nanoparticles requires an additional filtration or magnetic separation step.[17] Future efforts are

[a] Y. Du, C. Ding, S. Agarwal
Macromolecular Chemistry and Bavarian Polymer Institute
University of Bayreuth
Universitätsstrasse 30, 95440 Bayreuth (Germany)
E-mail: agarwal@uni-bayreuth.de
[b] J. Timm, R. Marschall
Department of Chemistry
Physical Chemistry IIII
University of Bayreuth
Universitätsstrasse 30, 95440 Bayreuth (Germany)

needed to design efficient incompatible catalyst supports that are easily reusable.

Previously, we reported a teabag-type concept for reusable heterogeneous catalysis in which catalysts can be removed easily, like a teabag from tea, and reused. For example, gold nanoparticles (AuNPs) were incorporated in high surface-to-volume hollow polymer fibers, forming a porous nonwoven membrane by randomly laying these fibers by electrospinning. It catalyzed the hydrolytic oxidation of dimethyl phenyl silane and the alcoholysis of dimethyl phenyl silane with n-butanol. The catalytic non-woven was taken out for reuse in the same way as a teabag after use.[18] Keeping our focus on the tea-bag-type concept for catalysts' reusability, we later prepared catalytic supports for incompatible acid and base catalysts. We electrospun and later cross-linked the fibers in nonwoven prepared from -SO₃H and -NH₂ functional polymers and used them in one-pot cascade reactions: deacetylation-and subsequent reaction of an aldehyde with reactive methylene compounds.[19] Efficient catalysis was observed, but the soft polymer catalyst membranes were easily swollen by the solvents used for reactions to form a gel, reducing the catalyst's service life.

In this work, we present a preparation procedure for making highly stable, easy-to-handle, reusable, efficient self-standing pure MOF membranes based on well-known MOF (UiO-66)[20] for use in acid-base catalyzed cascade reactions in one-pot in tea-bag-type concept. After use, the catalyst membranes can be simply removed, washed, and reused for the next cycles of reactions. A procedure for making such self-standing MOF membranes with functional groups −SO₃H and −NH₂ is described, followed by detailed studies regarding their catalytic ability in cascade reactions in one pot. The catalyst membranes exhibited excellent catalytic activity in the acid-base catalyzed reactions (the yield was as high as 99.9%). Moreover, it reveals the same activity on reusing at least 15 catalytic cycles. The details of the material preparation and use in one-pot acid-base

catalyzed reactions are described in detail in the results and discussion section.

Results and discussion

The synthesis strategy of making MOF (UiO-66-SO₃H) (acid-functionalized) and MOF (UiO-66-NH₂) (base-functionalized) individual porous membranes is shown in Figure 1. First, a fiber membrane of polyacrylonitrile (PAN) as a template polymer, together with ZrCl₄, was obtained by electrospinning a mixed solution of ZrCl₄ and PAN in DMF. The optical photographs of the PAN/ZrCl₄ membrane are shown in Figure S1. The membrane was obtained as a non-woven by random deposition of fibers (average diameter 500 nm and thickness 78 ± 10 μm) (Figure S1). Next, using the in-situ growth method, MOF (UiO-66-SO₃H and UiO-66-NH₂) were grown on PAN membrane using the acetic acid catalyst in the water together with either 2-aminobenzenedicarboxylic acid (BDC-NH₂) or 2-sulfobenzenedicarboxylic acid monosodium salt (BDC-SO₃Na). In the next step, the template polymer, PAN was removed by Soxhlet extraction with DMF leaves behind UiO-66-SO₃H and UiO-66-NH₂ membranes of thickness 240 ± 12 μm and 265 ± 10 μm, respectively.

A scanning electron microscope (SEM) was used to characterize the morphology of the synthesized UiO-66-SO₃H/-NH₂ membranes before and after PAN removal, as shown in Figure 2. Figures 2a, and 2b are PAN/UiO-66-SO₃H and PAN/UiO-66-NH₂ membranes, respectively. Through the in-situ growth, a large amount of MOF grows on the surface of PAN fiber and completely wraps them. Figure 2c, and 2d are the surface morphologies of the UiO-66-SO₃H membrane and UiO-66-NH₂ membrane observed under SEM after removing the template polymer PAN by Soxhlet extraction. After removing PAN, the membrane remained intact. Figure 2e, and 2f are the cross-sectional images of UiO-66-SO₃H and UiO-66-NH₂ membranes, respectively, after the removal of PAN, which shows
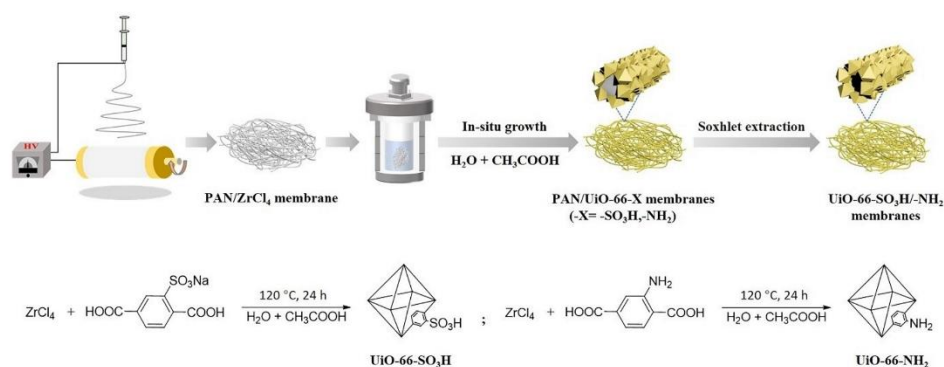

Figure 1. Strategy to fabricate the self-standing UiO-66-SO₃H and UiO-66-NH₂ membranes (top) and the reaction scheme to prepare corresponding MOFs (bottom).
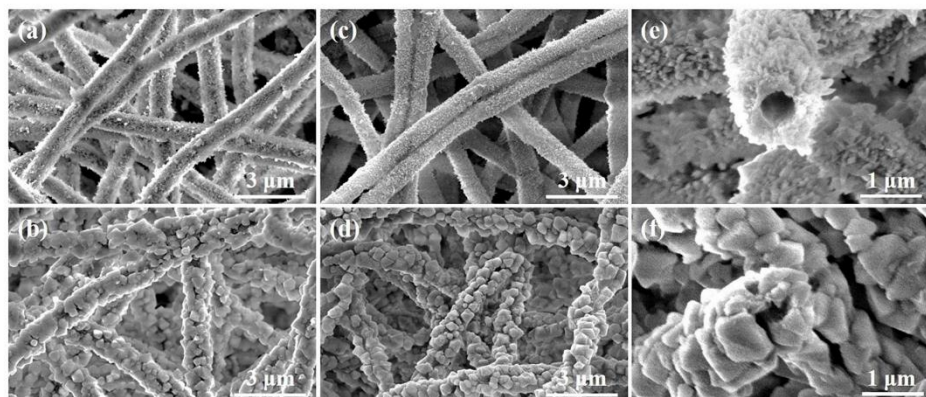
Figure 2. SEM morphology of a) PAN/UiO-66-SO$_3$H, b)PAN/UiO-66-NH$_2$, c) UiO-66-SO$_3$H, d) UiO-66-NH$_2$, Cross-sectional SEM morphology of e) UiO-66-SO$_3$H, f) UiO-66-NH$_2$ membranes.

hollow MOF fibers. The optical photographs of UiO-66-SO$_3$H and UiO-66-NH$_2$ membranes are shown in Figure S1.

The distinct peaks at $2\theta = 7.52°$, 8.69° and the absence of a peak at $2\theta = 17.07°$ originating from the template polymer (PAN) (Figure 3a) in XRD confirmed the preparation of UiO-66-SO$_3$H/-NH$_2$ membranes.[21] Compared with MOF powder, the characteristic peaks of MOF membranes are broader. But the main characteristic peak still exists, indicating that Soxhlet
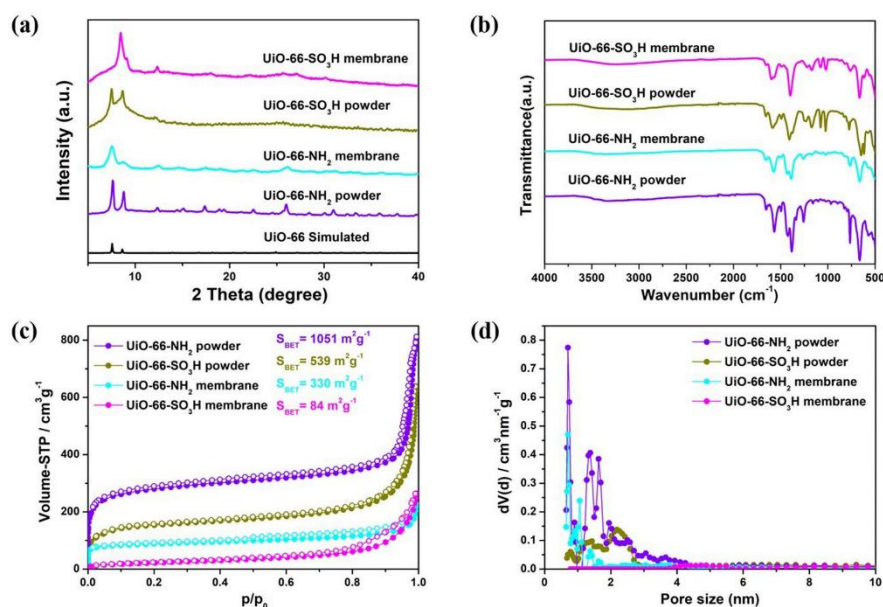
Figure 3. a) XRD patterns of UiO-66 simulated, UiO-66-SO$_3$H powder, UiO-66-SO$_3$H membrane, UiO-66-NH$_2$ powder and UiO-66-NH$_2$ membrane. b) FT-IR spectra of UiO-66-SO$_3$H powder, UiO-66-SO$_3$H membrane, UiO-66-NH$_2$ powder and UiO-66-NH$_2$ membrane. c) N$_2$ physisorption isotherms of UiO-66-SO$_3$H powder, UiO-66-SO$_3$H membrane, UiO-66-NH$_2$ powder and UiO-66-NH$_2$ membrane. d) Pore size distribution and cumulative pore volume of UiO-66-SO$_3$H powder, UiO-66-SO$_3$H membrane, UiO-66-NH$_2$ powder and UiO-66-NH$_2$ membrane.

extraction has caused a certain degree of disorder or inhomogeneity in crystallite size within the framework, but the overall phase integrity is preserved.[22]

In the infrared spectrum of the UiO-66-SO$_3$H membrane, the characteristic stretching bands at 1074 cm^{-1} and 1024 cm^{-1} are S—O, and at 1253 cm^{-1} and 1167 cm^{-1} from O=S=O could be observed (Figure 3b).[23] In the infrared spectrum of the UiO-66-NH$_2$ membrane, the appearance of an absorption band at 1572 cm^{-1} indicates the reaction of -COOH with Zr^{4+}. The 1502 cm^{-1} band is from aromatic C=C.[15a] The main characteristic peak of polyacrylonitrile C≡N was seen at 2245 cm^{-1}. By comparison, the self-standing UiO-66-SO$_3$H and UiO-66-NH$_2$ membranes did not show the characteristic peak of C≡N at 2245 cm^{-1} (Figure S2b). This confirms the successful preparation of independent self-standing UiO-66-SO$_3$/-NH$_2$ membranes.

N$_2$ physisorption isotherm provided pore size distribution and specific surface area of the powders and membranes, as shown in Figure 3. The Nitrogen physisorption isotherms of all samples indicate micropores in the materials due to a sharp increase at very low relative pressures (p/p$_0$) (Figure 3c). Additionally, small mesopores were found in all materials (Figure 3d).[24] At p/p$_0$ > 0.5, the shape of the physisorption isotherms of the powders and the membranes are different. This change might be explained by the formation of the nanostructured fiber morphology and cavitation effects (effects not visible in the pore size distribution due to fitting the adsorption of the physisorption isotherm).[25] When comparing the pore size distributions (PSD) of the powders and the membranes, the similarity is very impressive and shows that even characteristics of MOFs (high porosity and well-defined pores) could be assigned to a membrane by the used synthetic approach. The specific surface areas of the membranes, as calculated using the BET (Brunauer Emmet Teller) model with the Roquerol correction for microporous materials[26] are significantly lower (UiO-66-NH$_2$: 330 m^{2}g^{-1}, UiO-66-SO$_3$H: 84 m^{2}g^{-1}) than the specific surface areas of powder samples (UiO-66-NH$_2$: 1051 m^{2}g^{-1} UiO-66-SO$_3$H: 539 m^{2}g^{-1}). This de-

crease in the surface area could be explained by the partial change in the crystal structure or surface tension of the crystals of the UiO-66 materials, which was already observed due to the broadening of the reflections in the XRD pattern (Figure 3a).

Further, the self-supporting MOFs were studied in one pot as acid-base catalysts for a sequence of two steps, as shown in Scheme 1 (for reaction mechanism, please refer to Scheme S1). Three different one-pot reactions were studied. In each of the three reactions, the UiO-66-SO$_3$H membrane is intended to catalyze the conversion of benzaldehyde dimethyl acetal to benzaldehyde as the first step. At the same time, the UiO-66-NH$_2$ membrane is designed to catalyze the subsequent reaction of benzaldehyde with different active methylene compounds, such as malononitrile and ethyl cyanoacetate, and diethyl malonate. Benzaldehyde undergoes cyanation by malononitrile, whereas ethyl cyanoacetate and diethyl malonate undergo Knoevenagel condensation with benzaldehyde.

Before starting one-pot reactions, the acid and base-MOF membranes were tested for the individual reaction steps in different pots. The UiO-66-SO$_3$H membrane catalyzed the deacetylation reaction, as shown in Scheme 1-step a to b and Figure S3a. The molar ratio of benzaldehyde dimethyl acetal to UiO-66-SO$_3$H catalyst was 1:0.0233. The reaction was fast. About 85% of the theoretical amount of benzaldehyde was already obtained in 15 minutes. The conversion rate as determined from the initial portion of the % conversion vs. time curve (Figure S3a) till about 15 minutes was 5.69%·min^{-1}. After this, although there was a slow down in the rate of reaction, still very high conversion (>95% of benzaldehyde) was obtained in about 60 minutes (rate = 1.56%·min^{-1}). The UiO-66-NH$_2$ membrane catalyzed the reaction of benzaldehyde and malononitrile, as shown in Figure S3b. The molar ratio of benzaldehyde to UiO-66-NH$_2$ catalyst was 1:0.0565. Approximately after 30 minutes, 80% of benzaldehyde was converted to 2-benzylidene malononitrile (rate = 2.49%·min^{-1}). The benzaldehyde was almost completely converted into 2-benzylidene malononitrile when the reaction proceeded for 120 minutes.
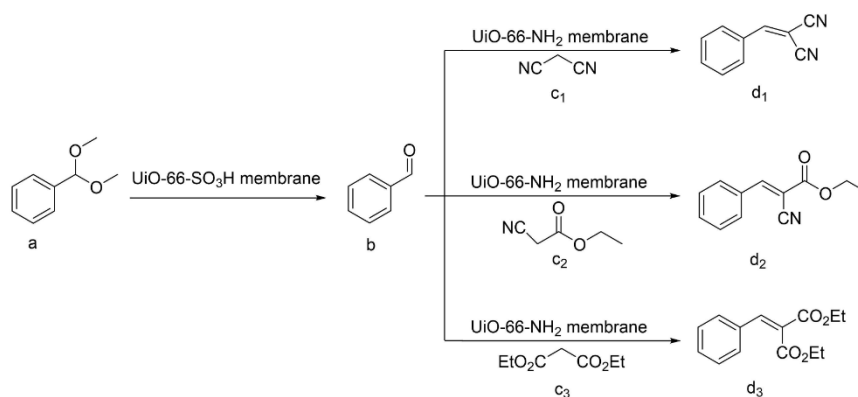
Scheme 1. Wolf-Lamb-type one-pot cascade reactions were studied in the present work.

The one-pot, two-step catalysis experiment results are shown in Figure 4a. For one-pot two steps reactions, both The UiO-66-NH$_2$ and UiO-66-SO$_3$H membranes were inserted in a reaction vessel, and all reagents were added simultaneously. Benzaldehyde dimethyl acetal (0.0025 mol), UiO-66-SO$_3$H catalyst (0.58×10^{-4} mol) and UiO-66-NH$_2$ catalyst (1.4×10^{-4} mol) were used for the reaction. The reaction was monitored for the formation of products by gas chromatography (GC). After 30 minutes, more than 80% of benzaldehyde dimethyl acetal was consumed (rate=2.81%·min^{-1}). After a small induction period, the final product 2-benzylidene malononitrile started forming with a ~1.11%min^{-1} conversion rate until about 60 minutes. After this, although the production rate of 2-benzylidene malononitrile decreased (1.06%·min^{-1}), the reaction was still completed until very high conversions (99.9% in 4 h).

Since the first step, the UiO-66-SO$_3$H membrane catalyzed reaction, is the same, we only studied the base UiO-66-NH$_2$ catalyzed conversion of benzaldehyde in the next set of reactions to ethyl-2-cyano-3-phenyl acrylate, as shown in Figure S3c. No inhibition time was found. 70% of the benzaldehyde was converted into the product ethyl-2-cyano-3-phenyl acrylate after only 90 minutes (rate=0.78%·min^{-1}), and about 95% conversion to the product was achieved after 7 hours of reaction. Afterward, acid UiO-66-SO$_3$H and base UiO-66-NH$_2$ membranes were used together to study the kinetics of acid-

base-catalyzed two-step reactions in one pot. The results of the one-pot, two-step reaction of the production of benzaldehyde from benzaldehyde dimethyl acetal and its further reaction with ethyl cyanoacetate are shown in Figure 4b. The results were very promising. After a slow start, the rate of reaction increased. About 88% of the product was achieved in 7 h (rate= 12.6%·h^{-1}) with almost quantitative conversion in 8 h.

Encouraged by the above results, we tested the reaction of benzaldehyde dimethyl acetal with diethyl malonate. The base UiO-66-NH$_2$ catalyzed the conversion of benzaldehyde to diethyl 2-benzylidene malonate, as shown in Figure S3d.

Unfortunately, the reaction proceeded very slowly, with only 37% of diethyl 2-benzylidene malonate produced (rate= 3.21%·h^{-1}). The results of the one-pot, two-step reaction of the production of benzaldehyde from benzaldehyde dimethyl acetal and its further reaction with diethyl malonate are shown in Figure 4c. The dimethoxybenzyl acetal was only 74% converted in this reaction, and at the end of the reaction, only 36.7% of the product was produced (rate=2.42%·h^{-1}). We speculate that this may be because the pKa value of diethyl malonate is too high. Malononitrile (pKa=11.1), ethyl cyanoacetate (pKa=13.2), diethyl malonate (pKa=16.3).[27] Due to the high pKa of diethyl malonate, deprotonation of methylene groups is extremely difficult, resulting in low product yields in one-pot reactions. There have been similar reports of this phenomenon before.[28] In addition, we investigated blank
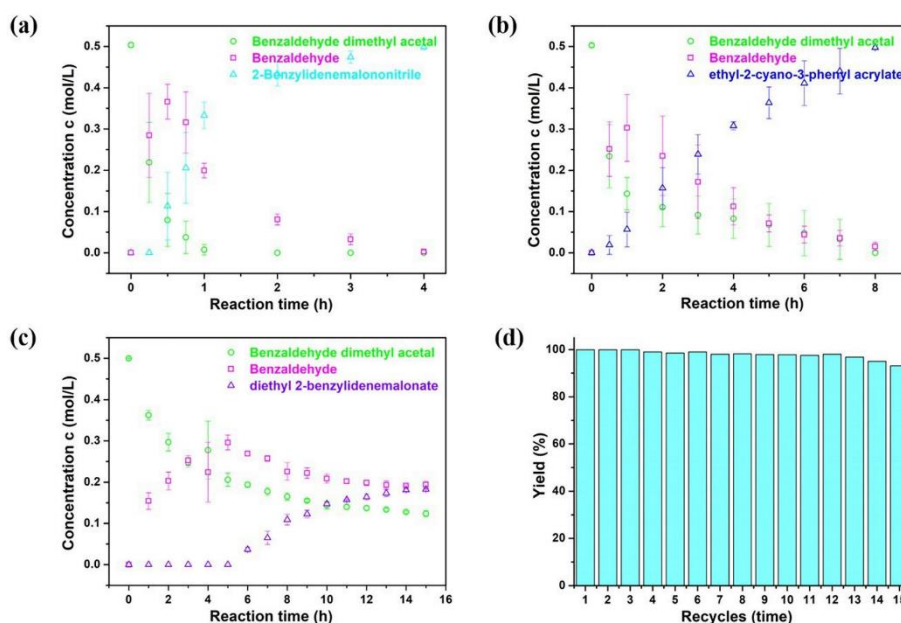

Figure 4. Acid (UiO-66-SO$_3$H membrane) and base (UiO-66-NH$_2$ membrane) catalyzed reactions: a) from benzaldehyde dimethyl acetal to 2-benzylidene malononitrile in one-pot; b) from benzaldehyde dimethyl acetal to ethyl-2-cyano-3-phenyl acrylate in one-pot; c) from benzaldehyde dimethyl acetal to diethyl 2-benzylidene malonate in one-pot. d) Catalyst recycling studies. Reaction conditions: (2.5 mmol) dimethoxybenzyl acetal, (3 mmol) malononitrile, 50 mg UiO-66-SO$_3$H membrane and 50 mg UiO-66-NH$_2$ membrane, solvent: DMF (5 mL), 80°C.

experiments (without a catalyst) of the tandem reaction of benzaldehyde dimethyl acetal with different active methylene compounds (Table S4). Without the catalyst, the products 2-benzylidene malononitrile, ethyl-2-cyano-3-phenyl acrylate, and diethyl 2-benzylidene malonate were not detected in the one-pot two-step reactions. It indicated that the addition of the catalyst played an important role in the reaction process.

Next, we tested the recycling ability of the UiO-66-SO$_3$H/-NH$_2$ membranes for the one-pot, two-step reaction of benzaldehyde dimethyl acetal with malononitrile. After the reaction is completed, the catalyst membranes only need to be simply taken out, washed with acetone and methanol, and dried in a vacuum oven at 80 °C. After this, it was directly used for the next catalytical cycles under the same reaction conditions. The results are shown in Figure 4d. When the catalyst membranes are reused 15 times, 2-benzylidene malononitrile can still be obtained as high as 93.1%. We carried out XRD characterization on the used catalyst membranes, as shown in Figure S4a, by comparison, there is no obvious difference between the used catalyst membranes and the fresh catalyst membranes, indicating that the catalyst membranes have good chemical resistance. In addition, we conducted Fourier-transform infrared (FT-IR) tests on the used catalyst membranes, as shown in Figure S4b, and the catalyst membranes can still maintain their integrity after 15 cycles of use. The performance of self-standing MOF membranes in one-pot reactions is compared with bifunctional acid-base MOF powders reported in the literature (Table S5). It can be seen that the self-supporting MOF membranes (UiO-66-SO$_3$H/-NH$_2$ membranes) exhibit excellent catalytic activity and efficient recycling performance. As there was no change in the structure and physical integrity of the MOF membranes, they are expected to work for many more cycles, not limited to the 15 cycles as tested in this work.

Conclusions

In conclusion, we present highly stable, easy-to-handle, reusable, efficient functional MOF self-standing membranes (UiO-66-SO$_3$H and UiO-66-NH$_2$ membranes) for sustainable use as Wolf-Lamb-type (acid-base) catalysts in one-pot cascade reactions in a tea-bag-type concept. First, a simple procedure for making UiO-66-SO$_3$H and UiO-66-NH$_2$ membranes based on in-situ growth of respective MOFs on seeded template polymer fibers in a non-woven is established. The membranes were characterized using routine analytical methods for porosity, morphology, and functionality and showed morphologically made up of hollow fibers. The membranes efficiently catalyzed both steps of a cascade one-pot reaction, i.e., deacetylation of benzaldehyde dimethyl acetal to benzaldehyde and reaction of active methylene compounds malononitrile and ethyl cyanoacetate with benzaldehyde. A high overall yield of the final products could be obtained. MOF membranes with -NH$_2$ base groups are limited as catalysts for the reaction of benzaldehyde with active methylene compounds having high pKa, such as diethyl malonate.

The membranes are easy to use and, after completion of the reaction, can be pulled out, washed, and reused without any significant drop in reaction efficiency, even after 15 cycles. This work provides an important step forward in preparing and using MOF membranes of macroscopic dimensions as sustainable catalysts.

Experimental Section

Materials

Zirconium(IV) chloride (ZrCl$_4$, Alfa Aesar company, 99.5%), 2-amino-benzenedicarboxylic acid (BDC-NH$_2$, Alfa Aesar company, 99%), 2-sulfobenzenedicarboxylic acid monosodium salt (BDC-SO$_3$Na, Sigma Aldrich company), polyacrylonitrile (Mw = 80,000, Carl Roth), benzaldehyde dimethyl acetal (Alfa Aesar company, 99%), benzaldehyde (Alfa Aesar company, 99%), ethyl cyanoformate (Sigma Aldrich company, >99%), malononitrile (Alfa Aesar company, 99.5+%), diethyl malonate (Acros Organics company, >99%), Dodecane (Alfa Aesar company, 99%), acetic acid (Fisher Chemical Company, 99.7%), N, N-dimethylformamide (Fisher Chemical company, 99.5%) were purchased as stated.

Preparation of UiO-66-SO$_3$H particles and UiO-66-NH$_2$ particles

The solvothermal reaction was used to synthesize UiO-66-SO$_3$H particles. 0.233 g ZrCl$_4$ and 0.268 g 2-sulfobenzenedicarboxylic acid monosodium salt (BDC-SO$_3$Na) dissolved in 10 mL DI water and 1 mL acetic acid. Afterward, the mixture was transferred to a 50 mL Teflon-lined autoclave and reacted in an oven at 120 °C for 24 h. After cooling to room temperature, the white powder could be obtained by centrifugation and washing with 20 mL methanol 3–4 times, and finally dried at 100 °C overnight in an oven. The UiO-66-NH$_2$ particles are also synthesized by the solvothermal method. Just use 2-aminobenzenedicarboxylic acid instead of 2-sulfobenzenedicarboxylic acid monosodium salt (BDC-SO$_3$Na). Other conditions are the same as synthetic UiO-66-SO$_3$H particles.

Preparation of UiO-66-SO$_3$H membrane and UiO-66-NH$_2$ membrane

First, 0.33 g of ZrCl$_4$ and 1.0 g PAN were stirred in 5.6 g of DMF in 10 mL glass bottle for 3 h. The solution was used for electro-spinning with an applied voltage 18.0 KV, flow rate 1.5 mL·h^{-1}, and a 20.0 cm distance between the electrodes. This results in a PAN/ZrCl$_4$ fiber membrane. Next, 0.115 g ZrCl$_4$ and 0.134 g 2-sulfobenzenedicarboxylic acid monosodium salt (BDC-SO$_3$Na) dissolved in 10 mL DI water and 1 mL acetic acid in 50 mL Teflon-lined autoclave. And then, 25 mg PAN/ZrCl$_4$ fiber membrane was added. The reaction was carried out in an oven at 120 °C for one day resulting in PAN/UiO-66-SO$_3$H fiber membranes. Finally, the PAN was removed from the membranes by Soxhlet extraction at 165 °C for one day with DMF. The resulting UiO-66-SO$_3$H fiber membrane free of PAN were dried. The preparation of the UiO-66-NH$_2$ membrane is the same as the UiO-66-SO$_3$H fiber membrane. Use 2-aminobenzenedicarboxylic acid (BDC-NH$_2$) instead of 2-sulfobenzenedicarboxylic acid monosodium salt (BDC-SO$_3$Na).

The amount of acid and base groups were calculated based on the elemental analysis.

For UiO-66-SO$_3$H membrane:

Elemental analysis: C 27.28%, H 3.63%, S 3.73%.

The amount of S = 3.73/(32*100) = 0.0011625 mol/g of UiO-66-SO$_3$H membrane = amount of acid group = 0.58 × 10^{-4} mol/50 mg membrane.

For UiO-66-NH$_2$ membrane:

Elemental analysis: C 34.26%, H 4.14%, N 3.96%.

The amount of N = 3.96/(14*100) = 0.002828 mol/g of UiO-66-NH$_2$ membrane =

the amount of base groups (–NH$_2$) = 1.41 × 10^{-4} mol/50 mg membrane.

Catalytic experiment

One-step acid-catalyzed reaction

Before catalyzing the reaction, the catalyst was activated in an oven at 353 K for 12 h to remove the solvent molecules. The reaction is carried out in the liquid phase under air. Typically, 2.5 mmol benzaldehyde dimethyl acetal, 5 mmol distilled water, 50 mg UiO-66-SO$_3$H membrane, 0.75 mmol dodecane (as an internal standard), and 5 mL DMF were taken in a 25 mL glass reactor vial. The reaction mixture was then heated to 80 °C with stirring at 200 rpm. At regular intervals, 10 μL of the reaction mixture was taken using a pipette and the progress of the reaction was monitored by the GC-FID system (GC-2010 Plus, Shimadzu). After the reaction, the membrane is directly taken out of the reaction medium, washed with acetone (3 × 20 mL) and methanol (3 × 20 mL), dried at 80 °C in a vacuum oven, and reused for recycle runs.

One-step base-catalyzed reaction

Before catalyzing the reaction, the catalyst was activated in an oven at 353 K for 12 h to remove the solvent molecules. The reaction is carried out in the liquid phase under air. 2.5 mmol benzaldehyde, 3 mmol active methylene compounds, 50 mg UiO-66-NH$_2$ membrane, 0.75 mmol dodecane (as an internal standard), and 5 mL DMF were taken in a 25 mL glass reactor vial. The reaction mixture was then heated to 80 °C with stirring at 200 rpm. At regular intervals, 10 μL of the reaction mixture was taken using a pipette and the progress of the reaction was monitored by GC-FID system (GC-2010 Plus, Shimadzu). After the reaction, the membrane is directly taken out of the reaction medium, washed with acetone (3 × 20 mL) and methanol (3 × 20 mL), dried at 80 °C in a vacuum oven, and reused for recycle runs.

One-pot two-step acid-base catalyzed reaction

Before catalyzing the reaction, the catalyst was activated in an oven at 353 K for 12 h to remove the solvent molecules. The reaction is carried out in the liquid phase under air. Typically, 2.5 mmol benzaldehyde dimethyl acetal, 5 mmol distilled water, 3 mmol active methylene compounds, 50 mg UiO-66-SO$_3$H membrane and 50 mg UiO-66-NH$_2$ membrane, 0.75 mmol dodecane (as an internal standard), and 5 mL DMF were taken in a 25 mL glass reactor vial. The reaction mixture was then heated to 80 °C with stirring at 200 rpm. At regular intervals, 10 μL of the reaction mixture was taken using a pipette and the progress of the reaction was monitored by GC-FID system (GC-2010 Plus, Shimadzu). After the reaction, the membranes are directly taken out of the reaction medium, washed with acetone (3 × 20 mL) and methanol (3 × 20 mL), dried at 80 °C in a vacuum oven, and reused for recycle runs.

[1] a) H. Demir, G. O. Aksu, H. C. Gulbalkan, S. Keskin, *Carbon Capture Science & Technology* **2022**, *2*, 100026; Technology **2022**, *2*, 100026; b) Y. Deng, Yanni. Wu. G. Chen, X. Zheng, M. Daia, C. Peng, *Chem. Eng. J.* **2021**, *405*, 127004.
[2] O. M. Yaghi, G. Li, H. Li, *Nature* **1995**, *378(6558)*, 703.
[3] a) Y. Y. Liu, E. P. Hu, E. A. Khan, Z. P. Lai, *J. Membr. Sci.* **2010**, *353*, 36; b) A. Huang, H. Bux, F. Steinbach, J. Caro, *Angew. Chem.* **2010**, *122*, 5078.
[4] X. Qin, Y. X. Sun, N. X. Wang, Y. B. Xie, J. R. Li, *Chem. Ind. Eng.* **2017**, *36*, 1306.
[5] L. Fan, M. Xue, Z. Kang, S. Qiu, *J. Mater. Chem.* **2012**, *22*, 25272.
[6] T. Toyao, M. Saito, Y. Horiuchi, M. Matsuoka, *Cata. Sci. Technol.* **2014**, *4*, 625.
[7] a) Y. Huang, A. M. Walji, C. H. Larsen, D. W. C. MacMillan, *J. Am. Chem. Soc.* **2005**, *127*, 43, 15051; b) J. Barluenga, F. Rodríguez, F. J. Fananµs, *Chem. Asian J.* **2009**, *4*, 1036; c) P. F. Xu, W. Wang, in *Catalytic cascade reactions*, John Wiley & Sons, **2013**; d) A. Behr, A. J. Vorholt, K. A. Ostrowski, T. Seidensticker, *Green Chem.* **2014**, *16*, 982; e) Q. J. Liang, Y. H. Xu, T. P. Loh, *Org. Chem. Front.* **2018**, *5*, 2765; f) H. Pellissier, *Adv. Synth. Catal.* **2020**, *362*, 2289.
[8] a) L. F. Tietze, *Chem. Rev.* **1996**, *96*, 115; b) I. R. Baxendale, S. V. Ley, C. Piutti, *Angew. Chem.* **2002**, *114*, Nr. 12; c) M. J. Climent, A. Corma, S. Iborra, *ChemSusChem* **2009**, *2*, 500; d) C. Grondal, M. Jeanty, D. Enders, *Nat. Chem.* **2010**, *2*, 167; e) A. Belluati, I. Craciun, J. Liu, C. G. Palivan, *Biomacromolecules* **2018**, *19*, 4023; f) Y. Liu, J. A. Izzo, D. McLeod, S. Ričko, E. B. Svenningsen, T. B. Poulsen, K. A. Jørgensen, *J. Am. Chem. Soc.* **2021**, *143*, 8208; g) W. Xu, L. Jiao, Y. Wu, L. Hu, W. Gu, C. Zhu, *Adv. Mater.* **2021**, *33*, 2005172.
[9] B. J. Cohen, M. A. Kraus, A. Patchornik, *J. Am. Chem. Soc.* **1981**, *103*, 7621.
[10] a) N. T. S. Phan, C. S. Gill, J. V. Nguyen, Z. J. Zhang, C. W. Jones, *Angew. Chem. Int. Ed.* **2006**, *45*, 2209; b) J. P. H. Li, A. A. Adesina, E. M. Kennedy, M. Stockenhuber, *Phys. Chem. Chem. Phys.* **2017**, *19*, 26630; c) X. Yuan, Z. Wang, Q. Zhang, J. Luo, *RSC Adv.* **2019**, *9*, 23614.
[11] a) K. Motokura, N. Fujita, K. Mori, T. Mizugaki, K. Ebitani, K. Kaneda, *J. Am. Chem. Soc.* **2005**, *127*, 9674; b) A. Erigoni, M. C. Hernández-Soto, F. Rey, C. Segarra, U. Díaz, *Catal. Today* **2020**, *345*, 227.
[12] a) T. Ge, Z. Hua, Y. Zhu, Y. Song, G. Tao, X. Zhou, L. Chen, W. Ren, H. Yao, J. Shi, *RSC Adv.* **2014**, *4*, 64871; b) K. A. Almeida, D. Cardoso, *Catal. Today* **2013**, *213*, 122; c) A. Kawano, T. Moteki, M. Ogura, *Microporous Mesoporous Mater.* **2020**, *299*, 110104.
[13] a) M. Mu, X. Yan, Y. Li, L. Chen, *J. Nanopart. Res.* **2017**, *19*, 148; b) J. H. Zhao, Y. Yang, J. X. Che, J. Zuo, X. H. Li, Y. Z. Hu, X. W. Dong, L. Gao, X. Y. Liu, *Chem. Eur. J.* **2018**, *24*, 9903; c) S. Mistry, A. Sarkar, S. Natarajan, *Cryst. Growth Des.* **2019**, *19*, 747; d) T. Zurrer, K. Wong, J. Horlyck, E. C.

Lovell, J. Wright, N. M. Bedford, Z. Han, K. Liang, J. Scott, R. Amal, *Adv. Funct. Mater.* **2021**, *31*, 2007624.

[14] a) Y. B. Huang, J. Liang, X. S. Wang, R. Cao, *Chem. Soc. Rev.* **2017**, *46*, 126; b) A. Dhakshinamoorthy, Z. Li, H. Garcia, *Chem. Soc. Rev.* **2018**, *47*, 8134; c) X. Zhang, J. Sun, G. Wei, Z. Liu, H. Yang, K. Wang, H. Fei, *Angew. Chem. Int. Ed.* **2019**, *58*, 2844; d) S. Yuan, J. Zhang, L. Hu, J. Li, S. Li, Y. Gao, Q. Zhang, L. Gu, W. Yang, X. Feng, B. Wang, *Angew. Chem.* **2021**, *133*, 21853; e) W. Yang, X. Liu, X. Chen, Y. Cao, S. Cui, L. Jiao, C. Wu, C. Chen, D. Fu, I. D. Gates, Z. Cao, H. Jiang, *Adv. Mater.* **2022**, 2110123.

[15] a) P. Rani, R. Srivastava, *J. Colloid Interface Sci.* **2019**, *557*, 144; b) Y. Hu, J. Zhang, H. Huo, Z. Wang, X. Xu, Y. Yang, K. Lin, R. Fan, *Catal. Sci. Technol.* **2020**, *10*, 315; c) Y. R. Lee, X. H. Do, S. S. Hwang, K. Y. Baek, *Catal. Today* **2021**, *359*, 124.

[16] Q. Dang, H. Huang, L. Li, X. Lyu, S. Zhong, Y. Yu, D. Xu, *Chem. Mater.* **2021**, *33*, 5690.

[17] J. Liu, T. A. Goetjen, Q. Wang, J. G. Knapp, M. C. Wasson, Y. Yang, Z. H. Syed, M. Delferro, J. M. Notestein, O. K. Farha, J. T. Hupp, *Chem. Soc. Rev.* **2022**, *51*, 1045.

[18] F. Mitschang, H. Schmalz, S. Agarwal, A. Greiner, *Angew. Chem. Int. Ed.* **2014**, *53*, 4972.

[19] M. O. Pretscher, S. Gekle, S. Agarwal, *Macromol. Rapid Commun.* **2019**, *40*, 1900148.

[20] J. H. Cavka, S. Jakobsen, U. Olsbye, N. Guillou, C. Lamberti, S. Bordiga, K. P. Lillerud, *J. Am. Chem. Soc.* **2008**, *130*, 13850.

[21] M. J. Katz, Z. J. Brown, Y. J. Colón, P. W. Siu, K. A. Scheidt, R. Q. Snurr, J. T. Hupp, O. K. Farha, *Chem. Commun.* **2013**, *49*, 9449.

[22] Y. Yang, H. F. Yao, F. G. Xi, E. Q. Gao, *J. Mol. Catal. A* **2014**, *390*, 198.

[23] R. G. Vaghei, D. Azarifar, S. Daliran, A. R. Oveisi, *RSC Adv.* **2016**, *6*, 29182.

[24] M. Thommes, K. Kaneko, A. V. Neimark, J. P. Olivier, F. Rodriguez-Reinoso, J. Rouquerol, K. S. W. Sing, *Pure Appl. Chem.* **2015**, *87*, 1051.

[25] C. Schlumberger, M. Thommes, *Adv. Mater. Interfaces* **2021**, *8*, 2002181.

[26] J. Rouquerol, F. Rouquerol, P. Llewellyn, G. Maurin, K. S. W. Sing, Academic press, **2013**.

[27] W. S. Matthews, J. E. Bares, J. E. Bartmess, F. G. Bordwell, F. J. Cornforth, G. E. Drucker, Z. Margolin, R. J. McCallum, G. J. McCollum, N. R. Vanier, *J. Am. Chem. Soc.* **1975**, *97*, 7006.

[28] a) D. Wang, Z. Li, *Catal. Sci. Technol.* **2015**, *5*, 1623; b) H. Liu, F. G. Xi, W. Sun, N. N. Yang, E. Q. Gao, *Inorg. Chem.* **2016**, *55*, 12, 5753.

128

ChemCatChem

Supporting Information

Template-assisted Preparation of Self-standing 2D-MOF Membranes for Application in Cascade Reactions

Yingying Du, Chenhui Ding, Jana Timm, Roland Marschall, and Seema Agarwal*

WILEY-VCH

Characterization

The Fourier transform infrared spectra (FTIR, 500-4000 cm^{-1}) were obtained using a spectrometer (Digilab Excalibur FTS-3000).

Scanning electron microscopy (SEM): The surface morphology was observed with a Zeiss LEO 1530, operating at an acceleration voltage of 3 kV employing an Everhart-Thornley secondary electron detector. Before imaging, the samples were sputtered with a thin platinum layer of 2 nm (Sputter Coater 208HR, Cressington).

The Xray diffraction (XRD, Cu Kα, λ = 1.540598 Å) patterns were recorded on a Bragg-Brentanotype diffractometer (XPERT-PRO, PANalytical B.V.), and each XRD pattern was scanned over a range of 2θ = 2° to 40° at a rate of 0.5° min^{-1}.

N$_2$ adsorption/desorption isotherms were measured on Quantachrome iQ and kept at 77 K by a liquid nitrogen bath. The data were analyzed using the ASIQ v 3.0 software package.

Gas Chromatography (GC): GC measurements were performed on a GC-FID system (GC-2010 Plus, Shimadzu), using nitrogen as a carrier gas. An amount of 10 µL of the reaction mixture was dissolved in 1 mL acetonitrile. 1 µL of this solution was injected with a split ratio of 1:50 and measured from 50 °C (2 min hold) up to 300 °C at a heating rate of 15K min^{-1}.

1

WILEY-VCH

Supporting Figures and Tables
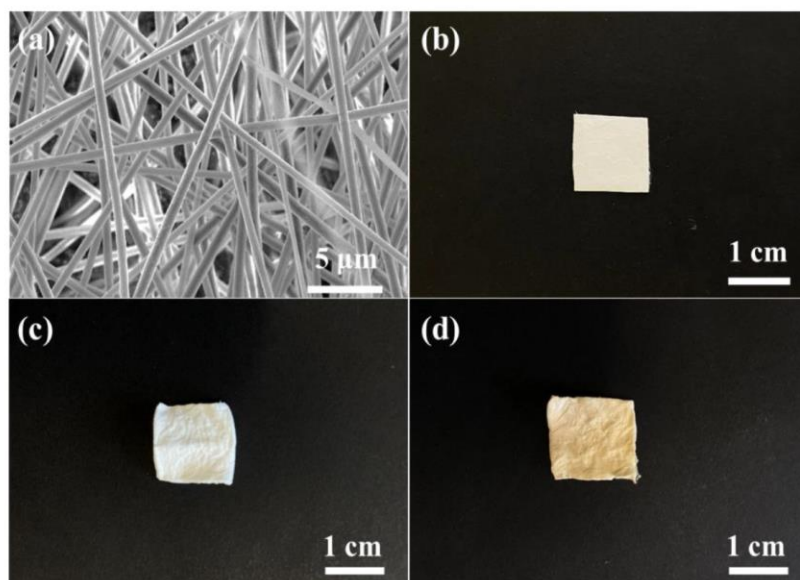
Figure S1. SEM images of a) PAN/ZrCl$_4$ membrane. Photographs of b) PAN/ZrCl$_4$ membrane,

c) UiO-66-SO$_3$H membrane and d) UiO-66-NH$_2$ membrane.

2

WILEY-VCH
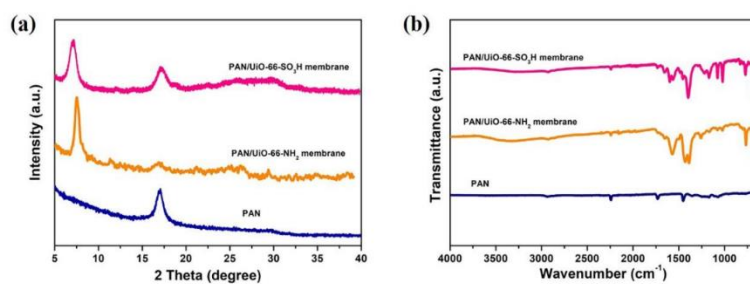
Figure S2. a) XRD patterns of PAN, PAN/UiO-66-NH$_2$ membrane and PAN/UiO-66-SO$_3$H membrane. b) FT-IR spectra of PAN, PAN/UiO-66-NH$_2$ membrane and PAN/UiO-66-SO$_3$H membrane.

3

WILEY-VCH
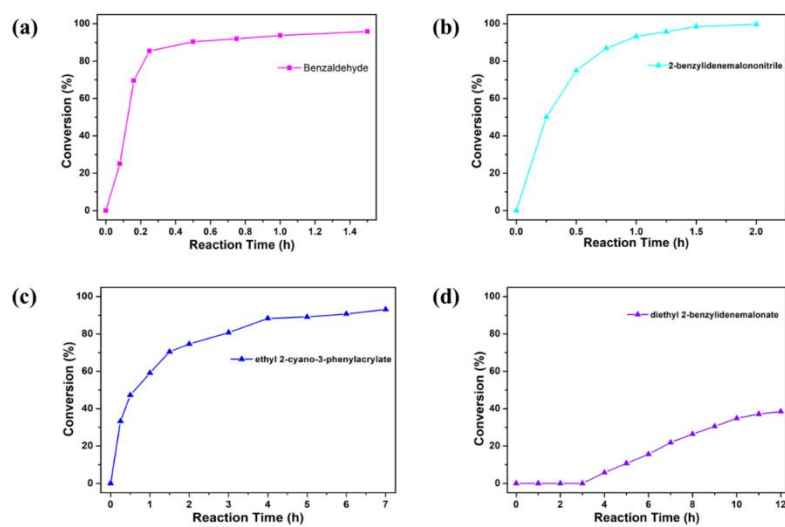
Figure S3. a) UiO-66-SO₃H membrane catalyzed reaction from benzaldehyde dimethyl acetal to benzaldehyde. b) UiO-66-NH₂ membrane catalyzed reaction of benzaldehyde to 2-benzylidenemalononitrile. c) UiO-66-NH₂ membrane catalyzed reaction of benzaldehyde to ethyl-2-cyano-3-phenyl acrylate. d) UiO-66-NH₂ membrane catalyzed reaction of benzaldehyde to diethyl 2-benzylidene malonate.

4

WILEY-VCH
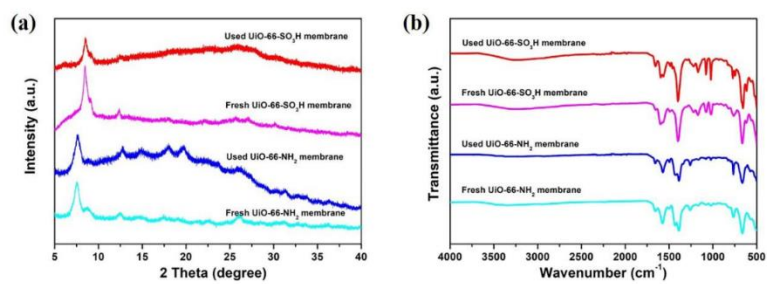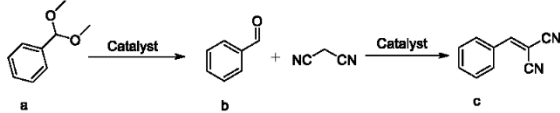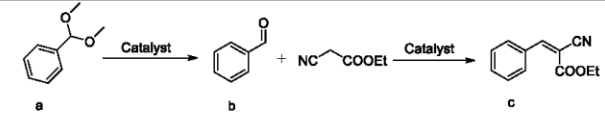
Figure S4. a) XRD patterns of fresh and used UiO-66-SO$_3$H/-NH$_2$ membranes. b) FT-IR spectra of the fresh and used UiO-66-SO$_3$H/-NH$_2$ membranes.

5

Table S1. The kinetic experiments for the conversion of benzaldehyde dimethyl acetal to 2-benzylidenemalononitrile in one-pot.
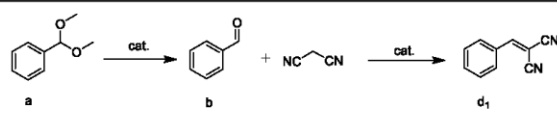

Reaction time (h)	Concentration of a (mol/L)	Concentration of b (mol/L)	Concentration of c (mol/L)
0	0.504±0.006	-	-
0.5	0.079±0.064	0.366±0.043	0.113±0.082
0.75	0.037±0.039	0.316±0.074	0.206±0.086
1	0.007±0.012	0.199±0.018	0.333±0.033
2	-	0.080±0.013	0.433±0.029
3	-	0.032±0.013	0.47±0.0148
4	-	0.002±0.004	0.499±0.006

6

WILEY-VCH

Table S2. The kinetic experiments for the conversion of benzaldehyde dimethyl acetal to ethyl-2-cyano-3-phenyl acrylate in one-pot.

Reaction time (h)	Concentration of a (mol/L)	Concentration of b (mol/L)	Concentration of c (mol/L)
0	0.503±0.005	0	-
0.5	0.234±0.076	0.252±0.066	0.019±0.023
1	0.143±0.039	0.303±0.081	0.057±0.042
2	0.111±0.046	0.235±0.096	0.157±0.050
3	0.091±0.046	0.172±0.089	0.239±0.047
4	0.082±0.048	0.112±0.046	0.307±0.010
5	0.068±0.052	0.071±0.021	0.36±0.038
6	0.048±0.054	0.044±0.020	0.411±0.054
7	0.033±0.048	0.036±0.019	0.440±0.055
8	-	0.015±0.009	0.497±0.005

7

136

WILEY-VCH

Table S3. The kinetic experiments for the conversion of benzaldehyde dimethyl acetal to to diethyl 2-benzylidene malonate in one-pot.

Reaction time (h)	Concentration of a (mol/L)	Concentration of b (mol/L)	Concentration of c (mol/L)
0	0.499±0.012	0	-
1	0.362±0.012	0.154±0.020	-
2	0.297±0.022	0.203±0.022	-
3	0.248±0.012	0.253±0.012	-
4	0.278±0.070	0.224±0.072	-
5	0.206±0.016	0.296±0.018	-
6	0.194±0.006	0.269±0.005	0.037±0.006
7	0.178±0.010	0.257±0.007	0.065±0.016
8	0.165±0.009	0.226±0.021	0.109±0.013
9	0.155±0.004	0.222±0.013	0.123±0.009
10	0.144±0.010	0.209±0.011	0.148±0.004
11	0.140±0.005	0.202±0.005	0.157±0.002
12	0.137±0.005	0.199±0.007	0.164±0.007
13	0.134±0.003	0.193±0.010	0.173±0.008
14	0.128±0.002	0.193±0.00	0.182±0.003
15	0.124±0.007	0.193±0.008	0.182±0.002

8

137

WILEY-VCH

Table S4. The blank experiment for the reaction of benzaldehyde dimethyl acetal with different active methylene compounds (without catalyst) [a].

entry	R$_1$	R$_2$	Product (c)	conv. of a (%)	yield of c (%)
1	CN	CN		Trace	0
2	CN	COOEt		Trace	0
3	COOEt	COOEt		0	0

[a] Reaction condition: 1.5 mmol benzaldehyde dimethyl acetal, 3 mmol distilled water, 1.8 mmol methylene compounds, 0.15 mmol dodecane (as an internal standard), and 3 mL DMF to a 10mL glass reactor vial. The reaction mixture was then heated to 80 °C with stirring at 200 rpm.

9

138

WILEY-VCH

Table S5. One-pot acid-base cascade reactions: comparison of MOF particles with MOF membranes as catalysts.

entry	catalyst	conv. of a (%)	yield of d_l (%)	Recycle times	Ref.
1	UiO-66-SO$_3$H FM [a] UiO-66-NH$_2$ FM	99.9	99.9	15	this work
2	MIL-101-AB-0.26[b]	92.0	91.0	3	1
3	MIL-101(Al/Fe)-NH$_2$ [c]	100	99.8	5	2
4	MIL-101(Cr)@CS[d] [MIL-101(Cr)/CS=2.86]	99.0	99.0	5	3
5	Yb-BDC-NH$_2$[e]	97.0	97.0	4	4
6	ZIF8-A61-SO$_3$H[f]	100.0	98.0	5	5

Reaction conditions: [a] Benzaldehyde dimethyl acetal (1 mmol), malononitrile (1.2 mmol), distilled water (108 µL), 50 mg UiO-66-SO$_3$H membrane, 50 mg UiO-66-NH$_2$ membrane, DMF (2 mL), 80 ∘C. [b] Benzaldehyde dimethyl acetal (1 mmol), malononitrile (2 mmol), DMF 2 mL, catalyst 0.04 mmol, 363K. [c] Benzaldehyde dimethyl acetal (1.0 mmol), malononitrile (1.5 mmol), toluene (3 mL), catalyst (20 mg). [d] Benzaldehyde dimethyl acetal (2 mmol), malononitrile (2.1 mmol), acetonitrile (2 mL), distilled water (50 µL), and catalyst (50 mg); 80 °C; reaction time 12 h. [e] Benzaldehyde dimethyl acetal (2.0 mmol), malononitrile (2.1 mmol) and DMSO-d6 (2 mL), catalyst (100 mg), 50 °C and 24 h. [f] Benzaldehyde dimethyl acetal (1 mmol), malononitrile (5 mmol),1,4-dioxane (4 ml), catalyst (100 mg).

10

139

Scheme S1. Mechanism of acid-base reaction catalyzed by catalyst membrane.
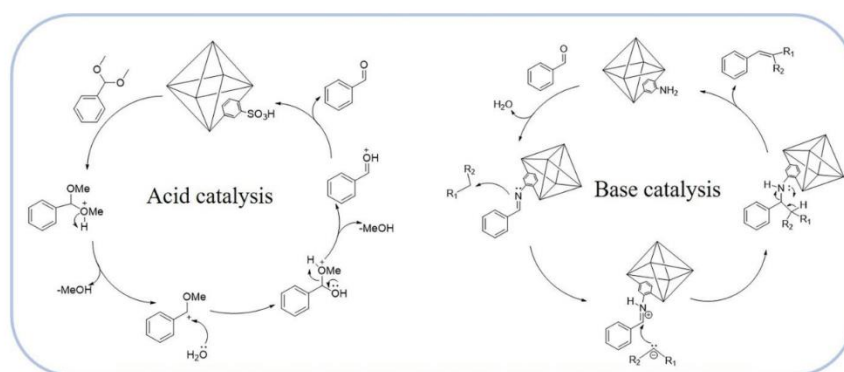
References

[1] H. Liu, F. G. Xi, W Sun, N. N. Yang, E. Q. Gao, *Inorg. Chem.* **2016**, 55, 12, 5753.

[2] Y. Hu, J. Zhang, H. Huo, Z. Wang, X. Xu, Y. Yang, K. Lin, R. Fan, *Catal. Sci. Technol.* **2020**, 10, 315.

[3] Z. S. Zhao, Y. Zhang, T. Fang, Z. B. Han, F. S. Liang, *ACS Appl. Nano Mater.* **2020**, 3, 6316.

[4] Y. Zhang, Y. Wang, L. Liu, N. Wei, M. L. Gao, D. Zhao, Z. B. Han, *Inorg. Chem.* **2018**, 57, 4, 2193.

[5] Y. R. Lee, X. H. Do, S. S. Hwang, K. Y. Baek, *Catal. Today.* **2021**, 359, 124.

4.3 Electrospun, non-woven fiber membranes of porous polyimides with high carbon dioxide uptakes and selectivities

Marion Breunig, Jian Zhu, **Chenhui Ding**, Renée Siegel, Seema Agarwal, Jürgen Senker. Electrospun, non-woven fiber membranes of porous polyimides with high carbon dioxide uptakes and selectivities. Microporous and Mesoporous Materials, **2022**, 329, 111519.

Electrospun, non-woven fiber membranes of porous polyimides with high carbon dioxide uptakes and selectivities

Marion Breunig [a], Jian Zhu [b], Chenhui Ding [b], Renée Siegel [a], Seema Agarwal [b,**], Jürgen Senker [a,*]

[a] University of Bayreuth, Inorganic Chemistry III and Northern Bavarian NMR Centre (NBNC), Universitätsstraße 30, 95440, Bayreuth, Germany
[b] University of Bayreuth, Macromolecular Chemistry II and Bavarian Polymer Institute, Universitätsstraße 30, 95440 Bayreuth, Germany

A R T I C L E   I N F O

A B S T R A C T

Microporous organic polyimides are well suited for carbon dioxide separation from gas mixtures based on their polar surface and their tendency towards ultramicroporosity. Nevertheless, their application potential is limited due to an inherent insolubility and infusibility, preventing an easy processing into functional objects like membranes. By establishing a three-step synthesis procedure for the literature known network NPI-I, here, a solution to this challenge is demonstrated. The central step is electrospinning of a solution of the linkers tetrakis (4-aminophenyl)methane and naphthalene 1,4,5,8-tetracarboxylic dianhydride and the auxiliary polymer polyvinylpyrrolidone into a precursor fiber mat. The mat was then heated to polymerize the linkers into the polyimide. Subsequently, PVP was removed by pyrolysis obtaining a robust, flexible and self-standing membrane. The NPI-I fiber mat exhibits a remarkable microporosity with a BET surface area of 222 m^2/g, a total pore volume of 0.121 cm^3/g and a high amount of ultramicropores. Its CO_2 uptake of 3.0 mmol/g (0 °C, 1 bar) and its CO_2/ CH_4 selectivity of about 20 (0 °C, 1 bar) even exceed the literature values for bulk NPI-I. This study reveals that PVP acts as a template on molecular level influencing, primarily the micropore formation, reducing the BET surface area by roughly a factor of three compared to the bulk material. In contrast, the ultramicroporosity of the porous polyimides remains mainly unaffected. We envision that this three-step synthesis can be transferred to a broad variety of porous polymers. With electrospinning the large-scale production of self-standing membranes becomes realistic rendering the application of porous polymers for gas separation more likely.

1. Introduction

Carbon dioxide, which represents the largest proportion of greenhouse gases, is recognized for its impact on the global climate leading among other things to more frequently occurring extreme weather conditions [1,2]. To stop this trend, the global CO_2 emissions into the atmosphere must be reduced [3–5]. Possible strategies are capturing and storing or further utilizing the produced CO_2 [6–9]. One of the most convenient sources for the removal of CO_2 are flue gases, produced during the production of energy from fossil fuels [6,7]. The main method to separate the flue gas into its individual components used up to now is amine scrubbing, which separates CO_2 with high selectivities but is extremely cost- and time-intensive [8,10–13]. An alternative is physisorption employing porous materials, which is commonly done either discontinuously like for PSA (pressure swing adsorption), VSA (vacuum swing adsorption) and TSA (temperature swing adsorption) or in a continuous process using membrane technology [10,11,13–16].

Separation by physisorption requires high selectivity for CO_2 in the gas mixture in order to achieve good separation from the flue gas [17, 18]. The selectivity can be achieved by either preferred adsorption sites or with size selective ultramicropores (<0.7 nm) like for porous organic polymers (POPs) [19–21]. Excellent examples are PI-NO2 and MOPI-IV with CO_2 uptakes up to 4 mmol/g and selectivity of 17 (CO_2/CH_4 5:95 at 0 °C) [22,23]. Both exhibit in addition to their ultramicroporous structure a polar surface due to their electron-rich imide groups [23–25]. Despite the above mentioned advantages, it is still quite difficult to produce macroscopic objects such as membranes or hollow tubes, since their high degree of crosslinking makes them neither soluble nor fusible [26,27]. This challenge generally applies to amorphous POPs and their crystalline counterparts covalent organic frameworks (COFs)

likewise, as they are based on the reticular synthesis concept [28,29].

To process POPs and COFs into functional macroscopic objects, the principle of mixed matrix membranes (MMMs) has been applied recently. Here the insoluble COF is embedded in a dense membrane of a soluble and thus processable matrix polymer [30,31]. The often poor compatibility between filler and the organic polymer matrix is significantly improved with COFs, as these are also completely organic [32]. Using the example of COF-300 embedded in 6FDA-DAM (glassy polymer) or Pebax (rubbery polymer), Cheng et al. showed a significant increase in permeability with increasing filler content [30]. Nevertheless, the interfacial compatibility of COFs is also not ideal. This leads to voids and defects, which prevent the full potential of the COFs from being exploited. In addition, agglomeration leads to reduced mechanical stability [32]. Alternately, COFs have also been successfully prepared as membranes via in-situ growth or by layer-by-layer deposition [33,34]. However, both mentioned methods require a support giving rise to similar problems as for the MMMs.

Therefore, being able to shape microporous organic polymers into self-standing membranes is desirable, as this would provide the full potential of porous materials such as high surface areas and selectivities [35]. A promising support free method is electrospinning, which allows for a simple and inexpensive large-scale production of non-woven nanofibrous membranes [36]. Nanofiber membranes exhibit good mechanical stability and are expected to have low resistance during gas transport [36]. Due to the open structure of the fiber mats, macropores are introduced into the system, which can improve the gas transport towards the small pores. This hierarchical structuring is expected to result in rapid diffusion and equilibration kinetics of the ultra-microporous domains [37,38]. Recently, it was demonstrated, that it is possible to shape non-soluble polymers like polybisbenzimidazobenzophenanthroline-dione (BBB) into self-standing nanofibrous membranes via electrospinning [39]. For this, the auxiliary polymer polyvinylpyrrolidone (PVP) was dissolved in DMF together with two monomers 1,4,5,8-naphthalenetetracarboxylic acid (NTCA) and 3,3′-diaminobenzidine (DAB) and spun to a fibrous membrane. Subsequent heat treatment resulted in conversion of the monomers into BBB and removal of PVP by pyrolysis [39].

In this work, we extend this approach of electrospinning monomeric educts and convert them into self-standing membranes to porous organic polymers. The material class of POPs often feature large proportions of ultramicropores, which usually cannot be achieved with COFs due to their higher degree of translational order [26,40,41]. Whether the inherent nanoporosity of POPs is maintained with this synthesis strategy has not yet been addressed. Using the microporous organic polyimide (MOPI) NPI-I as a model compound, the potential of this method for nanoporous polymers was demonstrated. NPI-I is synthesized by condensation of tetrakis(4-aminophenyl)methane (TAPM) and naphthalene-1,4,5,8-tetracarboxylic dianhydride (NTDA) and exhibits a high CO_2 uptake of 12.3 wt%, a selectivity of 88.6 (CO_2/N_2, 0 °C) and, due to its fully aromatic structure, an excellent thermal stability (weight loss of 2.5% over 480 °C) [42]. The monomers were electrospun together with the auxiliary polymer PVP and polymerized via several heating steps. For comparison, bulk materials were prepared by conventional synthesis strategies with and without addition of PVP, respectively. The networks were fully characterized by multi-dimensional solid-state nuclear magnetic resonance (NMR) spectroscopy (^{1}H, ^{13}C, ^{15}N) and infrared (IR) spectroscopy, powder X-ray diffraction (PXRD), elemental analysis (CHN), thermogravimetric analysis (TGA) and scanning electron microscopy (SEM). Physisorption experiments were performed with argon, CO_2, CH_4 and N_2 to analyze the porosity, sorption capacities and selectivities of the corresponding gas mixtures.

2. Experimental section

2.1. Materials and methods

All chemicals were purchased at Sigma-Aldrich Chemistry GmbH, VWR Chemicals, TCI, Merck, Bernd Kraft, Grüssing, Carl Roth or abcr GmbH and were, if not mentioned otherwise, used without further purification (Table S1). *M*-cresol was freshly distilled over CaH_2 and stored under dry argon prior to use. The inert gas argon was dried over KOH and molecular sieves (3 Å) and residual O_2 was removed by a BTS-catalyst.

2.2. Synthesis

The amino-monomer was synthesized according to the literature [23]. The synthesis of the fiber mats as well as the bulk synthesis were adapted from our former work [23,38,39] and optimized to make bead-free fibers. A solution of 0.11 g PVP in 0.45 mL DMF was added to 0.10 g TAPM (0.26 mmol, 1 eq.) and 0.16 g NTCA (0.53 mmol, 2 eq.) in 0.99 mL DMF and stirred for 2 h at room temperature. Further 0.30 mL DMF were added. A house-made electrospinning machine was used for the preparation of all fiber mats using the same conditions. The applied voltage of 15 kV, a flow rate of 1.1 ml/h and the tip-to-collector distance of 20 cm was employed. The finally obtained **PIM_pre** was dried under vacuum at 40 °C for 6 h. More detailed information is given in the Supporting Information.

2.3. Techniques

Argon sorption measurements were carried out on a Quantachrome Autosorb-1 pore analyzer at 87 K. The data were analyzed using the ASIQ v 3.0 software package. For the Ar-based isotherms, the specific surface area was calculated with Brunauer-Emmet-Teller (BET) as well as with quasistationary density functional theory (QSDFT) kernels. The valid points for determining the BET surface area were calculated according to the method by Rouquerol et al. [43]. The choice of the QSDFT kernel (equilibrium mode) for slit pores in carbon-based materials depended on the calculated fitting error. CO_2, N_2 and CH_4 adsorption isotherms were measured on a Quantachrome Nova surface analyzer at 273, 298, and 313 K, respectively. The isosteric heat of adsorption was calculated using the CO_2 and CH_4 adsorption isotherms for these temperatures. For the CO_2 isotherms at 273 K, calculations of the specific surface areas, pore volumes and pore size distributions were derived using the nonlocal density functional theory (NLDFT) slit-pore model for carbon materials. Selectivities were calculated using the IAST method according to the literature [44,45]. For the calculations the IAST++ software of Lee et al. was used [45]. The polymers were degassed under vacuum (10^{-2} kPa) at 120 °C for 24 h before starting the adsorption experiments.

All solid-state NMR spectra were acquired on a Bruker Avance III HD spectrometer operating at a B_0 field of 9.4 T ($\nu_0(^{13}C)$ = 100.6 MHz, $\nu_0(^{15}N)$ = 40.6 MHz). ^{13}C and ^{15}N MAS spectra were obtained with ramped cross-polarization (CP) experiments where the $^{13}C/^{15}N$ nutation was set to 50/45 kHz and the ^{1}H nutation frequency ν_{nut} was varied linearly from 50 to 100% on average matching the Hartmann-Hahn conditions. The samples were spun at 12.5/10.0 kHz ($^{13}C/^{15}N$) in a 3.2 mm MAS triple resonance probe. The contact time was set to 3/5 ms ($^{13}C/^{15}N$). Proton broadband decoupling with spinal-64 and ν_{nut} = 70 kHz was applied during acquisition. The ^{13}C and ^{15}N NMR spectra were referenced with respect to TMS (tetramethylsilane) and CH_3NO_2 using the secondary standards adamantane and glycine. All ^{1}H NMR spectra were acquired on a Bruker Avance III HD spectrometer operating at a B_0 field of 14.1 T ($\nu_0(^{1}H)$ = 600.1 MHz) using a Bruker 1.3 mm double-resonance MAS probe with a spinning frequency of 62.5 kHz. High-resolution ^{1}H MAS single-pulse (SP) spectra were recorded after a 90° pulse of 1.3 μs with a recycle delay of 5.0–30.0 s. Double-quantum-
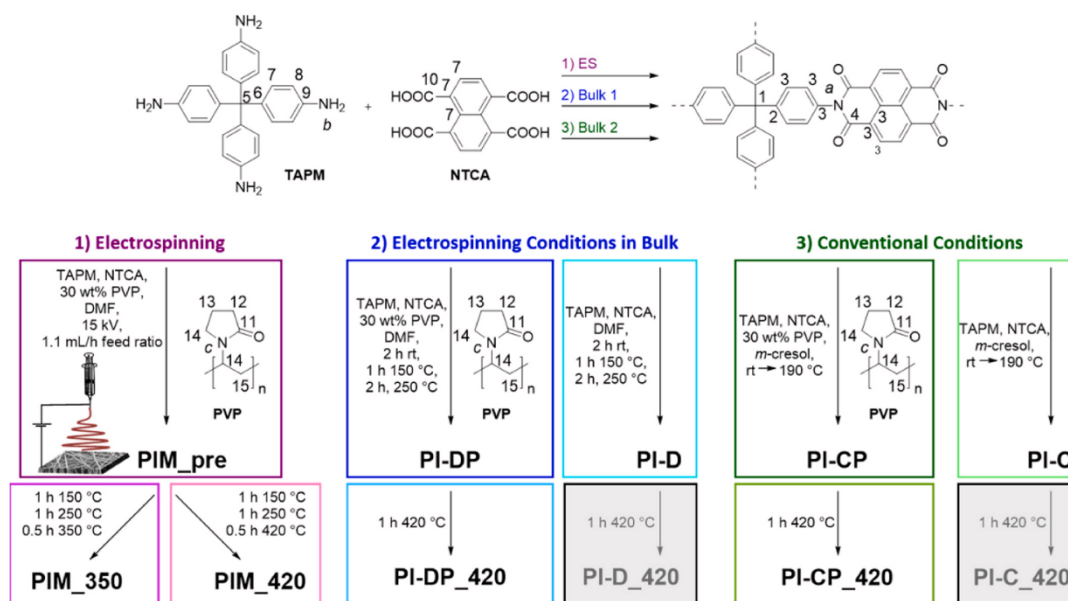
Fig. 1. Sketch of the reaction conditions for the reaction of tetrakis(4-aminophenyl)methane (TAPM) and naphthalene-1,4,5,8-tetracarboxylic acid (NTCA). The three arrows represent the three reaction routes: 1) Electrospinning (PIM series), 2) Bulk with electrospinning conditions (PI-D series) and 3) Bulk with conventional conditions (PI–C series). **PIM_pre** denotes PVP fibers spun with TAPM and NTCA.

single-quantum (DQ-SQ) ^1H–^1H correlation NMR spectra were acquired using the R12$_2$^{5} symmetry-based sequence with a 180° pulse as basic R-element and with DQ excitation and reconversion times of 64 μs [46]. ^1H NMR spectra are referenced indirectly with respect to tetramethylsilane (TMS) using adamantane as secondary reference.

For infrared spectra (IR) a JASCO FT/IR-6100 Fourier transform infrared spectrometer with an attenuated total reflectance (ATR) unit was used. CHNS analysis was carried out at a UNICUBE elementar with sulfanilamid as standard (C [41.85], H [4.68], N [16.27]). Thermogravimetric analysis (TGA) was carried out on a Mettler Toledo TGA/SDTA851 in a range of 30–1000 °C under N_2 atmosphere with a heating rate of 10 K/min. Powder X-ray diffraction (PXRD) measurements were performed on a PANalytical Empyrian diffractometer. Here, a region from 5 to 30° 2θ was measured with a 1/4 antiscatter slit and Cu K$_\alpha$ radiation (nickel filtered). Scanning electron microscopy (SEM) was measured with a scanning electron microscope, Zeiss (Oberkochen, Germany) LEO 1530 FESEM with an acceleration voltage of 3 kV. All samples were sputtered with platinum or platinum and carbon by a Cressington Sputter Coater 108.

3. Results and discussion

3.1. Synthesis

For the synthesis of a self-standing NPI-I fiber mat (Fig. 1, left), the two monomers tetrakis(4-aminophenyl)methane (TAPM) and naphthalene-1,4,5,8-tetracarboxylic acid (NTCA) were dissolved in DMF in the required stoichiometric ratio of 1:2 and a solution of polyvinylpyrrolidone (PVP) in DMF was added. A weight ratio of 70:30 (monomers:PVP) with an overall weight content of 18 wt% turned out to be optimal for the electrospinning conditions. The electrospun fiber mat (polyimide precursor membrane: **PIM_pre**) was heated in two steps, first to 150 °C for 1 h and then to 250 °C for 2 h, adjusted to the two-step polymerization process of polyimides [47]. PVP was removed

afterwards by pyrolysis under inert gas. Two pyrolysis temperatures were tested, either 350 °C for 0.5 h (**PIM_350**) or 420 °C for 0.5 h (**PIM_420**).

The first series of bulk syntheses (Fig. 1, middle) was adapted to the conditions of the electrospinning experiments. DMF solutions with the same weight content of monomers were heated to 150 °C (1 h) and 250 °C (2 h) with (**PI-DP**) and without addition of PVP (**PI-D**). Afterwards, **PI-DP** and **PI-D** were heated to 420 °C (**PI-DP_420, PI-D_420**). With this, it was possible to evaluate the influence of PVP and the pyrolysis conditions on the porosity of the systems.

As the electrospinning conditions differ strongly from the classical approach in terms of heating steps, temperature protocol, solvent and concentration, two additional networks **PI-C** and **PI-CP** were synthesized for comparison (Fig. 1, right) [25,38]. Both networks were synthesized in *m*-cresol, **PI-C** without and **PI-CP** with addition of PVP (weight ratio monomers:PVP is 70:30). After heating both samples to 420 °C the compounds **PI-CP_420** and **PI-C_420** were obtained. This series intends to reveal, if the significant lower educt concentrations used for the classical synthesis influence the detangling of PVP and thus the incorporation of the auxiliary polymer into the polyimide network.

3.2. Characterization

The ^{13}C and ^{15}N CP MAS as well as the IR spectra of **PIM_pre** (Fig. 2 and S11-S13) confirm the incorporation of the monomers (TAPM and NTCA) and PVP into the fibers of the mat. This is particularly evident in the ^{15}N CP MAS NMR spectra, exhibiting the typical peaks for the amide nitrogen of PVP at about −249 ppm and the amine nitrogen of TAPM at about −324 ppm [23,25,38,42]. In the ^{13}C CP MAS NMR spectra, the typical peaks for PVP at 176 and between 19 and 43 ppm were observed. The peaks of the monomers are apparent at 169 ppm for the carbonyl-C of NTCA and at 64 ppm for the quaternary carbon of TAPM [23,25,38, 42].

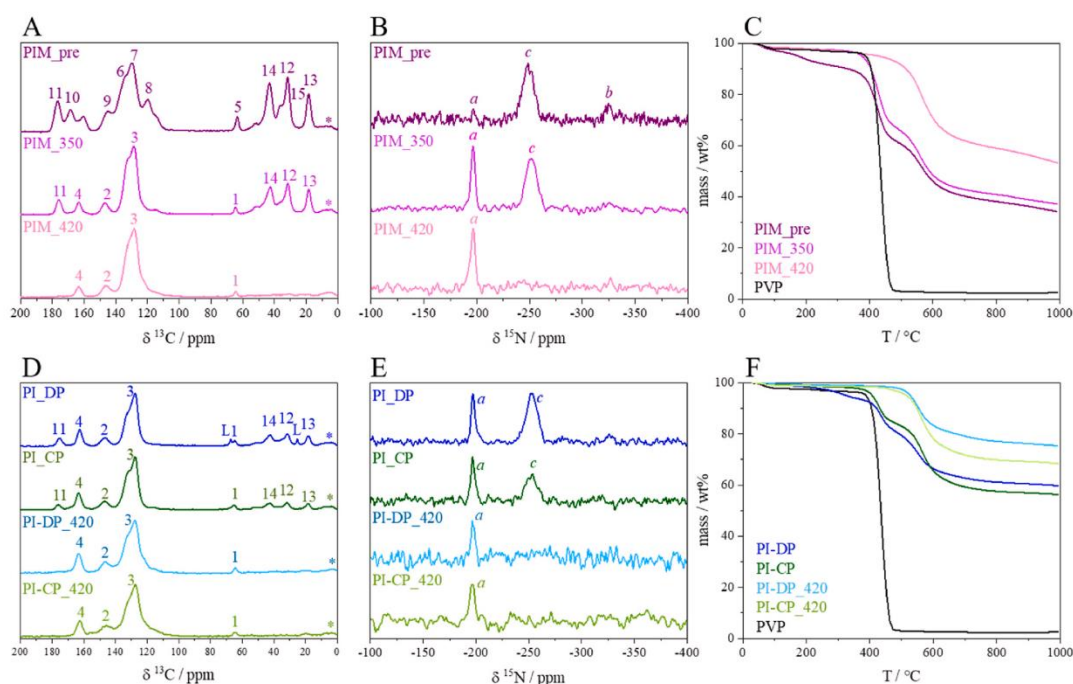For **PIM_350**, **PI-D**, **PI-DP**, **PI-C** and **PI-CP** the spectroscopic analysis

3

Fig. 2. ^{13}C and ^{15}N CP MAS NMR spectra of the electrospun (A and B) and the bulk polymers (D and E). TG analyses of the electrospun (C) and the bulk polymers (F).
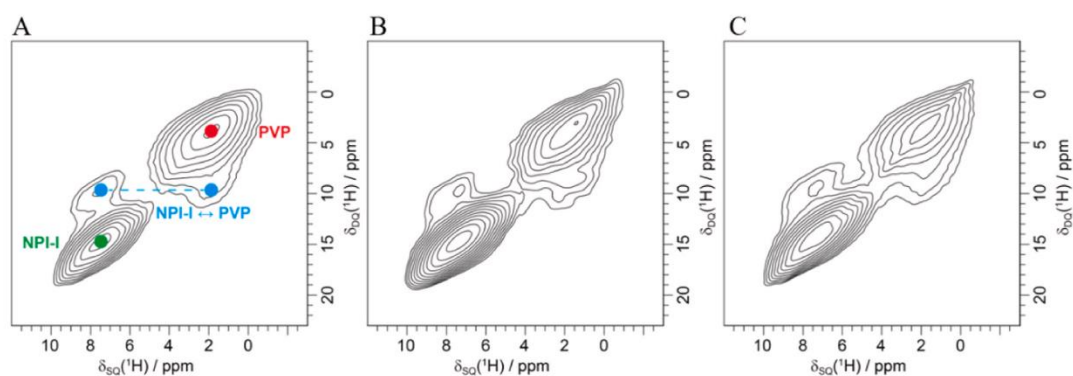

Fig. 3. ^{1}H DQ SQ MAS spectra of **PIM_350** (A), **PI-DP** (B) and **PI-CP** (D).

(Fig. 2 and Figs. S11-13) corroborates the successful conversion of the monomers TAPM and NTCA into the polyimide NPI-I. In the ^{15}N CP MAS NMR spectra, the typical imide resonance is prominent at −196 ppm, with essentially no amine resonance at −324 ppm left, which supports high cross-linking degrees >95%. Correspondingly, the imide formation is demonstrated by conversion of the carboxylic carbon of NTCA at 169 ppm to the carboxylic carbon of the imide function at 163 ppm. In **PIM_350**, **PI-DP** and **PI-CP** PVP is still present as the typical resonances indicate. The two components NPI-I and PVP are also nicely resolved within the high resolution ^{1}H MAS NMR spectra (Fig. S10) with typical resonances at 7.5 ppm and 1.9 ppm. Within the ^{1}H DQ-SQ spectra, in

addition to the expected self-correlation resonances (Fig. 3) for PVP ($\delta_{DQ} = 3.8$ ppm) and NPI-I ($\delta_{DQ} = 15.0$ ppm), a clear cross-correlation signal, at $\delta_{DQ} = 9.4$ ppm was observed. Thus, PVP is incorporated into the polyimide on an atomic scale, acting as template. After pyrolysis (**PIM_420**, **PI-CP_420**, **PI-DP_420**) the spectroscopic data (Fig. 2) demonstrate that PVP was successfully removed without degrading the polyimide networks [42].

These results agree with the TGA data. Samples measured before pyrolysis exhibit a prominent two step degradation process with turning points at ~430 °C and ~560 °C (Figs. 2 and S14), while the ones after pyrolysis feature a one-step degradation only. The latter matches the
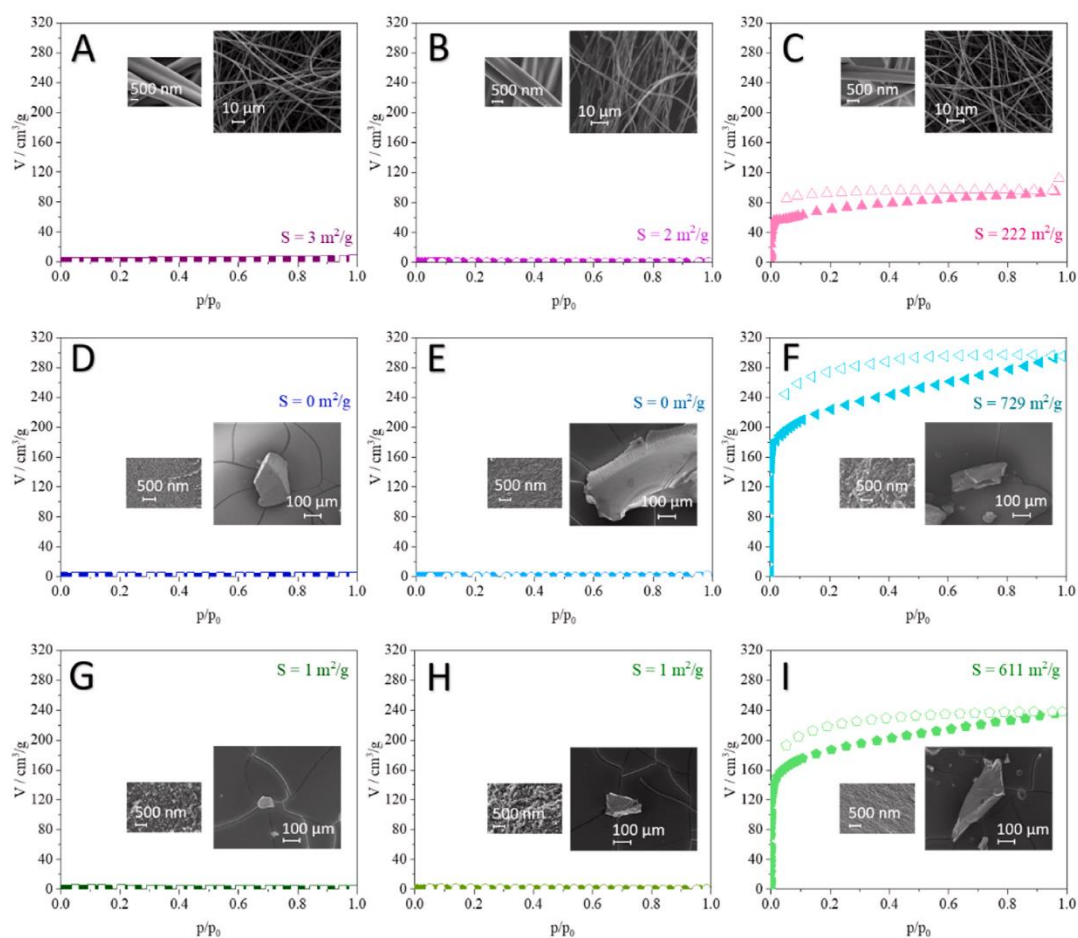
Fig. 4. Argon isotherms (A–I) measured at 87 K with the surface area calculated based on the BET equation (full symbols indicate adsorption isotherms, hollow symbols indicate the according desorption curve) and SEM images of **PIM_pre** (A), **PIM_350** (B), **PIM_420** (C), **PI-DP** (D), **PI-DP_420** (E), **PI-D** (F), **PI-CP** (G), **PI-CP_420** (H) and **PI-C** (I). It should be noted that due to the large difference in size of the particles between membrane and bulk, the magnification is chosen individually.

second mass loss step for the samples before pyrolysis and was thus assigned to the degradation of the polyimide itself. The first mass loss event is attributed to the removal of PVP. For the polymers after PVP removal the decomposition temperature (5% weight loss under N_2 atmosphere, Table S7) varies between 471 and 531 °C [39,42].

All polymers are amorphous according to the PXRD measurements (Fig. S15). The experimental data of the elemental analysis are in reasonably good agreement with the calculated values for a 100% conversion (Table S6). Except for **PIM_420**, the deviation between observed and calculated atomic percentages are less than 1.5% for H and N and less than 5% for C.

3.3. Morphology and porosity

Electrospinning of the monomer-PVP-solution yields fiber mats (**PIM_pre**) of twisted double–strand fibers with an average diameter of ~1.5 μm (Fig. 4A). Neither the thermal conversion into NPI-I (**PIM_350**, Fig. 4B) nor the removal of PVP by pyrolysis (**PIM_420**, Fig. 4C) effects

Table 1

Surface areas determined from argon and CO_2 isotherms and calculated by BET, QSDFT (slit pores, equilibrium mode) and NLDFT methods. A full representation of the pore size distributions and cumulative pore volumes is given in Figs. S16 and S18.

Polymer	S_{BET} (Ar@87 K)/ m²/g	S_{DFT} (Ar@87 K)/ m²/g	S_{DFT} (CO$_2$@273 K)/ m²/g
PIM_pre	3	2	211
PIM_350	2	1	324
PIM_420	222	269	678
PI-DP	0	1	518
PI-DP_420	0	0	403
PI-D	729	880	841
PI-CP	1	2	430
PI-CP_420	1	3	617
PI-C	611	714	728

5
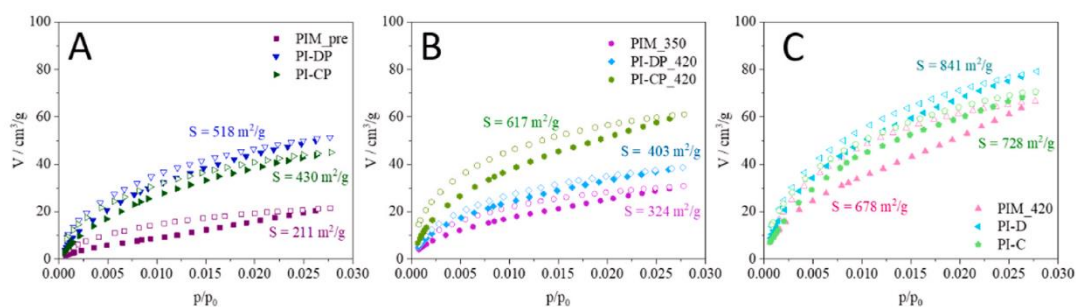
Fig. 5. CO_2 isotherms (A–C) measured at 273 K (surface areas calculated based on NLDFT with a slit-pore model for carbon materials). Full symbols indicate adsorption isotherms, hollow symbols indicate the according desorption curve.).

the morphology and texture of the strands significantly. The resulting fiber mats are not harmed by bending, rolling and twisting (Fig. S25), respectively, which shows a good mechanical stability and flexibility. While **PIM_pre** and **PIM_350** are unporous for argon, **PIM_420** regains microporosity with an apparent BET surface area of 222 m²/g (Fig. 4, Table 1) which is only roughly three times smaller compared to the reported value of NPI-I in the literature [42].

The materials from the bulk syntheses with PVP (**PI-DP** Fig. 4D, **PI-CP** Fig. 4G) and without PVP (**PI-D** Fig. 4F, **PI-C** Fig. 4I) exhibit a particular morphology with particle sizes on the order of hundreds of micrometers, consisting of agglomerated smaller particles on the order of tens of nanometer. All samples prepared with PVP are unporous with respect to argon even after pyrolysis. In contrast, for the reference experiments without PVP (**PI-D** and **PI-C**) surface areas between 610 and 720 m²/g (Fig. 4, Table 1) were observed matching the literature data [42].

3.4. CO_2 and CH_4 uptake and selectivity

Additionally, all samples exhibit a detectable surface area with CO_2 ranging from 211 to 829 m²/g (Fig. 5A–C, Table S9). In recent years it has been discovered that especially an ultramicroporous structure (pores <0.7 nm) and a very polar surface can increase the CO_2 adsorption drastically [19,20]. This phenomenon occurs due to the high quadrupole moment and the smaller size of CO_2 compared to other gases like argon, N_2 and CH_4 [21,23]. The values determined by CO_2 sorption for the surface areas might, therefore, be slightly overestimated as a result of

the strong interactions of CO_2 with polar groups such as amine, amide and imide groups (Figs. 2 and S13).

For the PIM series, the values of **PIM_pre** and **PIM_350** exhibit the lowest CO_2 surface areas. In contrast, **PIM_420**, with a surface area of 678 m²/g, is comparable to the reference polymers synthesized without PVP **PI-D** (841 m²/g) and **PI-C** (728 m²/g). For **PI-CP**, an increase in surface area from 430 to 617 m²/g is observed after removal of PVP by pyrolysis, while the opposite effect is observed for **PI-DP** (518 m²/g before, 403 m²/g after pyrolysis).

These observations suggest that PVP tends to have a negative effect, in particular, on the supermicro- and mesopore formation. Pore blocking by degradation components of PVP due to the pyrolysis is unlikely, as no residues in neither the ^{13}C nor the ^{15}N CP MAS NMR spectra were detected. Thus, PVP probably acts as a kind of pore filler for the microporous regions. This probably reduces the efficiency of the structure directing effect of the linkers leading to the microporosity of **PI-D** and **PI-C**. As a consequence, the created pore space collapses upon removal of PVP, leaving only the ultramicroporosity intact. This effect is more pronounced for the large particles of **PI-DP** and **PI-CP**. Here, even a small percentage of collapsed pores will cause a reduction in the length of the percolation pathways of gas molecules into the material. In case of the much thinner fibers of the membranes, on the other hand, significantly shorter paths are sufficient to achieve reliable gas absorption throughout the material.

This hypothesis is in agreement with the observed CO_2 surface areas for **PI-CP_420**, as it is comparable to **PIM_420** and **PI-C** and **PI-D** (synthesized without PVP) after annealing at 420 °C (Fig. S17). Therefore, it
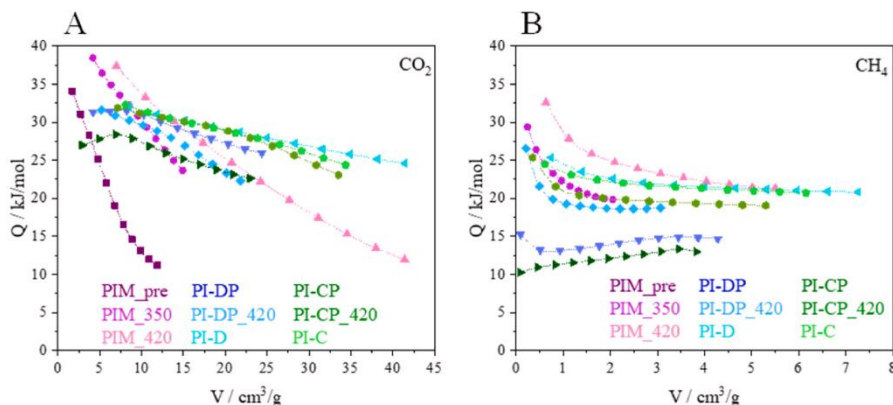

Fig. 6. Isosteric heats of adsorption for CO_2 (A) and CH_4 (B) calculated from adsorption isotherms at 273, 298, and 313 K. The dotted lines are guides for the eye.
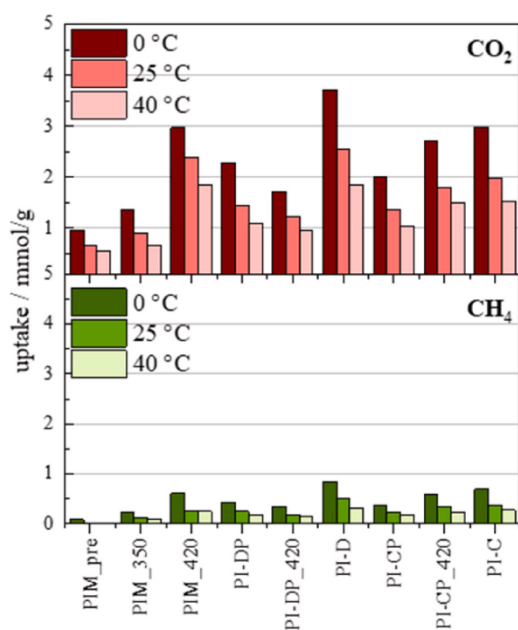
Fig. 7. Uptake values of the respective isotherms at p = 1 bar.

is likely that small pores are present but not accessible to argon due to the described collapse. CO_2 is able to resolve the small pores since the measurement temperature is 186 K higher, making the network more flexible and allowing CO_2 to reach the small pores [38].

For zero coverage strong physisorptive interactions were observed for **PIM_420**, **PI-DP_420, PI-CP_420, PI-D** and **PI-C** with values between 33 and 38 kJ/mol (Fig. 6). In particular, for **PIM_420** the adsorption enthalpies decline strongly with increasing CO_2 uptake down to 12 kJ/mol. This suggests a broader size distribution of the ultramicropores compared to **PI-D** and **PI-C**. The broader distribution of the ultra-micropores might well be caused by the higher concentrated solutions needed for electrospinning. Additionally, the solvent evaporates fast leading to a higher degree of structural disorder. This disorder, however, prevents a total pore collapse upon removal of PVP as dense packing is not possible.

The CO_2 uptakes (Fig. 7) of the PIM series at 0 °C increases from 1.0 mmol/g for **PIM_pre** to 3.0 mmol/g (13.1 wt%) for **PIM_420**. The latter value exceeds the literature one of 12.3 wt% and is comparable to the reference bulk materials **PI-D** and **PI-C** (3.5 and 3.2 mmol/g). Comparing the polymers after PVP removal with each other, **PIM_420**

achieves the best values. **PI-CP_420** exhibits a nearly comparable uptake of 2.7 mmol/g, while the uptake for **PI-DP_420** is reduced by ~40%. This shows, that the partial collapse of the micropores caused by PVP removal in the bulk syntheses also influences the ultramicropores but less pronounced.

Significantly lower uptake values were determined for the two gases N_2 and CH_4 (Fig. 7 bottom, Figs. S20 and S21 as well as Table S10). For N_2, typical for MOPIs, the observed values are very low, rendering the IAST analyses unreliable (Table S10) [23,48]. Nevertheless, they promise high CO_2/N_2 selectivities for separation applications (Table 2). For CH_4 a similar trend as for CO_2 is observed. The IAST analysis leads to selectivities for the separation of CH_4 and CO_2 between 8 and 34 apparently independent from the CO_2 content of the simulated gas feed mixture. Two concentrations one typical for natural gas sweetening (5:95) and gas mixtures in biogas plants (50:50) (Table 2) were simulated [49–51].

4. Conclusion

The possibility of shaping microporous organic polyimides (MOPIs) into non-woven, fibrous and self-standing membranes by electro-spinning was evaluated with the model compound NPI-I [42]. We succeeded, by introducing a three-step procedure (Fig. 1). In the first step, a solution of the linkers (TAPM and NTCA) and the auxiliary polymer PVP was electrospun into a precursor fiber mat. In the second step, the precursor mat was heated to polymerize TAPM and NTCA into the poly-imide NPI-I. In the third step, PVP was removed by pyrolysis. The NPI-I fiber mat exhibits a remarkable microporosity with a high amount of ultramicropores. Its CO_2 uptake of 3.0 mmol/g (0 °C, 1 bar) and its CO_2/CH_4 selectivity of about 20 (0 °C, 1 bar) even exceed the literature values for bulk NPI-I [42].

To investigate the influence of PVP on the properties of NPI-I, also bulk material with synthesis conditions either adapted to the ones of the electrospinning route or taken from a conventional route with or without the addition of PVP were synthesized [25,38]. If used, PVP was integrated into the NPI-I network on an atomic level, demonstrating that the auxiliary polymer acts as a molecular template during the syntheses. For this reason, all materials which still contain PVP are neither microporous nor mesoporous. Although the pyrolysis at 420 °C allowed to remove PVP, a pronounced micro- and mesoporosity was only observed for the electrospun membrane (**PIM_420**) with a surface area of 222 m^2/g (BET, Ar@87 K). This is attributed to a partial collapse of the micropore space, which has a stronger effect for the bulk materials. The ultramicroporosity remains almost unaffected.

In summary, we were able to shape a porous polyimide into a membrane retaining the excellent properties of the bulk polyimide. The presented three-step electrospinning approach will be promising for a broad variety of other systems based on linkers and the reticular syn-thesis concept. Being able to create self-supporting 1D, 2D and 3D ob-jects by electrospinning closes a gap for processing the usually non-soluble porous polymers and thus broadens their application potential in the future.

Table 2
CO2/N2 and CO2/CH4 selectivities at 1 bar calculated by IAST from the correspondent isotherms.

Polymer	CO_2/CH_4 5:95			CO_2/CH_4 50:50			CO_2/N_2 15:85		
	0 °C	25 °C	40 °C	0 °C	25 °C	40 °C	0 °C	25 °C	40 °C
PIM_pre	47	–	–	190	–	–	–	–	–
PIM_350	34	19	9	33	22	13	5E+8	–	–
PIM_420	22	17	8	23	19	11	1E+8		
PI-DP	18	15	8	9	30	5	1070	52	38
PI-DP_420	25	17	14	25	8	9	71	7074	21,020
PI-D	21	12	10	24	12	11	160	40	140
PI-CP	18	13	9	22	13	12	1E+4	5E+4	79
PI-CP_420	21	14	12	34	9	13	6443	–	–
PI-C	15	11	9	18	11	10	90	45	105

CRediT authorship contribution statement

Marion Breunig: Conceptualization, Data curation, Methodology, Formal analysis, Investigation, Visualization, Validation, Writing – review & editing. **Jian Zhu:** Data curation, Formal analysis. **Chenhui Ding:** Investigation, Writing – review & editing, Methodology, Visualization. **Renée Siegel:** Formal analysis, Investigation, Methodology, Validation, Writing – original draft. **Seema Agarwal:** Supervision, Funding acquisition, Conceptualization, Writing – review & editing. **Jürgen Senker:** Conceptualization, Funding acquisition, Supervision, Writing – review & editing.

Declaration of competing interest

The authors declare that they have no known competing financial interests or personal relationships that could have appeared to influence the work reported in this paper.

Appendix

Supporting Information with synthesis details, IR spectroscopy, CHN analysis, x-ray diffraction, nitrogen physisorption, heats of adsorption, IAST selectivity and details.

Appendix A. Supplementary data

Supplementary data to this article can be found online at https://doi.org/10.1016/j.micromeso.2021.111519.

References

[1] J.M. Vadillo, L. Gómez-Coma, A. Garea, A. Irabien, Energy Fuels 35 (2021) 111–136.
[2] S.-Y. Lee, S.-J. Park, J. Ind. Eng. Chem. 23 (2015) 1–11.
[3] D. Cebrucean, V. Cebrucean, I. Ionel, Energy Procedia 63 (2014) 18–26.
[4] A. Raza, R. Gholami, R. Rezaee, V. Rasouli, M. Rabiei, Petroleum 5 (2019) 335–340.
[5] H. Yang, Z. Xu, M. Fan, R. Gupta, R.B. Slimane, A.E. Bland, I. Wright, J. Environ. Sci. 20 (2008) 14–27.
[6] F. Russo, F. Galiano, A. Iulianelli, A. Basile, A. Figoli, Fuel Process. Technol. 213 (2021) 106643.
[7] R.M. Cuéllar-Franca, A. Azapagic, J. CO_2 Util. 9 (2015) 82–102.
[8] J. Liu, J. Baeyens, Y. Deng, T. Tan, H. Zhang, J. Environ. Manag. 260 (2020) 110054.
[9] M. Zaman, J.H. Lee, Kor. J. Chem. Eng. 30 (2013) 1497–1526.
[10] P. Markewitz, W. Kuckshinrichs, W. Leitner, J. Linssen, P. Zapp, R. Bongartz, A. Schreiber, T.E. Müller, Energy Environ. Sci. 5 (2012) 7281–7305.
[11] M. Bui, C.S. Adjiman, A. Bardow, E.J. Anthony, A. Boston, S. Brown, P.S. Fennell, S. Fuss, A. Galindo, L.A. Hackett, J.P. Hallett, H.J. Herzog, G. Jackson, J. Kemper, S. Krevor, G.C. Maitland, M. Matuszewski, I.S. Metcalfe, C. Petit, G. Puxty, J. Reimer, D.M. Reiner, E.S. Rubin, S.A. Scott, N. Shah, B. Smit, J.P.M. Trusler, P. Webley, J. Wilcox, N. Mac Dowell, Energy Environ. Sci. 11 (2018) 1062–1176.
[12] M. Ramdin, S.P. Balaji, J.M. Vicent-Luna, J.J. Gutiérrez-Sevillano, S. Calero, T. W. de Loos, T.J.H. Vlugt, J. Phys. Chem. C 118 (2014) 23599–23604.
[13] C. Chao, Y. Deng, R. Dewil, J. Baeyens, X. Fan, Renew. Sustain. Energy Rev. (2020) 110490.
[14] C. Ma, M. Wang, Z. Wang, M. Gao, J. Wang, J. CO_2 Util. 42 (2020) 101296.
[15] G. Ji, M. Zhao, Recent advances in carbon capture and storage, IntechOpen, 2016.
[16] R. Ben-Mansour, M.A. Habib, O.E. Bamidele, M. Basha, N.A.A. Qasem, A. Peedikakkal, T. Laoui, M. Ali, Appl. Energy 161 (2016) 225–255.
[17] R. Yuan, H. Ren, Z. Yan, A. Wang, G. Zhu, Polym. Chem. 5 (2014) 2266–2272.
[18] T.M. McDonald, W.R. Lee, J.A. Mason, B.M. Wiers, C.S. Hong, J.R. Long, J. Am. Chem. Soc. 134 (2012) 7056–7065.
[19] K. Wang, H. Huang, D. Liu, C. Wang, J. Li, C. Zhong, Environ. Sci. Technol. 50 (2016) 4869–4876.
[20] S. Wu, S. Gu, A. Zhang, G. Yu, Z. Wang, J. Jian, C. Pan, J. Mater. Chem. 3 (2015) 878–885.
[21] M. Thommes, K. Kaneko, A.V. Neimark, J.P. Olivier, F. Rodriguez-Reinoso, J. Rouquerol, K.S.W. Sing, Pure Appl. Chem. 87 (2015) 1051–1069.
[22] C. Shen, Z. Wang, J. Phys. Chem. C 118 (2014) 17585–17593.
[23] C. Klumpen, M. Breunig, T. Homburg, N. Stock, J. Senker, Chem. Mater. 28 (2016) 5461–5470.
[24] J. Yan, B. Zhang, Z. Wang, ACS Appl. Mater. Interfaces 10 (2018) 26618–26627.
[25] M.R. Liebl, J. Senker, Chem. Mater. 25 (2013) 970–980.
[26] S. Xiong, L. Li, L. Dong, J. Tang, G. Yu, C. Pan, J. CO2 Util. 41 (2020) 101224.
[27] H. Wang, Z. Zeng, P. Xu, L. Li, G. Zeng, R. Xiao, Z. Tang, D. Huang, L. Tang, C. Lai, D. Jiang, Y. Liu, H. Yi, L. Qin, S. Ye, X. Ren, W. Tang, Chem. Soc. Rev. 48 (2019) 488–516.
[28] J. Liu, G. Han, D. Zhao, K. Lu, J. Gao, T.-S. Chung, Sci. Adv. 6 (2020) 1110.
[29] T. Zhang, G. Xing, W. Chen, L. Chen, Mater. Chem. Front. 4 (2020) 332–353.
[30] Y. Cheng, L. Zhai, Y. Ying, Y. Wang, G. Liu, J. Dong, D.Z.L. Ng, S.A. Khan, D. Zhao, J. Mater. Chem. 7 (2019) 4549–4560.
[31] Z. Kang, Y. Peng, Y. Qian, D. Yuan, M.A. Addicoat, T. Heine, Z. Hu, L. Tee, Z. Guo, D. Zhao, Chem. Mater. 28 (2016) 1277–1285.
[32] Z. Wang, S. Zhang, Y. Chen, Z. Zhang, S. Ma, Chem. Soc. Rev. 49 (2020) 708–735.
[33] D. Hao, J. Zhang, H. Lu, W. Leng, R. Ge, X. Dai, Y. Gao, Chem. Commun. 50 (2014) 1462–1464.
[34] Y. Ying, D. Liu, J. Ma, M. Tong, W. Zhang, H. Huang, Q. Yang, C. Zhong, J. Mater. Chem. 4 (2016) 13444–13449.
[35] S. Yuan, X. Li, J. Zhu, G. Zhang, P. Van Puyvelde, B. Van der Bruggen, Chem. Soc. Rev. 48 (2019) 2665–2681.
[36] B. Ding, J. Yu, Electrospun nanofibers for energy and environmental applications, Springer Berlin Heidelberg, Berlin, Heidelberg, 2014.
[37] A.K. Mohammed, S. Usgaonkar, F. Kanheerampockil, S. Karak, A. Halder, M. Tharkar, M. Addicoat, T.G. Ajithkumar, R. Banerjee, J. Am. Chem. Soc. 142 (2020) 8252–8261.
[38] M. Breunig, M. Dorner, J. Senker, J. Mater. Chem. 9 (2021) 12797–12806.
[39] J. Zhu, Y. Ding, S. Agarwal, A. Greiner, H. Zhang, H. Hou, Nanoscale 9 (2017) 18169–18174.
[40] C. Klumpen, F. Radakovitsch, A. Jess, J. Senker, Molecules 22 (2017) 1343.
[41] C. Xu, N. Hedin, Mater. Today 17 (2014) 397–403.
[42] G. Li, Z. Wang, J. Phys. Chem. C 117 (2013) 24428–24437.
[43] J. Rouquerol, P. Llewellyn, F. Rouquerol, Is the bet equation applicable to microporous adsorbents? Stud. Surf. Sci. Catal. (2007) 49–56.
[44] H.O.R. Landa, D. Flockerzi, A. Seidel-Morgenstern, AIChE J. 59 (2013) 1263–1277.
[45] S. Lee, J.H. Lee, J. Kim, Kor. J. Chem. Eng. 35 (2018) 214–221.
[46] M.H. Levitt, Symmetry-based pulse sequences in magic-angle spinning solid-state NMR, in: Encycl. Magn. Reson., John Wiley & Sons, Ltd, Chichester, UK, 2007.
[47] R.L. Kaas, J. Polym, Sci. Polym. Chem. Ed. 19 (1981) 2255–2267.
[48] G. Li, Z. Wang, Macromolecules 46 (2013) 3058–3066.
[49] D.M. D'Alessandro, B. Smit, J.R. Long, Angew Chem. Int. Ed. Engl. 49 (2010) 6058–6082.
[50] T.E. Rufford, S. Smart, G.C.Y. Watson, B.F. Graham, J. Boxall, J.C. Diniz da Costa, E.F. May, J. Petrol. Sci. Eng. 94 (2012) 123–154.
[51] F. Falbo, A. Brunetti, G. Barbieri, E. Drioli, F. Tasselli, Appl. Petrochemical Res. 6 (2016) 439–450.

Supporting Information

For

Electrospun, non-woven fiber membranes of porous polyimides with high carbon dioxide uptakes and selectivities

Marion Breunig,[,a] Jian Zhu,[,b] Chenhui Ding,[b] Renée Siegel,[a] Seema Agarwal,[*b] Jürgen Senker[*a]

a. University of Bayreuth, Inorganic Chemistry III and Northern Bavarian NMR Centre(NBNC), Universitätsstraße 30, 95440 Bayreuth, Germany. E-mail: juergen.senker@uni-bayreuth.de

b. University of Bayreuth, Macromolecular Chemistry II and Bavarian Polymer Institute, Universitätsstraße 30, 95440 Bayreuth, Germany. E-mail: agarwal@uni-bayreuth.de

Content

152

152

153

1 Chemicals

Table S1. List of used chemicals, their purities and distributor.

Chemicals	Company	Purity
Acetic Acid	Sigma Aldrich	≥99.8 %
Acetic Anhydride	Sigma Aldrich	≥99 %
Amyl nitrite	Sigma Aldrich	96 %
Aniline	TCI Chemicals	≥98 %
Ethanol	Sigma Aldrich	≥99.8 %
Hydrazine monohydrate	Sigma Aldrich	98 %
Hydrochloric acid	Grüssing	37 %
Hypophosphorous acid	Sigma Aldrich	50 wt% in H_2O
Isoquinoline	Sigma Aldrich	97 %
m-Cresol	abcr	99 %
Methanol	VWR Chemicals	100 %
Methylene chloride	VWR Chemicals	99.8 %
Naphthalene-1,4,5,8-tetracarboxylic acid	Sigma Aldrich	97 %
Nitric acid	Merck	100 %
N,N-Dimethylformamide	Grüssing	99.5 %
Polyvinylpyrrolidone	Roth	purest
Raney®-Nickel	Sigma Aldrich	Slurry in H_2O
Sulfonic acid	Sigma Aldrich	97 %
Tetrahydrofuran	Bernd Kraft	99.5 %
Toluene	Sigma Aldrich	≥99.7 %
Triphenylmethyl chloride	Sigma Aldrich	97 %

S 1

153

2 Synthesis and Characterization of Monomer

2.1 Synthesis of Monomers
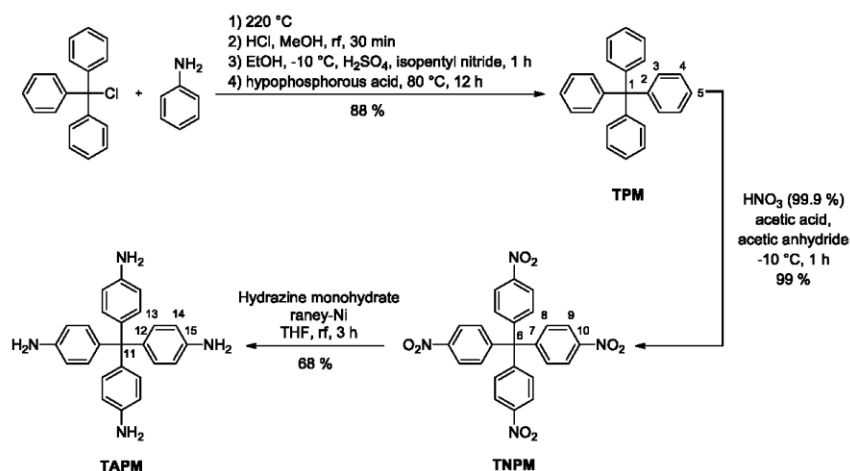
Fig. S1. Sketch of the three-step synthesis of the monomer tetrakis(4-aminophenyl)methane (TAPM).

All NMR- and IR-spectra are given in Fig. S2-S8.[1,2]

2.1.1 Tetraphenylmethane

A total amount of 5.00 g (17.93 mmol, 1 eq.) triphenylchloromethane was added to 4.42 mL (48.43 mmol, 2.7 eq.) aniline and stirred at 220 °C until the solution solidifies. The resulting solid was crushed and added to 20 mL of 2 M HCl and 20 mL of MeOH. After 30 min reflux the solid was filtrated and added to 200 mL of EtOH. The suspension was cooled to -10 °C and 5.4 mL (10.76 mmol, 0.6 eq.) of conc. H_2SO_4 and 3.62 mL (26.89 mmol, 1.5 eq.) of isopentylnitrite was added dropwise and stirred at -10 °C for one hour. At room temperature 8.82 mL (0.20 mol, 11.1 eq.) of hypophosphorous acid (50 %) was added to the solution and stirred at 50 °C for 24 h. The resulting solid was filtered, washed with EtOH, DMF and H_2O and dried *in vacuo*.

Tetraphenylmethane was observed as light brown solid. Yield: 5.03 g (15.70 mmol, 88 %). ^{1}H NMR (500 MHz, DMSO-d_6): δ = 7.14-7.16 (d, 8H, C_3-*H*), 7.19-7.22 (t, 4H, C_5-*H*), 7.29-7.32 (t, 8H, C_4-*H*) ppm. ^{13}C NMR (125 MHz, DMSO-d_6): δ = 64.94 (C-1), 126.46 (C-5), 128.21 (C-4), 130.96 (C-3), 146.86 (C-2) ppm. Anal. Found: C [94.83], H [7.30], N [0.15]. Calcd: C [93.71], H [6.29], N [0]. EI-MS [m/z] = 320. FT-IR (ATR): ν [cm⁻¹] = 3085, 3055, 3029, 3016, 1591, 1491, 1439.

S 2

154

2.1.2 Tetrakis(4-nitrophenyl)methane

To 24.5 mL HNO$_3$ (99.9 %) 4.50 mg (14.04 mmol, 1 eq.) tetraphenylmethane, 15.75 mL acetic acid and 7.56 mL acetic anhydride were added at -10 °C. After stirring the suspension for 1 h, 3.50 mL acetic acid were added and the solid was filtered. For purification, the product was recrystallized from DMF and dried *in vacuo*.

Tetrakis(4-nitrophenyl)methane was observed as yellow solid. Yield: 3.93 g (7.87 mmol, 56 %). ^{1}H NMR (500 MHz, DMSO-d$_6$): δ = 7.60-7.62 (d, 8H, C$_8$-*H*), 8.23-8.25 (d, 8H, C$_9$-*H*) ppm. ^{13}C NMR (125 MHz, DMSO-d$_6$): δ = 65.76 (C-6), 124.31 (C-9), 131.97 (C-8), 146.57 (C-10), 151.54 (C-7) ppm. Anal. Found: C [59.89], H [3.55], N [10.45]. Calcd: C [60.00], H [3.22], N [11.20]. EI-MS [m/z] = 500. FT-IR (ATR): ν [cm^{-1}] = 3108, 3077, 1510, 1330, 837.

2.1.3 Tetrakis(4-aminophenyl)methane

Under argon atmosphere 2.5 g (5.00 mmol, 1 eq.) tetrakis(4-nitrophenyl)methane were solved in 50 mL THF. A catalytic amount of Raney-nickel and 3.20 mL (66.45 mmol, 13.3 eq.) hydrazine-monohydrate were added and the solution was stirred for 2 h at rt. The reaction was stirred under reflux for 24 h, filtered and washed with THF. The solvent was removed under vacuum resulting in a white solid. For further purification the product was washed with DCM and dried *in vacuo*.

Tetrakis(4-aminophenyl)methane was observed as white solid. Yield: 1.28 g (3.37 mmol, 68 %). ^{1}H NMR (500 MHz, DMSO-d$_6$): δ = 4.85 (s, 8H, C$_{15}$-N*H$_2$*), 6.38-6.39 (d, 8H, C$_{14}$-*H*), 6.66-6.68 (d, 8H, C$_{13}$-*H*) ppm. ^{13}C NMR (125 MHz, DMSO-d$_6$): δ = 61.57 (C-11), 113.03 (C-14), 131.52 (C-13), 136.29 (C-12), 146.16 (C-15) ppm. Anal. Found: C [79.93], H [6.55], N [14.54]. Calcd: C [78.92], H [6.36], N [14.73]. EI-MS [m/z] = 380. FT-IR (ATR): ν [cm^{-1}] = 3165, 3062, 3025, 2994, 1610, 1273, 1172.

S 3

155

2.2 NMR Spectra of Monomers

Fig. S2. Liquid-state ^{1}H NMR spectra of TPM.

Fig. S3. Liquid-state ^{13}C NMR spectra of TPM.

S 4
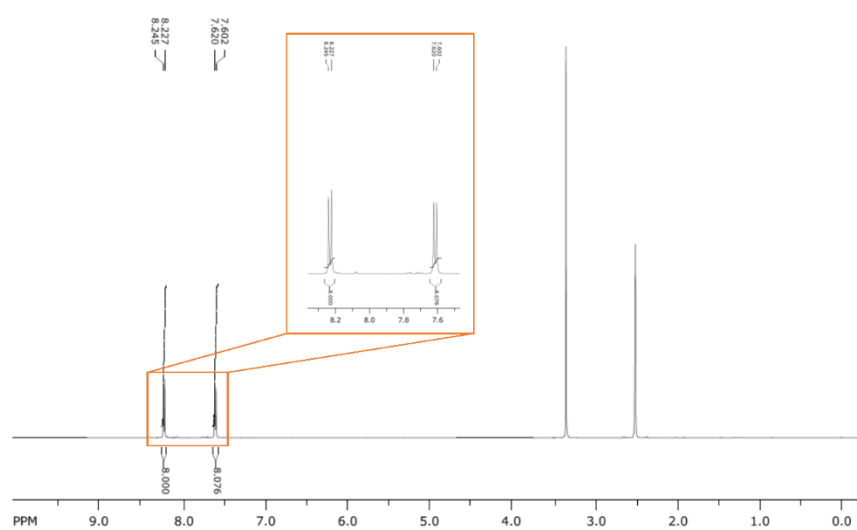
Fig. S4. Liquid-state ^{1}H NMR spectra of TNPM.
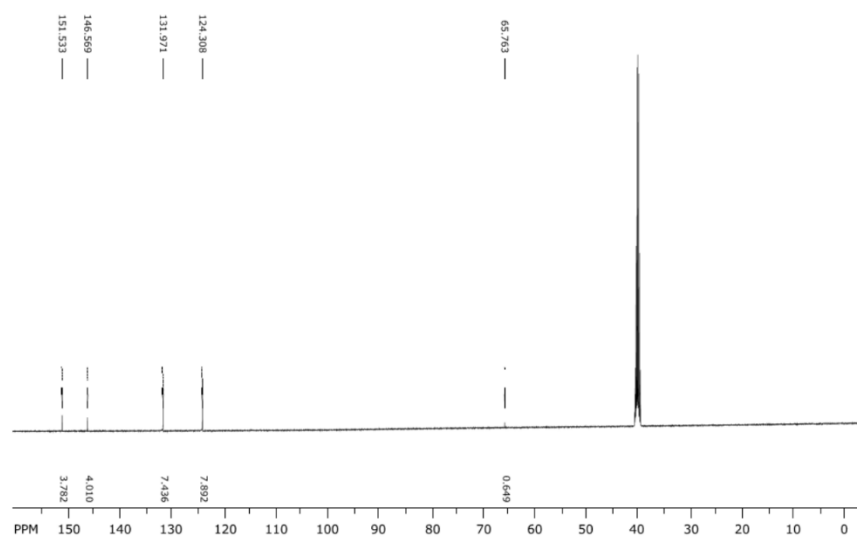
Fig. S5. Liquid-state ^{13}C NMR spectra of TNPM.

S 5

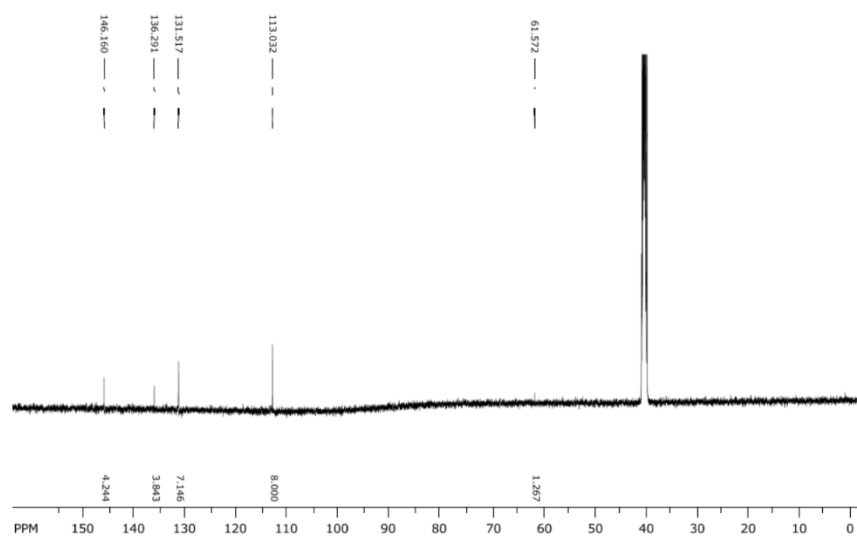157
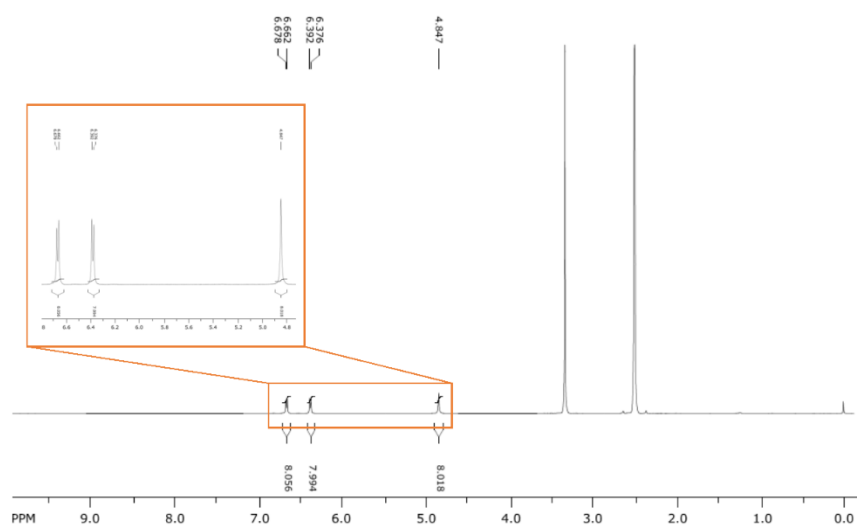
Fig. S6. Liquid-state ¹H NMR spectra of TAPM.

Fig. S7. Liquid-state ¹³C NMR spectra of TAPM.
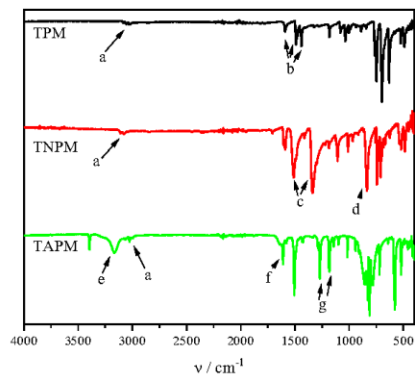
S 6

158

2.3 IR Spectra of Monomers

Fig. S8. FTIR spectra of the Monomers TPM (black), TNPM (red) and TAPM (green) measured at 450-4000 cm^{-1}. a: aromatic C-H stretching vibration, b: aromatic C=C stretching vibration, c: asymmetric (~1510 cm^{-1}) and symmetric (~1330 cm^{-1}) stretching vibration of aromatic -NO$_2$ group, d: aromatic -NO$_2$ deformation vibration, e: primary aromatic amine N-H stretching vibration, f: primary aromatic amine N-H deformation vibration, g: aromatic =C-N stretching vibration.

S 7

159

3 Synthesis of Polymers
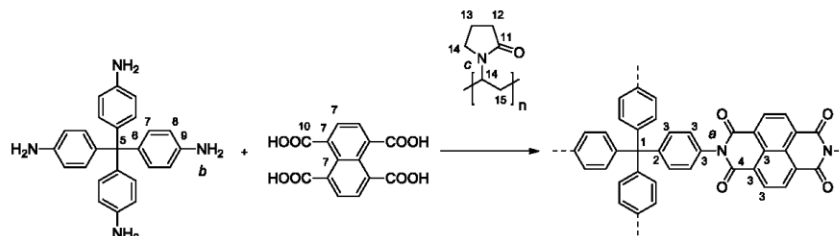
Fig. S.9. Sketch of the synthesis of all polymer series.

Table S2. Synthesis conditions of all polymers.

Name	Shape	PVP	Solvent	Name after heat treatment	
				350 °C	420 °C
PIM_pre	Fiber mat	30 wt%	DMF	PIM_350	PIM_420
PI-DP	Bulk	30 wt%	DMF		PI-DP_420
PI-D	Bulk	-	DMF		
PI-CP	Bulk	30 wt%	m-Cresol		PI-CP_420
PI-C	Bulk	-	m-Cresol		

3.1 Fiber mat

A solution of 0.11 g PVP in 0.45 mL DMF was added to 0.10 g TAPM (0.26 mmol, 1 eq.) and 0.16 g NTCA (0.53 mmol, 2 eq.) in 0.99 mL DMF and stirred for 2 h at room temperature. Further 0.30 mL DMF were added. A house-made electrospinning machine was used for the preparation of fiber mats. The applied voltage of 15 kV, a flow rate of 1.1 ml/h and the tip-to-collector distance of 20 cm was employed. The finally obtained PIM_pre was dried under vacuum at 40 °C for 6 h.

PIM_pre was observed as white fiber mat. ^{13}C NMR (CP-MAS, 12.5 kHz): δ [ppm] = 176 (C-11), 169 (C-10), 146 (C-9), 134 (C-6), 130 (C-7), 120 (C-8), 64 (C-5), 43 (C-14), 32 (C-12), 19 (C-13, C-15). ^{15}N NMR (CP-MAS, 5 kHz): δ [ppm] = -197 (-CO-N-CO-), -249 (-NH-CO-), -324 (-NH$_2$). Anal. Found: C [64.60], H [6.03], N [8.41]. Calcd: C [64.23], H [5.30], N [7.76]. FT-IR (ATR): ν [cm^{-1}] = 1714, 1670, 1593, 1505, 1437, 1780, 1735.

S 8

160

3.2 Bulk Polymer

3.2.1 PI-DP

A solution of 0.25 g PVP in 1.01 mL DMF was added to 0.23 g TAPM (0.59 mmol, 1 eq.) and 0.36 g NTCA (1.18 mmol, 2 eq.) in 2.23 mL DMF and stirred for 2 h at room temperature. Further 0.68 mL DMF were added and the solution was stirred for 1 h at 150 °C and 2 h at 250 °C. The solid was filtered and washed with toluene, dichloromethane and methanol and a Soxhlet extraction with tetrahydrofuran was used. The resulting polymer was dried in *vacuo* at 120 °C

PI-DP was observed as brown solid. Yield: 0.46 g, after subtraction of PVP: 0.34 g (0.41 mmol, 69 %). ^{13}C NMR (CP-MAS, 12.5 kHz): δ [ppm] = 175 (C-11), 163 (C-4), 147 (C-2), 128 (C-3), 65 (C-1), 43 (C-14), 32 (C-12), 18 (C-13). ^{15}N NMR (CP-MAS, 5 kHz): δ [ppm] = -197 (-CO-*N*-CO-), -253 (-*N*H-CO-), -327 (-*N*H$_2$). Anal. Found: C [70.48], H [4.20], N [7.84]. Calcd: C [72.20], H [4.45], N [8.42]. FT-IR (ATR): ν [cm^{-1}] = 1715, 1670, 1579, 1499, 1445, 1789, 1748.

3.2.2 PI-D

A solution of 0.10 g TAPM (0.26 mmol, 1 eq.) and 0.16 g NTCA (0.53 mmol, 2 eq.) in 1.78 mL DMF was stirred for 1 h at 150 °C and 2 h at 250 °C. The solid was filtered and washed with toluene, dichloromethane and methanol. For further purification a Soxhlet extraction with tetrahydrofuran was used and the resulting polymer was dried in *vacuo* at 120 °C

PI-D was observed as brown solid. Yield: 0.22 g (0.26 mmol, 98 %). ^{13}C NMR (CP-MAS, 12.5 kHz): δ [ppm] = 163 (C-4), 147 (C-2), 127 (C-3), 65 (C-1). ^{15}N NMR (CP-MAS, 5 kHz): δ [ppm] = -197 (-CO-*N*-CO-). Anal. Found: C [71.90], H [3.21], N [6.16]. Calcd: C [75.35], H [2.86], N [6.63]. FT-IR (ATR): ν [cm^{-1}] = 1714, 1670, 1579, 1503, 1445, 1787, 1748.

3.2.3 PI-CP

A total amount of 0.23 mg TAPM (0.59 mmol, 1 eq.), 0.36 mg NTCA (1.18 mmol, 2 eq.) and 0.25 g PVP were added to 48 mL of *m*-cresol under argon atmosphere. The mixture was stirred for 24 h at 0 °C. Afterwards, a catalytic amount ($\approx$ 1 mg) of isoquinoline was added and the mixture was again stirred for 24 h at room temperature. The polymerization reaction was carried out according to the following temperature protocol: 40 °C for 4 h, 60 °C for 4 h, 80 °C for 6 h, 100 °C for 6 h, 120 °C for 8 h, 140 °C for 8 h, 160 °C for 18 h, 190 °C for 24 h. After cooling down to room temperature, the resulting solid was filtered and washed with toluene,

dichloromethane, and methanol. Additional purification was achieved by extraction in a Soxhlet apparatus with tetrahydrofuran overnight. The product was dried in *vacuo* at 120 °C.

PI-CP was observed as black solid. Yield: 0.57 g, after subtraction of PVP: 0.32 g (0.38 mmol, 63 %). ^{13}C NMR (CP-MAS, 12.5 kHz): δ [ppm] = 176 (C-11), 163 (C-4), 147 (C-2), 128 (C-3), 65 (C-1), 43 (C-14), 31 (C-12), 19 (C-13). ^{15}N NMR (CP-MAS, 5 kHz): δ [ppm] = -197 (-CO-*N*-CO-), -253 (-*N*H-CO-). Anal. Found: C [70.43], H [4.24], N [6.92]. Calcd: C [72.20], H [4.45], N [8.42]. FT-IR (ATR): ν [cm^{-1}] =1717, 1671, 1578, 1497, 1443, 1790, 1747.

3.2.4 PI-C

A total amount of 0.10 mg of TAPM (0.26 mmol, 1 eq.) and 0.16 mg NTCA (0.53 mmol, 2 eq.) were added to 21 mL of *m*-cresol under argon atmosphere. The mixture was stirred for 24 h at 0 °C. Afterwards, a catalytic amount (≈ 1 mg) of isoquinoline was added and the mixture was again stirred for 24 h at room temperature. The polymerization reaction was carried out according to the following temperature protocol: 40 °C for 4 h, 60 °C for 4 h, 80 °C for 6 h, 100 °C for 6 h, 120 °C for 8 h, 140 °C for 8 h, 160 °C for 18 h, 190 °C for 24 h. After cooling down to room temperature, the resulting solid was filtered and washed with toluene, dichloromethane, and methanol. Additional purification was achieved by extraction in a Soxhlet apparatus with tetrahydrofuran overnight. The product was dried in *vacuo* at 120 °C.

PI-C was observed as brown solid. Yield: 0.22 g (0.25 mmol, 96 %). ^{13}C NMR (CP-MAS, 12.5 kHz): δ [ppm] = 163 (C-4), 147 (C-2), 127 (C-3), 65 (C-1). ^{15}N NMR (CP-MAS, 5 kHz): δ [ppm] = -197 (-CO-*N*-CO-). Anal. Found: C [71.66], H [3.13], N [5.31]. Calcd: C [75.35], H [2.86], N [6.63]. FT-IR (ATR): ν [cm^{-1}] = 1715, 1671, 1578, 1501, 1445, 1790, 1751.

3.3 Heating Procedure

For all polymers and fibers with PVP as an addition the following heating procedure was carried out to obtain a self-standing material of polyimide. The samples were heated to 350 °C (PIM_350) or 420 °C (PIM_420, PI-DP_420, PI-CP_420) for 1 h under argon.

PIM_350 was observed as yellow fiber mat. ^{13}C NMR (CP-MAS, 12.5 kHz): δ [ppm] = 176 (C-11), 163 (C-4), 147 (C-2), 129 (C-3), 65 (C-1), 43 (C-14), 32 (C-12), 18 (C-13). ^{15}N NMR (CP-MAS, 5 kHz): δ [ppm] = -197 (-CO-*N*-CO-), -251 (-*N*H-CO-). Anal. Found: C [67.42], H [3.82], N [7.51]. Calcd: C [72.20], H [4.45], N [7.76]. FT-IR (ATR): ν [cm^{-1}] = 1741, 1670, 1593, 1505, 1437, 1780, 1735.

PIM_420 was observed as brown fiber mat. ^{13}C NMR (CP-MAS, 12.5 kHz): δ [ppm] = 163 (C-4), 146 (C-2), 129 (C-3), 65 (C-1). ^{15}N NMR (CP-MAS, 5 kHz): δ [ppm] = -196

S 10

162

(-CO-*N*-CO-). Anal. Found: C [67.33], H [3.41], N [7.01]. Calcd: C [75.35], H [2.86], N [6.63]. FT-IR (ATR): ν [cm^{-1}] = 1717, 1673, 1583, 1505, 1447.

PI-DP_420 was observed as black solid. ^{13}C NMR (CP-MAS, 12.5 kHz): δ [ppm] = 147 (C-2), 164 (C-4), 128 (C-3), 64 (C-1). ^{15}N NMR (CP-MAS, 5 kHz): δ [ppm] = -197 (-CO-*N*-CO-). Anal. Found: C [71.15], H [3.98], N [6.87]. Calcd: C [75.35], H [2.86], N [6.63]. FT-IR (ATR): ν [cm^{-1}] = 1710, 1666, 1578, 1501, 1445.

PI-CP_420 was observed as black solid. ^{13}C NMR (CP-MAS, 12.5 kHz): δ [ppm] = 163 (C-4), 146 (C-2), 127 (C-3), 65 (C-1). ^{15}N NMR (CP-MAS, 5 kHz): δ [ppm] = -196 (-CO-*N*-CO-). Anal. Found: C [75.54], H [3.41], N [6.47]. Calcd: C [75.35], H [2.86], N [6.63]. FT-IR (ATR): ν [cm^{-1}] = 1710, 1666, 1575, 1499, 1448.

S 11

4 NMR- and IR-Spectra

4.1 ^{1}H MAS NMR Spectra
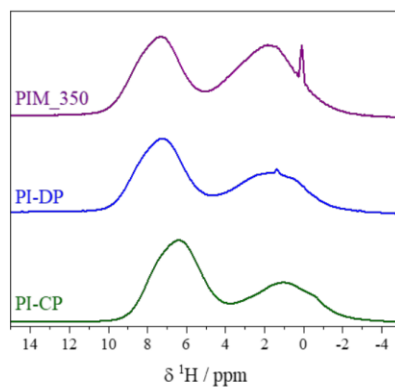
Fig. S10. ^{1}H MAS NMR spectra for PIM_350, PI-DP and PI-CP.

4.2 ^{13}C CP MAS NMR Spectra

Table S3. Assignment of ^{13}C NMR shifts (All values are given in ppm).

Polymer	1	2	3	4	5	6	7	8	9	10	11	12	13	14	15
PIM_pre	-	-	-	-	64	134	130	120	146	169	176	32	19	43	19
PIM_350	65	147	129	163	-	-	-	-	-	-	176	32	18	43	-
PIM_420	65	146	129	163	-	-	-	-	-	-	-	-	-	-	-
PI-DP	65	147	128	163	-	-	-	-	-	-	175	32	18	43	-
PI-DP_420	64	147	128	164	-	-	-	-	-	-	-	-	-	-	-
PI-D	65	147	127	163	-	-	-	-	-	-	-	-	-	-	-
PI-CP	65	147	128	163	-	-	-	-	-	-	176	31	19	43	-
PI-CP_420	65	146	127	163	-	-	-	-	-	-	-	-	-	-	-
PI-C	65	147	128	163	-	-	-	-	-	-	-	-	-	-	-

S 12

164
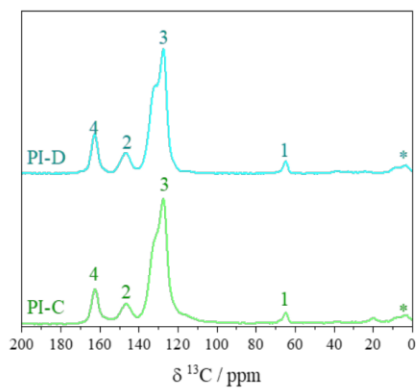
Fig. S11. ^{13}C CP MAS NMR spectra for PI-D and PI-C. The asterisks mark spinning side bands.

4.3 ^{15}N CP MAS NMR Spectra

Table S4. Assignment of ^{15}N NMR shifts (All values are given in ppm).

Polymer	a	b	c
PIM_pre	-197	-324	-249
PIM_350	-197	-	-251
PIM_420	-196	-	-
PI-DP	-197	-327	-253
PI-DP_420	-197	-	-
PI-D	-197	-	-
PI-CP	-197	-	-253
PI-CP_420	-196	-	-
PI-C	-197	-	-
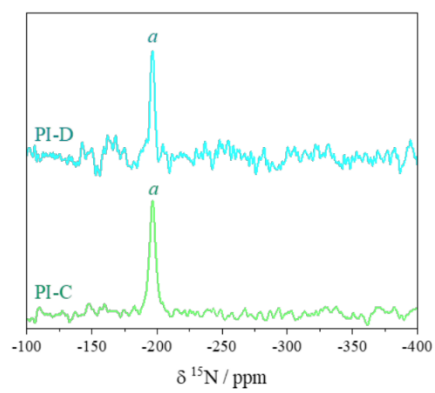
Fig. S12. ^{15}N CP MAS NMR spectra for PI-D and PI-C.

S 14
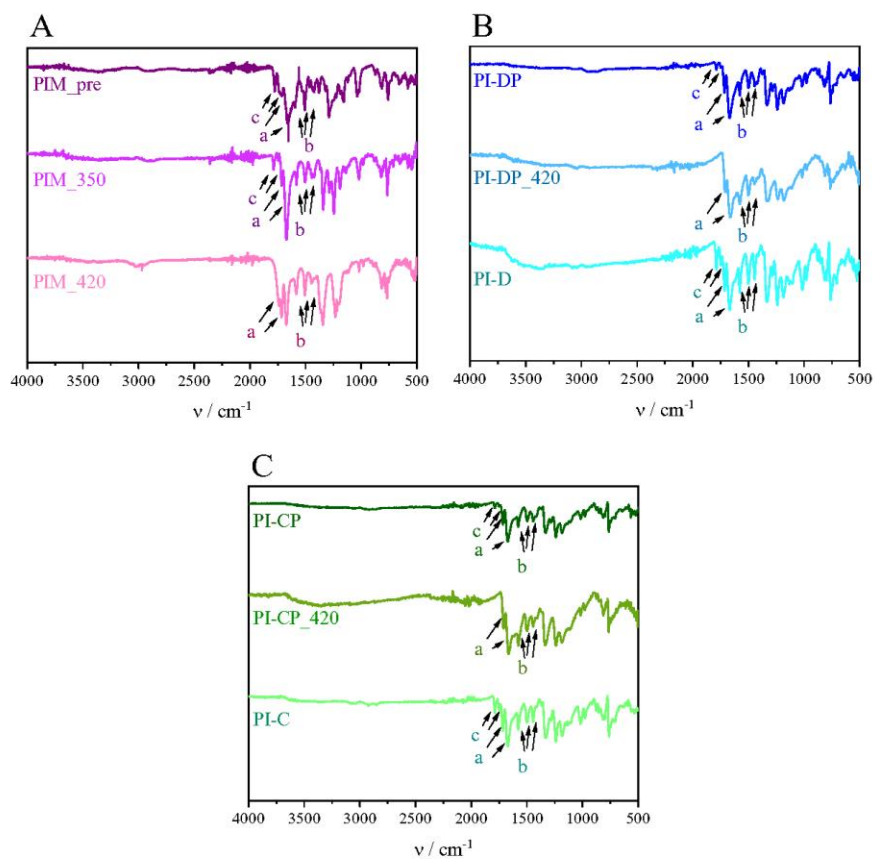
4.4 IR Spectra

Fig. S13. FTIR spectra of the PIM (A), the PI-D (B) and the PI-C (C) series (450-4000 cm⁻¹). a: imide six- and five-membered ring, b: aromatic C=C stretching vibration, c: C=O stretching vibration for saturated six membered ring acid anhydrides.

S 15

167

Table S5. Assignment of IR signals (All values are given in cm^{-1}). a: imide six- and five-membered ring, b: aromatic C=C stretching vibration, c: C=O stretching vibration for saturated six membered ring acid anhydrides.

Polymer	a		b			c	
PIM_pre	1714	1670	1593	1505	1437	1780	1735
PIM_350	1715	1672	1582	1505	1447	1789	1748
PIM_420	1717	1673	1583	1505	1447	-	-
PI-DP	1715	1670	1579	1499	1445	1789	1748
PI-DP_420	1710	1666	1578	1501	1445	-	-
PI-D	1714	1670	1579	1503	1445	1787	1748
PI-CP	1717	1671	1578	1497	1443	1790	1747
PI-CP_420	1710	1666	1575	1499	1448	-	-
PI-C	1715	1671	1578	1501	1445	1790	1751

5 Elemental Analysis

Table S6. Experimental data, theoretical data and the calculated deviation of CHN analysis. Red marks high deviations. PIM_pre was calculated with 27 wt% TAPM, 43 wt% NTCA and 30 wt% PVP. PIM_350, PI-DP and PI-CP are calculated with a ratio of 30/70 (PVP/PI).

	Exp.			Theo.			Deviation		
Polymer	C / %	H / %	N / %	C / %	H / %	N / %	C / %	H / %	N / %
PIM_pre	64.60	6.03	8.41	64.23	5.30	7.76	0.07	0.73	0.65
PIM_350	67.42	3.82	7.51	72.20	4.45	8.42	4.78	0.63	0.91
PIM_420	67.33	3.41	7.01	75.35	2.86	6.63	8.02	0.55	0.38
PI-DP	70.48	4.20	7.84	72.20	4.45	8.42	1.72	0.25	0.58
PI-DP_420	71.15	3.98	6.87	75.35	2.86	6.63	4.20	1.12	0.24
PI-D	71.90	3.21	6.16	75.35	2.86	6.63	3.45	0.35	0.47
PI-CP	70.43	4.24	6.92	72.20	4.45	8.42	1.77	0.21	1.50
PI-CP_420	75.54	3.41	6.47	75.35	2.86	6.63	0.19	0.55	0.16
PI-C	71.66	3.13	5.31	75.35	2.86	6.63	3.69	0.27	1.32

S 16

168

6 TGA patterns

Table S7. Temperature at which 5 wt% mass loss occurs detected from TGA for all polymers.

Polymer	$T_{-5wt\%}$ / °C
PIM_pre	250
PIM_350	390
PIM_420	471
PI-DP	346
PI-DP_420	531
PI-D	445
PI-CP	413
PI-CP_420	524
PI-C	483
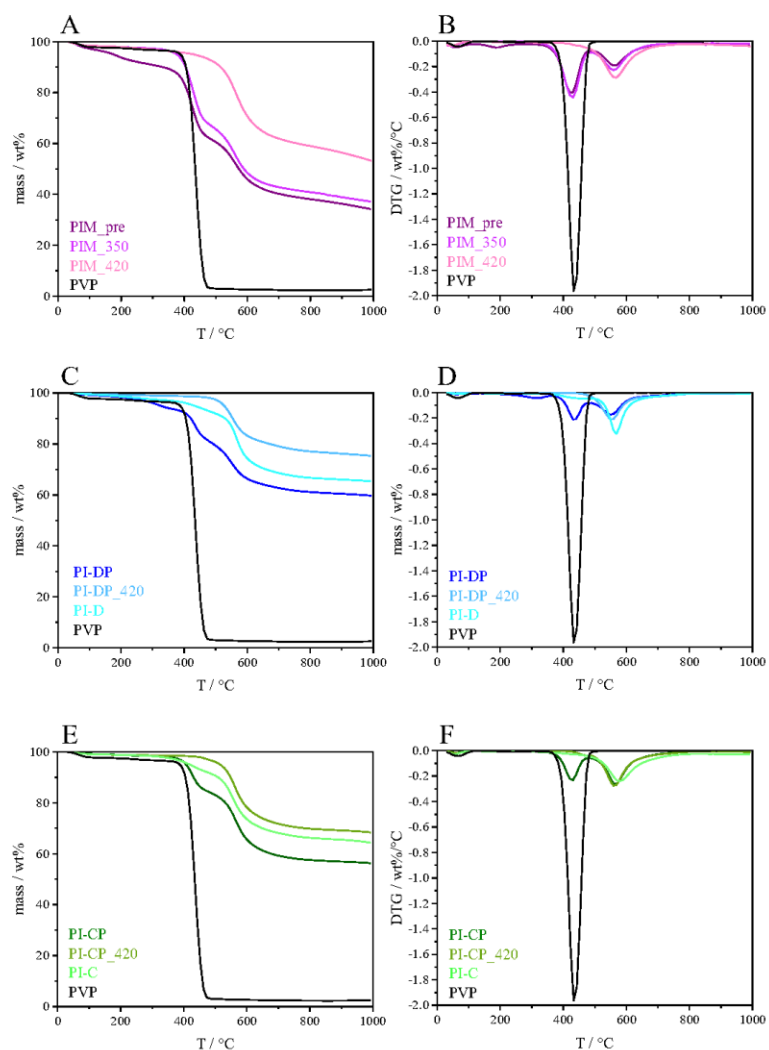
Fig. S14. Thermogravimetric analysis of the PIM_pre (A), PI-D (C) and PI-C (E) series (30-1000 °C, 10 K/min, under N_2). Derivation of the thermogravimetric analysis according to temperature of the corresponding series (B, D, F) (30-1000 °C, 10 K/min, under N_2).

S 18

7 Powder X-ray diffraction
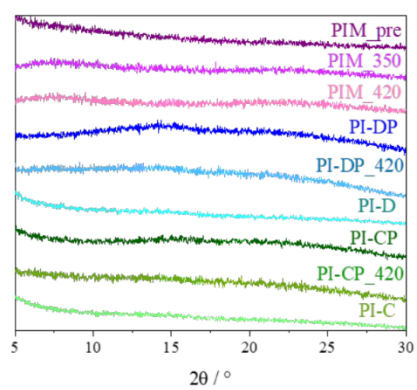
Fig. S15. Powder x-ray diffraction pattern of all materials (5-30 °2θ, Cu-K$_\alpha$).

S 19

8   Physisorption

8.1   Argon isotherms

Table S 8: pore volumes determined from argon isotherms and calculated by QSDFT (slit pores, equilibrium mode) method.
A full representation of the pore size distributions and cumulative pore volumes is given in Fig. S16.

Polymer	$V_{pore,tot}$ / cm^3/g	$V_{pore,mic}$ / cm^3/g	$V_{pore,mic}$ / $V_{pore,tot}$
PIM_pre	-	-	-
PIM_350	-	-	-
PIM_420	0.121	0.121	1
PI-DP	-	-	-
PI-DP_420	-	-	-
PI-D	0.370	0.356	0.96
PI-CP	-	-	-
PI-CP_420	-	-	-
PI-C	0.295	0.285	0.97

S 20

172
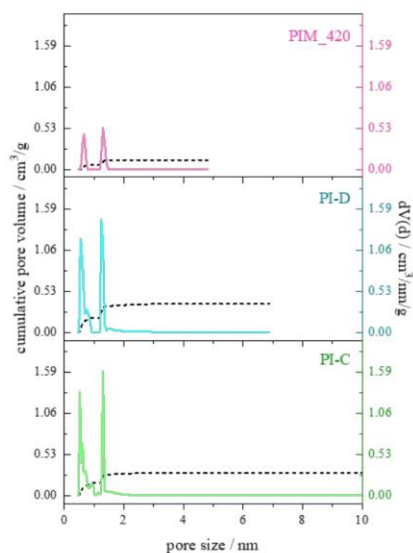
Fig. S16. Pore size distributions of PIM_420, PI-D and PI-C calculated by QSDFT kernel (equilibrium mode) for slit pores in carbon based materials.
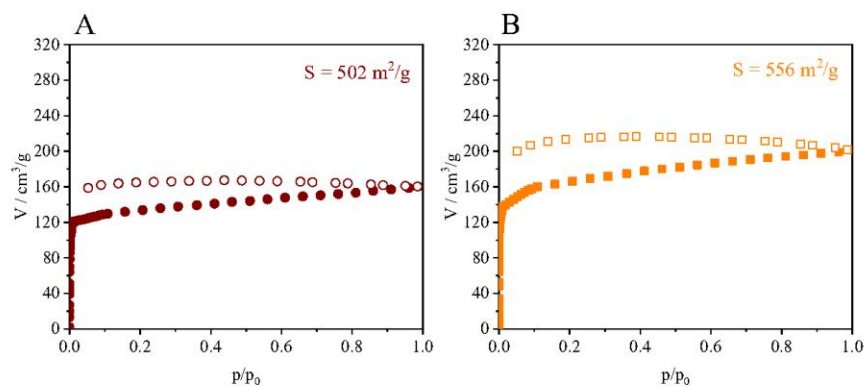
Fig. S17. Argon isotherms of PI-D_420 (A) and PI-C_420 (B) measured at 87 K. Full symbols characterize adsorption isotherms, hollow symbols the corresponding desorption curve

S 21

173

8.2 CO₂ isotherms

Table S9. Pore volume determined from CO_2 Isotherms and calculated by NLDFT method. A full representation of the pore size distributions and cumulative pore volumes is given in Fig. S18.

Polymer	V_{pore} / cm³/g
PIM_pre	0.072
PIM_350	0.102
PIM_420	0.220
PI-DP	0.154
PI-DP_420	0.120
PI-D	0.249
PI-CP	0.123
PI-CP_420	0.179
PI-C	0.220
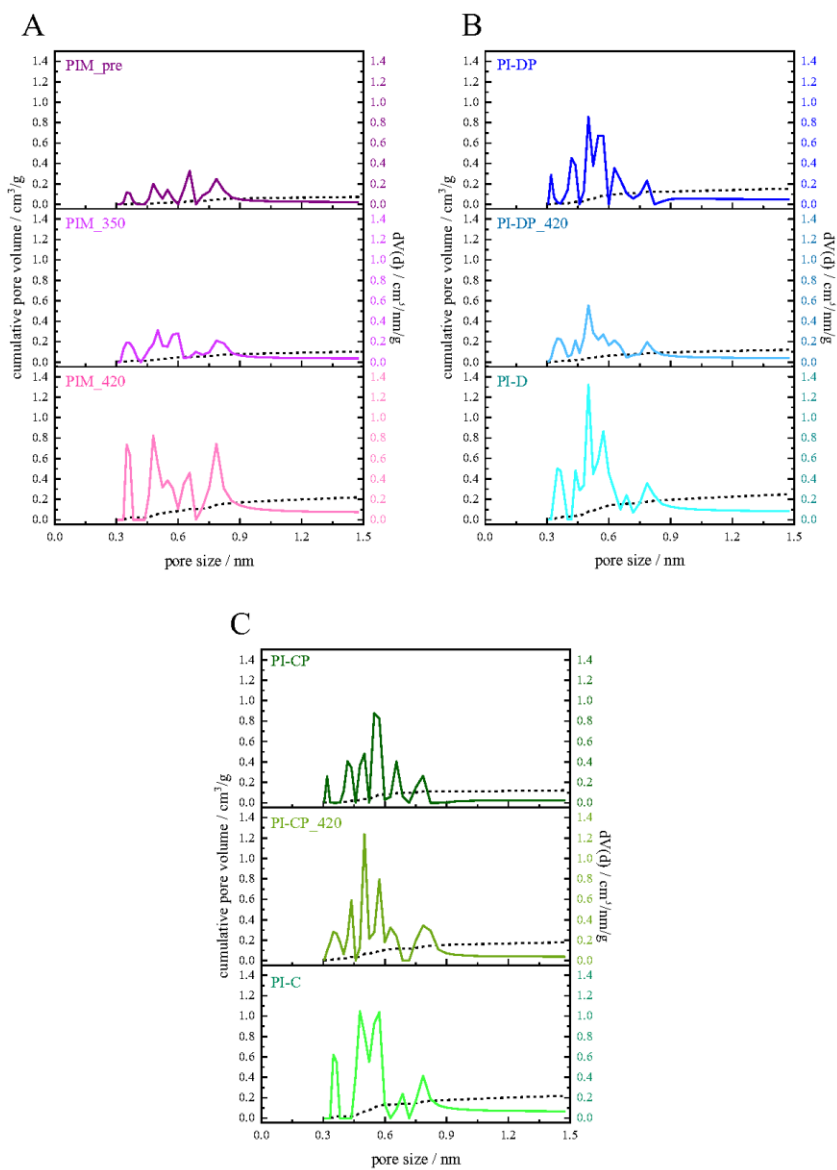
Fig. S18. Pore size distributions of the PIM (A). the PI-D (B) and the PI-C (C) series calculated by NLDFT kernel for slit pores in carbon-based materials.

S 23

8.3 CO₂, N₂, CH₄ isotherms as function of temperature
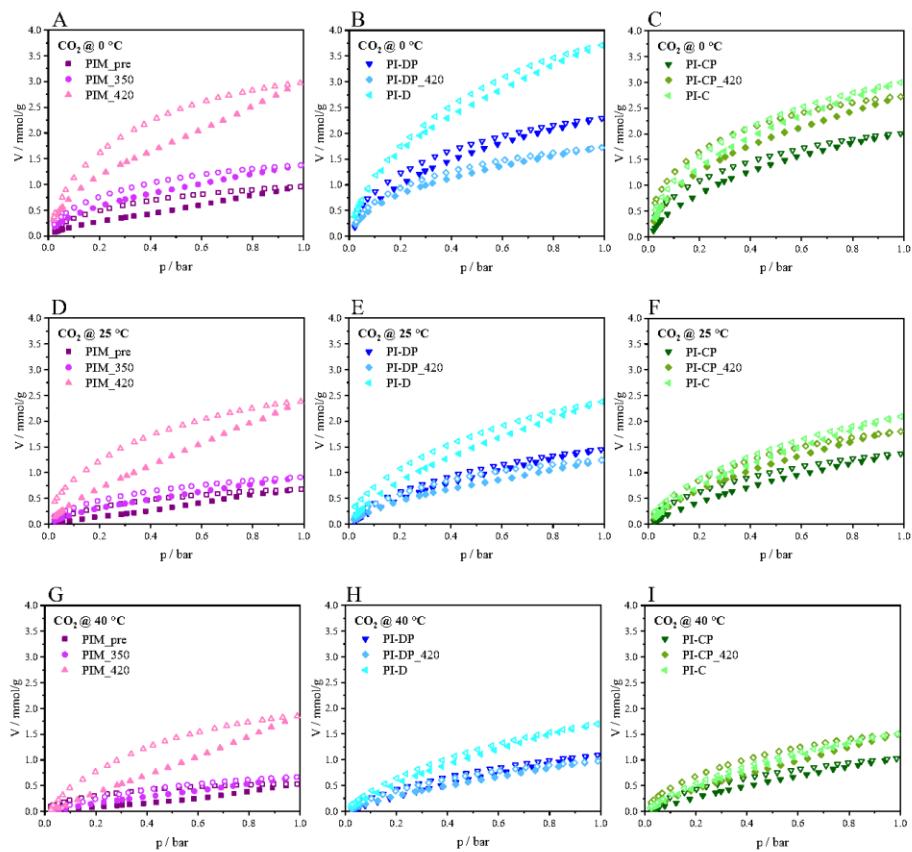
Fig. S19. CO₂ isotherms measured at 0 °C (A-C), 25 °C (D-F) and 40 °C (G-I) and 1 bar for the PIM (A, D, G), the PI-D (B, E, H) and the PI-C series (C, F, I).
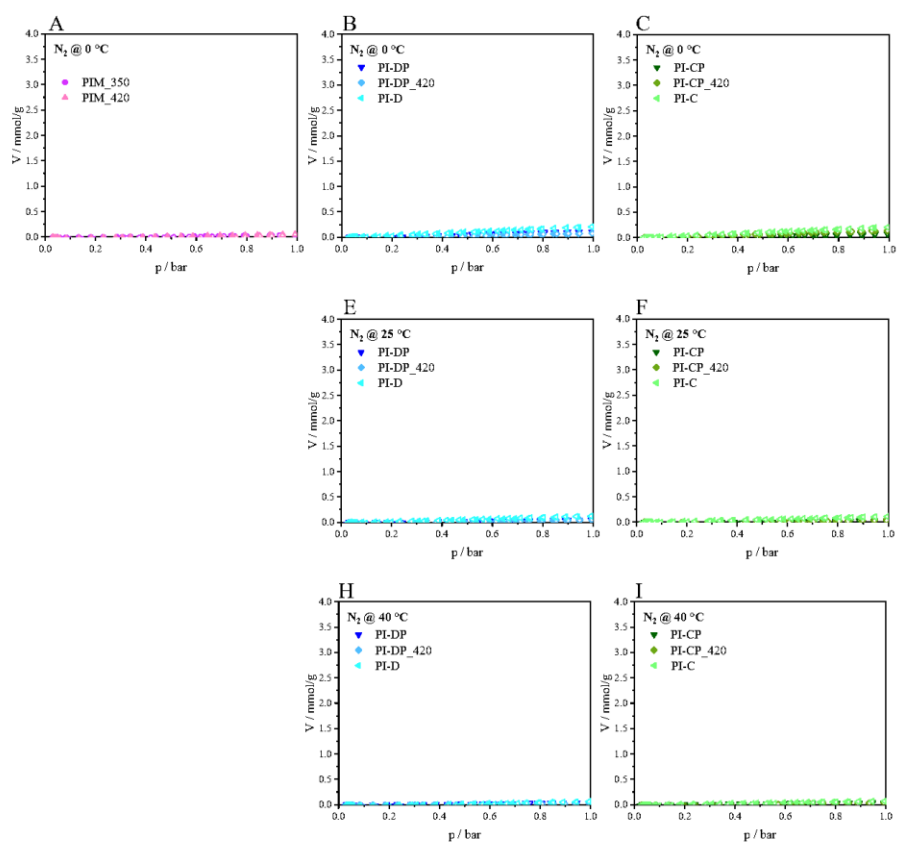
Fig. S20. N$_2$ isotherms measured at 0 °C (A-C), 25 °C (D-F) and 40 °C (G-I) and 1 bar for the PIM (A, D, G), the PI-D (B, E, H) and the PI-C series (C, F, I).

S 25
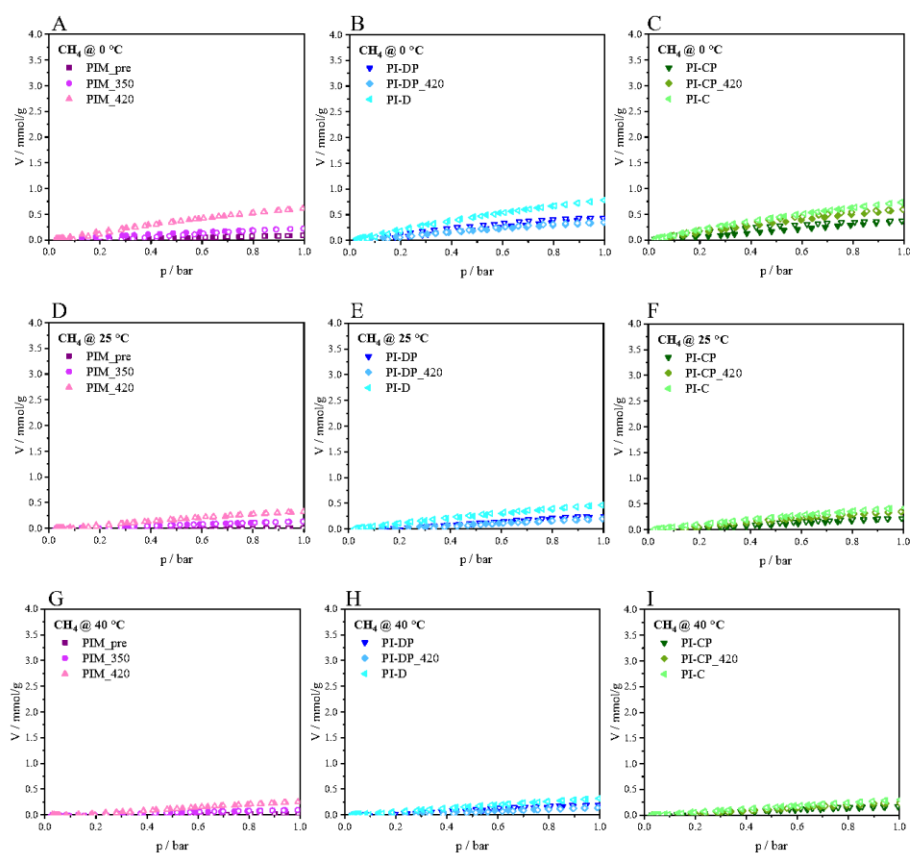
Fig. S21. CH₄ isotherms measured at 0 °C (A-C), 25 °C (D-F) and 40 °C (G-I) and 1 bar for the PIM (A, D, G), the PI-D (B, E, H) and the PI-C series (C, F, I).

S 26

178

Table S10. Uptakes taken from individual isotherms. The values were determined at p = 1 bar.

	CO_2 / mmol/g			N_2 / mmol/g			CH_4 / mmol/g		
	0 °C	25 °C	40 °C	0 °C	25 °C	40 °C	0 °C	25 °C	40 °C
PIM_pre	1	0.7	0.5	-	-	-	0.1	0.0	0.0
PIM_350	1.4	0.9	0.7	0.0	-	-	0.2	0.1	0.1
PIM_420	3.0	2.4	1.9	0.1	-	-	0.6	0.3	0.3
PI-DP	2.3	1.5	1.1	0.1	0.1	0.0	0.4	0.3	0.2
PI-DP_420	1.7	1.2	1.0	0.1	0.1	0.0	0.4	0.2	0.1
PI-D	3.5	2.4	1.7	0.2	0.1	0.1	0.8	0.5	0.3
PI-CP	2.0	1.4	1.0	0.1	0.0	0.0	0.4	0.2	0.2
PI-CP_420	2.7	1.8	1.5	0.1	0.0	0.0	0.6	0.4	0.2
PI-C	3.2	2.1	1.5	0.2	0.1	0.1	0.7	0.4	0.3

8.4 Heats of adsorption

Table S 11: Isosteric heats of adsorption for CO_2 and CH_4 calculated from adsorption isotherms at 273, 298, and 313 K.

Polymer	Q_{CO2} / kJ/mol	Q_{CH4} / kJ/mol
PIM_420	37.4	32.6
PI-DP_420	31.6	26.6
PI-D	32.9	23.4
PI-CP_420	31.9	25.4
PI-C	29.0	23.2

S 27

179

8.5 Selectivities
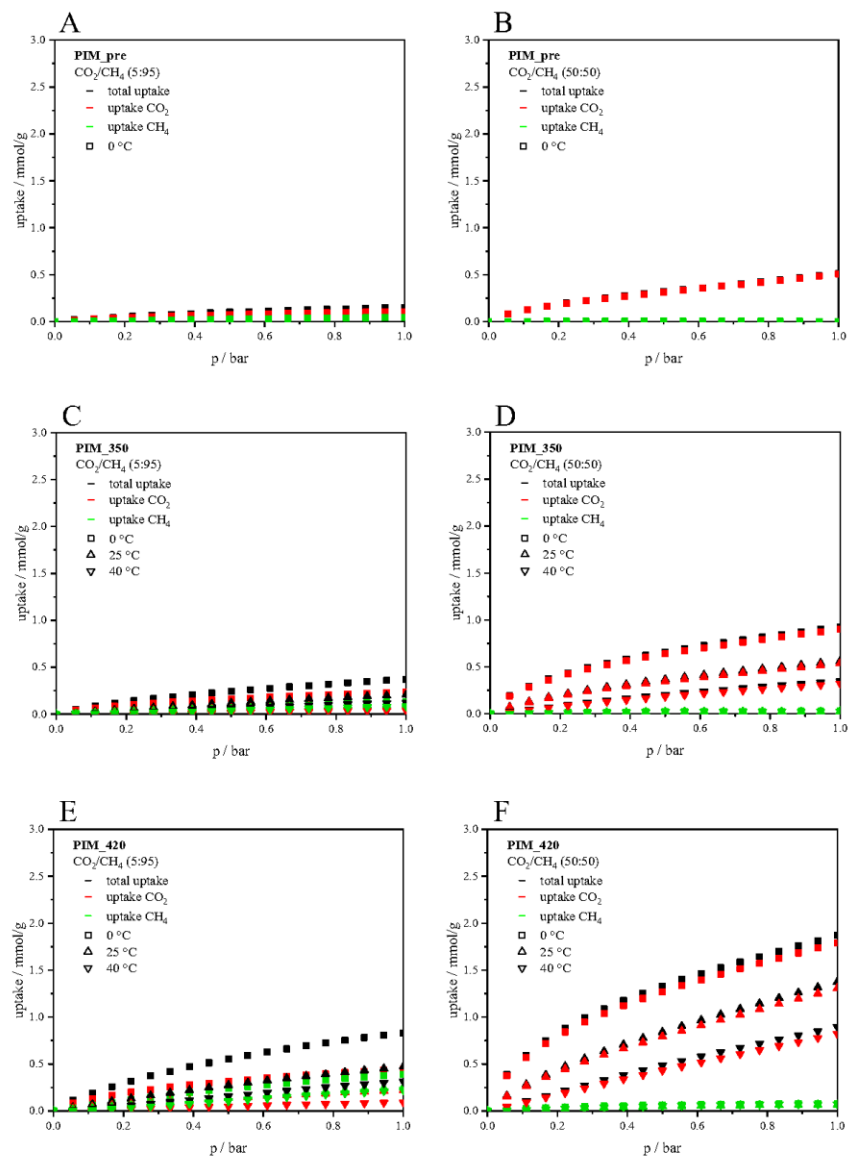
Fig. S22. Isotherms calculated by IAST for gas mixtures of 5:95 CO_2/CH_4 (left) and 50:50 CO_2/CH_4 (right) for the PIM series. Black indicates the total uptake, red the uptake of CO_2 and green the uptake of CH_4 in the mixture at 0 °C (square symbol), 25 °C (triangle with apex up) and 40 °C (triangle with apex down).

S 28

180
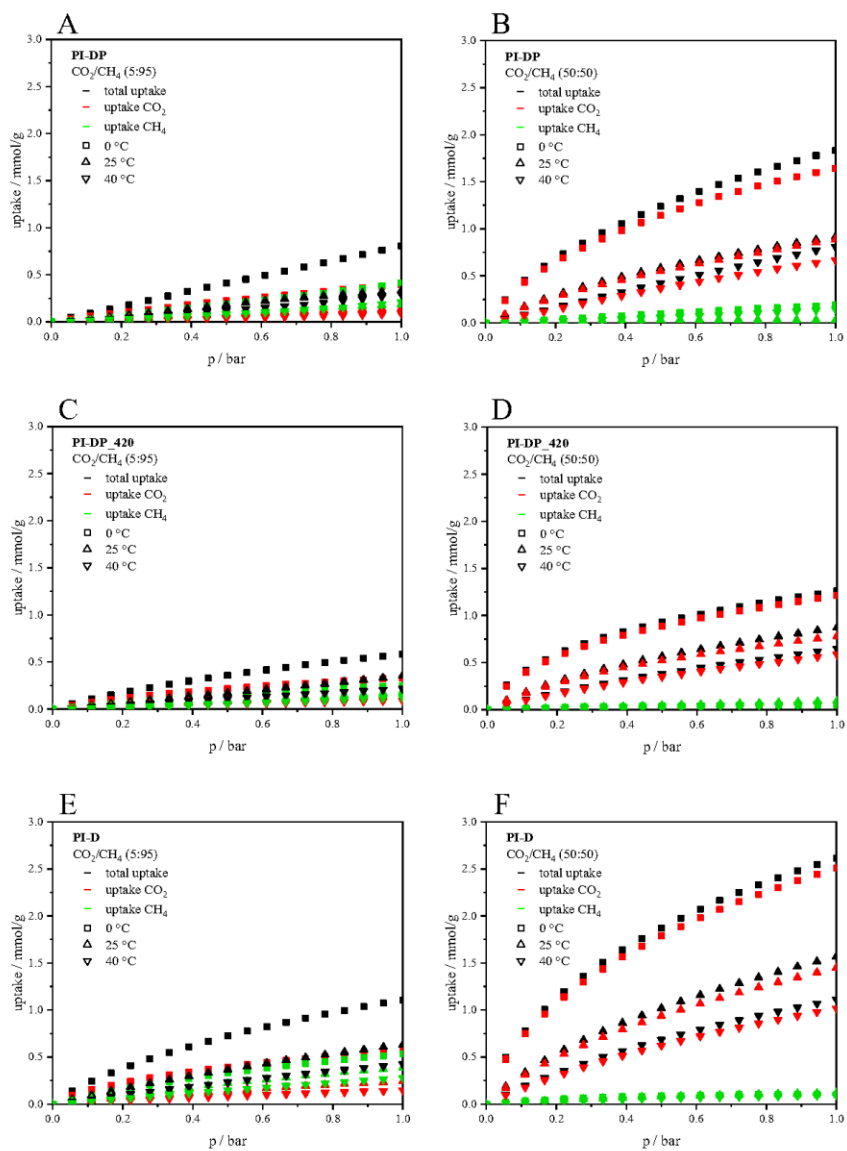
Fig. S23. Isotherms calculated by IAST for gas mixtures of 5:95 CO_2/CH_4 (left) and 50:50 CO_2/CH_4 (right) for the PI-D series. Black indicates the total uptake, red the uptake of CO_2 and green the uptake of CH_4 in the mixture at 0 °C (square symbol), 25 °C (triangle with apex up) and 40 °C (triangle with apex down).

S 29
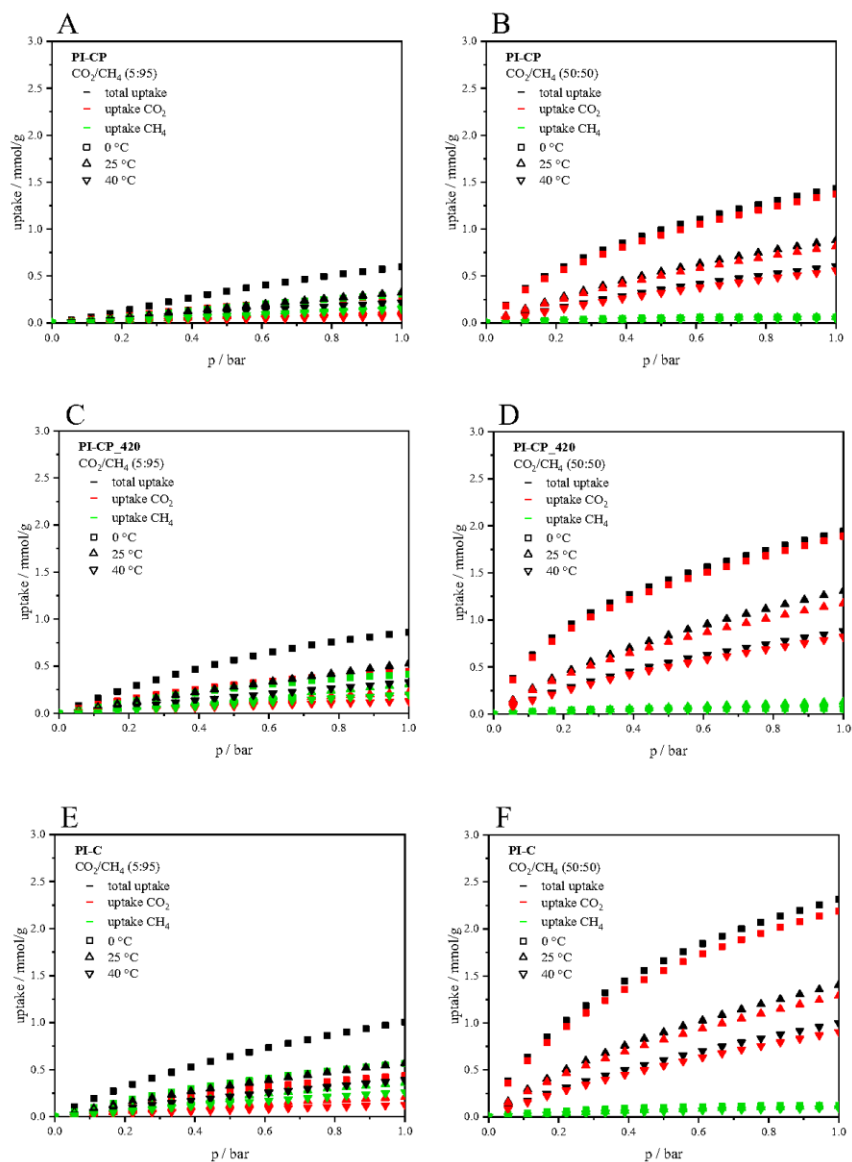
Fig. S24. Isotherms calculated by IAST for gas mixtures of 5:95 CO_2/CH_4 (left) and 50:50 CO_2/CH_4 (right) for the PI-C series. Black indicates the total uptake, red the uptake of CO_2 and green the uptake of CH_4 in the mixture at 0 °C (square symbol), 25 °C (triangle with apex up) and 40 °C (triangle with apex down).

S 30

9   Optical appearance and stability of the polyimide membranes

Fig. S25. Pure polyimide membranes (PIM_420), after heat treatment to remove the auxiliary polymer PVP, exposed to different bending states. They include folding, twisting and curling and indicate good flexibility and mechanical stability of the membranes.

10 References

[1]   C. Klumpen, M. Breunig, T. Homburg, N. Stock, J. Senker, Chem. Mater. 28 (2016) 5461–5470.

[2]   N. Popp, T. Homburg, N. Stock, J. Senker, J. Mater. Chem. A. 3 (2015) 18492–18504.

4.4 Open-Cell Robust COF-Nanowire Network Sponges as Sustainable Adsorbent and Filter

Open-Cell Robust COF-Nanowire Network Sponges as Sustainable Adsorbent and Filter

Chenhui Ding, Yingying Du, and Seema Agarwal*

Constructing crystalline covalent organic frameworks (COF) robust 3D reusable macroscopic objects exposing more adsorption sites with high water flux for use as a filter is an unresolved challenge. A simple scalable procedure is shown for making a robust, highly compressible 3D crystalline COF nanowire interconnected porous open-cell sponge. The compressive strength and Young's modulus (80% strain) of the sponge are 175 and 238 kPa, respectively. The sponge can withstand multiple compression-release cycles and a load of 2800 times its weight without collapsing. As an exemplary application, the use of a COF sponge in the selective removal and separation of cationic model dye from a mixture of dyes in water by adsorption and filtration with >99% efficiency is shown. Depending on the dye concentration, the dye removal time can be as short as 2 min, and dye adsorption efficiency can be as high as 653 mg g^{-1} (COF in the sponge). During filtration, the sponges as filters show a high water flux of 2355 L h^{-1} m^{-2} under ambient conditions and maintain their performance for many cycles. The lightweight, reusability, and efficiency make present sponges sustainable materials as adsorbents and filters.

1. Introduction

Covalent organic frameworks (COFs) in the last decades have become an undisputed advanced material type for wide applications in fields, such as gas storage,[1] separation,[2] catalysis,[3] water purification,[4] molecular separations,[5] energy storage,[6] and light-emitting diodes.[7] Vulnerability concerning the degree of crystallinity, chemical structure, functionality, pore size, surface area, and porosity in addition to high chemical and thermal stability make COFs promising candidates for applications mentioned above. Due to their chemically cross-linked structure, they are obtained as an insoluble and infusible powder after

synthesis. The powder form makes their utility in several applications including contaminant removal from solutions non-sustainable and tedious.[8] The separation of COF powder after use is an energy-intensive process. Further, for sustainability, it is important to reuse COFs as far as possible.[9] In addition, the irregularly packed agglomerated COF powders reduce the accessible adsorption sites and hinder the mass transport and adsorption of contaminants, such as dyes during water purification.

Therefore, COFs in the form of self-standing robust easy-to-handle macro-objects with access to all active sites that can be easily separated and reused will be more promising.[10] Various methods are studied to get COFs in the form of 2D membranes. For example, growing on a solid-substrate,[11] liquid–liquid interface polymerization,[12] phase-switching process,[13] and template-assisted framework (TAF) process.[14] The COF precursors are also mixed with graphene oxide (GO)/polymer binder, freeze-dried, and heated to produce a 3D macro-object.[15] In addition to COF precursors, readymade COF nanoparticles are also mixed with GO/polymer binders and converted to 3D objects by freeze-drying/supercritical drying.[16] Also, melamine-formaldehyde foams coated with COF were prepared by dipping the foam into a precursor solution of COF followed by heating.[17] Pure COF 3D macro-objects in general are mechanically brittle and show shrinkage during preparation. Tian et al. grew COF in situ on the microporous channels of wood to obtain wood/COF composites.[18] The robust wood skeleton ensures the recyclability of the composite material. However, due to the lack of strong force between COF and wood, the COF powder does not completely cover the surface of the wood, and the wood itself does not have a highly interconnected porous structure, which limits the diffusion of organic pollutants.

COFs are advanced materials showing benefits as porous adsorbents, a property that is highly useful for the removal of pollutants.[19] In the form of self-standing robust 3D macro-objects COFs can provide additional advantages of ease of separation, reusability, and excellent mass transfer in applications like pollutant removal. Therefore, the design of COF macro-objects as adsorbents should include some important aspects: robustness (mechanical stability), high porosity, and open inter-connected porous structure to ensure the rapid mass transfer and recycling

C. Ding, Y. Du, S. Agarwal
Macromolecular Chemistry and Bavarian Polymer Institute
University of Bayreuth
Universitätsstrasse 30, 95440 Bayreuth, Germany
E-mail: agarwal@uni-bayreuth.de

The ORCID identification number(s) for the author(s) of this article can be found under https://doi.org/10.1002/adfm.202309938
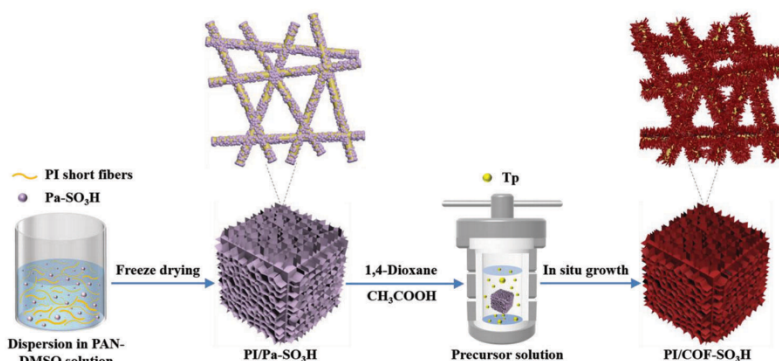
Figure 1. Schematic illustration of the preparation of polyimide / sulfonic acid functionalized COF composite sponges (PI/COF—SO$_3$H). PI = polyimide, PAN = polyacrylonitrile, Pa—SO$_3$H = 2,5-diaminobenzenesulfonic acid, Tp = 1,3,5-triformylphloroglucinol, DMSO = dimethylsulfoxide, CH3COOH = acetic acid.

of adsorbent, the availability of COF adsorbing sites not only on the surface but also in the bulk of 3D macro-objects, and appropriate functionality to improve the adsorption capacity. Besides this, the production of 3D COF macro-objects should be up scalable, and easy. The prime challenge is to prepare such a robust crystalline COF macro-object fulfilling all these requirements. For wastewater purification applications, in addition, a large water flux through 3D macro-objects should also be secured by a tailor-made COF structure.

3D electrospun short fiber sponges with high porosity, good mechanical properties, and highly interconnecting porous structure have been applied in oil-water separation, protein purification, and seawater desalination, and show high stability and high flux.[20] Previously we established preparation methods for such sponges from short electrospun fibers in our group.[21] The compressible, robust sponges are formed by the percolation of short electrospun fibers during freeze-drying giving a dual porous structure: small pores between the fibers in the sponge cell walls and big pores (≈100 μm) formed by sublimation of ice during freeze-drying. Such sponges should be an ideal candidate as the skeleton for the preparation of robust 3D COF crystalline macro-objects. The continuous growth of COF not only on the surface but also in the bulk is expected from the electrospun skeleton sponge structure and pore size.

In this work, we show first the preparation of robust polyimide (PI)/sulfonic acid functionalized crystalline COF nanowire (PI/COF—SO$_3$H) composite sponges with highly interconnected open-cell structures. Since composite sponge structure and functionality are highly promising for high water flux, mass transfer, and adsorption of selective organic dyes from water, methylene blue removal from the water was studied as an exemplary example. Also, the selectivity of the sponges for the adsorption of positively charged dye from a mixture of dyes is investigated. The superiority of present COF sponges is evident from high adsorption, high selectivity and filtration efficiency, high water flux, and reusability. The sponge preparation procedure is simple, scalable and opens up new avenues for materials not only for water purification but several other applications.

2. Results and Discussion

The open-cell porous sponges were prepared through two steps of template sponge construction using PI short electrospun fibers and in situ growth of COF, as shown in **Figure 1**.

First, PI short fibers (average diameter $d = 526 \pm 98$ nm, average fiber length $L = 77 \pm 23$ μm, Figure S1, Supporting Information), and Pa—SO$_3$H were dispersed in a solution of PAN in DMSO by stirring at high speed, and a porous spongy template (PI/Pa—SO$_3$H) was constructed by freeze-drying. During freeze-drying self-assembly of PI short fibers and their percolation provides an open-cell sponge with interconnected pores (**Figure 2**a–d). PAN, as a binder, further ensured the stability of the sponge and provided a site for the growth of COF. Instead of PI, any other polymer can also be used if stable under solution and temperature conditions used for growing COF.

In the second step, COF was grown in situ on the template sponge in the form of nanowires by solvothermal method by letting Pa—SO$_3$H on the template sponge react with Tp. The resulting sponge is designated as PI/COF—SO$_3$H sponge (Figure 2e–h). The optical pictures of the template PI/Pa—SO$_3$H and PI/COF—SO$_3$H sponges are shown in Figure 2a–e. There was a color change to red due to the formation of COF the on PI/Pa—SO$_3$H template sponge.

PI/COF—SO$_3$H sponges were prepared using different loading of Pa—SO$_3$H in template PI/Pa—SO$_3$H sponges. Depending upon the amount of Pa—SO$_3$H loading the sponges are designated as PI/Pa—SO$_3$H-X and PI/COF—SO$_3$H-X, respectively. X (0.5, 1.0, 1.5, and 2.0) is the mass ratio of Pa—SO$_3$H and PI short fibers. The SEM images of PI/Pa—SO$_3$H sponges with different loadings of Pa—SO$_3$H are shown in (Figure S2, Supporting Information) and the corresponding COF decorated sponges (PI/COF—SO$_3$H) are shown in Figure S3 (Supporting Information). The growth of COF in the form of nanowires (average diameter $d = 59 \pm 17$ nm) was obvious from the SEM images. The growth of COF in the form of nanowires is generally rare. This morphology is achieved in literature by special modifications and methods, such as core-planarity and interfacial synthesis methods.[22] The nanowire COF morphology is the result of
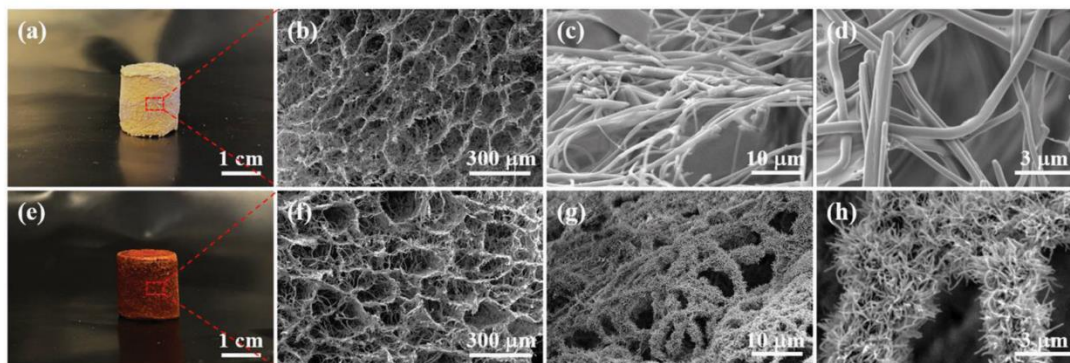
2309938 (2 of 10)

Figure 2. a–d) Photographs and SEM images of PI/Pa—SO$_3$H-2.0, and e–h) PI/COF—SO$_3$H-2.0.

the preferred growth along the z-direction in comparison to the x and y directions due to the stronger π–π interactions among the layers. In the work of Luo et al. COF was assembled in the form of 1D structure, supposedly due to the special arrangement of —SO$_3$H in the different layers in an opposite mode rather than the common same-side mode.[23] In our case, it might be a combination of π–π interactions and a special arrangement of —SO$_3$H.

The increased amount of Pa—SO$_3$H on the surface of PI short fibers led to the growth of denser COF and more nanowires, and the density of the PI/COF—SO$_3$H sponge also increased (Tables S1 and S2, Supporting Information). Although, the density of PI/COF—SO$_3$H-0.5 was 11.2 mg cm^{-3}, whereas it increased to 34.8 mg cm^{-3} for PI/COF—SO$_3$H-2.0 still the sponges are lightweight.

The cross-sectional investigations by SEM showed the growth of COF not only on the surface of the template PI/Pa—SO$_3$H but throughout the bulk.

Figure 3a and Figure S4a (Supporting Information) show the Fourier-transform infrared (FT-IR) spectra of the samples. First, characteristic peaks of PI (C=O at 1719 cm^{-1}, C—N at 1370 cm^{-1}), and PAN (C≡N at 2242 cm^{-1}) were found in all composite sponges.[24] Second, PI/Pa—SO$_3$H showed obvious characteristic peaks of Pa—SO$_3$H (—NH$_2$ at 3300–35 000 cm^{-1}, —SO$_3$H at 1082 and 1024 cm^{-1}).[25] Finally, with the growth of COF—SO$_3$H in situ, the characteristic peaks at 3300–3500 cm^{-1} (—NH$_2$) disappeared, and the new characteristic peaks were displayed at 1574 cm^{-1} (C=C) and 1236 cm^{-1} (C—N), indicating that conversion of PI/Pa—SO$_3$H to PI/COF—SO$_3$H.[26] The formation of COF—SO$_3$H was further characterized by ^{13}C cross-polarized magic angle spinning (CP MAS) NMR spectra. The chemical structures with carbon numbered and the corresponding NMR are given in Figure 3b,c. The characteristic peaks of PI and Pa—SO$_3$H were seen in the PI/Pa—SO$_3$H sponge. As the reaction progresses for the formation of PI/COF—SO$_3$H, the characteristic peaks of Pa—SO$_3$H disappear and typical COF—SO$_3$H resonances such as imine carbon peaks ($\approx$147 ppm) and carbonyl carbon peaks ($\approx$184 ppm) were observed in PI/COF—SO$_3$H sponge.[27]

The powder X-ray diffraction (PXRD) patterns of COF—SO$_3$H powder and PI/COF—SO$_3$H sponges are shown in Figure 3d and Figure S4b (Supporting Information). It can be found that

the peaks of COF—SO$_3$H at 2θ = 4.8° (100), 8.2° (210), and 27.1° (001) are in good agreement with the simulated AA stacking model, and consistent with the literature reports for COF powder.[28] The reflection at 2θ = 17.2° was attributed to PAN, whereas no peak of PI was found because it was a non-crystalline polymer.

PI/COF—SO$_3$H sponges are super hydrophilic as tested by contact angle measurements (water contact angle of 0°). The water penetrates the sponge instantly, as shown in Video S1 (Supporting Information). At the same time, Figure S5 (Supporting Information) shows the thermogravimetric analysis curves of PI/COF—SO$_3$H sponges under a nitrogen atmosphere. PI/COF—SO$_3$H sponges show good thermal stability, with almost no mass loss before 200 °C, which provides the possibility for their application in high-temperature environments.

Excellent mechanical properties and good deformation recovery performance provide a guarantee for the reusability of PI/COF—SO$_3$H sponges. **Figure 4** shows the recovery performance (50% strain) and compressive strength (80% strain) of different composite sponges, which are summarized in Table S3 (Supporting Information). It can be found that all composite sponges exhibit good mechanical properties and deformation recovery performance, and there is no obvious change in the maximum stress and recovery height after 50 compression-release cycles (50% strain). The addition of COF greatly improved the compressive strength and deformation recovery performance of the PI/COF—SO$_3$H sponge. Compared with PI/COF—SO$_3$HCOF—SO$_3$H-0.5, the compressive strength and Young's modulus (80% strain) of PI/COF—SO$_3$H-2.0 increased from 47 to 175 kPa and 46 to 238 kPa, respectively. This indicates that the highly interconnected porous structure of PI/COF—SO$_3$H can effectively absorb and release stress, and thus withstand multiple compression-release cycles. The dense COF nanowires grown on the surface of PI fibers serve as a protective layer, which further strengthens the fiber network framework, thereby improving the compressive strength and deformation recovery performance of PI/COF—SO$_3$H sponges. In addition, 71.4 mg of PI/COF—SO$_3$H-2.0 can withstand a weight (200 g) of 2800 times its weight without collapsing, further demonstrating its excellent compression resistance (Figure 4g).
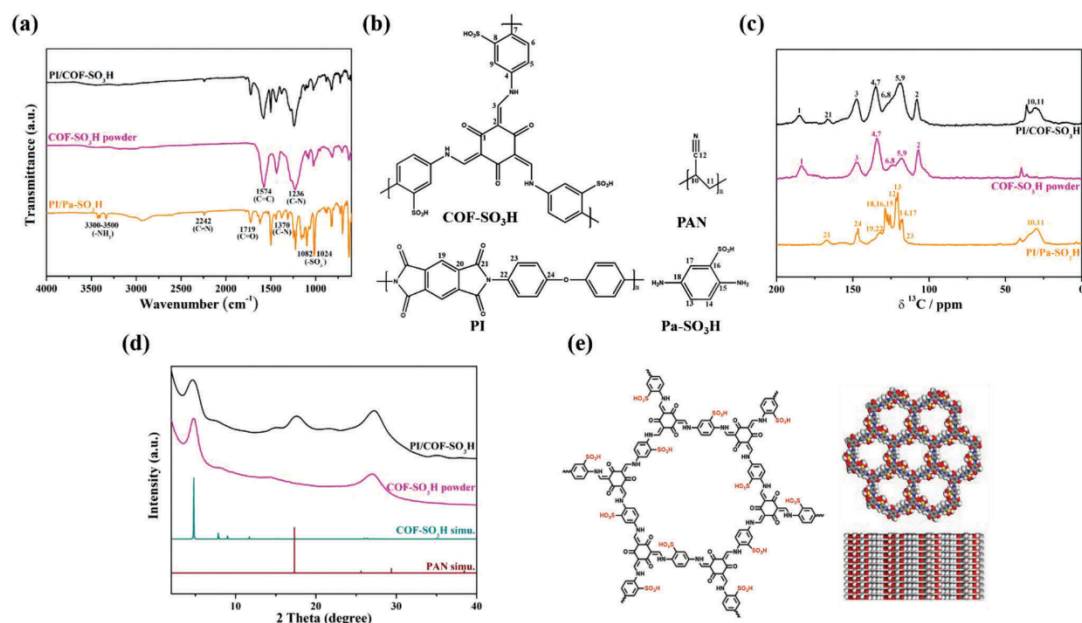
2309938 (3 of 10)

Figure 3. a) Chemical structural formulas of COF—SO$_3$H, PAN, Pa—SO$_3$H, and PI. b) FT-IR spectrum of PI/Pa—SO$_3$H sponge, COF—SO$_3$H powder, and PI/COF—SO$_3$H sponge. c) ^{13}C CP MAS NMR spectra of PI/Pa—SO$_3$H sponge, COF—SO$_3$H powder and PI/COF—SO$_3$H sponge. d) PXRD patterns of COF—SO$_3$H powder, PI/COF—SO$_3$H sponge, and simulated PXRD patterns of PAN and COF—SO$_3$H. e) The structure and space-filled model of COF—SO$_3$H.

As COF—SO$_3$H contains a sulfonic acid group, the average Zeta potential measured on COF powder is −76.9 mV (Figures S6 and S7, Supporting Information), showing negative charge characteristics, which makes it appropriate for the adsorption of cationic dyes such as methylene blue (MB).[29] Therefore, MB was used as the toxic model substance in this work. First, the adsorption capacity of different PI/COF—SO$_3$H sponges for MB was explored by taking a definite amount of the sponge (10 mg) and using 100 mL (20 mg L^{-1}) MB solution as shown in **Figure 5**. The remaining concentration of MB in the solution after 4 h was calculated using a calibration curve based on absorbance at 664 nm versus concentration by a UV–vis spectrophotometer (Figure S8, Supporting Information). The MB adsorption capacity (calculated using the total mass of the sponge) increased with the increased content of COF in the sponge. The maximum dye adsorption capacity and removal efficiency were 197.2 mg g^{-1} (sponge) and ≈99% for PI/COF—SO$_3$HCOF—SO$_3$H-2.0, respectively. The blank sponge prepared with PI-PAN without any COF was also tested for MB adsorption and showed negligible adsorption (Figure S9, Supporting Information). Since the COF is the actual active species in the sponge responsible for the dye removal, the corresponding dye adsorption capacity was also calculated using the actual amount of the COF in the sponges. The COF in sponges showed an extremely high adsorption capacity of ≈350 mg g^{-1} (COF in sponge) under the mentioned experimental conditions (Figure S10, Supporting Information).

Further, taking PI/COF—SO$_3$H-2.0 as a representative candidate, the concentration of residual dye in the solution at different time intervals was determined, and the adsorption kinetics of MB were obtained, as shown in **Figure 6**a. It can be seen that the adsorption capacity of PI/COF—SO$_3$H-2.0 for MB increases significantly within the first 60 min, and increases with the contact time within 180 min, after which the adsorption equilibrium is reached. To explore the possible adsorption mechanism of MB by PI/COF—SO$_3$H-2.0 different probable kinetic models as suggested in the literature were fitted (Figure 6b–d; Table S4, Supporting Information).[30] The pseudo-second-order kinetic model with a higher correlation coefficient ($R^2 = 0.9865$), and a more consistent dye adsorption capacity (q_e) theoretical value with the experimental value is the best fit. The pseudo-second-order kinetic model is based on the assumption that the adsorption rate is controlled by chemisorption.[31] Therefore, the adsorption behavior of MB on PI/COF—SO$_3$H-2.0 is most probably chemisorption.[32] Further, the plot of dye adsorption capacity at any particular time (t) versus $t^{1/2}$ showed two distinct stages. In the first stage, a fast adsorption rate and a large slope of the curve are seen. The highly interconnected open-cell structure of PI/COF—SO$_3$H-2.0 and a large number of negatively charged functional groups on the surface most probably accelerated diffusion and adsorption of MB on the COF surface. In the second stage, MB molecules pass from the surface of the COF to the interior through the nanochannel, and there is a repulsive force between MB molecules, which increases the diffusion resistance
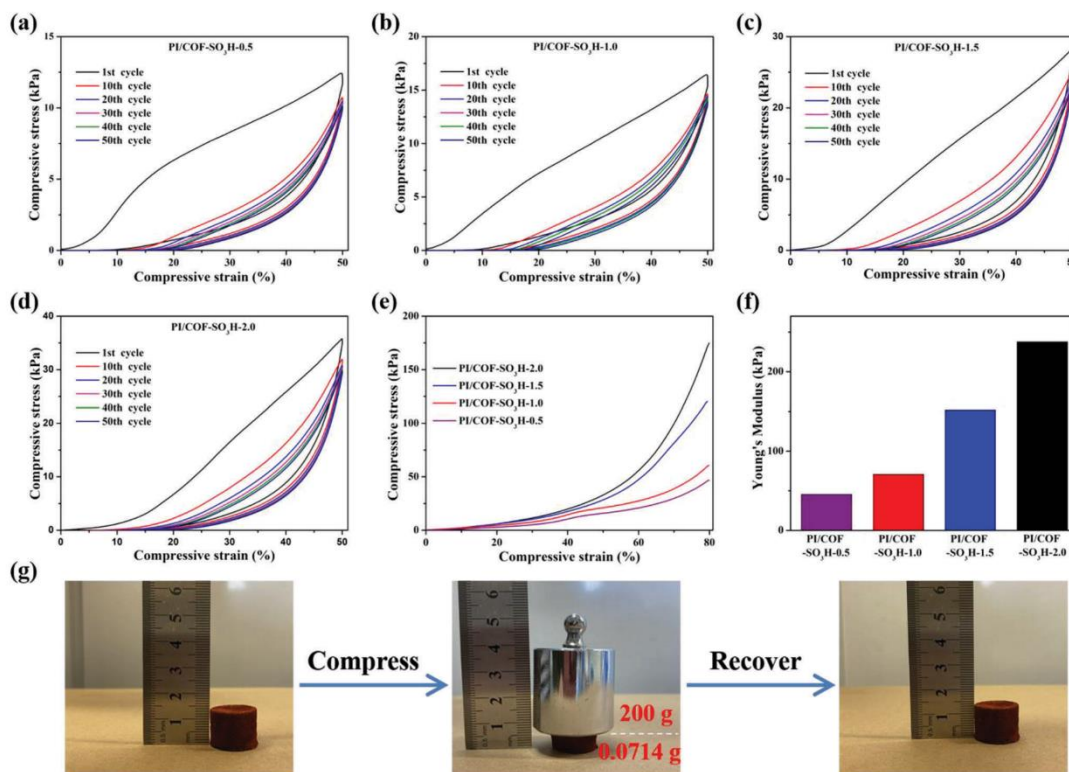
188

Figure 4. a–e) Compression-release stress–strain and compressive stress–strain curves of PI/COF—SO$_3$H sponges, f) the corresponding compressive Young's modulus, g) and compressive capacity (weight load test) of PI/COF—SO$_3$H-2.0.

and reduces the diffusion rate, resulting in a decreased slope of the curve.

To compare the dye removal efficiency of COF powder and COF immobilized on sponges, an experiment was done using 10 mg PI/COF—SO$_3$H-2.0 sponge and 5.84 mg of the COF powder for the removal of MB from 5 mL water solution of MB concentration 20 mg L^{-1} (Figure S11, Supporting Information). 5.84 mg of the COF powder was used for the experiment as

10 mg of PI/COF—SO$_3$H-2.0 sponge has 5.84 mg of the active MB adsorbing COF. Rapid separation of MB was observed by the sponge (≈99.5% removal of MB in 2 min), whereas, at the same time, the removal efficiency of COF powder was ≈80%. This may be because the highly interconnected open-cell structure of PI/COF—SO$_3$H sponges is conducive to the rapid diffusion of dyes, and COF nanowires uniformly grow on the surface of PI short fibers, exposing more adsorption sites.
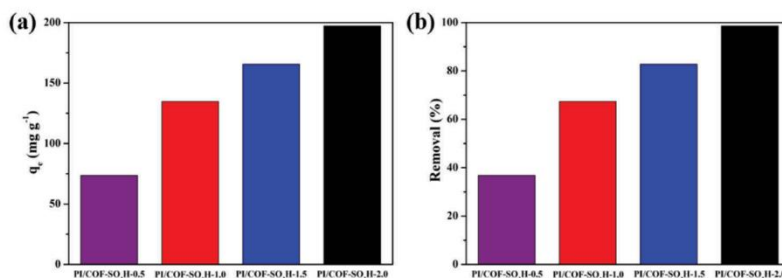
Figure 5. a) Adsorption capacity, and b) removal efficiency of MB by PI/COF—SO$_3$H sponges.
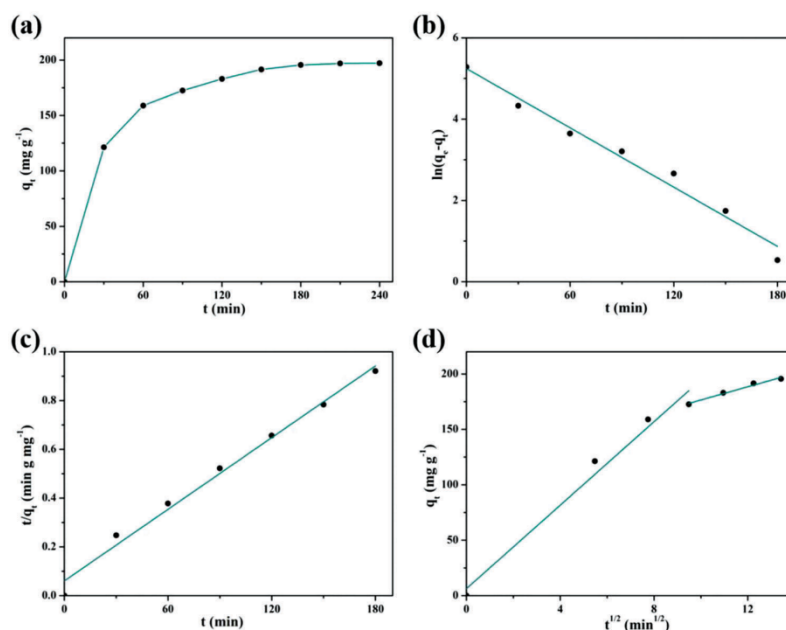
Figure 6. a) The adsorption capacity of PI/COF—SO$_3$H-2.0 for MB as a function of time. b) The data fitted to the pseudo-first-order kinetic model, c) the pseudo-second-order kinetic model, and d) the intra-particle diffusion kinetic model.

In additional experiments, the PI/COF—SO$_3$H-2.0 (10 mg) was immersed in MB solution with different initial dye concentrations (20–400 mg L^{-1}), and the concentration of residual dye in the solution after reaching adsorption equilibrium was determined. As shown in **Figure 7**, with the increase of dye concentration in MB solution, the dye adsorption capacity of PI/COF—SO$_3$H-2.0 first increased and then approached equilibrium, with the maximum dye adsorption capacity of ≈379 mg g^{-1} (sponge). Taking into account that the actual amount of COF in

the sponge is only 0.58 g, the actual dye adsorption capacity is ≈653 mg g^{-1} (COF-in sponge). Meanwhile, Langmuir and Freundlich isotherm models were introduced to fit the adsorption data,[33] and the adsorption isotherm was constructed (the fitting data is summarized in Table S5, Supporting Information). It can be found that the correlation coefficient ($R^2 = 0.9845$) of the Langmuir model is larger than that of the Freundlich model, and the theoretical value of maximum adsorption capacity is 413.93 mg g^{-1} (sponge), which is closer to the experimental value and can accurately explain the experimental data. The Langmuir isothermal model is suitable for monolayer adsorption, which indicates that the adsorption of MB by PI/COF—SO$_3$H-2.0 is monolayer adsorption.[34]

The pH value affects the surface charge of the adsorbent and dye molecules and is a key factor in adsorption experiments. The effect of pH value on the dye adsorption performance of PI/COF—SO$_3$H-2.0 was further explored. Wherein, 10 mg of PI/COF—SO$_3$H-2.0, 200 mL (20 mg L^{-1}) MB solution was taken, and the pH value of the solution was adjusted to 3–11 by adding 0.1 M HCl or 0.1 M NaOH. From Figure S12 (Supporting Information), it can be found that increasing the pH value can effectively increase the adsorption capacity of PI/COF—SO$_3$H-2.0 for MB, and the maximum dye adsorption capacity is 231.3 mg g^{-1} was observed under alkaline conditions. The same sponge showed a dye adsorption capacity of <100 mg g^{-1} under acidic conditions. This is because the surface of COF contains a large number of anionic groups, and the electrostatic interaction plays an important role in the adsorption of cationic dye MB. When the MB solution is acidic, a large number of hydrogen ions in
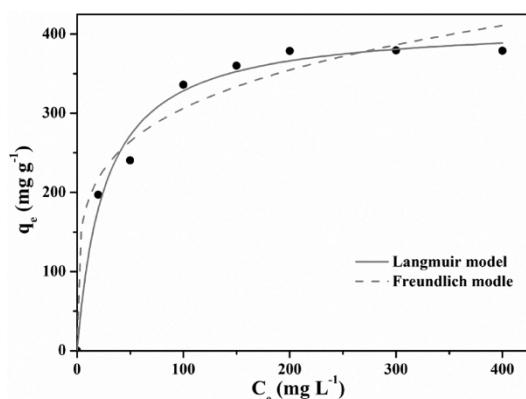

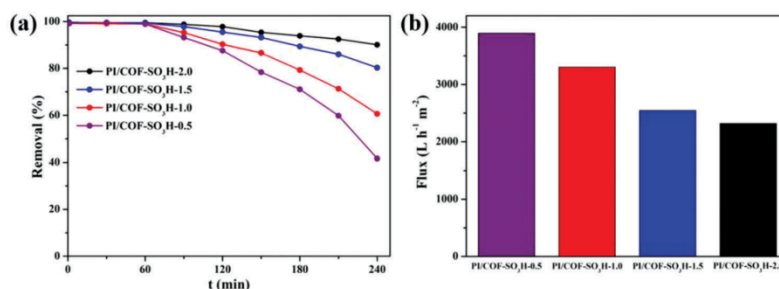**Figure 7.** Equilibrium adsorption isotherm of MB on PI/COF—SO$_3$H-2.0.

Figure 8. a) Filtration removal efficiency, and b) water flux of MB by PI/COF—SO$_3$H sponges.

the solution compete with MB and protonate the sulfonic acid group, repelling MB, and resulting in a low adsorption capacity of PI/COF—SO$_3$H-2.0 for MB. When the MB solution is alkaline, a large amount of hydroxide ions in the solution is conducive to the ionization of the sulfonic acid groups on the surface of COF, which makes it easier to adsorb MB.[35] Therefore, a neutral or alkaline MB solution is more conducive to the adsorption of MB by PI/COF—SO$_3$H-2.0.

Due to the mechanical robustness of the sponges, they can also be used as filters. Therefore, a simple filtration device is constructed by placing cylindrical PI/COF—SO$_3$H sponges in a syringe, as shown in Figure S13a (Supporting Information). Due to the highly interconnected open-cell structure of the PI/COF—SO$_3$H sponges, no external driving force is required, and the dye solution could pass through the PI/COF—SO$_3$H sponges by its gravity and get to the clarified water, as shown in Video S2 (Supporting Information). The loading capacity of COF affects the structure and the dye adsorption capacity of PI/COF—SO$_3$H sponges and further affects the filtration performance of PI/COF—SO$_3$H sponges for MB solution. Therefore, the filtration performance of MB solution with different PI/COF—SO$_3$H sponges was investigated. As can be seen from **Figure 8**, the removal efficiency of MB for all composite sponges is over 99%. At the same time, all the composite sponges showed high water flux. The worth noting is the high water flux without the development of any back pressure. Once the COF in sponge filters is saturated with MB, the filtration efficiency decreased. PI/COF—SO$_3$H showed after 4 h of filtration still a very high dye removal efficiency of ≈90%. The proof-of-concept shows the possibility of technological upgrading in the future.

Also, in a laboratory experiment, to satisfy the long-term continuous filtration of MB solution by PI/COF—SO$_3$H sponges, four filtration devices (each having ≈60 mg of the sponge) are connected in series, as shown in Figure S13b (Supporting Information). For sustainable optimum use, sponge filters can also be used in modular form attaching them in a sequence at different times of filtration. Using PI/COF—SO$_3$H-2.0 as a filter, the whole filter device worked continuously for 24 h. The system showed excellent filtration performance (removal efficiency was 99.3%) for MB solution up to 12 h (Figure S14, Supporting Information) with a water flux of 2355 L h^{-1} m^{-2} that is far superior to COF nanofiltration membranes.[36] Therefore, the filter device based on PI/COF—SO$_3$H sponges can process large quantities of MB solution quickly and efficiently.

Due to its excellent mechanical properties and good deformation recovery, PI/COF—SO$_3$H sponges could be regenerated after use. The reusability of regenerated PI/COF—SO$_3$H-2.0 as adsorbent and filter was also explored (Figure S15, Supporting Information). The PI/COF—SO$_3$H-2.0 has been regenerated by stirring in a methanol solution having 1 mM HCl. The regenerated sponge maintained extremely high MB removal efficiency even after 10 cycles for both as adsorbent and filter. Moreover, the MB adsorption and recycling performance of PI/COF—SO$_3$H sponge were compared with other works of literature (Table S6, Supporting Information). The results show that the PI/COF—SO$_3$H sponge exhibits a combination of high adsorption capacity and excellent recycling performance.

Due to the —SO$_3$H groups in COF, the present sponges can also be used for the separation of oppositely charged dyes by specifically adsorbing only positively charged dye. Therefore, in an experiment with the negative fluorescein sodium salt (FL), the PI/COF—SO$_3$H-2.0 sponge retained only 8% of the dye as measured by the absorbance at 490 nm by UV–vis spectroscopy (Figure S16, Supporting Information). Further, the anionic dye FL was mixed with MB to explore the selectivity of our sponge filter (**Figure 9**a; Video S3, Supporting Information). The mixed dye solution was green in color, whereas pure FL solution had yellow color and MB had blue color. The first indication of the dye separation was the change in the color from green to yellow of the solution eluting out from the filter. The yellow color is consistent with the initial FL solution color, and the absorbance of FL at 490 nm remains unchanged (Figure 9b). No absorbance of MB at 664 nm was seen in the eluted solution showing efficient separation of dyes.

3. Conclusion

A simple method of making robust, compressible 3D COF macro-object with an open-cell structure (sponge) is established in the present work. The COF nanowires were grown on a template light-weight sponge prepared from short electrospun fibers. Since the process of electrospinning and freeze-drying (the methods used in the preparation of the sponge) on a large scale are possible, the present method of making PI/COF—SO$_3$H will be up scalable. The chemical functionality and the network framework structure in sponges are ideally suitable for use as adsorbents and filters. The maximum adsorption capacity of PI/COF—SO$_3$H-2.0 to MB reached ≈653 mg g^{-1} (COF-in sponge). Compared
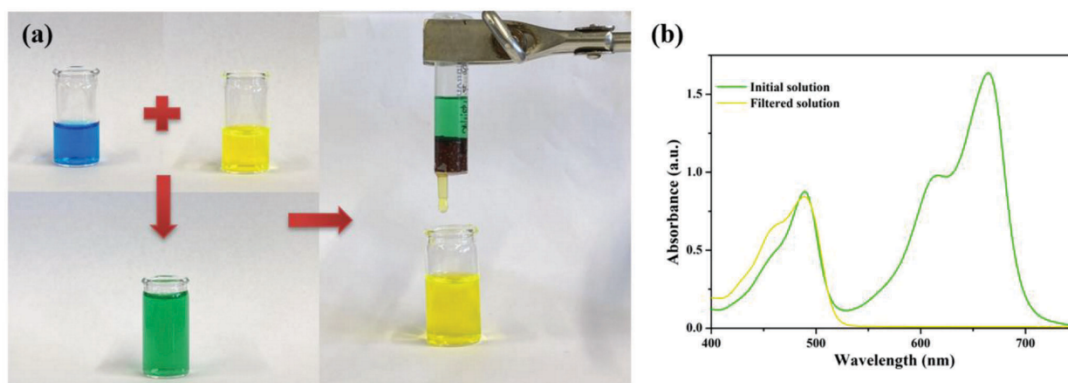
2309938 (7 of 10)

Figure 9. a) Selective filtration separation of a mixed solution of MB and FL by PI/COF—SO$_3$H-2.0. b) UV–vis spectra of the mixed dye solution before and after filtration.

with COF—SO$_3$H powder, PI/COF—SO$_3$H-2.0 was able to remove MB faster (99.5% removal within 2 min). In addition, using PI/COF—SO$_3$H sponges as a filter, high dye removal efficiency (99.3%), high flux (2355 L h^{-1} m^{-2}), and rapid adsorption and separation of a mixture of dyes were possible. Meanwhile, in the adsorption and filtration experiments, PI/COF—SO$_3$H sponges still exhibited excellent dye removal performance after 10 cycles of regeneration.

4. Experimental Section

Materials and Chemicals: Electrospun polyimide (PI) short fiber from Jiangxi Xiancai nanofiber Technology Co.Ltd. Polyacrylonitrile (PAN, Mw = 80 000, Carl Roth), 2,5-Diaminobenzenesulfonic acid (Pa—SO$_3$H), 1,3,5-triformylphloroglucinol (Tp), methylene blue (MB, powder), and fluorescein sodium salt (FL, powder) were purchased from Sigma–Aldrich. Dimethyl sulfoxide (DMSO, 99.9%), 1,4-Dioxane (99.9%), and acetic acid (AcOH, 99.7%) were purchased from Fisher Chemical. All chemicals were used directly without further purification.

Preparation of the PI/COF—SO$_3$H Sponges: The PI/COF—SO$_3$H sponges were prepared in two steps, as shown in Figure 1. The first step was to construct the PI/Pa—SO$_3$H sponges: 100 mg of PI short fibers, 100 mg of PAN powder, and a certain amount of Pa—SO$_3$H (50, 100, 150, and 200 mg) were uniformly dispersed in 25 g of DMSO by high-speed stirring, and the PI/Pa—SO$_3$H sponges were obtained after freeze-drying. Depending upon the amount (X is the mass ratio of Pa—SO$_3$H and PI short fibers, X = 0.5, 1.0, 1.5, and 2.0) of Pa—SO$_3$H loading the sponge was designated as PI/Pa—SO$_3$H-X. The second step, in situ growth of COF—SO$_3$H: take PI/Pa—SO$_3$H-2.0 as an example. The PI/Pa—SO$_3$H-2.0 (400 mg) was added to a 1,4-Dioxane (74.4 g) solution containing Tp (148.8 mg) and acetic acid (1.48 g) and reacted at 120 °C for 3 days to obtain dark red PI/COF—SO$_3$H-2.0. Then it was washed multiple times with 1,4-Dioxane and acetone, and dried under vacuum at 60 °C for 24 h. The prepared composite sponges were named PI/COF—SO$_3$H-0.5, PI/COF—SO$_3$H-1.0, PI/COF—SO$_3$H-1.5, and PI/COF—SO$_3$H-2.0, respectively. And, by measuring the weight change of the composite sponge before and after growing COF, the weight ratio of each component can be obtained, which is summarized in Tables S1 and S2 (Supporting Information). Also, prepare a PI-PAN blank sponge without any COF using the same method.

Synthesis of COF—SO$_3$H Powder: Tp (63 mg (0.3 mmol)) and 84.7 mg (0.45 mmol) of Pa—SO$_3$H were added into an autoclave with 1,4-dioxane (31.5 mg) and acetic acid (0.63 mg) reacted at 120 °C for 3 days. The result-

ing dark red product was washed multiple times with DMSO, 1,4-dioxane, and acetone, and dried under vacuum at 60 °C for 24 h.

Batch Adsorption and Continuous Filtration Experiments: The absorbance at the maximum absorption wavelength (664 nm for MB) of MB solutions with standard concentrations of 0.1, 0.2, 0.5, 1, 2, and 3 mg L^{-1} was measured by a UV–vis spectrophotometer, and the standard curve and fitting equation was obtained.

The adsorption capacity of different composite sponges on MB was explored. At room temperature, soak 10 mg of adsorbent in 100 mL of MB solution (20 mg L^{-1}, pH value was 7), place it on a stirrer with a rotation speed of 200 rpm, until the adsorption equilibrium is reached, and use UV–vis spectroscopy to determine the residual dye in the solution. The concentration of the solution was obtained according to the standard curve and the fitting equation. The dye adsorption capacity (q_e) and removal efficiency (Removal %) are determined by Equations (1) and (2):[37]

$$q_e = \frac{(C_0 - C_e) \cdot V}{m} \tag{1}$$

$$Removal \% = \frac{100 \cdot (C_0 - C_e)}{C_0} \tag{2}$$

where q_e (mg g^{-1}) is the adsorption capacity of the dye at equilibrium; C_0 (mg L^{-1}) is the initial dye concentration; C_e (mg L^{-1}) is the residual dye concentration at equilibrium; V (L) is the volume of dye solution used and m (g) is the mass of adsorbent.

Pseudo-first-order, pseudo-second-order, and intra-particle diffusion kinetic models were used to explore possible adsorption mechanisms and to determine the concentration of residual dye in solution at each time point.[30]

The pseudo-first-order kinetic model equation is as follows:

$$\ln (q_e - q_t) = \ln q_e - k_1 t \tag{3}$$

The pseudo-second-order kinetic model equation is as follows:

$$\frac{1}{q_t} - \frac{1}{q_e} = \frac{1}{k_2 q_e^2 t} \tag{4}$$

The intra-particle diffusion kinetic model equation is as follows:

$$q_t = k_i t^{1/2} + C_i \tag{5}$$

where q_e (mg g^{-1}) is the adsorption capacity of dye at equilibrium, q_t (mg g^{-1}) is the adsorption capacity of dye at time t (min), C_i is the in-

tercept described the effects of boundary layer thickness, k_1 (min^{-1}), k_2 (g mg^{-1} min^{-1}) and k_i (mg g^{-1} min$^{-1/2}$) are the adsorption rate constant of the three models, respectively.

In order to obtain the maximum adsorption capacity and adsorption isotherm of PI/COF—SO$_3$H-2.0 on MB, add 10 mg of PI/COF—SO$_3$H-2.0 to 100 mL of MB with an initial concentration of 20, 50, 100150, 200, 300, and 400 mg L^{-1} respectively. After reaching adsorption equilibrium, measure the concentration of residual dye in the solution and calculate the adsorption amount. The adsorption isotherms were analyzed using the Langmuir and Freundlich isotherm model.[33]

The Langmuir isotherm model was expressed according to the following equation:

$$\frac{C_e}{q_e} = \frac{1}{K_L q_m} + \frac{C_e}{q_m} \tag{6}$$

The Freundlich isotherm model was expressed according to the following equation:

$$\log q_e = \log K_F + \frac{1}{n} \log C_e \tag{7}$$

where C_e (mg L^{-1}) is the concentration of dye in solution at equilibrium, q_e (mg g^{-1}) is the adsorption capacity of dye at equilibrium, K_L (dm^3 mg^{-1}) is the Langmuir constant, q_m (mg g^{-1}) is the Langmuir maximum adsorption capacity, K_F ((mg g^{-1}) (L mg^{-1})$^{1/n}$) is the Freundlich constant, and n indicates the Freundlich exponent.

In the rapid adsorption contrast experiment of PI/COF—SO$_3$H-2.0 and COF—SO$_3$H powder, 10 mg PI/COF—SO$_3$H-2.0, and 5.84 mg COF—SO$_3$H powder were immersed in 5 mL MB (20 mg L^{-1}) solution respectively and placed on a stirrer with a rotation speed of 200 rpm, until the adsorption equilibrium was reached. The concentration of residual dye in the solution at each time point was determined by UV–vis spectroscopy and the removal rate of MB was calculated.

The pH value of the solution affects the adsorption of MB by PI/COF—SO$_3$H-2.0. The pH value of the MB solutions adjusted to pH ranging from 3 to 11 by 0.1 м HCl or 0.1 м NaOH. Then 10 mg of PI/COF—SO$_3$H-2.0 was added to 200 mL of MB solutions (20 mg L^{-1}) with different pH values. After the adsorption equilibrium was reached, the concentration of residual dye in the solution was measured by UV–vis spectroscopy, and the adsorption amount of PI/COF—SO$_3$H-2.0 to MB was calculated.

Put the cylindrical PI/COF—SO$_3$H sponge with a diameter of 1.5 cm and a height of 1 cm into the syringe to make a simple filter device. The pH value of the filtered solution was 7 and the concentration of MB was 10 mg L^{-1}. After filtration, the concentration of residual dye in the filtrate was determined by UV–vis spectroscopy, and the removal efficiency of the dye was calculated according to Equation (2), and the flux was calculated by Equation (8):[38]

$$Flux = \frac{V}{A \cdot t} \tag{8}$$

Where *Flux* (L h^{-1} m^{-2}) is the volume of the dye solution passing through the PI/COF—SO$_3$H sponge per unit time and unit area under self-gravity; A (m^2) is the cross-sectional area of the PI/COF—SO$_3$H sponge; t (h) is the time for the dye solution to filter; V (L) is the volume of dye solution that passes through the sample in time t.

Four simple filtration devices with PI/COF—SO$_3$H-2.0 as filters were connected in series as a whole to filter MB (10 mg L^{-1}, pH value was 7) solution continuously for 24 h. The concentration of residual dye in filtrate at each time point and the corresponding MB removal rate were determined by UV–vis spectroscopy.

In the recyclability experiment, all PI/COF—SO$_3$H sponges were washed with methanol containing 1 mм HCl several times after dye adsorption until completely desorbed as checked by the absence of any MB in the washing solution. The regenerated sponges could be reused after drying in a vacuum.

At room temperature, soak 10 mg of PI/COF—SO$_3$H-2.0 in 100 mL of FL solution (20 mg L^{-1}, pH value was 7), place it on a stirrer with a rotation speed of 200 rpm, until the adsorption equilibrium is reached, and the absorbance of the solution was measured by UV–vis spectroscopy. PI/COF—SO$_3$H-2.0 was used as a filter to filter the mixed solution of 10 mg L^{-1} MB and FL, and the absorbance of residual dye in the filtrate and the corresponding dye removal rate were measured by UV–vis spectroscopy.

Supporting Information

Supporting Information is available from the Wiley Online Library or from the author.

Conflict of Interest

The authors declare no conflict of interest.

Author Contributions

Concepts and resources were generated by S.A.. C.D. designed experiments in consultation with S.A.. C.D. performed all experiments, and analyzed data. Y.D. performed filtration experiments with C.D.. The manuscript was written with the help of all coauthors.

Data Availability Statement

The data that support the findings of this study are available in the supplementary material of this article.

[1] C. J. Doonan, D. J. Tranchemontagne, T. G Glover, J. R. Hunt, O. M. Yaghi, *Nat. Chem.* **2010**, *2*, 235.

[2] S. Wang, Y. Yang, Xu Liang, Y. Ren, H. Ma, Z. Zhu, J. Wang, S. Zeng, S. Song, X. Wang, Y. Han, G. He, Z. Jiang, *Adv. Funct. Mater.* **2023**, *33*, 2300386.

[3] J. Li, S.-Y. Gao, J. Liu, S. Ye, Y. Feng, D.-H. Si, R. Cao, *Adv. Funct. Mater.* **2023**, 2305735.

[4] Q. Sun, B. Aguila, Y. Song, S. Ma, *Acc. Chem. Res.* **2020**, *53*, 812.

[5] H. Yang, L. Yang, H. Wang, Z. Xu, Y. Zhao, Y. Luo, N. Nasir, Y. Song, H. Wu, F. Pan, Z. Jiang, *Nat. Commun.* **2019**, *10*, 2101.

[6] J. Li, X. Jing, Q. Li, S. Li, X. Gao, X. Feng, B. Wang, *Chem. Soc. Rev.* **2020**, *49*, 3565.

[7] N. Keller, T. Bein, *Chem. Soc. Rev.* **2021**, *50*, 1813.

[8] H. S. Sasmal, H. B. Aiyappa, S. N. Bhange, S. Karak, A. Halder, S. Kurungot, R. Banerjee, *Angew. Chem., Int. Ed.* **2018**, *130*, 11060.

[9] K. Dey, S. Kunjattu H, A. M. Chahande, R. Banerjee, *Angew. Chem., Int. Ed.* **2020**, *132*, 1177.

[10] L. Huang, J. Yang, Y. Zhao, H. Miyata, M. Han, Q. Shuai, Y. Yamauchi, *Chem. Mater.* **2023**, *35*, 2661.

[11] a) M. Di, X. Sun, L. Hu, L. Gao, J. Liu, X. Yan, X. Wu, X. Jiang, G. He, *Adv. Funct. Mater.* **2022**, *32*, 2111594; b) S. Hao, T. Zhang, S. Fan, Z. Jia, Y. Yang, *Chem. Eng. J.* **2021**, *421*, 129750.

[12] Y. Li, Q. Wu, X. Guo, M. Zhang, B. Chen, G. Wei, X. Li, X. Li, S. Li, L. Ma, *Nat. Commun.* **2020**, *11*, 599.

[13] C. Fan, H. Wu, J. Guan, X. You, C. Yang, X. Wang, L. Cao, B. Shi, Q. Peng, Y. Kong, Y. Wu, N. A. Khan, Z. Jiang, *Angew. Chem., Int. Ed.* **2021**, *60*, 18051.

[14] C. Ding, M. Breunig, J. Timm, R. Marschall, J. Senker, S. Agarwal, *Adv. Funct. Mater.* **2021**, *31*, 2106507.

[15] A. K. Mohammed, S. Usgaonkar, F. Kanheerampockil, S. Karak, A. Halder, M. Tharkar, M. Addicoat, T. G. Ajithkumar, R. Banerjee, *J. Am. Chem. Soc.* **2020**, *142*, 8252.

[16] a) F. Li, L.-G. Ding, B.-J. Yao, N. Huang, J.-T. Li, Q-J. Fu, Y.-B Dong, *J. Mater. Chem. A* **2018**, *6*, 11140; b) Z. Liu, H. Wang, J. Ou, L. Chen, M. Ye, *J. Hazard. Mater.* **2018**, *355*, 145.

[17] a) Q. Sun, B. Aguila, J. A. Perman, T. Butts, F.-S. Xiao, S. Ma, *Chem* **2018**, *4*, 1726; b) J. Li, Y. Yang, W. Ma, G. Li, Q. Lu, Z. Lin, *J. Hazard. Mater.* **2021**, *411*, 125190.

[18] Y. Xu, T. Wu, Z. Cui, L. Kang, Y. Cai, J. Li, D. Tian, *Sep. Purif. Technol.* **2022**, *303*, 122275.

[19] S. Karak, K. Dey, A. Torris, A. Halder, S. Bera, F. Kanheerampockil, R. Banerjee, *J. Am. Chem. Soc.* **2019**, *141*, 7572.

[20] a) M. Dilamian, M. Joghataei, Z. Ashrafi, C. Bohr, S. Mathur, H. Maleki, *Appl. Mater. Today* **2021**, *22*, 100964; b) X. Xie, Z. Zheng, X. Wang, D. Lee Kaplan, *ACS Nano* **2021**, *15*, 1048; c) X. Dong, L. Cao, Y. Si, B. Ding, H. Deng, *Adv. Mater.* **2020**, *32*, 1908269; d) Q. Fu, Y. Si, C. Duan, Z. Yan, L. Liu, J. Yu, B. Ding, *Adv. Funct. Mater.* **2019**, *29*, 1808234.

[21] a) S. Jiang, B. Uch, S. Agarwal, A. Greiner, *ACS Appl. Mater. Interfaces* **2017**, *9*, 32308; b) G. Duan, S. Jiang, V. Jérôme, J. H. Wendorff, A. Fathi, J. Uhm, V. Altstädt, M. Herling, J. Breu, R. Freitag, S. Agarwal, A. Greiner, *Adv. Funct. Mater.* **2015**, *25*, 2850.

[22] K. Dey, S. Mohata, R. Banerjee, *ACS Nano* **2021**, *15*, 12723.

[23] X. H. Xiong, Z. W. Yu, L. L. Gong, Y. Tao, Z. Gao, L. Wang, W. H. Yin,

[24] a) X. Liao, M. Dulle, J. M. De Souza E Silva, R. B. Wehrspohn, S. Agarwal, S. Förster, H. Hou, P. Smith, A. Greiner, *Science* **2019**, *366*, 1376; b) K. Ruan, Y. Guo, J. Gu, *Macromolecules* **2021**, *54*, 4934.

[25] Y. Han, Q. Zhang, N. Hu, X. Zhang, Y. Mai, J. Liu, X. Hua, H. Wei, *Chin. Chem. Lett.* **2017**, *28*, 2269.

[26] S. Kandambeth, A. Mallick, B. Lukose, M. V. Mane, T. Heine, R. Banerjee, *J. Am. Chem. Soc.* **2012**, *134*, 19524.

[27] P. Pachfule, S. Kandmabeth, A. Mallick, R. Banerjee, *ChemComm* **2015**, *51*, 11717.

[28] L. Liu, L. Yin, D. Cheng, S. Zhao, H.-Y. Zang, N. Zhang, G. Zhu, *Angew. Chem., Int. Ed.* **2021**, *133*, 15001.

[29] a) C. Li, P. Guggenberger, S. W. Han, W. L. Ding, F. Kleitz, *Angew. Chem., Int. Ed.* **2022**, *61*, e202206564; b) Y. Chen, M. Hanshe, Z. Sun, Y. Zhou, C. Mei, G. Duan, J. Zheng, E. Shiju, S. Jiang, *Int. J. Biol. Macromol.* **2022**, *207*, 130.

[30] a) C.-H. Wu, *J. Hazard. Mater.* **2007**, *144*, 93; b) D.-S. Kim, S.-B. Lim, *Sep. Purif. Technol.* **2020**, *250*, 117259.

[31] a) J. Huo, B. Luo, Y. Chen, *ACS Omega* **2019**, *4*, 22504; b) X. Ma, S. Zhao, Z. Tian, G. Duan, H. Pan, Y. Yue, S. Li, S. Jian, W. Yang, K. Liu, S. He, S. Jiang, *Chem. Eng. J.* **2022**, *446*, 136851.

[32] a) S. Jiang, T. Yu, R. Xia, X. Wang, M. Gao, *Mater. Chem. Phys.* **2019**, *232*, 374; b) X. Zhong, Z. Lu, W. Liang, B. Hu, *J. Hazard. Mater.* **2020**, *393*, 122353.

[33] a) L. You, K. Xu, G. Ding, X. Shi, J. Li, S. Wang, J. Wang, *J. Mol. Liq.* **2020**, *320*, 114456; b) B.-C Hu, H.-R. Zhang, S.-C Li, W.-S. Chen, Z.-Yu Wu, H.-W. Liang, H.-P. Yu, S.-H. Yu, *Adv. Funct. Mater.* **2023**, *33*, 2207532.

[34] a) R. Ezzati, *Chem. Eng. J.* **2020**, *392*, 123705; b) S. S. A. Alkurdi, R. A. Al-Juboori, J. Bundschuh, L. Bowtell, A. Marchuk, *J. Hazard. Mater.* **2021**, *405*, 124112.

[35] a) D. Chen, J. Chen, X. Luan, H. Ji, Z. Xia, *Chem. Eng. J.* **2011**, *171*, 1150; b) K. Azam, N. Shezad, I. Shafiq, P. Akhter, F. Akhtar, F. Jamil, S. Shafique, Y.-K. Park, M. Hussain, *Chemosphere* **2022**, *306*, 135566.

[36] a) S. Kandambeth, B. P. Biswal, H. D. Chaudhari, K. C. Rout, S. Kunjattu H, S. Mitra, S. Karak, A. Das, R. Mukherjee, U. K. Kharul, R. Banerjee, *Adv. Mater.* **2017**, *29*, 1603945; b) C. Mao, S. Zhao, P. He, Z. Wang, J. Wang, *Chem. Eng. J.* **2021**, *414*, 128929.

[37] a) G.-H. Ning, Z. Chen, Q. Gao, W. Tang, Z. Chen, C. Liu, B. Tian, X. Li, K. P. Loh, *J. Am. Chem. Soc.* **2017**, *139*, 8897; b) Y. Chen, S. Li, X. Li, C. Mei, J. Zheng, E. Shiju, G. Duan, K. Liu, S. Jiang, *ACS Nano* **2021**, *15*, 20666.

[38] Y. Liu, W. Li, C. Yuan, L. Jia, Y. Liu, A. Huang, Y. Cui, *Angew. Chem., Int. Ed.* **2022**, *61*, e202113348.

194

**ADVANCED
FUNCTIONAL
MATERIALS**

Supporting Information

Open-Cell Robust COF-Nanowire Network Sponges as Sustainable Adsorbent and Filter

Chenhui Ding, Yingying Du and Seema Agarwal*

Supporting Information

Open-cell robust COF-nanowire sponges as sustainable adsorbent and filter

Chenhui Ding, Yingying Du, Seema Agarwal*

C. Ding, Y. Du, Prof. S. Agarwal
Macromolecular Chemistry and Bavarian Polymer Institute
University of Bayreuth
Universitätsstrasse 30, 95440 Bayreuth, Germany
E-mail: agarwal@uni-bayreuth.de

Characterization and instruments

Scanning electron microscopy (SEM, FEI Quanta FEG 250) was used to observe the morphology of COF-SO_3H powder and composite sponges. The Fourier transform infrared (FT-IR) spectra were measured between 650-4000 cm^{-1} on a spectrometer (Digilab Excalibur FTS-3000). The powder X-ray diffraction (PXRD) patterns were carried out on a Bragg-Brentanotype diffractometer (XPERT-PRO, PANalytical B.V.) using Cu Kα radiation (λ = 1.540598 Å). The measuring range of each sample is 2θ = 2° to 40° at a rate of 0.5° min^{-1}. ^{13}C solid-state NMR spectra were obtained on a Bruker Avance III spectrometer operating at a B_0 field of 9.4 T ($v_0(^{13}C)$ = 100.6 MHz and 100.7 MHz). The samples were spun at 12.5 kHz in a 4.0 mm MAS double resonance probe. The MAS spectra were obtained by ramped cross-polarization (CP) experiments under the condition of 70 kHz (4.0 mm) at ^{13}C nutation, and the ^1H nutation frequency v_{nut} varies linearly between 50-100%, conforming to Hartmann-Hahn condition. The contact time was set between 1 to 3 ms. In the acquisition process using proton broadband decoupling, ridge -64 and v_{nut} = 70 kHz. The spectra of TMS (tetramethylsilane) are referenced by secondary standard adamantine. A tensile tester (ZwickiLine Z0.5; BT1-FR0.5TN.D14; Zwick/Roell, Germany) was used for compression testing and cyclic compression testing of the composite sponges at a compression rate of 5 mm min^{-1}. In a freeze dryer, all the dispersion was cooled from room temperature to -50 °C at a cooling rate of 5 °C min^{-1}, kept for 60 minutes, then heated to 20 °C, and dried at 0.25 mbar for 24 hours to obtain various composite sponges. The water contact angle was measured by an automatic

1

WILEY-VCH

goniometer/tensiometer 7 (KRUSS, DSA100, Germany). The thermal stability analysis of PAN/COF-SO$_3$H sponges was carried out using a thermogravimetric analyzer (TGA, TG 209 F1 Libra). Ultraviolet−visible (UV-vis) spectra were recorded on a Jasco Spectrometer V-670 with a measurement range of 400-750 nm (scan speed 200 nm min^{-1}). The concentration wavelengths of methylene blue and fluorescein sodium salt are 664 nm and 490 nm.
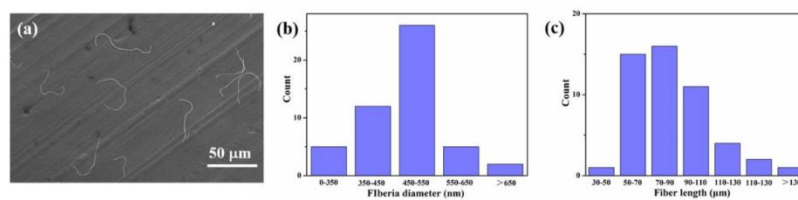
Figure S1. SEM image, diameter, and length distributions of PI short fibers.
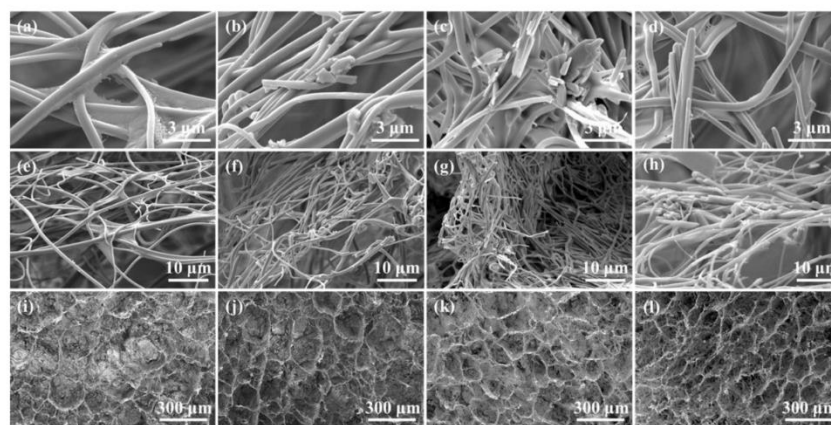
Figure S2. SEM images of PI/Pa-SO$_3$H-0.5 (a, e, i), PI/Pa-SO$_3$H-1.0 (b, f, j), PI/Pa-SO$_3$H-1.5 (c, g, k), PI/Pa-SO$_3$H-2.0 (d, h, l).

2

WILEY-VCH
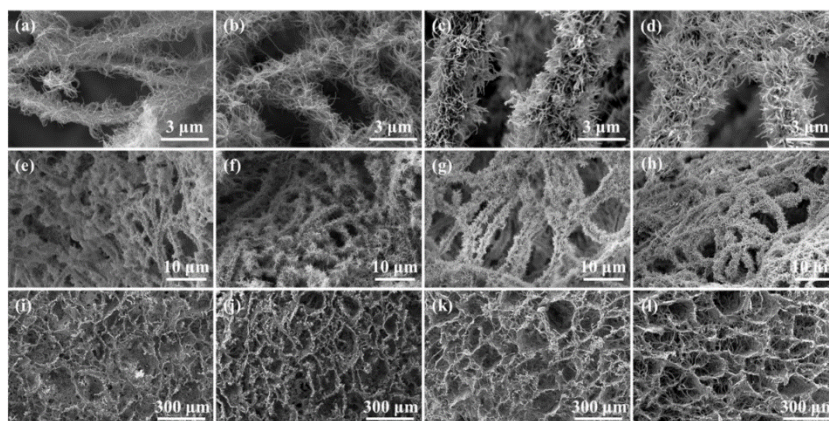
Figure S3. SEM images of PI/COF-SO$_3$H-0.5 (a, e, i), PI/COF-SO$_3$H-1.0 (b, f, j), PI/COF-SO$_3$H-1.5 (c, g, k), PI/COF-SO$_3$H-2.0 (d, h, l).

Table S1. The content of each component in the PI/Pa-SO$_3$H sponges based on the amounts taken during preparation.

Samples	PI (wt. %)	PAN (wt. %)	Pa-SO$_3$H (wt. %)
PI/Pa-SO$_3$H-0.5	40	40	20
PI/Pa-SO$_3$H-1.0	33.3	33.3	33.4
PI/Pa-SO$_3$H-1.5	28.6	28.6	42.8
PI/Pa-SO$_3$H-2.0	25	25	50

3

198

WILEY-VCH

Table S2. The density of PI/COF-SO$_3$H sponges and the content of each component. The total mass of PI and PAN was subtracted from the mass of the PI/ COF-SO$_3$H sponge to get the amount of COF-SO$_3$H.

Samples	density [mg cm^{-3}]	PI (wt. %)	PAN (wt. %)	COF-SO$_3$H (wt. %)
PI/COF-SO$_3$H-0.5	11.2	39.4	39.4	21.2
PI/COF-SO$_3$H-1.0	15.1	30.2	30.2	39.6
PI/COF-SO$_3$H-1.5	26.5	25.3	25.3	49.4
PI/COF-SO$_3$H-2.0	34.8	20.8	20.8	58.4
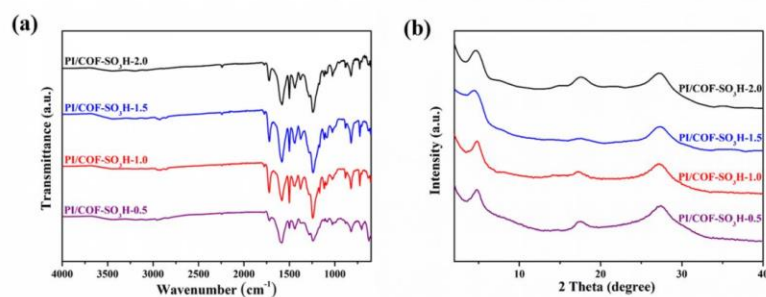
Figure S4. FT-IR spectra (a) and PXRD patterns (b) of PI/COF-SO$_3$H sponges.

4

199
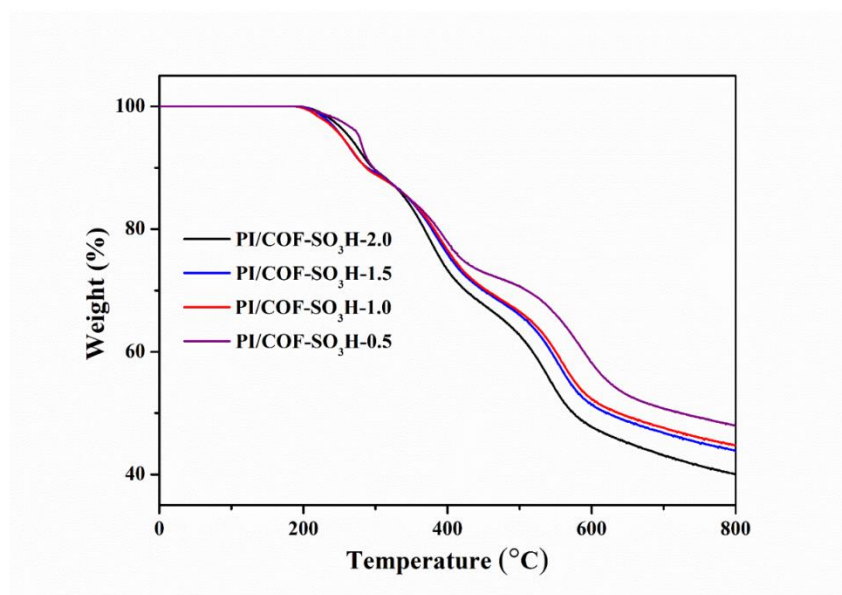
Figure S5. TGA curves of PI/COF-SO$_3$H sponges.

Table S3. Summary of mechanical properties of PI/COF-SO$_3$H sponges.

Samples	Compressive strength [kPa] at 50% strain	Compressive strength [kPa] at 80% strain	Young's modulus [kPa] at 80% strain
PI/COF-SO$_3$H-0.5	12	47	46
PI/COF-SO$_3$H-1.0	16	61	71
PI/COF-SO$_3$H-1.5	28	120	152
PI/COF-SO$_3$H-2.0	36	175	238

5
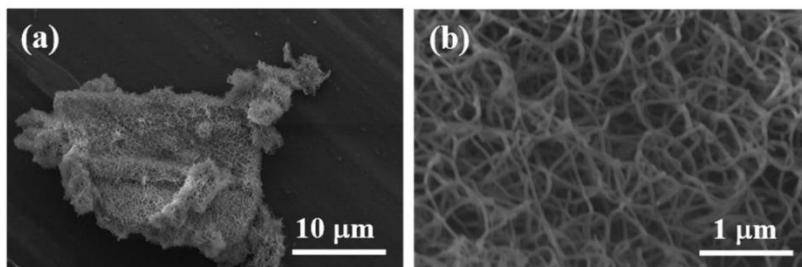
WILEY-VCH

Figure S6. SEM images of COF-SO₃H powder with different magnifications.
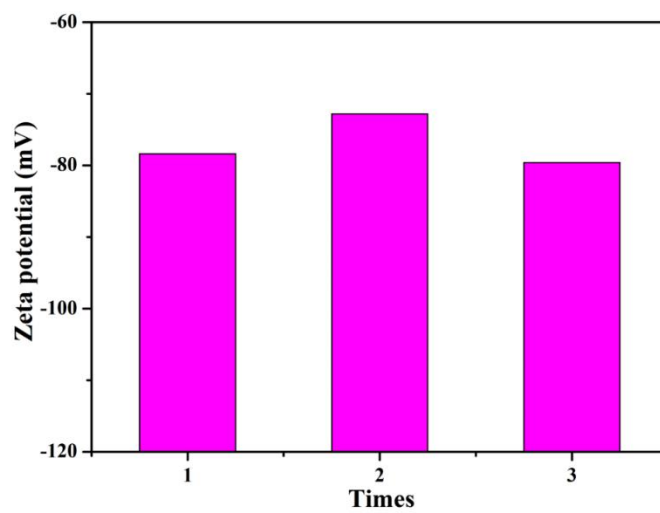
Figure S7. The zeta potential value of COF-SO₃H powder (measured 3 times).

6
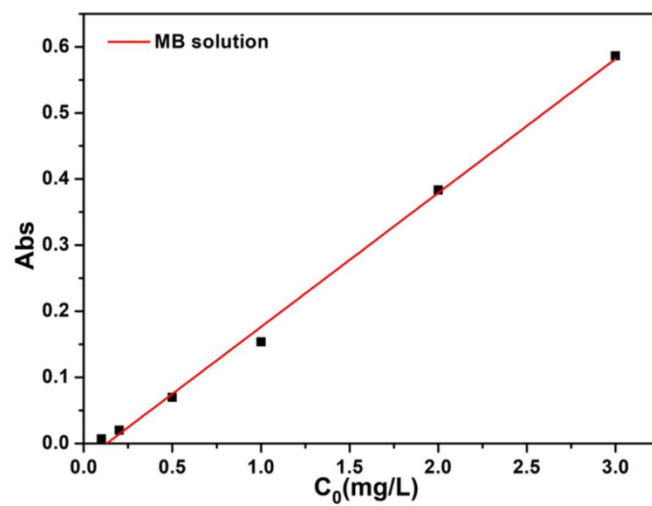
Figure S8. The standard curve and fitting equation of MB solution.

7
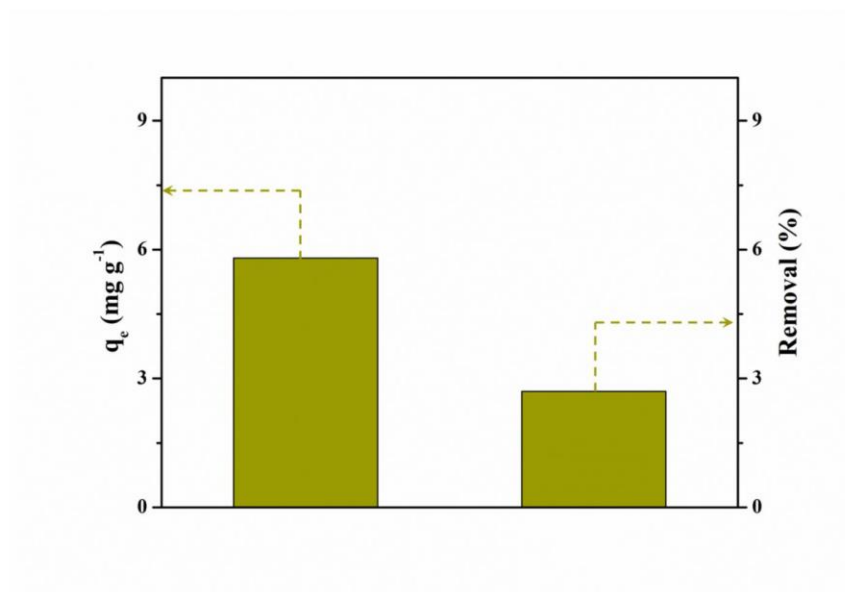
WILEY-VCH

Figure S9. The dye adsorption capacity and removal efficiency of MB by PI-PAN blank sponge.

8
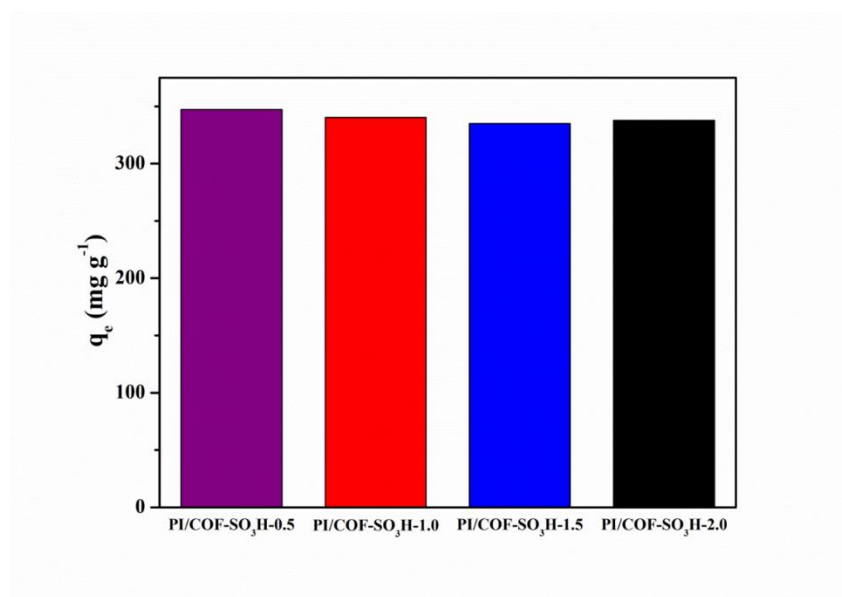
Figure S10. The dye adsorption capacity of MB by COF in PI/COF-SO₃H sponges.

9

WILEY-VCH

Table S4. Kinetic model parameters for MB adsorption by PI/COF-SO$_3$H-2.0.

Models	Parameters	PI/COF-SO$_3$H-2.0
Pseudo-first-order	k_1 (min^{-1})	0.0243
	qe (mg g^{-1})	189.54
	R^2	0.9744
Pseudo-second-order	k_2 (g mg min^{-1})	0.3981×10^{-3}
	qe (mg g^{-1})	204.08
	R^2	0.9865
Intra-particle diffusion	k_{i1}	0.1883×10^2
	k_{i2}	5.9713
	C_{i1}	6.2715
	C_{i2}	0.1167×10^3
	R_1^2	0.9691
	R_2^2	0.9719

10

205

WILEY-VCH
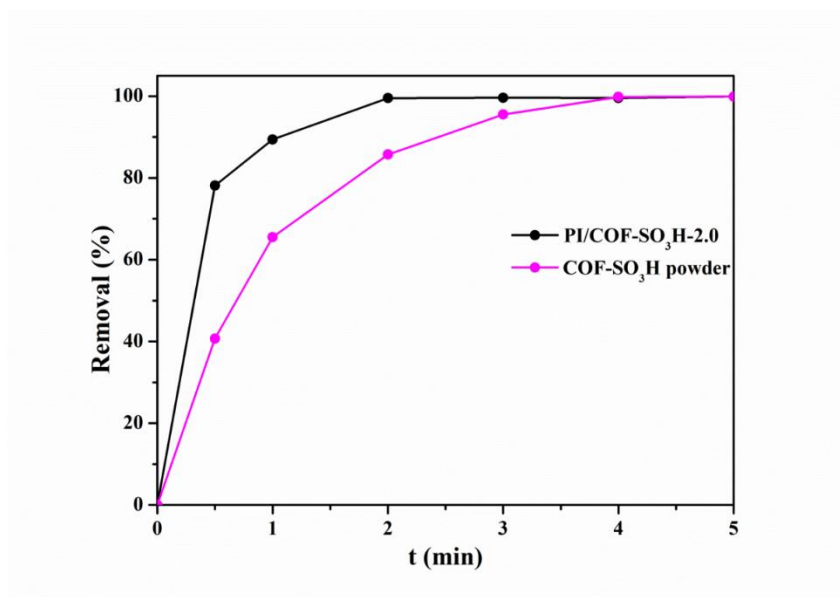
Figure S11. Comparison of equilibrium times of adsorption by PI/COF-SO$_3$H-2.0 and COF-SO$_3$H powder for MB.

11

Table S5. Equilibrium adsorption isotherm of MB on PI/COF-SO₃H-2.0.

Models	Parameters	PI/COF-SO₃H-2.0
	q_m (mg g^{-1})	413.93
Langmuir	k_L (L mg^{-1})	0.0383
	R^2	0.9845
	k_F ((mg g^{-1}) (L mg^{-1})$^{1/n}$)	0.1154×10^3
Freundlich	n	4.7189
	R^2	0.9609
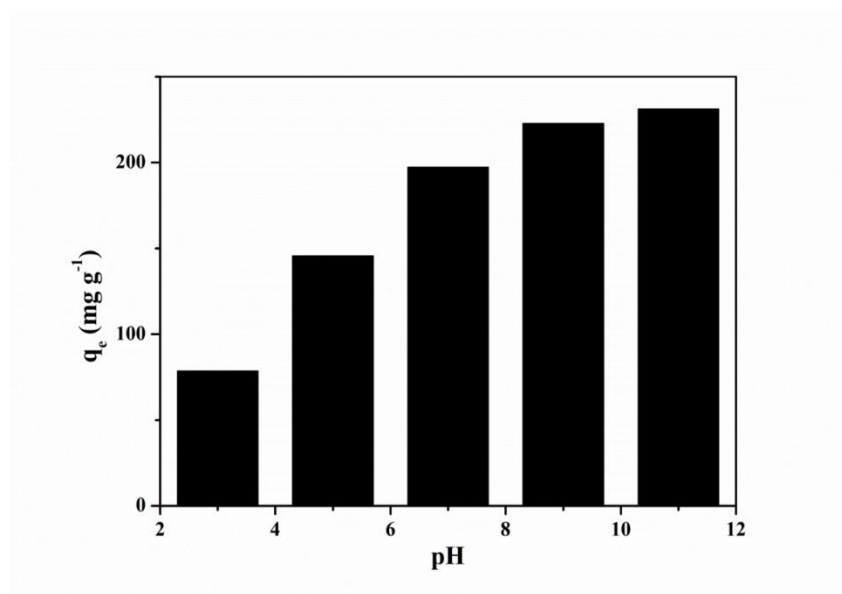
Figure S12. Effect of initial pH value on MB adsorption by PI/COF-SO₃H-2.0.

12
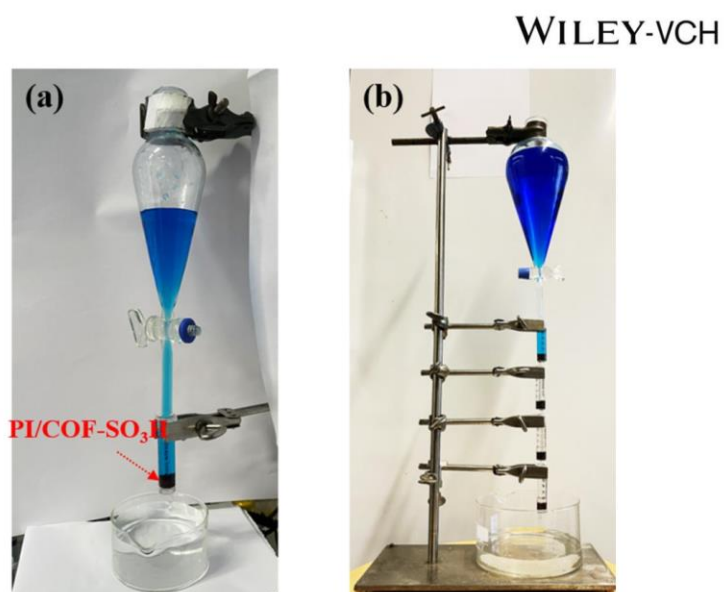
Figure S13. Photograph of PI/COF-SO$_3$H sponges and syringe assembled facile filter for removal of MB, one syringe (a), and four syringes (b).
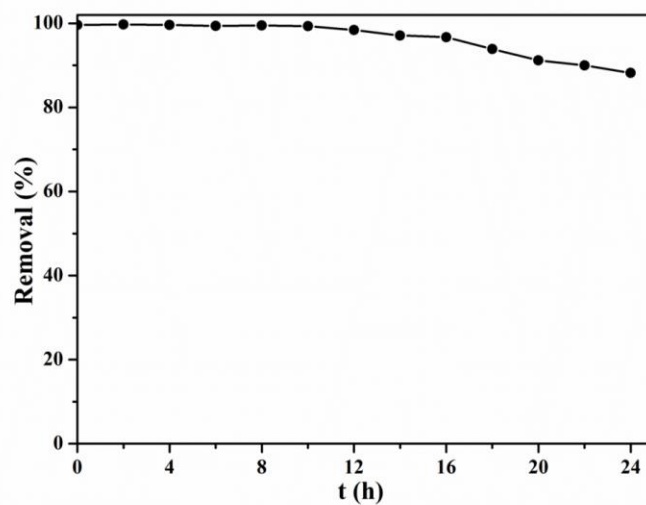
Figure S14. Filtration removal efficiency of MB by PI/COF-SO$_3$H-2.0 within 24 hours.

13

WILEY-VCH
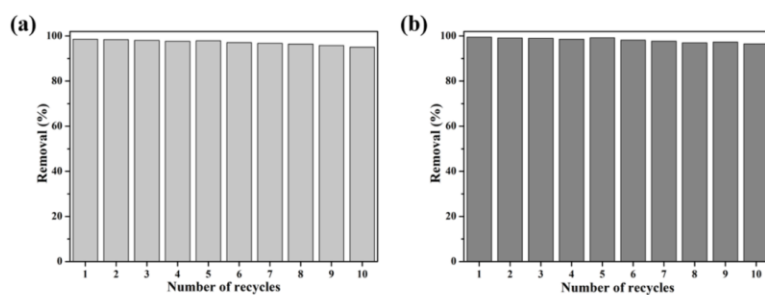
Figure S15. Removal efficiency after regeneration cycles of PI/COF-SO$_3$H-2.0, as adsorbent (a), and as filter (b).

Table S6. Comparison of MB adsorption capacity and recycling performance of different porous materials known in the literature.

Adsorbents	Capacity (mg g^{-1})	Number of cycles	Removal efficiency after recycling (%)	Ref.
Fe$_3$O$_4$-GS	526	10	37	[1]
CKS sponge	1250	5	93	[2]
Kg-Ch sponge	32.62	6	90	[3]
LFs-PSSS	409.67	5	>70	[4]
PU@D-ACB/CaA	386.49	5	77	[5]
CNF/rectorite composite sponge	214.6	6	82.6	[6]
RCE/GO composite aerogel	68	5	86	[7]
GO-CNF composite foam	173.3	3	~90	[8]

14

cellulose/AC composite monolith	159	8	89	[9]
CEF	447.69	4	~90	[10]
PI/COF-SO$_3$H sponge	653	10	95	This work

Abbreviations: Fe$_3$O$_4$-GS :Fe$_3$O$_4$ graphene sponge; CKS sponge: crosslinked (C) tree gum kondagogu (K) and sodium alginate (S) sponge; Kg-Ch sponge: karaya gum-chitosan sponge; LFs-PSSS: loofah sponge-Sodium 4-styrene sulfonate; PU@D-ACB.CaA: polyurethane@disc-derived activated carbon black/calcium alginate composite sponge; CNF/rectorite composite sponge: cellulose nanofibril/rectorite composite sponge; RCE/GO composite aerogel: regenerated cellulose/graphene oxide composite aerogel; GO-CNF composite foam: graphene oxide/chitin nanofibrils composite foam; cellulose/AC composite monolith: cellulose/activated carbon composite monolith; CEF: cellulose based cation-exchange fibrous bio-adsorbent; PI/COF-SO$_3$H sponge: polyimide/COF-SO$_3$H sponge.
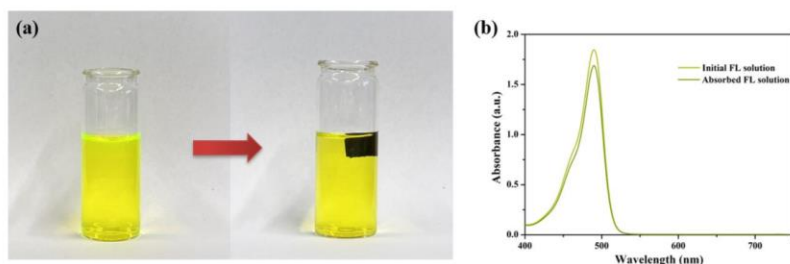
Figure S16. PI/COF-SO$_3$H-2.0 adsorption FL test (a). UV-vis spectra of FL before and after adsorption (b).

15

WILEY-VCH

References

[1]   C. J. Doonan, D. J. Tranchemontagne, T. G. Glover, J. R. Hunt, O. M. Yaghi, *Nat. Chem.* **2010**, *2*, 235-238.

[1]   B. Yu, X. Zhang, J. Xie, R. Wu, X. Liu, H. Li, F. Chen, H. Yang, Z. Ming, S.-T. Yang, *Appl. Surf. Sci.* **2015**, *351*, 765-771.

[2]   R. K. Ramakrishnan, V. V. T. Padil, S. Wacławek, M. Černík, D. Tiwari, *J. Environ. Chem. Eng.* **2022**, *10*, 108285.

[3]   R. K. Ramakrishnan, V. V. T. Padil, S. Wacławek, M. Černík, R. S. Varma, *Polymers (Basel)* **2021**, *13*, 1.

[4]   Y. Zhao, T. Chen, X.-F. Song, J.-Y. Yang, Y.-Y. Wang, Y.-S. Li, Y. Liu, *Arab. J. Chem.* **2022**, *15*, 104382.

[5]   S. Mallakpour, V. Behranvand, *J. Clean. Prod.* **2021**, *312*, 127513.

[6]   Y. Chen, M. Hanshe, Z. Sun, Y. Zhou, C. Mei, G. Duan, J. Zheng, S. E, S. Jiang, *Int. J. Biol. Macromol.* **2022**, *207*, 130-139.

[7]   F. Ren, Z. Li, W. Z. Tan, X. H. Liu, Z. F. Sun, P. G. Ren, D. X. Yan, *J. Colloid Interface Sci.* **2018**, *532*, 58-67.

[8]   Z. Ma, D. Liu, Y. Zhu, Z. Li, Z. Li, H. Tian, H. Liu, *Carbohydr. Polym.* **2016**, *144*, 230-237.

[9]   Q. Bai, Q. Xiong, C. Li, Y. Shen, H. Uyama, *Cellulose* **2017**, *24*, 4275-4289.

[10]   X. Shao, J. Wang, Z. Liu, N. Hu, M. Liu, C. Duan, R. Zhang, C. Quan, *Cellulose* **2021**, *28*, 9355-9367.

16

211

4.5 Sustainable Hierarchically Porous Reusable Metal-Organic Framework Sponge as a Heterogeneous Catalyst and Catalytic Filter for Degradation of Organic Dyes

Yingying Du, **Chenhui Ding**, Seema Agarwal. Sustainable Hierarchically Porous Reusable Metal-Organic Framework Sponge as a Heterogeneous Catalyst and Catalytic Filter for Degradation of Organic Dyes. Advanced Energy and Sustainability Research, **2023**, 2300218.

Sustainable Hierarchically Porous Reusable Metal–Organic Framework Sponge as a Heterogeneous Catalyst and Catalytic Filter for Degradation of Organic Dyes

Yingying Du, Chenhui Ding, and Seema Agarwal*

Advanced oxidation processes based on sulfate radical are considered one of the most promising wastewater treatment technologies currently. Among heterogeneous catalysts, cobalt metal–organic framework (MOF) has been widely reported. However, the inherent powder form of MOF hinders its practical application and reusability. Therefore, innovative methods to increase the loading capacity and the accessibility of MOF active sites in monolithic materials are required. Therefore, a simple and scalable method of fabricating a stable, hierarchical porous zeolitic imidazolate framework (ZIF-67) 3D sponge by growing MOF on a short electrospun fiber network is shown. The sponge can efficiently activate peroxymonosulfate and rapidly degrade an exemplary organic dye (Rhodamine B) with a degradation efficiency of 100%. The resulting multilevel, hierarchical porous structure is beneficial to the mass transfer of reagents making the catalytic process efficient. This also enables the use of the ZIF-67 as an efficient catalytic filter for continuous removal of dye. The sponge can be recycled and reused for several cycles due to its robustness without loss in efficiency. The proposed research strategy provides a new way to design MOF 3D monolithic materials.

1. Introduction

Water resources are an integral part of human development and life. However, organic dye discharges from industries such as textiles, cosmetics, papermaking, and leather pollute water resources every year.[1] Organic dyes are generally toxic and highly stable and are difficult to degrade and handle.[2] The consumption of dye-contaminated water can lead to serious health issues.[3] Therefore, the wastewater treatment of organic dyes has always been an important issue that researchers have paid close attention. At present, the technical means commonly used in wastewater treatment include adsorption,[4] filtration,[5] membrane separation,[6] coagulation,[7] and so on. However, these methods only transfer the dye to the material, and there are still secondary pollution problems, which greatly increase the operation and time costs of the treatment. Therefore, other cost-effective wastewater treatment technologies should be further developed.

The advanced oxidation process is to oxidize active species to decompose organic dyes into low-toxic small molecules or water and carbon dioxide through redox reactions.[8] It is one of the most promising wastewater treatment technologies at present. Among them, sulfate radical based advanced oxidation processes (SR-AOPs) have attracted extensive attention of researchers due to the wide source of sulfate radical, high oxidation potential (2.5–3.1 V), wide pH value working range (3.0–9.0), and excellent reaction selectivity.[9] Sulfate radicals are usually produced by activating peroxomonosulfate (PMS) and peroxydisulfate through photolysis, ultrasound, transition metal ions, and their metal oxides.[10] However, the traditional activation method still has problems such as insufficient catalytic performance and secondary contamination (difficult recovery of catalyst).[11] Therefore, the development of materials with immobilized catalysts/catalytic species with high activity and stability is the development trend of SR-AOPs.

Metal–organic frameworks (MOFs) are emerging porous materials, which are widely used in catalysis, separation, sensing, and other fields due to their high specific surface area, ordered porous structure, and multifunctional active sites.[12] In particular, cobalt (Co)-based zeolite-like imidazole-based organic frameworks (ZIFs) with Co as the metal ion and imidazolium salt as the organic ligand have been reported for the degradation of organic dyes by activating persulfate.[13] However, due to the inherent difficulty of processing and recycling of ZIFs in the form of powder nanocrystals, their application in practical use is hindered.[14] In order to solve this problem, researchers usually immobilize ZIF particles on supporting carriers, such as films,[15] foams,[16] resins,[17] and so on to obtain ZIF composites with higher practicability and functionality. However, there are still problems such as insufficient loading

Y. Du, C. Ding, S. Agarwal
Macromolecular Chemistry and Bavarian Polymer Institute
University of Bayreuth
Universitätsstrasse 30, 95440 Bayreuth, Germany
E-mail: agarwal@uni-bayreuth.de

ⓘ The ORCID identification number(s) for the author(s) of this article can be found under https://doi.org/10.1002/aesr.202300218.

213

of ZIF and poor availability of active sites of ZIF in composites.[14a,18]

In this work, we first show a procedure of loading ZIF-67 in large amounts (as large as 72%) on a 3D porous fibrous network skeleton of polyimide (PI) electrospun short fibers. In our previous works, we established a method of making PI porous frameworks (sponges) using short electrospun fibers and showed its use as pressure sensors, heat insulation, etc., and skeleton for the growth of covalent organic framework.[19] The present method allows in situ growth of ZIF-67 onto the surface of PI network fibers of the 3D skeleton and thereby bringing ZIF-67 in the shape of a 3D sponge with hierarchical porosity and mechanical stability. The hierarchically porous network facilitates the transport of reagents required for the efficient degradation of organic dyes and at the same time, it exposes a plenty of active sites (ZIF-67) for degradation reaction. After establishing the preparation procedure, the practicability of polymer–MOF sponge as a reusable catalyst to activate PMS for the degradation of organic dye Rhodamine B (Rh B) under different conditions was shown. The unique hierarchical porous structure of the sponge leads to a good water flux and therefore, its utility as a filter for continuous degradation of organic dye is also shown by assembling a simple filter device. This work provides a new avenue for applying MOF-based composites to practical wastewater treatment technologies as efficient reusable heterogeneous materials and filters.

2. Results and Discussion

The preparation process of PI/PAN@ZIF-67 sponge is shown in **Figure 1**. First, PI short fibers, polyacrylonitrile (PAN), and $Co(NO_3)_2 \cdot 6H_2O$ are dispersed in dimethyl sulfoxide (DMSO), and the PI/PAN/Co^{2+} sponge with honeycomb frame structure is obtained by freeze-drying. PI short fibers were prepared by mechanical cutting of a PI nonwoven prepared by electrospinning as described in our previous work.[20] PI fibers had an average diameter $d = 521 \pm 143.0$ nm and length $L = 77 \pm 33$ μm, respectively. Fifty short fibers were randomly selected in scanning electron microscope (SEM) images for calculating the average diameter and length using ImageJ software (Figure S1, Supporting Information). PAN as a binder ensures the stability of PI short fibers in the 3D structure and makes Co^{2+} uniformly dispersed on the surface of PI short fibers, providing a great deal of sites for the growth of ZIF-67. Then the PI/PAN/ Co^{2+} sponge was put into the precursor solution of ZIF-67 (aqueous solution of Co nitrate hexahydrate and 2-methylimidazole), and ZIF-67

grew in situ on the surface of the PI fiber to obtain a sponge in which ZIF-67 was grown on the surface of fibers making network porous PI/PAN template sponge. The final sponge is designated as PI/PAN@ZIF-67. It is worth noting that stirring is necessary during the preparation of PI/PAN@ZIF-67 sponge. If there is no stirring, the nucleation of ZIF-67 is slow, and it is easy to generate larger sized particles, which leads to nonadherence and easy detachment from the sponge surface giving defects and low ZIF-67 loading (Figure S2, Supporting Information). The loading of ZIF-67 was determined according to the mass change of PI/PAN/Co^{2+} sponge after the growth of ZIF-67. The loading of ZIF-67 could be as high as 72%.

The morphology of the samples was analyzed by SEM. **Figure 2**a shows the optical picture of PI/PAN@Co^{2+} sponge. A honeycomb structure with uniform macroscopic and microscopic pores was visible (Figure 2b). The wall of the sponge is composed of PI short fibers interwoven with each other, and the PI short fibers have a relatively smooth and clean surface (Figure 2c,d). It can be clearly observed that the wall of the PI/PAN@Co^{2+} sponge is a porous network structure with micron-scale pores (4–30 μm) formed by percolation of fibers. This porous network structure provides amount of growth sites and reaction space for ZIF-67 formation, indicating its excellent performance as a carrier. The energy dispersive spectrometer (EDS) spectrum of PI/PAN/Co^{2+} sponge proves that Co^{2+} was successfully attached to the surface of PI short fibers and dispersed uniformly (Figure 2e–h). This provides lots of nucleation sites for the growth of ZIF-67. The honeycomb porous network structure of PI/PAN@Co^{2+} sponge was maintained after in situ growth of ZIF-67 (Figure 2j). The surface of PI short fibers is completely covered by lots of ZIF-67 particles (Figure 2k,l). The in situ growth of ZIF-67 on the PI short fiber enables the internal active sites in the ZIF-67 structure to be well preserved. The nanopores of the ZIF-67 itself, the micropores between the cross-linked PI short fibers, and the macroscopic and regular honeycomb macropores of the sponge form a 3D structure of multilevel and hierarchical macro–micropores. This structure can not only expose the active site of ZIF-67 to promote the activation of PMS, but also facilitate the intermolecular mass transfer in the solution to accelerate the degradation of the dye.

We used X-Ray diffraction (XRD) to analyze the crystal properties of PI/PAN and PI/PAN@ZIF-67 sponges, as shown in **Figure 3**a. For the PI/PAN sponge, 2θ at 17.5° corresponding to the (0 0 1) has a broad characteristic diffraction peak.[21] The peaks at 7.4°, 10.5°, 12.9°, 14.8°, 16.6°, and 18.2° belong
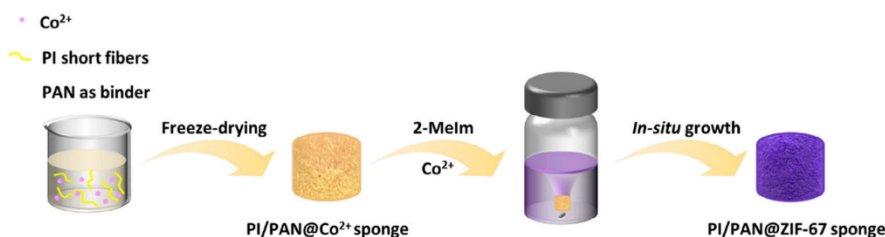

Figure 1. Preparation of the PI/PAN@ZIF-67 sponge: Co^{2+} comes from $Co(NO_3)_2 \cdot 6H_2O$; 2-MeIm is 2-methylimidazole.
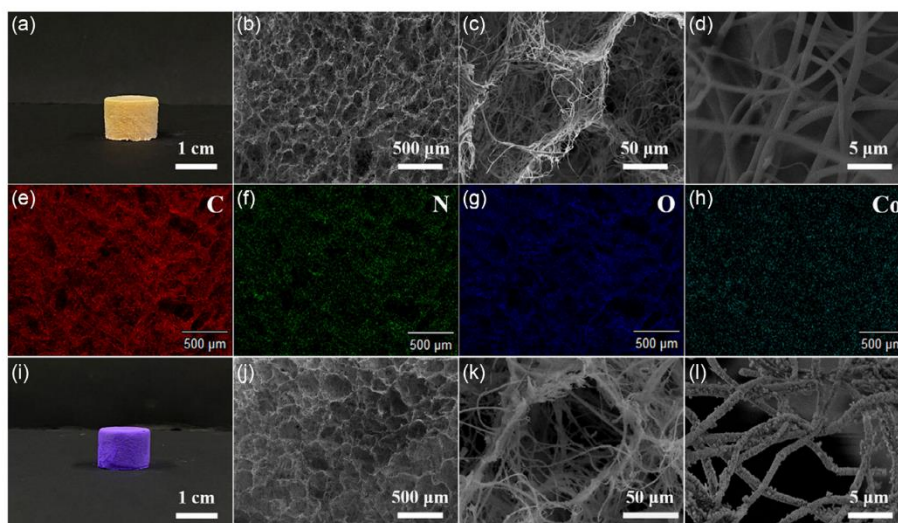
2300218 (2 of 9)

Figure 2. The photo of a) PI/PAN@Co^{2+} sponge and i) PI/PAN@ZIF-67 sponge, b–d) SEM images of PI/PAN@Co^{2+} sponge, e–h) EDS spectrum of PI/PAN@Co^{2+} sponge, and j–l) SEM images of PI/PAN@ZIF-67 sponge.
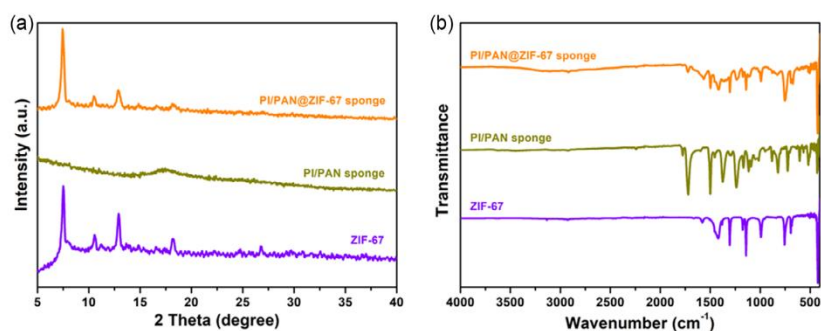

Figure 3. a) The XRD patterns of ZIF-67 powder, PI/PAN sponge, and PI/PAN@ZIF-67 sponge; b) FT-IR spectra of ZIF-67, PI/PAN sponge, and PI/PAN@ZIF-67 sponge.

to the (011), (0 0 2), (11 2), (0 0 2), (0 1 3), and (2 2 2) crystalline planes of ZIF-67.[13a] In the XRD pattern of PI/PAN@ZIF-67 sponge, the characteristic diffraction peaks of PI/PAN and ZIF-67 could be well confirmed. This indicates the successful preparation of PI/PAN@ZIF-67 sponges.

The Fourier transform infrared (FT-IR) spectrum of the PI/PAN@ZIF-67 sponge is shown in Figure 3b. The characteristic stretching bands at 425, 992, and 1570 cm^{-1} are attributed to the Co—N, C—N, and C=N of ZIF-67.[22] The peak at 1364 cm^{-1} is the C—N stretching of the PI imide ring; 1715 and 1779 cm^{-1} are the symmetric and asymmetric stretching vibration peaks of C=O in the PI imide ring, respectively.[23] 2240 cm^{-1} is attributed to the C≡N stretching vibration peak in PAN.[24]

The mechanical properties and shape recovery ability of the sponge are particularly important for any practical use, and they

were evaluated by cyclic compression experiments. **Figure 4**a,b shows the cyclic compressive stress–strain curves of PI/PAN and PI/PAN@ZIF-67 sponges, respectively. It can be found that the compressive strength of PI/PAN is only 5.0 kPa (50% strain), and the sponge height is compressed by about 25.8% after 50 cycles of compression, indicating that the internal structure has undergone serious collapse. The compressive strength of the PI/PAN@ZIF-67 sponge was 28.1 kPa (50% strain), and the height decreased only by 9.9% after 300 cycles of compression. This is due to the fact that the PI/PAN@ZIF-67 sponge consists of two parts: the soft PI short fibers and the hard ZIF-67. The hard ZIF-67 grown on the surface of PI short fibers in situ can significantly improve the mechanical properties of PI/PAN@ZIF-67 sponge and ensure its structural stability. In addition, the 0.1 g PI/PAN@ZIF-67 sponge can withstand
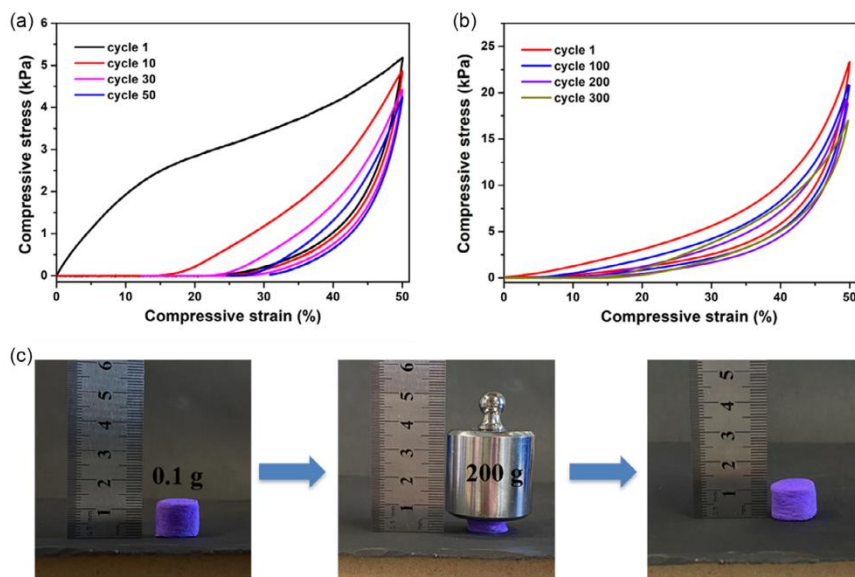
Figure 4. Cyclic compressive stress–strain curves at 50% strain for a) PI/PAN sponge, b) PI/PAN@ZIF-67 sponge, an c) compressive capacity of PI/PAN@ZIF-67 sponge.

a weight of 200 g without collapsing (Figure 4c), further demonstrating its excellent robustness.

Using Rh B as a typical example, we explored the potential of PI/PAN@ZIF-67 sponge as a catalyst in activating PMS for the degradation of organic dyes. **Figure 5** shows the degradation of Rh B under different catalytic systems. To rule out the possible adsorption effect of the sponge in the removal of Rh B from the aqueous solution, we tested the change in the dye concentration
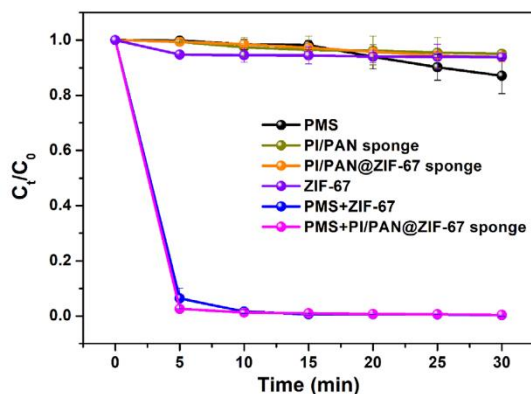
Figure 5. Plots of C_t/C_0 versus time for studying the degradation of Rh B under different conditions. Reaction conditions: Rh B concentration $= 50\,mg\,L^{-1}$, PMS concentration $= 1.5\,mM$, catalyst amount $= 100\,mg\,L^{-1}$, pH $= 7$, temperature $= 25\,°C$.

after putting PI/PAN sponge, PI/PAN@ZIF-67 sponge, and ZIF-67 in the Rh B solution, respectively. The results showed a small decrease (4.9%, 6.2%, and 5.2%, respectively) in Rh B concentration after 30 min as determined by UV–vis spectrophotometer (the concentration of Rh B was evaluated at a wavelength of 555 nm). A Rhodamine solution with only PMS (no sponge) showed 12.9% of Rh B degradation. This indicates that without the activation by a catalyst, PMS cannot effectively degrade dyes. However, when PMS was activated by PI/PAN@ZIF-67 sponge, the Rh B dye was degraded up to 97.4% within 5 min and completely degraded within 30 min. These results indicate that PI/PAN@ZIF-67 sponge can efficiently activate PMS. In addition, we also studied the degradation of Rh B in the presence of ZIF-67 particles and PMS, and the results showed that 93.6% of Rh B degraded within 5 min. This shows that in comparison to ZIF-67 powder, the degradation effect of PI/PAN@ZIF-67 sponge is not compromised. In addition, the degradation kinetics of Rh B conform to the pseudo-first-order rate law-ln $C_t/C_0 = kt$, and the kinetic rate is shown in Figure S3, Supporting Information.

Dye solution of different concentrations (from 25 to $100\,mg\,L^{-1}$) was used to study the degradation by PI/PAN@ZIF-67 sponge-activated PMS (**Figure 6**a). When the initial concentration of the dye was reduced from 100 to $25\,mg\,L^{-1}$, the degradation of Rh B within 5 min increased from 68.8% to 100%. It is worth mentioning that when the dye concentration is $25\,mg\,L^{-1}$, the dye can be completely degraded within 20 s as shown in Figure S4, Supporting Information. However, when the dye concentration was $20\,mg\,L^{-1}$ or below, the degradation was immediate. The degradation kinetics could not be followed due to the very fast rate of degradation for
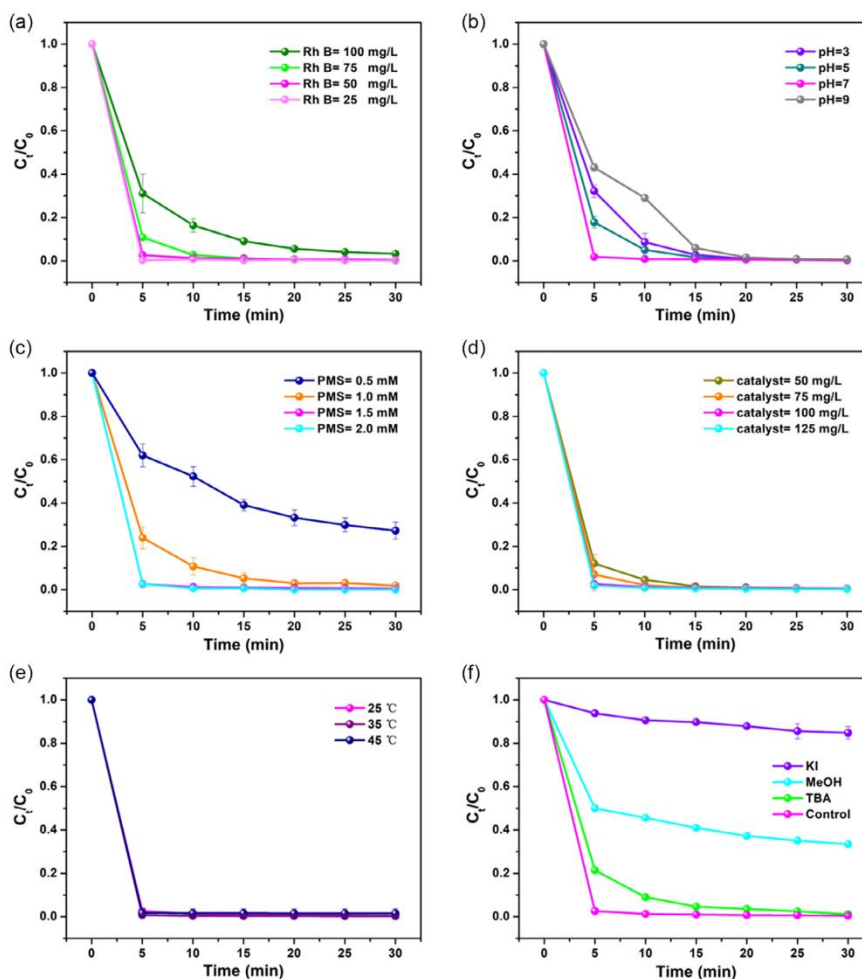
Figure 6. Plots of C_t/C_0 versus time for studying the effect of a) the dye (Rh B) concentration, b) pH, c) the concentration of PMS, d) the dosage of catalyst (PI/PAN@ZIF-67 sponge), e) temperature, and f) radical scavengers on the Rh B degradation. The data for (a) were collected using PMS concentration $= 1.5$ mM, catalyst amount $= 100$ mg L^{-1}, pH $= 7$, temperature $= 25$ °C. The data for (b) were collected using Rh B solution concentration $= 50$ mg L^{-1}, PMS concentration $= 1.5$ mM, catalyst amount $= 100$ mg L^{-1}, and temperature $= 25$ °C. The data for (c) were collected using Rh B solution concentration $= 50$ mg L^{-1}, catalyst amount $= 100$ mg L^{-1}, pH $= 7$, temperature $= 25$ °C. The data for (d) were collected using Rh B solution concentration $= 50$ mg L^{-1}, PMS concentration $= 1.5$ mM, PH $= 7$, and temperature $= 25$ °C. The data for (e) were collected using Rh B solution $= 50$ mg L^{-1}, PMS concentration $= 1.5$ mM, catalyst mount $= 100$ mg L^{-1}, pH $= 7$. The data for (f) were collected using Rh B solution concentration $= 50$ mg L^{-1}, PMS concentration $= 1.5$ mM, catalyst amount $= 100$ mg L^{-1}, pH $= 7$ and temperature $= 25$ °C.

concentrations below 20 mg L^{-1}. Therefore, 50 mg L^{-1} dye concentration was chosen as a benchmark for further experiments.

pH of the solution can have a significant effect on the degradation process. Figure 6b shows the effect of different pH (3.0–9.0) values on the degradation of dye by PI/PAN@ZIF-67 sponges. When pH $= 3.0$, only 67.8% of Rh B degraded within 5 min. This may be because, under acidic conditions, H$^+$ makes HSO$_5^-$ more stable, which inhibits the formation of free radicals and reduces the degradation rate.[25] When pH $= 5.0$, 82.1% of

Rh B was degraded within 5 min, which was close to that of pH $= 7.0$. However, when pH $= 9.0$, only 56.9% of Rh B could be degraded within 5 min. Under alkaline conditions, PMS self-decomposes, and the content of free radicals generated therefore decreases slowing down the degradation of dyes.[26] But fortunately, the degradation of Rh B can be as high as more than 99% under different pH values within 30 min. This indicated that PI/PAN@ZIF-67 sponge can activate PMS to degrade organic pollutant dyes in a wide pH range. When the pH is

3.0, 5.0, 7.0, and 9.0, the rate constant K values for degradation are 0.24, 0.30, 0.47, and 0.09 min^{-1}, respectively (Figure S5, Supporting Information).

As the main source of free radicals, the added amount of PMS is very important in the degradation process of dyes. The effect of PMS content on the degradation of Rh B is shown in Figure 6c. When the content of PMS was 0.5 mM, only 37.9% of the Rh B was degraded within 5 min, and only 72.7% of the dye was degraded within 30 min. However, when the content of PMS was increased to 1 mM, the degradation of dye increased to 76.1% within 5 min and Rhodamine degradation reached 98.1% within 30 min, which significantly improved the degradation situation. The results showed that an optimum amount of PMS is required so that sufficient free radicals are generated making the degradation occur effectively. This shows that the content of added PMS is very important to the degradation of the dye. Furthermore, when the content of PMS continued to increase to 2 mM, there was little difference compared to the time when PMS was 1.5 mM. This is because the content of the PI/PAN@ZIF-67 sponge was fixed, and the active sites of the PI/PAN@ZIF-67 sponge for activating PMS had reached saturation. Even if the content of PMS continues to increase, the catalyst cannot continue to activate the excess PMS. Therefore, the PMS content of 1.5 mM is the best choice. This result is also reflected in the kinetics. When the PMS content increases from 0.5 to 2.0 mM, the k values were 0.06, 0.22, 0.44 and 0.44 min^{-1}, respectively (Figure S6, Supporting Information).

Figure 6d shows the effect of the amount of catalyst (sponge) on the degradation of dyes. The degradation of the dye increased from 87.8% to 97.4% within 5 min on increasing the amount of catalyst from 50 to 100 mg L^{-1}. The k value increased from 0.31 to 0.44 min^{-1} (Figure S7, Supporting Information). On further increase in the catalyst content to increase to 125 mg L^{-1}, 98% of the Rh B was degraded within 5 min ($k = 0.44$ min^{-1}). Compared with the catalyst addition of 100 mg L^{-1}, there is no obvious increase. This suggests that at high catalyst dosage, the efficiency of PMS to utilize the excess active sites at the PI/PAN@ZIF-67 sponge to generate free radicals is limited. Therefore, 100 mg L^{-1} catalyst is the optimal input amount.

In addition, we also examined the effect of PI/PAN@ZIF-67 sponge-activated PMS on dye degradation at different temperatures (Figure 6e). There was no significant difference in the % degradation observed on raising the temperature from 25 to 45 °C (Figure S8, Supporting Information).

To understand the catalytic process of PI/PAN@ZIF-67 sponge, we explored the reaction mechanism. In previous reports, it has been proved that Co ions in ZIF-67 can undergo cyclic conversion in divalent and trivalent states, activating PMS to produce sulfate and hydroxide radicals, which have higher oxidation-reduction potential, can eventually oxidize the dye to water and carbon dioxide as in Equation (S1)–(S4), Supporting Information.[17] We conducted a series of reactive oxygen species (ROS) capture experiments to find out which radical is mainly taking part in the degradation process. It is known that potassium iodide (KI) can effectively capture both sulfate and hydroxide radicals, whereas methanol (MeOH) is selective in capturing sulfate radicals. On the other hand, tert-butanol (TBA) traps hydroxide radicals.[15] As shown in Figure 6f, when KI was added to the catalytic system, only 15.1% Rh B was degraded within

30 min. As KI captures both types of radicals, it could not be said which radical played the major role in the degradation process. When methanol was added to the catalytic system, only 66.5% of the dye was degraded within 30 min. When TBA was added, the Rh B can be degraded up to 99%. The addition of TBA quencher has little effect on the degradation of dye. The results indicated that sulfate radical played major role in the degradation of Rh B. The mechanism of activating PMS by PI/PAN@ZIF-67 sponge to generate free radical degradation of Rh B is shown in Figure S9, Supporting Information. The degradation mechanism of Rh B by the attack of ROS generating several different intermediates through de-ethylation, followed by deamination, dealkylation, decarboxylation, and chromophore cleavage to form other smaller molecule intermediates, is described in the literature. Finally, these small molecules are further mineralized by ROS into H_2O and CO_2.[27]

For any practical sustainable application, it is important that the catalysts are stable and reusable. **Figure 7** shows the degradation efficiency after reusing the regenerated PI/PAN@ZIF-67 sponge. After the first degradation cycle, the PI/PAN@ZIF-67 sponge only needs to be removed from the reaction solution with tweezers. There is no need for elaborate centrifugation or filtration. It is very simple and convenient. Then wash it three times with water and methanol respectively. After vacuum drying at 80 °C, it is directly used for the next cycle. As a result, after five cycles of use, degradation of the dye was negligibly reduced by only 3%. The XRD patterns of the PI/PAN@ZIF-67 sponge before and after use are also shown in Figure S10, Supporting Information. Through comparison, it can be found that the diffraction peaks of the used PI/PAN@ZIF-67sponge and fresh PI/PAN@ZIF-67 sponge are basically consistent, indicating that the PI/PAN@ZIF-67 sponge exhibits good stability during the degradation process of Rh B.

In addition, in order to further expand the application of PI/PAN@ZIF-67 sponge in real-life application, we constructed the PI/PAN@ZIF-67 sponge as a simple filtration device to evaluate its performance for the continuous treatment of dye wastewater solutions (**Figure 8**a). Thanks to the multilevel hierarchical porous structure of the PI/PAN@ZIF-67 sponge, the Rh B
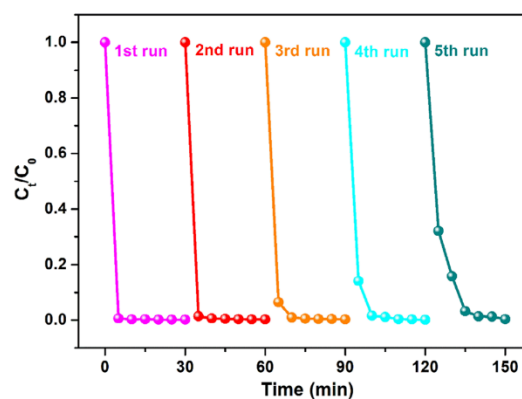

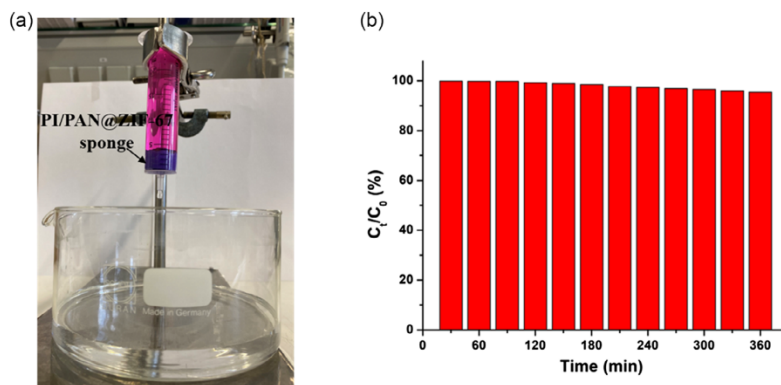**Figure 7.** Reusability test of PI/PAN@ZIF-67 sponge.

Figure 8. a) Photograph of the assembly showing degradation of Rh B by filtration process. PI/PAN@ZIF-67 sponge was fitted in a syringe for use as a catalytic filter to degrade Rh B. b) Continuous degradation experiment of Rh B with PI/PAN@ZIF-67 sponge as a filter. Reaction condition: pH = 7.0, 25 °C, dye (Rh B) concentration = 25 mg L^{-1}, PMS concentration = 1.5 mM.

solution can quickly pass through the PI/PAN@ZIF-67 sponge under self-gravity and its catalytic action provided a clear solution after passing through the sponge. The removal efficiency of Rh B is still as high as 95% after the filter device continuously treats the Rh B solution for 6 h (as shown in Figure 8b, Video 1, Supporting Information). As a result, the PI/PAN@ZIF-67 sponge can also be used as a catalytic filter to activate PMS for the degradation of dyes which makes it promising for scaling up in the future.

Although the present work was carried out using Rh B as an exemplary dye, our system should be valid for the degradation of other dyes, such as methylene blue, acid yellow-17 (AY), and orange II (AO7) that are known to undergo degradation by PMS activation.[28]

3. Conclusion

In this work, we prepared PI/PAN@ZIF-67 sponges with high ZIF-67 loading (up to 72 wt%), multilayered, and hierarchical macro–microporous honeycomb structure by in situ growth of ZIF-67 on the surface of PI short fibers. The 3D porous framework and high ZIF-67 loading provided the sponge with excellent mechanical properties and compression resistance, making the PI/PAN@ZIF-67 sponge reusable for practical use. The PI/PAN@ZIF-67 sponge exhibited high efficiency in the removal of organic dye by PMS activation. We explored that the optimal conditions for PI/PAN@ZIF-67 sponge to activate PMS to degrade Rh B organic dye were pH = 7, PMS = 1.5 mM, catalyst (PI/PAN@ZIF-67 sponge) = 100 mg L^{-1}, and the initial concentration of dye was 50 mg L^{-1}. Also, filtration experiments using PI/PAN@ZIF-67 sponge as a catalytic filter were very promising. This study opens new opportunities to explore MOF-based materials in the form of porous robust 3D sponges for water remediation. Furthermore, this strategy can also be applied to prepare monolithic materials of other types of MOFs and is expected to be suitable for other applications as well.

4. Experimental Section

Materials: PAN ($M_w = 80\,000$) and PI electrospun nonwovens were provided by Jiangxi Xiancai Nanofiber Technology Co., Ltd; cobaltous nitrate hexahydrate ($Co(NO_3)_2 \cdot 6H_2O$) and KI were purchased from Alfa Aesar. 2-MeIM and Oxone ($2KHSO_5 \cdot KHSO_4 \cdot K_2SO_4$) were brought from Thermo Fisher Scientific. Rh B was purchased from Sigma–Aldrich. DMSO ($\geq$99.7%), MeOH ($\geq$99.7%), and TBA ($\geq$99.7%) were supplied by Fisher Chemical company. All reagents were used without further purification.

Preparation of PI Short Fibers: PI short fibers were prepared by cutting PI electrospun nonwoven through a mechanical cutting process. Briefly, 10 g of PI electrospun nonwovens were first cut with scissors into small pieces and put into 1 L of solvent consisting of isopropanol/water (v/v = 3/1). The mixture was cooled using liquid nitrogen and then cut with a mechanical cutter (Robot Coupe Blixer 4, Rudolf Lange GmbH & Co. KG) at 3000 rpm for 25 h. Then, short PI fibers were filtered and freeze-dried for 24–36 h.

Preparation ZIF-67 Particles: ZIF-67 particles were prepared based on the literature that has been reported with a little modification.[29] In brief, 0.145 g cobaltous nitrate hexahydrate was dissolved in 10 mL of Milli-Q water (designated as solution A); 2.37 g 2-methylimidazole was dissolved in 10 mL of Milli-Q water (designated as solution B). Then solution B was quickly poured into solution A and stirred at room temperature for 24 h to obtain purple particles. The purple particles were collected by centrifugation, washed three times with water and methanol, respectively, and finally, dried at 80 °C in the oven to obtain ZIF-67 particles.

Preparation of Template PI/PAN Sponge: 0.5 g PI short fibers and 0.5 g PAN were dissolved in 12.5 mL DMSO in a 25 mL flask. The mixture was cooled to −20 °C in a refrigerator for 2 h. Afterward, it was freeze-dried to get the PI/PAN sponge.

Preparation of PI/PAN@ZIF-67 Sponge: In the first step, a PI/PAN@Co^{2+} sponge was prepared using the same method as described above for PI/PAN sponge. Briefly, 0.1 g PI short fibers, 0.1 g PAN, and 0.1 g Co(NO$_3$)$_2 \cdot 6H_2O$ were dissolved in 25 mL DMSO in a 50 mL flask. Then free-drying after cooling to −20 °C provided PI/PAN@Co^{2+} sponge. 0.145 g of Co nitrate was dissolved in 10 mL of Mili-Q water, which was designated as solution A. Subsequently, the PI/PAN@Co^{2+} sponge was placed in solution A and allowed to stand for 2 h. 2.32 g of 2-methylimidazole was dissolved in Mili-Q 10 mL of water (designated as solution B). Afterward, solution B was quickly poured into solution A. The mixed solution with the sponge inside was stirred at room temperature for 24 h to

2300218 (7 of 9)

give a purple sponge. Finally, the sponge was washed with water and methanol several times to remove excess of unreacted materials and dried at 80 °C to obtain PI/PAN@ZIF-67 sponge.

Catalytic Batch Experiments: All degradation experiments were carried out in 150 mL glass containers with magnetic stirring at 300 rpm. The pH value of the solution was adjusted by adding 0.1 M HCl and 0.1 M NaOH, respectively. Typically, a known amount of PI/PAN@ZIF-67 sponge was added to 100 mL of 50 mg L^{-1} Rh B solution. Subsequently, a certain amount of PMS was added to the solution and the time was noted. Every 5 min 1 mL sample was pipetted out, quenched with 0.5 mL methanol. Then, the degradation of the Rh B was measured using a UV–vis spectrophotometer at a wavelength of 555 nm. The degradation efficiency of Rh B was calculated according to Equation (1)

$$R\% = \frac{100\% \times (C_0 - C_t)}{C_0} \qquad (1)$$

where R is the degradation efficiency of Rh B (%), and C_0 and C_t are the concentrations of Rh B at time 0 and time t (mg L^{-1}), respectively. And the kinetics of Rh B degradation process was investigated according to the pseudo first-order kinetics Equation (2)

$$-\ln(C_t/C_0) = kt \qquad (2)$$

in which k is a rate constant and t is the degradation time (min). Besides, all batch experiments were repeated, and the average value with the standard deviation was presented for the results.

Reusability of Sponges: After the initial degradation experiment, the PI/PAN@ZIF-67 sponge was taken out from the reaction solution using tweezers, followed by simple cleaning with water and methanol. It was directly used for the next cycle after drying.

Continuous Flow Catalytic Test Using Sponge as Catalytic Filter: The sponge was also tested as a catalytic filter. For this, the PI/PAN@ZIF-67 sponge with a diameter of 2.5 cm and a height of 1.5 cm was loaded in a 20 mL plastic syringe, and the Rh B solution (25 mg L^{-1}) containing PMS (1.5 mM) was filtered under the action of gravity, during which the Rh B solution was continuously added to ensure that it can be continuously filtered, and the filtered solution was collected and analyzed to determine the concentration as described above.

Supporting Information

Supporting Information is available from the Wiley Online Library or from the author.

Conflict of Interest

The authors declare no conflict of interest.

Data Availability Statement

The data that support the findings of this study are available in the Supporting Information of this article.

[1] a) J. Wang, M. Gao, T. Shen, M. Yu, Y. Xiang, J. Liu, *J. Hazard. Mater.* **2019**, *366*, 501; b) D. Yaseen, M. Scholz, *Int. J. Environ. Sci. Technol.* **2019**, *16*, 1193; c) B. Zhu, H. Cheng, J. Ma, Y. Qin, Y. Kong, S. Komarneni, *Mater. Lett.* **2020**, *261*, 127099; d) Y. Lv, C. Zhang, A. He, S. J. Yang, G. P. Wu, S. B. Darling, Z. K. Xu, *Adv. Funct. Mater.* **2017**, *27*, 1700251.

[2] a) Z. H. Zhu, Y. Liu, C. Song, Y. Hu, G. Feng, B. Z. Tang, *ACS Nano* **2021**, *16*, 1346; b) D. Lan, H. Zhu, J. Zhang, S. Li, Q. Chen, C. Wang, T. Wu, M. Xu, *Chemosphere* **2022**, *293*, 133464; c) P. Chanikya, P. Nidheesh, D. S. Babu, A. Gopinath, M. S. Kumar, *Sep. Purif. Technol.* **2021**, *254*, 117570; d) Y. Chen, D. Zhao, T. Sun, C. Cai, Y. Dong, *J. Environ. Chem. Eng.* **2023**, *11*, 110353.

[3] a) Y. Kang, J. Jang, S. Kim, J. Lim, Y. Lee, I. S. Kim, *ACS Appl. Mater. Interfaces* **2020**, *12*, 36148; b) F. Yang, M. Du, K. Yin, Z. Qiu, J. Zhao, C. Liu, G. Zhang, Y. Gao, H. Pang, *Small* **2022**, *18*, 2105715; c) Z. Yin, C. Cui, H. Chen, X. Yu, W. Qian, *Small* **2020**, *16*, 1902301; d) G. Wu, Q. Liu, J. Wang, S. Xia, X. Huang, J. Han, W. Xing, *Colloids Surf. A Physicochem. Eng. Asp.* **2022**, *653*, 130048.

[4] a) J. Rostami, T. Benselfelt, L. Maddalena, C. Avci, F. A. Sellman, G. Cinar Ciftci, P. A. Larsson, F. Carosio, F. Akhtar, W. Tian, *Adv. Mater.* **2022**, *34*, 2204800; b) F. Haase, P. Hirschle, R. Freund, S. Furukawa, Z. Ji, S. Wuttke, *Angew. Chem. Int. Ed.* **2020**, *59*, 22350.

[5] X. Li, B. Wang, Y. Cao, S. Zhao, H. Wang, X. Feng, J. Zhou, X. Ma, *ACS Sustainable Chem. Eng.* **2019**, *7*, 4548.

[6] a) R. Guo, X. Cai, H. Liu, Z. Yang, Y. Meng, F. Chen, Y. Li, B. Wang, *Environ. Sci. Technol.* **2019**, *53*, 2705; b) F. Ahmadijokani, H. Molavi, A. Bahi, R. Fernández, P. Alaee, S. Wu, M. Arjmand, *Adv. Funct. Mater.* **2022**, *32*, 2207723.

[7] M. Peydayesh, T. Suta, M. Usuelli, S. Handschin, G. Canelli, M. Bagnani, R. Mezzenga, *Environ. Sci. Technol.* **2021**, *55*, 8848.

[8] a) V. K. Sharma, M. Feng, *J. Hazard. Mater.* **2019**, *372*, 3; b) A. Yusuf, A. Giwa, J. O. Eniola, H. K. Amusa, M. R. Bilad, *J. Hazard. Mater.* **2022**, 100108; c) L. Zhu, J. Ji, J. Liu, J. Zhang, *Angew. Chem. Int. Ed.* **2020**, *132*, 14072; d) J. Wang, Z. Zhang, F. Wu, W. Sun, F. Wang, J. Han, G. Wu, *Opt. Mater.* **2023**, *143*, 114156.

[9] a) X. Du, M. Zhou, *Chem. Eng. J.* **2021**, *403*, 126346; b) Z. Xiong, Y. Jiang, Z. Wu, G. Yao, B. Lai, *Chem. Eng. J.* **2021**, *421*, 127863; c) U. Ushani, X. Lu, J. Wang, Z. Zhang, J. Dai, Y. Tan, S. Wang, W. Li, C. Niu, T. Cai, *Chem. Eng. J.* **2020**, *402*, 126232.

[10] a) A. Hassani, J. Scaria, F. Ghanbari, P. J. Nidheesh, *Environ. Res.* **2022**, 114789; b) W.-D. Oh, Z. Dong, T.-T. Lim, *Appl. Catal. B* **2016**, *194*, 169; c) L. Ismail, C. Ferronato, L. Fine, F. Jaber, J.-M. Chovelon, *Appl. Catal. B* **2017**, *201*, 573; d) G. Tai, G. Li, Z. Cai, Y. Pan, J. Han, J. Shi, G. Wu, *Colloids Surf. A Physicochem. Eng. Asp.* **2023**, 131925.

[11] a) C. Wang, J. Kim, V. Malgras, J. Na, J. Lin, J. You, M. Zhang, J. Li, Y. Yamauchi, *Small* **2019**, *15*, 1900744; b) G. Li, Z. Cai, K. Su, Y. Zhao, Y. Zhu, J. Han, G. Wu, *Colloids Surf. A Physicochem. Eng. Asp.* **2023**, *677*, 132353.

[12] a) J. Guo, Y. Qin, Y. Zhu, X. Zhang, C. Long, M. Zhao, Z. Tang, *Chem. Soc. Rev.* **2021**, *50*, 5366; b) G. Li, P. Yan, L. Zhang, H.-C. Zhou, H.-L. Jiang, *Chem. Rev.* **2021**, *121*, 12278; c) Y. Ye, L. Gong, S. Xiang, Z. Zhang, B. Chen, *Adv. Mater.* **2020**, *32*, 1907090;

d) R. Banerjee, A. Phan, B. Wang, C. Knobler, H. Furukawa, M. O'Keeffe, O. M. Yaghi, *Science* **2008**, *319*, 939;

[13] a) X.-W. Zhang, M.-Y. Lan, F. Wang, X.-H. Yi, C.-C. Wang, *J. Environ. Chem. Eng.* **2022**, *10*, 107997; b) M. Zhang, C. Xiao, C. Zhang, J. Qi, C. Wang, X. Sun, L. Wang, Q. Xu, J. Li, *ACS Est. Eng.* **2021**, *1*, 249.

[14] a) W. Ren, J. Gao, C. Lei, Y. Xie, Y. Cai, Q. Ni, J. Yao, *Chem. Eng. J.* **2018**, *349*, 766; b) A. Du, H. Fu, P. Wang, C. Zhao, C.-C. Wang, *J. Hazard. Mater.* **2022**, *426*, 128134.

[15] C. Wang, P. Cheng, Y. Yao, Y. Yamauchi, X. Yan, J. Li, J. Na, *J. Hazard. Mater.* **2020**, *392*, 122164.

[16] L. Peng, X. Gong, X. Wang, Z. Yang, Y. Liu, *RSC Adv.* **2018**, *8*, 26377.

[17] C.-H. Wu, W.-C. Yun, T. Wi-Afedzi, K.-Y. Lin, *J. Colloid. Interface Sci.* **2018**, *514*, 262.

[18] a) X. Jia, M. Peydayesh, Q. Huang, R. Mezzenga, *Small* **2022**, *18*, 2105502; b) K. Ma, Y. H. Cheung, K. O. Kirlikovali, H. Xie, K. B. Idrees, X. Wang, T. Islamoglu, J. H. Xin, O. K. Farha, *Adv. Mater.* **2023**, 2300951.

[19] a) Q. Gao, T. Tran, X. Liao, S. Rosenfeldt, C. Gao, H. Hou, M. Retsch, S. Agarwal, A. Greiner, *ACS Appl. Mater. Interfaces* **2022**, *14*, 19918; b) S. Jiang, B. Uch, S. Agarwal, A. Greiner, *ACS Appl. Mater. Interfaces*

[20] J. Y. Cheong, L. Benker, J. Zhu, D.-Y. Youn, H. Hou, S. Agarwal, I.-D. Kim, A. Greiner, *Carbon* **2019**, *154*, 363.

[21] C. Ding, M. Breunig, J. Timm, R. Marschall, J. Senker, S. Agarwal, *Adv. Funct. Mater.* **2021**, *31*, 2106507.

[22] Q. Yang, S. Ren, Q. Zhao, R. Lu, C. Hang, Z. Chen, H. Zheng, *Chem. Eng. J.* **2018**, *333*, 49.

[23] C. A. Pryde, *Polym. Chem.* **1989**, *27*, 711.

[24] Y. Du, C. Ding, J. Timm, R. Marschall, S. Agarwal, *Chemcatchem.* **2022**, *14*, e202201040.

[25] K.-Y. A. Lin, H.-A. Chang, *J. Taiwan Inst. Chem. Eng.* **2015**, *53*, 40.

[26] K.-Y. A. Lin, F.-K. Hsu, W.-D. Lee, *J. Mater. Chem. A* **2015**, *3*, 9480.

[27] a) Y. Tian, Y. Wu, Q. Yi, L. Zhou, J. Lei, L. Wang, J. Zhang, *Chem. Eng. J.* **2021**, *425*, 128644; b) F. Wu, C. Zhou, G. Tai, Y. Ma, X. Yang, Y. Pan, G. Wu, *ACS Appl. Nano Mater.* **2023**, *6*, 17814.

[28] a) C. Wang, H. Wang, R. Luo, C. Liu, J. Li, X. Sun, J. Shen, W. Han, L. Wang, *Chem. Eng. J.* **2017**, *330*, 262; b) S. Zhang, M. Zhao, H. Li, C. Hou, M. Du, *Cellulose.* **2021**, *28*, 3585; c) D. Liu, J. Yin, H. Tang, H. Wang, S. Liu, T. Huang, Z. Xie, *Sep. Purif. Technol.* **2021**, *279*, 119755.

[29] J. Qian, F. Sun, L. Qin, *Mater. Lett.* **2012**, *82*, 220.

2017, *9*, 32308; c) C. Ding, Y. Du, S. Agarwal, *Adv. Funct. Mater.* **2023**, 2309938.

Supporting Information

Sustainable Hierarchically Porous Reusable Metal–Organic Framework Sponge as a Heterogeneous Catalyst and Catalytic Filter for Degradation of Organic Dyes

Yingying Du, Chenhui Ding, Seema Agarwal*

Y. Du, C. Ding, Prof. S. Agarwal
Macromolecular Chemistry and Bavarian Polymer Institute
University of Bayreuth
Universitätsstrasse 30, 95440 Bayreuth, Germany
E-mail: agarwal@uni-bayreuth.de

Characterization and instruments

The morphology and structure of the samples were investigated by scanning electron microscopy (SEM, FEI Quanta FEG 250) with a Zeiss LEO 1530, operating at an acceleration voltage of 3 kV employing an Everhart-Thornley secondary electron detector. The X-ray diffraction (XRD) patterns of all the samples were obtained on a Bragg-Brentano type diffractometer (XPERT-PRO, PANalytical B.V.) with Cu-Kα X-ray radiation (λ = 1.540598 Å), and each XRD pattern was scanned over a range of 2θ = 2° to 40° at a rate of 0.5° min^{-1}. The functional groups and chemical structures of all the samples were performed using Fourier transform infrared spectra (FT-IR). The FT-IR spectroscopy was measured using a spectrometer (Digilab Excalibur FTS-3000) in the wavelength range of 4000 cm^{-1} to 400 cm^{-1}. The degradation of Rhodamine B was evaluated using a UV-vis spectrophotometer (Jasco Spectrometer V-670) in the range of 480-650 nm (scan speed 200 nm min^{-1}). The characteristic peak of Rhodamine B in UV-vis spectrophotometer is at 555 nm. The mechanical properties of the PI/PAN sponge and PI/PAN@ZIF-67 sponge were investigated by the tensile tester. machine (ZwickiLine Z0.5; BT1-FR0.5TN.D14; Zwick / Roell, Germany). The compression testing and cyclic compression testing of the composite sponges at a compression rate of 8 mm min^{-1}.
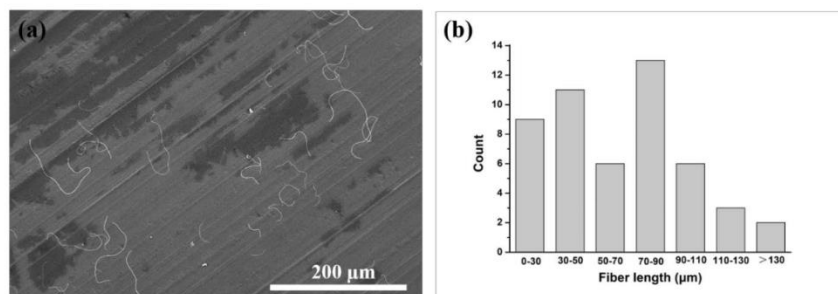
Figure S1. (a) SEM image of PI short fibers. Fibers average diameter (d) = 521 ± 143.0 nm and fibers length (L) = 77 ± 33 μm. (b) Fiber length distribution of the PI short fibers.
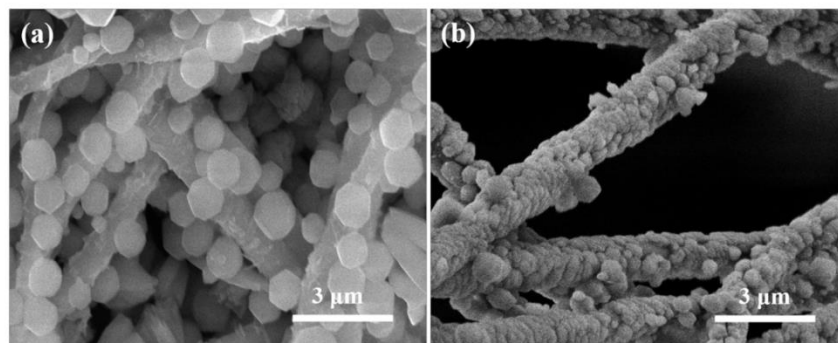

Figure S2. SEM image of PI/PAN@ZIF-67 sponge (a) During synthesis the solution was not stirred (b) During synthesis the solution was stirred.
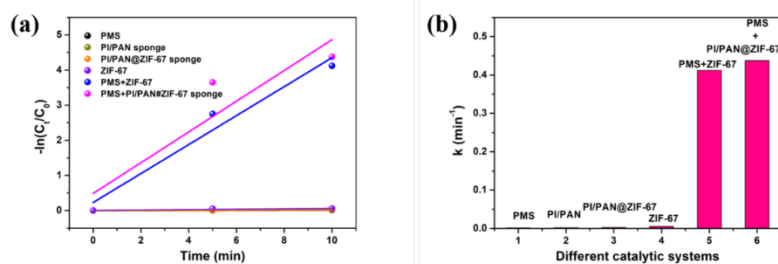
2

223

WILEY-VCH

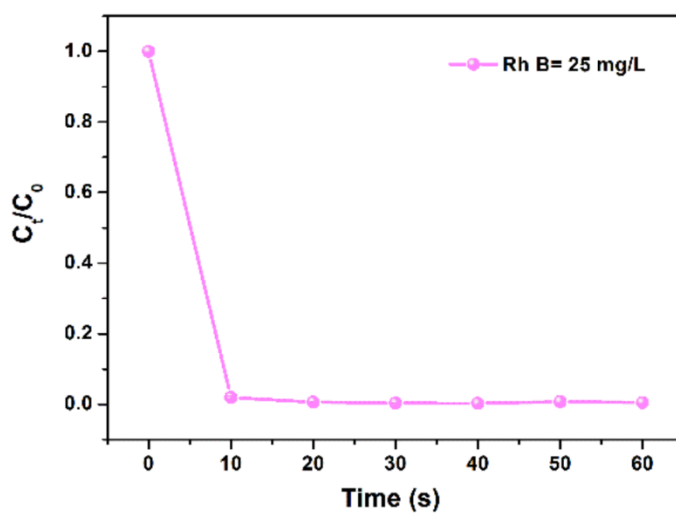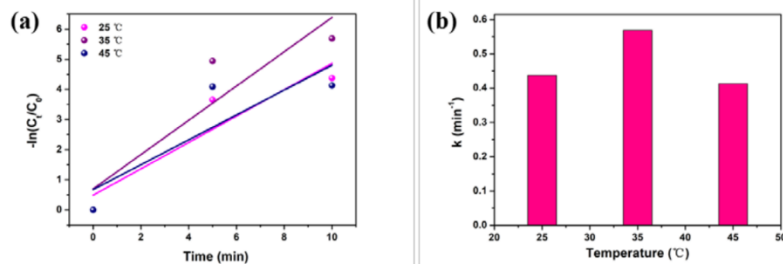**Figure S3.** (a) The kinetic rates and (b) the first kinetic constants of Rh B degradation under different catalytic conditions.

Figure S4. Degradation of Rh B. Reaction condition: Rh B = 25 mg L^{-1}, PMS = 1.5 mM, PI/PAN@ZIF-67 sponge =100 mg L^{-1} , pH=7.0 and temperature =25 °C.

3
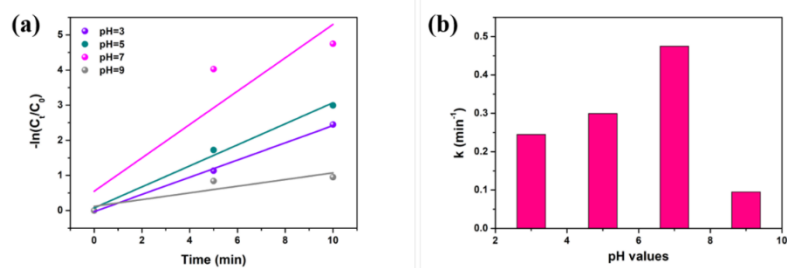
Figure S5. (a) The kinetic rates and (b) the first kinetic constants of Rh B degradation under different pH values.
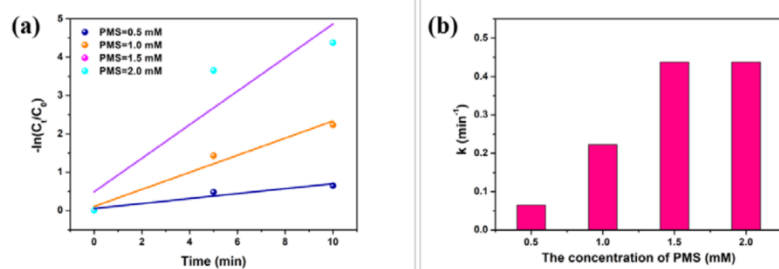
Figure S6. (a) The kinetic rates and (b) the first kinetic constants of Rh B degradation under different concentrations of PMS.

4
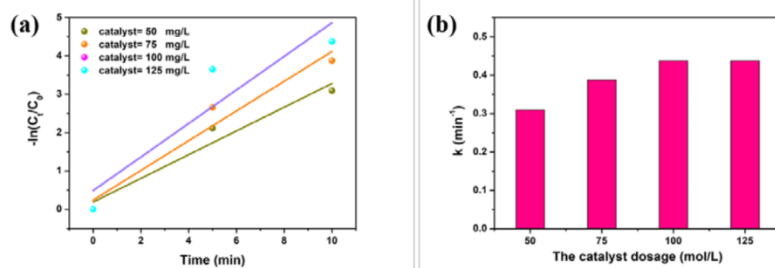
Fig. S7. (a) The kinetic rates and (b) the first kinetic constants of Rh B degradation under different catalyst dosage.

Fig. S8. (a) The kinetic rates and (b) the first kinetic constants of Rh B degradation under different temperatures.

5

WILEY-VCH

$$Co^{2+} + HSO_5^- \rightarrow Co^{3+} + SO_4^{\bullet-} + OH^- \tag{1}$$

$$SO_4^{\bullet-} + OH^- \rightarrow \cdot OH + SO_4^{2-} \tag{2}$$

$$Co^{3+} + HSO_5^- \rightarrow Co^{2+} + SO_4^{\bullet-} + H^+ \tag{3}$$

$$SO4^{\bullet-} + \cdot OH + dye \rightarrow .... H_2O + CO_2 \tag{4}$$

Equation S(1)-S(4). Cyclic transformation of cobalt ion (divalent and trivalent) in ZIF-67 activates PMS to generate sulfate radicals and hydroxide radicals that degrades organic dyes.
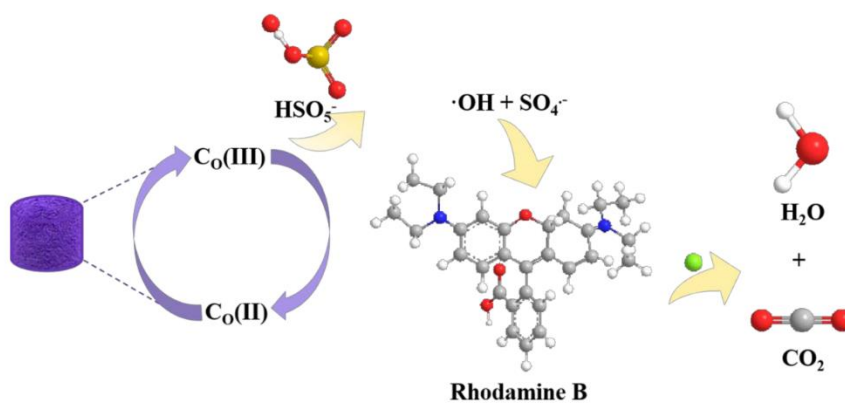
Fig. S9. Schematic diagram of the mechanism of PI/PAN@ZIF-67 sponge to activated PMS to degrade Rhodamine B.

6

227

WILEY-VCH
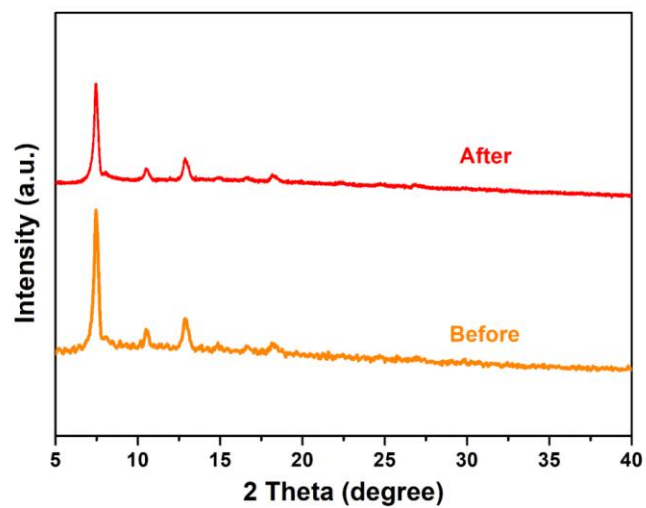
Figure S10. The XRD patterns of PI/PAN@ZIF-67 sponge before and after use.

7

Table S1. The kinetic constant values under different conditions.

Sample/Condition	Kinetic constant (min^{-1})
PMS	0.00158
PI/PAN sponge	0.00263
PI/PAN@ZIF-67 sponge	0.00263
ZIF-67	0.00565
PMS+ZIF-67 particles	0.41227
PMS+ PI/PAN@ZIF-67 sponge	0.43764
pH=3.0	0.24498
pH=5.0	0.29919
pH=7.0	0.47467
pH=9.0	0.09529
PMS content = 0.5 mM	0.06483
PMS content= 1.0 mM	0.22303
PMS content = 1.5 mM	0.43764
PMS content = 2.0 mM	0.43764
Catalyst dosage = 50 mg/L	0.30922
Catalyst dosage = 75 mg/L	0.38776
Catalyst dosage = 100 mg/L	0.43764
Catalyst dosage = 125 mg/L	0.43764
Dye solution = 25 mg/L	0.49879
Dye solution = 50 mg/L	0.43764
Dye solution = 75 mg/L	0.36378
Dye solution = 100 mg/L	0.18084
T= 25 ℃	0.43764
T= 35 ℃	0.56899
T= 45 ℃	0.41308

8

229

5. Acknowledgments

As time swiftly passes, I find myself at the culmination of my doctoral thesis, and I wish to express my heartfelt gratitude to all of you. I have been fortunate to receive care, support, and assistance from many individuals. It is this profound kindness that has played a crucial role in enabling me to successfully complete my doctoral studies.

First and foremost, I would like to express my sincere gratitude to my supervisor (academic mother) Professor Seema Agarwal. You have always been the guiding light on my academic path. Under your careful guidance, I not only learned professional knowledge, but also developed my ability to think independently and solve problems. And it made me full of enthusiasm and confidence in scientific research. At the same time, I would also like to thank you for your concern for my life and allowing me to feel the family affection from my elders in a foreign country.

Secondly, I would also like to express sincere gratitude to Professor Andreas Greiner for your invaluable suggestions on my work. Your tolerance and advice, particularly when I make mistakes, are invaluable treasures in my academic and personal growth.

I would like to express my gratitude to Professor Jürgen Senker for your suggestions on my work. At the same time, I sincerely thank Professor Haoqing Hou for his recommendation, which gave me the opportunity to complete my PhD in the MCII group.

I am very grateful to my collaborators, Marion Breunig for solid-state NMR measurements and data analysis, and Jana Timm for surface area measurements and data analysis.

I would like to thank Dr. Ulrich Mansfeld and Dr. Sabine Rosenfeldt for their training, which enabled me to use SEM and XRD proficiently.

Many thanks to all my colleagues in the MCII group, Dr. Holger Schmalz, Dr. Adrian Wambach, Dr. Qiang Gao, Dr. Christian Hils, Dr. Reza Gharibi, Dr. Ann-Kathrin Müller, Dr. Jian Zhu, Dr. Nikola Majstorovic, Dr. Simon Neumann, Dr. Pin Hu, Dr. Pazhaniswamy Sivaraj, Dr. Chao Deng, Sören Schumacher, Elmar Sehl, Rist, Maximilian, Joshi Sagar Avadhutrao, Yuanhu Zhang, Benedict Petran, Xue Lin, Anil

5. Acknowledgments

6. Eidesstattliche Versicherungen und Erklärungen

(§ 9 Satz 2 Nr. 3 PromO BayNAT)

Hiermit versichere ich eidesstattlich, dass ich die Arbeit selbstständig verfasst und keine anderen als die von mir angegebenen Quellen und Hilfsmittel benutzt habe (vgl. Art. 97 Abs. 1 Satz 8 BayHIG).

(§ 9 Satz 2 Nr. 3 PromO BayNAT)

Hiermit erkläre ich, dass ich die Dissertation nicht bereits zur Erlangung eines akademischen Grades eingereicht habe und dass ich nicht bereits diese oder eine gleichartige Doktorprüfung endgültig nicht bestanden habe.

(§ 9 Satz 2 Nr. 4 PromO BayNAT)

Hiermit erkläre ich, dass ich Hilfe von gewerblichen Promotionsberatern bzw. -vermittlern oder ähnlichen Dienstleistern weder bisher in Anspruch genommen habe noch künftig in Anspruch nehmen werde.

(§ 9 Satz 2 Nr. 7 PromO BayNAT)

Hiermit erkläre ich mein Einverständnis, dass die elektronische Fassung meiner Dissertation unter Wahrung meiner Urheberrechte und des Datenschutzes einer gesonderten Überprüfung unterzogen werden kann.

(§ 9 Satz 2 Nr. 8 PromO BayNAT)

Hiermit erkläre ich mein Einverständnis, dass bei Verdacht wissenschaftlichen Fehlverhaltens Ermittlungen durch universitätsinterne Organe der wissenschaftlichen Selbstkontrolle stattfinden können.

………………………………………………………………………….

Ort, Datum, Unterschrift

233